Evaluation and Design Aspects of Magnetic Gears and Magnetically Geared Electrical Machines

by

Stiaan Gerber

Dissertation approved for the degree of Doctor of Philosophy in the
Faculty of Engineering at Stellenbosch University

Department of Electrical and Electronic Engineering
Faculty of Engineering
Stellenbosch University
Private Bag X1, 7602 Matieland, South Africa.

Promoter: Prof. R-J. Wang

December 2015

Declaration

By submitting this dissertation electronically, I declare that the entirety of the work contained therein is my own, original work, that I am the sole author thereof (save to the extent explicitly otherwise stated), that reproduction and publication thereof by Stellenbosch University will not infringe any third party rights and that I have not previously in its entirety or in part submitted it for obtaining any qualification.

Signature: ....
S. Gerber

Date: 12 October 2015

Abstract

Evaluation and Design Aspects of Magnetic Gears and Magnetically Geared Electrical Machines

S. Gerber

Department of Electrical and Electronic Engineering
Faculty of Engineering
Stellenbosch University
Private Bag X1, 7602 Matieland, South Africa.

Dissertation: PhD (Electrical Engineering)

December 2015

In the past decade, magnetic gears and magnetically geared electrical machines have emerged as electromechanical devices with exceptionally high torque densities. Their distinct advantages such as low maintenance requirements and overload protection make these devices attractive for many applications. Although significant amount of research has been carried out in this fast-moving field, there are still many design related aspects that have not been thoroughly investigated. This study is concerned with the design optimization and performance evaluation of these devices.

An efficient design optimization methodology, specifically aimed at magnetically geared machines (MGMs), is proposed. This design approach allows the components of these integrated machines to be appropriately matched. Challenges associated with the accurate modeling of these special machines, such as the prediction of the impact of end-effects and the high computational cost of simulating movement, are investigated. The proposed design methodology is successfully applied to the design of two different MGMs, of which one features a novel rotor structure. Prototypes based on the designs have been constructed and experimentally evaluated. There is generally a good correlation between the predicted and measured performance results. A method of analyzing the operating points of these machines is also presented.

In addition to the two MGMs, a vernier machine, which is based on similar operating principles, is designed, constructed and experimentally evaluated.

A detailed comparison of these machines with a more conventional direct-drive permanent magnet machine is conducted in order to assess their respective advantages and disadvantages. The comparison considers small machines with an active stack length of 50 mm and an outer diameter of 140 mm. In this fixed-volume comparison, it is found that the MGMs are superior in terms of their torque capability and efficiency. The vernier machine also has a good efficiency and produces the highest torque per volume of magnet material.

Based on the merits of MGMs that are demonstrated in this study, further development of these machines is warranted.

Uittreksel

Evaluering en Ontwerpsaspekte van Magnetiese Ratte en Magneties-geratte Elektriese Masjiene

S. Gerber
Departement Elektriese en Elektroniese Ingenieurswese,
Universiteit van Stellenbosch,
Privaatsak X1, 7602, Matieland, Suid-Afrika.

Proefskrif: PhD (Elektriese Ingenieurswese)

Desember 2015

In die afgelope dekade het magnetiese ratte en magneties-geratte elektriese masjiene na vore gekom as toestelle met besondere hoë draaimomentdigthede. Hul merkbare voordele soos lae onderhoudsvereistes en oorbelastingbeskerming maak hierdie toestelle aantreklik vir baie toepassings. Alhoewel 'n beduidende hoeveelheid navorsing reeds in hierdie vinnig-bewegende veld gedoen is, is daar steeds verskeie ontwerpsaspekte wat nie behoorlik ondersoek is nie. Hierdie studie is gemoeid met die ontwerp optimering en werkverrigting evaluasie van hierdie toestelle.

'n Doeltreffende ontwerp optimeringsmetodiek wat spesifiek op magneties-geratte masjiene (MGMe) gemik is, word voorgestel. Dié ontwerpsbenadering maak dit moontlik om te verseker dat die komponente van hierdie geïntegreerde masjiene onderling geskik is. Uitdagings wat met die akkurate modellering van hierdie spesiale masjiene geassosieer word, soos die voorspelling van die impak van eindeffekte en die hoë berekeningskoste van simulasies met beweging, word ondersoek. Die voorgestelde ontwerpsmetodiek word suksesvol toegepas in die ontwerp van twee verskillende MGMe, waarvan een 'n nuwe rotorstruktuur het. Prototipes gebaseer op hierdie ontwerpe is vervaardig en eksperimenteel geëvalueer. In die algemeen is daar 'n goeie korrelasie tussen die voorspelde en gemete werkverrigtingsresultate. 'n Metode waarmee die bedryfspunte van hierdie masjiene geanaliseer kan word, word ook voorgelê.

Bykomend tot die twee MGMe is 'n vernier masjien, wat se werking op soortgelyke beginsels berus, ontwerp, vervaardig en eksperimenteel geëvalueer.

'n Gedetailleerde vergelyking van hierdie masjiene met 'n meer konvensionele permanente magneet masjien is uitgevoer om hul onderskeie voor- en nadele te evalueer. Die vergelyking beskou klein masjiene met 'n aktiewe stapel lengte van 50 mm and 'n buite diameter van 140 mm. In hierdie vaste-volume vergelyking word bevind dat die MGMe uitstyg in terme van hul draaimoment vermoë en benuttingsgraad. Die vernier masjien het ook 'n goeie benuttingsgraad en lewer die hoogste draaimoment per volume van magneet materiaal.

Verdere ontwikkeling van MGMe kan geregverdig word gebaseer op die meriete van hierdie masjiene wat in hierdie studie gedemonstreer is.

Acknowledgements

I would like to express my gratitude towards the following people and institutions whose support have been of great value to me:

Prof. Rong-Jie Wang, my promoter, for his support and guidance.

Pushman Tlali, Alex Matthee, Mario Slabber and Lodewijk Brönn for their valuable contributions.

Petro Petzer, André Swart, Murray Jumat and Howard Koopman for assistance and advice in manufacturing of prototypes and test benches.

Huba Boshoff and the staff of the post-graduate and international office at Stellenbosch University for supporting my exchange in Germany.

Wai Ying Fargel at the international office of the Technische Hochschule Nürnberg Georg Simon Ohm for her administrative support.

Jacques Germishuizen and his colleagues at Loher GmbH (Siemens) in Ruhstorf, Germany for receiving me.

The National Research Foundation of South Africa for financial support.

ABB Corporate Research in Sweden for financial support.

Fellow students at the EMLAB for interesting distractions.

My parents whose support I can always count on.

Sunett for sharing in life.

> *Enter his gates with thanksgiving and his courts with praise;*
> *give thanks to him and praise his name.*
> *For the Lord is good and his love endures forever;*
> *his faithfulness continues through all generations.*
>
> Psalm 100:4–5

List of publications

Local conferences

[1] S. Gerber and R-J. Wang, "Implementation of a moving band solver for finite element analysis of electrical machines," in *Southern African Universities Power Engineering Conference (SAUPEC)*, Durban, South Africa, January 2014.

[2] P.M. Tlali, S. Gerber, and R-J. Wang. "Gear ratio selection of an outer-stator magnetically geared machine," in *Southern African Universities Power Engineering Conference (SAUPEC)*, Durban, South Africa, January 2014.

[3] A. Matthee, S. Gerber, and R-J. Wang. "A high performance concentric magnetic gear," in *Southern African Universities Power Engineering Conference (SAUPEC)*, Pretoria, South Africa, January 2015.

International conferences

[4] S. Gerber and R-J. Wang. "Evaluation of a prototype magnetic gear," in *IEEE International Conference on Industrial Technology (ICIT)*, Cape Town, February 2013.

[5] S. Gerber and R-J. Wang. "Torque capability comparison of two magnetically geared PM machine topologies," in *IEEE International Conference on Industrial Technology (ICIT)*, Cape Town, February 2013.

[6] S. Gerber and R-J. Wang. "Design of a magnetically geared PM machine," in *Proc. 4th Int. Conf. Power Engineering, Energy and Electrical Drives*, Istanbul, May 2013.

[7] R-J. Wang, L. Brönn, S. Gerber, and P.M. Tlali. "Design and evaluation of a disc-type magnetically geared PM wind generator," in *Proc. 4th Int. Conf. Power Engineering, Energy and Electrical Drives*, Istanbul, May 2013.

[8] R-J. Wang and S. Gerber. "Magnetically geared wind generator technologies: Opportunities and challenges," in *International Conference on Applied Energy (ICAE)*, Pretoria, July 2013.

[9] S. Gerber and R-J. Wang. "Analysis of the end-effects in magnetic gears and magnetically geared machines," in *International Conference on Electrical Machines (ICEM)*, Berlin, September 2014.

[10] P.M. Tlali, R-J. Wang, and S. Gerber. "Magnetic gear technologies: A review," in *International Conference on Electrical Machines (ICEM)*, Berlin, September 2014.

[11] S. Gerber and R-J. Wang "Design and evaluation of a PM vernier machine," in *Energy Conversion Congress & Exposition (ECCE)*, Montreal, September 2015.

Journal Publications

[12] R-J. Wang and S. Gerber. “Magnetically geared wind generator technologies: Opportunities and challenges,” *Applied Energy*, 136:817–826, 2014.

[13] S. Gerber and R-J. Wang. “Evaluation of movement facilitating techniques for finite element analysis of magnetically geared electrical machines,” *IEEE Trans. Magn.*, 51(2), February 2015.

[14] S. Gerber and R-J. Wang. “Design and evaluation of a magnetically geared PM machine,” *IEEE. Trans. Magn.*, 51(8), April 2015.

[15] R-J. Wang, L. Brönn, S. Gerber, and P.M. Tlali. “An axial-flux magnetically geared PM wind generator,” *IEEJ. TEEE-D.*, 10(S1), October 2015.

[16] P.M. Tlali and S. Gerber and R-J. Wang. “Optimal design of an outer-stator magnetically geared permanent magnet machine,” *IEEE. Trans. Magn.*, 2015. (In press).

Vir my pa,
wat my altyd gemotiveer en gehelp het
om die beste te wees wat ek kan wees.

Brief Contents

Contents

Nomenclature

Electromagnetics

$\mathbf{A}$	Magnetic vector potential
$\mathbf{J}$	Current density
$\mathbf{H}$	Magnetic field intensity
$\mathbf{B}$	Magnetic flux density
W'	Co-energy
μ	Permeability
λ	Flux linkage
κ	Stacking factor

Modulation set

p_s	Number of sun gear pole-pairs
p_r	Number of ring gear pole-pairs
Q_m	Number of modulator segments
Q_s	Number of stator slots
G_{sm}	Gear ratio between sun gear and modulator with fixed ring gear
G_{sr}	Gear ratio between sun gear and ring gear with fixed modulator

Simple analytical model

θ_s	Sun gear position
θ_m	Modulator position
θ_r	Ring gear position
$\mathcal{F}_s$	Sun gear MMF
$\mathcal{F}_r$	Ring gear MMF
$\mathcal{P}_{avg}$	Average reluctance
$\mathcal{P}^l_{avg}$	Average reluctance per unit stack length
$\mathcal{P}_{mod}$	Modulating reluctance
$\mathcal{P}^l_{mod}$	Modulating reluctance per unit stack length

Equivalent circuit models

I_ϕ	Phase current
U_ϕ	Phase voltage
θ	Phase difference between terminal voltage and current
α	Current angle
ω	Electrical angular frequency

R_c	Core loss resistance
R_ϕ	Per phase resistance
L_s	Per phase synchronous inductance
L_d, L_q	Main dq inductances
L_e, L_{ed}, L_{eq}	Additional inductance due to end-windings (total, d-axis, q-axis)
λ_s	Flux linkage due to the sun gear magnets (vector defines the d-axis)
λ_r, λ_{rd}, λ_{rq}	Flux linkage due to the ring gear magnets (total, d-axis, q-axis)
λ_i, λ_{id}, λ_{iq}	Flux linkage due to the winding current (total, d-axis, q-axis)
λ_e, λ_{ed}, λ_{eq}	Additional flux linkage due to end-windings (total, d-axis, q-axis)
i_d, i_q	dq currents
u_d, u_q	dq terminal voltages

Magnetic gears and magnetically geared machines

T_s	Sun gear torque
T_m	Modulator torque
T'_m	Modulator stall torque
T_r	Ring gear torque
T_i	Stator torque
T'_i	Rated stator torque
ω_s	Sun gear angular velocity
ω_m	Modulator angular velocity
ω_r	Ring gear angular velocity
γ_i	Stator load factor
E_T	Torque end-effect ratio
E_{γ_i}	Stator load factor end-effect ratio

Geometric design variables

t_{sty}	Stator yoke thickness
t_{stt}	Stator tooth thickness
θ_{stb}	Stator slot base angle
θ_{sto}	Stator slot opening angle
β_{stp}	Stator tooth tip as fraction of tooth thickness
t_{sm}	Sun gear magnet thickness
t_{smi}	Sun gear inner magnet thickness (double sided configuration)
t_{sy}	Sun gear yoke thickness (double sided configuration)
t_{smo}	Sun gear outer magnet thickness (double sided configuration)
θ_{sm}	Sun gear magnet pitch (often expressed as fraction of pole pitch)
θ_{smi}	Sun gear inner magnet pitch (double sided configuration, fraction of pole pitch)
θ_{smo}	Sun gear outer magnet pitch (double sided configuration, fraction of pole pitch)
t_m	Modulator thickness
θ_{mi}	Modulator segment inner pitch (often expressed as fraction of pole pitch)
θ_{mo}	Modulator segment outer pitch (often expressed as fraction of pole pitch)
t_{rm}	Ring gear magnet thickness

t_{ry}	Ring gear yoke thickness
θ_{rm}	Ring gear magnet pitch (often expressed as fraction of pole pitch)
L	Stack length
D	Outer diameter
V_A	Active volume

Abbreviations

AGE	Air-gap element
CVT	Continuously variable transmission
FE	Finite element
FEA	Finite element analysis
FEM	Finite element method
FMMG	Flux-modulated magnetic gear
LCM	Lowest common multiple
MB	Moving band
MG	Magnetic gear
MGM	Magnetically geared machine
MMF	Magnetomotive force
MMFD	Modified method of feasible directions
PM	Permanent magnet
PSO	Particle swarm optimization
SQP	Sequential quadratic programming

List of Figures

List of Tables

Chapter 1

Introduction

1.1 Background

In the past decade, advances in magnetic gear technology have led to the development of a new class of electrical machine: magnetically geared machines. A magnetically geared machine (MGM) can be defined as an electrical machine which integrates a magnetic gear (MG) and a conventional permanent magnet (PM) machine in the same volume.[1] What sets these machines apart from other electrical machines is their high torque density. However, this being a new class of electrical machine, there are numerous possibilities and unanswered questions. These machines – their analysis, design and evaluation – are the subject of this thesis.

In order to fully appreciate the development of magnetically geared machines, an overview of the history of magnetic gears is provided in the following sections and it is explained how a breakthrough in magnetic gear design has led to the development of magnetically geared machines.

1.2 Early magnetic gear technology

The first recorded case of electromagnetic forces being used for geared torque transmission can be found in a patent by Armstrong [1]. Armstrong's device, shown in Fig. 1.1, can be likened to external spur gears. However, instead of torque being transferred from one gear to the next by contacting teeth, torque is transferred by the attractive forces between the electromagnets on one gear and the ferromagnetic teeth of another gear. Armstrong recognized that this electromagnetic gear did not suffer from mechanical wear and noise generated by contacting teeth. There are two problems with this type of early magnetic gear. Firstly, the torque density is very low because force is only generated in the limited space around the active teeth. Secondly, the torque transmission efficiency is not very high because a large current is required to excite the electromagnetic field. Thus, this type of gear cannot compete with mechanical gears in practical terms.

---

[1] Other authors have used the term *magnetically geared machine* to also include other machines which have similar operating principles, such as vernier machines, but the narrower definition given here is used throughout this work.

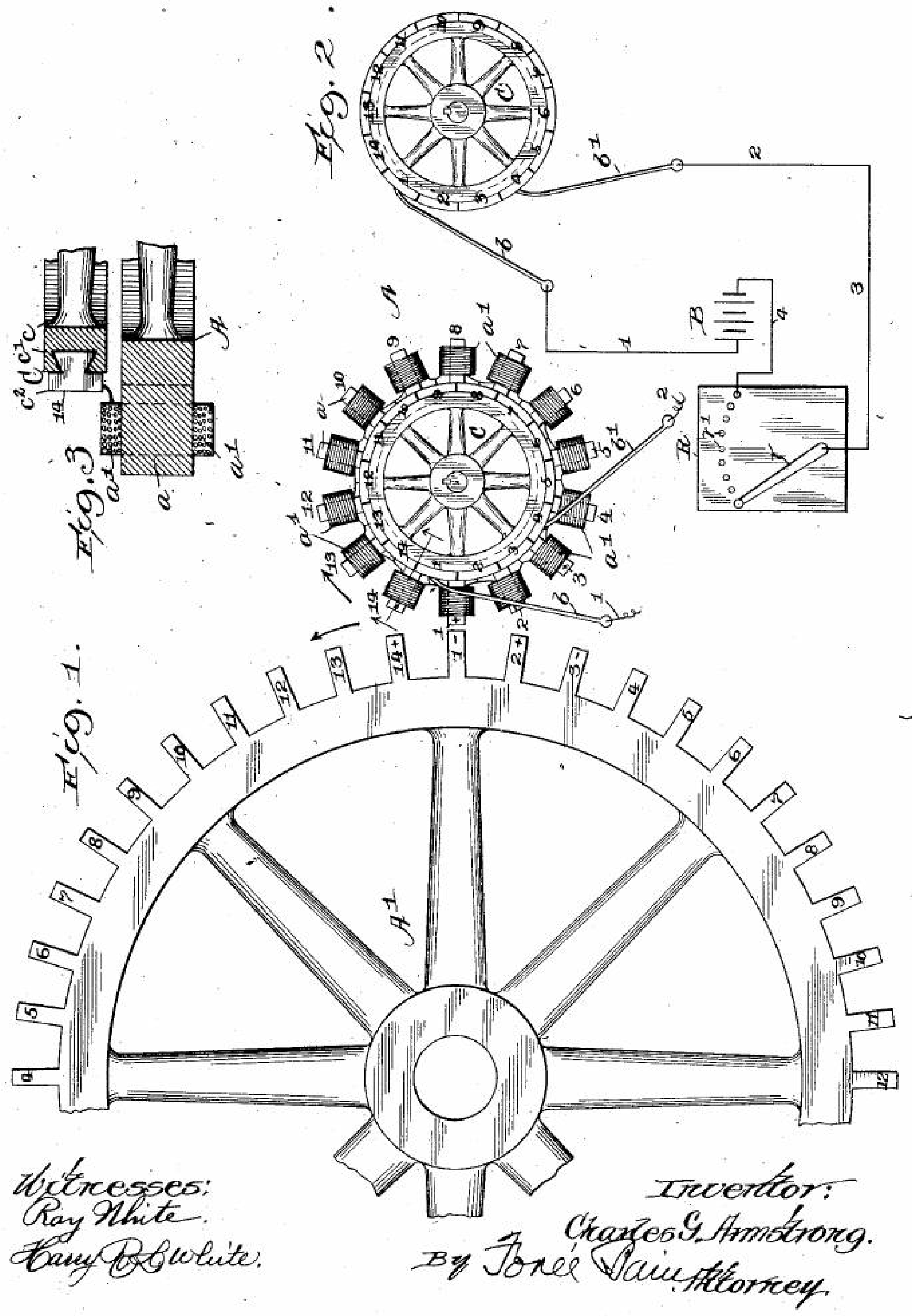

Figure 1.1: The first electromagnetic gear, designed by Armstrong in the year 1900 [1].

Since this first patent, many other spur type electromagnetic gears have been proposed and several studies on their performance have been conducted. Faus [2] proposed a permanent magnet spur gear which could easily be used in a parallel or a right-angle configuration, as shown in Fig. 1.2. Alternative arrangements of the magnets, such as illustrated in Fig. 1.3, were proposed by Rand [3]. A miniature magnetic gear drive train for use in clockwork was presented by Hetzel [4]. Further work on miniature gears was reported in [5]. Analytical analyses of the coupling between magnetic spur gears were conducted by Furlani [6] and Yao [7, 8]. However, none of these designs or studies have managed to realize magnetic gears that can widely compete with mechanical gears, and their application have been limited.

Worm type magnetic gears have also been proposed. The patent by Faus [2] also detailed a worm gear configuration. Later, in the early 1990's, Kikuchi and Tsurumoto [9] also designed and tested a magnetic worm gear, as shown in Fig. 1.4.

In essence, an analogous magnetic gear has been proposed in literature for almost every type of mechanical gear by substituting magnets for gear teeth. The vast majority of these magnetic

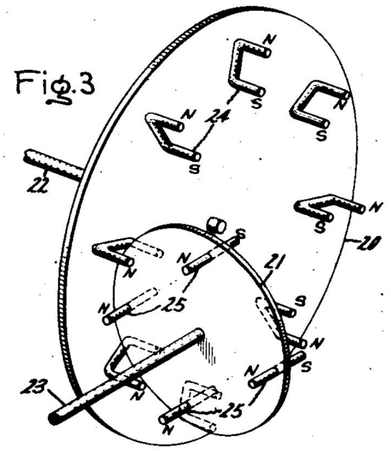

Figure 1.2: Faus' permanent magnet spur gear in a right-angle configuration.

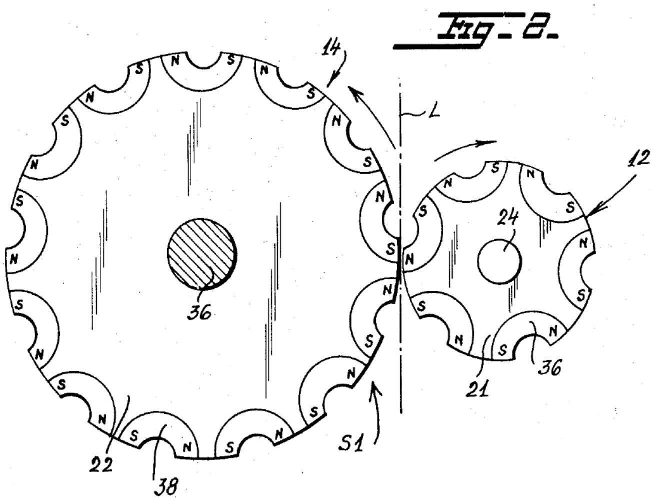

Figure 1.3: Rand's permanent magnet spur gear.

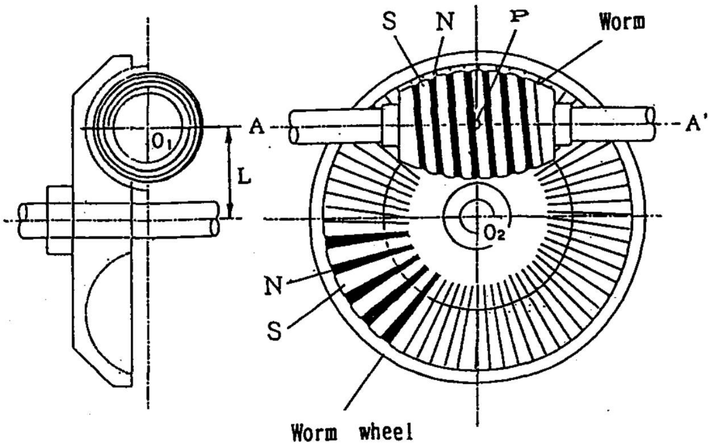

Figure 1.4: A magnetic worm gear, designed and tested by Kikuchi [9] in the 1990's.

gears have poor torque densities compared to their mechanical counterparts, and thus they do not provide a cost effective alternative.

Another early magnetic gear which does not have an obvious relation to a mechanical gear was patented by Neuland [10] in 1916. One incarnation of Neuland's gear is illustrated in Fig. 1.5. This gear operates on the principle of reluctance torque and uses permanent magnets to generate the magnetic field. In some ways, it can be seen as a precursor to the modern flux-modulated magnetic gear. However, at the time of its development, the coercive force of permanent magnets was much lower than what can be achieved today. Furthermore, the cogging torque generated by this type of gear could have been a significant problem. It did, however, make more efficient use of the exciting field, whether it be from electromagnets or permanent magnets, by having a larger active torque producing area. Despite its advantages, it too could not compete with mechanical gears.

An interesting alternative reluctance type gear was proposed by Reese in 1967 [11]. The following year, Martin [12] patented a magnetic transmission device which was later discovered, could be designed to achieve very high torque densities – even comparable to mechanical gears.

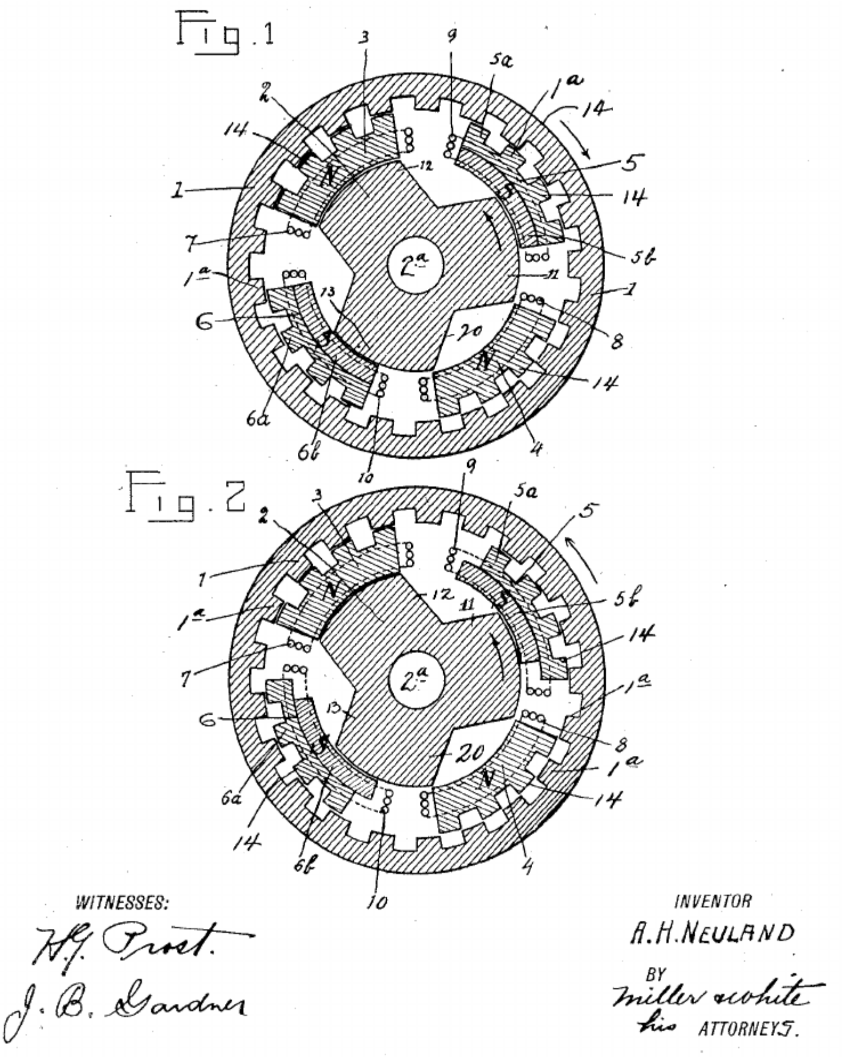

Figure 1.5: A magnetic gear based on varying reluctance, patented by Neuland in 1916 [10].

Reese's reluctance gear and Martin's magnetic transmission are illustrated in Figs. 1.6 and 1.7 respectively. Both of these devices consisted of a magnetized inner high-speed rotor, some form of assembly (modulator) which modulates the field from the high-speed rotor and an outer cylinder. The only difference between these two gears lies in the outer component. Reese's gear used a laminated structure with teeth to create a varying reluctance, while Martin's gear used permanent magnets. For Reese's gear, the relationship between the number of pole pairs on the high-speed rotor (p_h), the number of teeth on the modulator (Q_m) and the number of teeth on the outer ring (Q_r) is given by

$$Q_r = Q_m - 2p_h \tag{1.1}$$

and the gear ratio, assuming that the outer ring is fixed, is given by

$$G = \frac{Q_m}{2p_h} \tag{1.2}$$

A similar relationship holds for Martin's gear, where the number of pole pairs on the outer magnet ring (p_r) is given by

$$p_r = Q_m - p_h \tag{1.3}$$

and when the outer magnet ring is stationary, the gear ratio is

$$G = \frac{Q_m}{p_h} \tag{1.4}$$

Further study on Martin's gear was conducted by Laing [13, 14] who suggested several possible configurations of the modulator. Ackermann and Honds [15] proposed an especially simple configurations of this gear and later Ackermann [16] proposed an additional variant. The former design received great attention in later years. This gear, as it appears in the original patent, is shown in Fig. 1.8.

In this section only some of the earlier contributions to the field of magnetic gears have been highlighted. As has been shown, many good ideas have been around for quite some time and

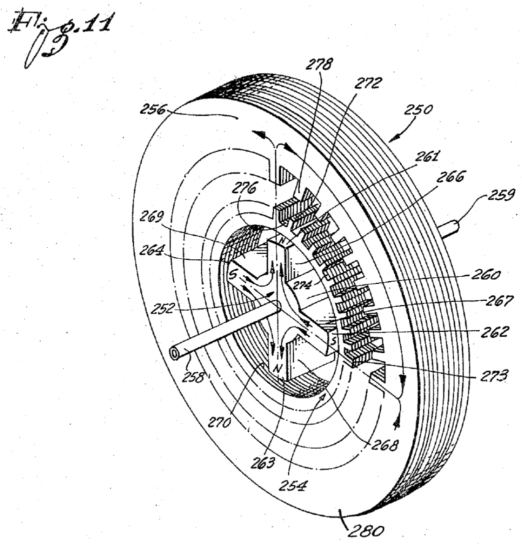

Figure 1.6: Reese's reluctance type gear.

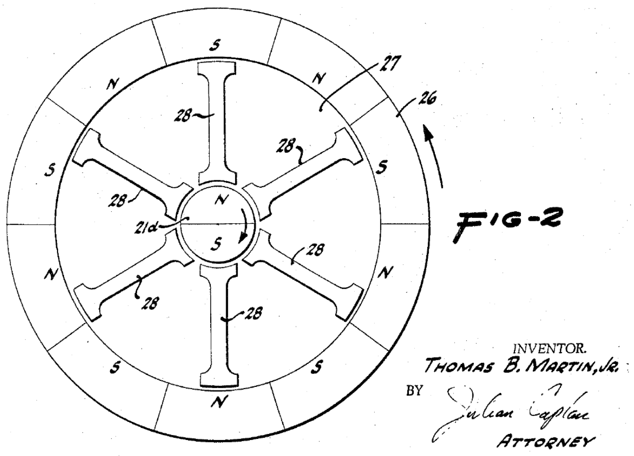

Figure 1.7: Martin's magnetic transmission device.

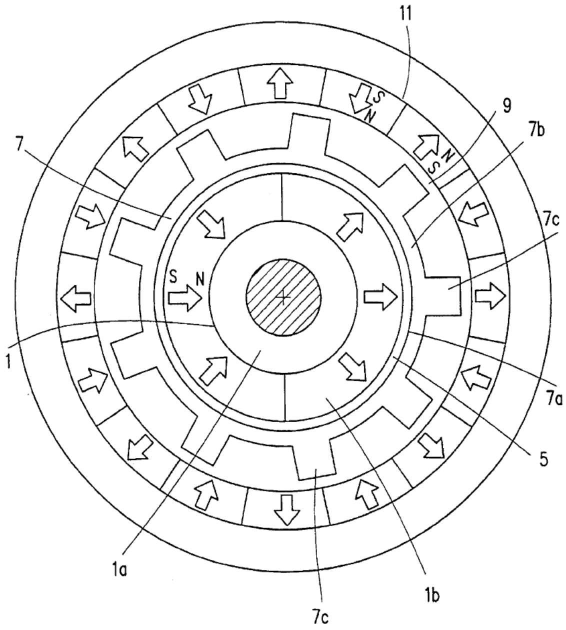

Figure 1.8: Illustration of a flux-modulated magnetic gear, as per Ackermann and Honds' patent [15].

several inventors deserve credit for their contributions. Of course, the introduction of high energy rare earth permanent magnets, specifically the Neodymium-Iron-Boron compound, has had a great impact on the torque density that can be achieved with any type of magnetic gear. In addition to advances in permanent magnet technology, a number of topologies, such as the one shown in Fig. 1.8, which make effective use of permanent magnet material, have emerged. These advances have made it possible for magnetic gears to achieve much greater torque densities and because of their inherent advantages over mechanical gears, most notably the absence of friction, a renewed interest in magnetic gear technology has been sparked.

1.3 Modern magnetic gears

In 2001, Atallah and Howe [17] published a paper which revealed the high torque density that can be achieved with flux-modulated magnetic gears and described their operating principle in some detail. In this study, a simulated torque density between 50 and 150 kNm/m^3 was reported. It was suggested that by combining such a magnetic gear with a conventional radial-field electrical machine, a system torque density higher than that of a state-of-the-art transverse-field machine can be achieved.

After the publication of the aforementioned paper, there has been a sharp increase in the number of publications related to the this type of magnetic gear. In fact, the term *magnetic gear* has become synonymous with this type of gear. However, there are other types of magnetic gear which also have the key characteristic that a large portion of the active magnetic material contributes to torque transfer at any instant and thus allows the realization of high torque density. In the following paragraphs, a brief review of recent literature on four types of high performance magnetic gears is given. The terminology used to describe these gears is discussed in detail in section 1.3.1.

1.3.1 Classification of magnetic gears

In general, the terminology used in the field of magnetic gears is not well established. This is to be expected in an emerging field of research. Authors follow several conventions. Some of these conventions are ambiguous. Others do not have a clear correlation to the terminology used when describing mechanical gears, although there is a clear similarity in operating principles and some form of agreement is expected. For the sake of clarity, the terminology used throughout this dissertation is described here.

Fig. 1.9 illustrates different kinds of high torque density magnetic gears. Fig. 1.9(a) is a planetary magnetic gear. It consists of an outer ring gear, several planet gears coupled to a planet carrier and an inner sun gear. The cycloidal magnetic gear, shown in Fig. 1.9(b) is primarily composed of four components. It also features an outer ring gear. A smaller eccentric gear *rolls* on the inside of the ring gear. The mechanical version is normally constructed with cycloidally shaped teeth, from which the name is derived. This allows all the teeth to maintain contact with the ring gear. The eccentric gear is mounted on an eccentric part of a high-speed shaft which is otherwise concentric with the ring gear. The cycloidal gear can be viewed as a special case of the general harmonic gear, shown in Fig. 1.9(c). In the general harmonic gear, the inner gear is a deformable member of which the shape is governed by the orientation of the high-speed wave generator. Finally, Fig. 1.9(d) depicts the magnetic gear proposed in [12, 15, 17]. From literature, it is evident that the name given to this type of magnetic gear is not well established. During a quick overview of recent papers, the following names for this type of gear were found:

- concentric planetary magnetic gear [18, 19, 20, 21, 22]
- coaxial magnetic gear [23, 24, 25, 26, 27, 28]
- concentric magnetic gear [29]
- planetary magnetic gear [30, 31, 32]
- shutter-type magnetic gear [33]
- surface permanent magnet-type magnetic gear [34, 32, 35]
- field modulated permanent magnetic gear [28]

Although the gear has much in common with planetary gears, the name *concentric planetary magnetic gear* is not preferred because it is cumbersome. Strictly speaking, harmonic gears can also be considered to be *coaxial*, and for this reason this term is not used. The term concentric magnetic gear does not describe axial flux configurations of this type of gear properly. In this thesis, this gear will be referred to as a flux-modulated magnetic gear.

The magnetic planetary, cycloidal and harmonic gears are obtained from their mechanical counterparts by replacing the teeth with alternating magnetic poles. The flux-modulated gear does not have a direct mechanical counterpart. Several variations of these topologies can be realized, such as the magnetic reluctance gears shown in Fig. 1.10. Interesting to note is that the flux-modulated magnetic reluctance gear shown in Fig. 1.10(d) is the same as the reluctance gear of Fig. 1.6.

1.3.2 Planetary gears

Magnetic planetary gears are simply mechanical planetary gears with the teeth replaced by magnetic poles. This design variation of a planetary gear was introduced by Mabe [36] in 1991. More recently, Huang [37] developed a successful prototype which achieved a torque density of nearly 100 kNm/m^3. Kong et al. [38] presented work on the reduction of cogging torque in magnetic planetary gears.

1.3.3 Cycloidal gears

The concept of the magnetic cycloidal gear was patented by Schuesler and Lindner [39] in 1995. Jørgenson [40] published work on this type of gear and tested a prototype. An optimized design was reported to have a calculated torque density of 183 kNm/m^3. Rens et al. [41, 42] also arrived at this design for a magnetic gear, starting from a harmonic gear. A dual stage prototype was constructed with a gear ratio of 360:1 (with opposite rotational directions) and an active torque density of 75 kNm/m^3.

1.3.4 Harmonic gears

Harmonic gears could also be constructed using permanent magnets instead of mechanical teeth. Rens et al. [43] notes that the practical implementation of such a gear is difficult because it requires a many-pole permanent magnet rotor which can deform under the influence of a high-speed wave generator. This flexible rotor must also be coupled to a rigid external shaft. Nevertheless, a design with a calculated torque density of 110 kNm/m^3 was presented and simulations have shown that the transmitted torque is ripple free.

1.3.5 Flux-modulated gears

The vast majority of recent publications in the field of magnetic gears focus on flux-modulated gears. This is probably due to the high torque density that these gears offer, but perhaps more importantly, to the simplicity and elegance of the topology. This type of gear is much simpler to realize, considering the mechanical construction. Various aspects of this type of gear have been investigated.

For many applications, torque ripple and cogging torque are important factors. Frank and Toliyat [18, 19] have investigated the effect of gear ratio on the torque ripple while Niguchi and Hirate [35] analyzed the harmonic content of the cogging torque.

Several alternative magnet arrangements and magnetization patterns have been proposed [24, 29, 25, 27, 44, 45]. The objective has been either to increase the torque density that can be realized or to reduce the amount of magnet material required to achieve a certain specification.

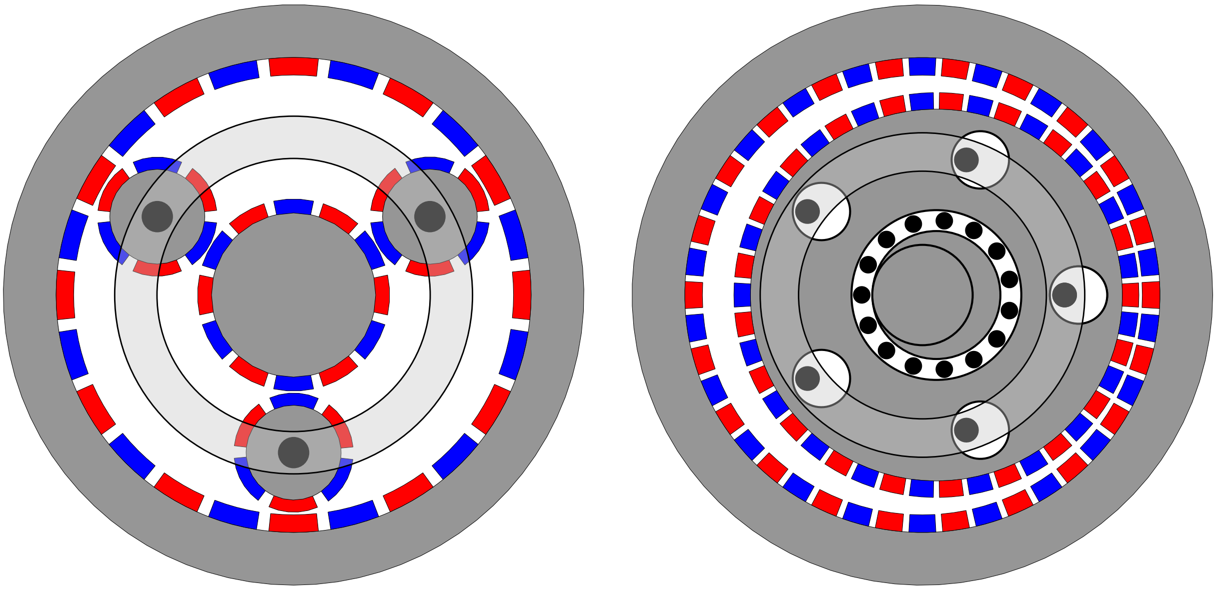

(a) Planetary magnetic gear.

(b) Cycloidal magnetic gear.

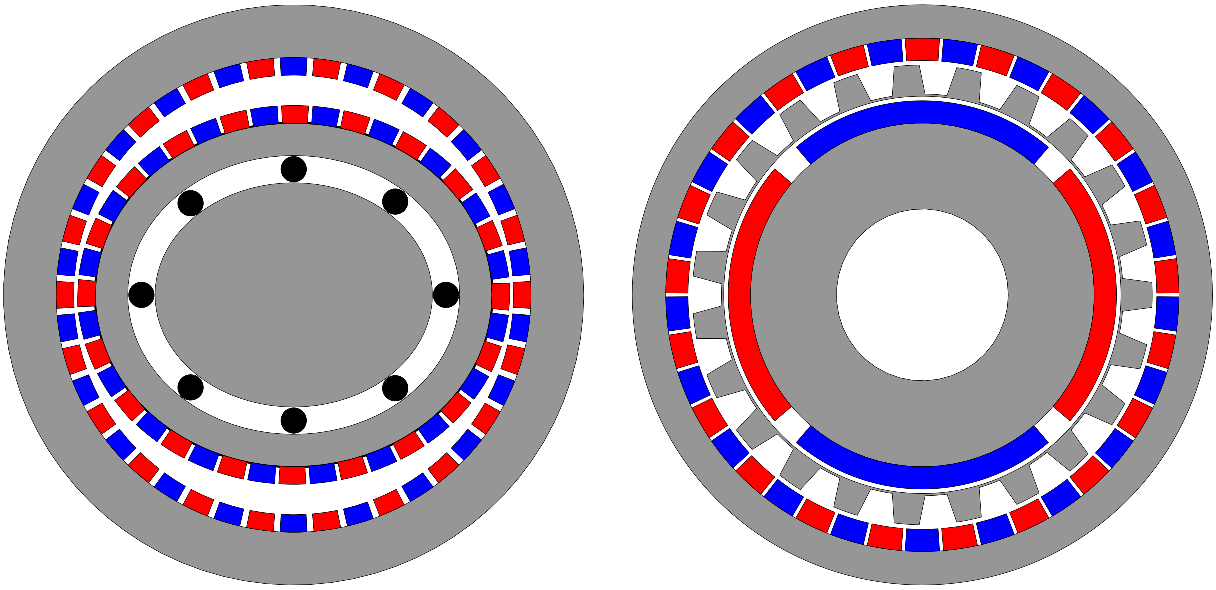

(c) Harmonic magnetic gear.

(d) Flux-modulated magnetic gear.

Figure 1.9: High torque density magnetic gears.

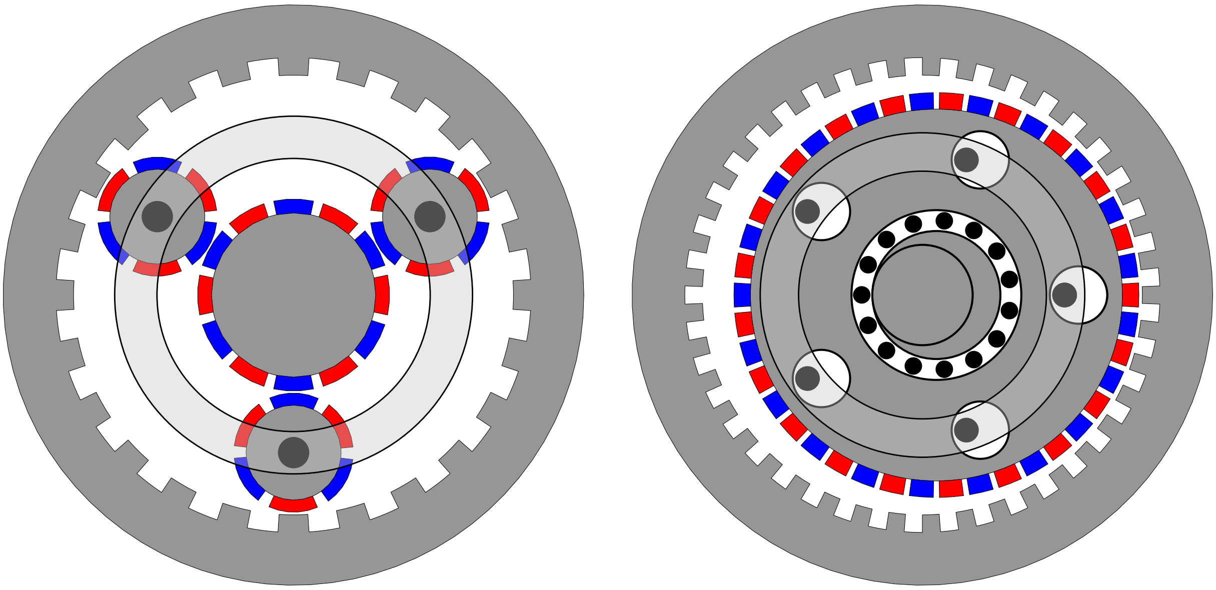

(a) Planetary magnetic reluctance gear.

(b) Cycloidal magnetic reluctance gear.

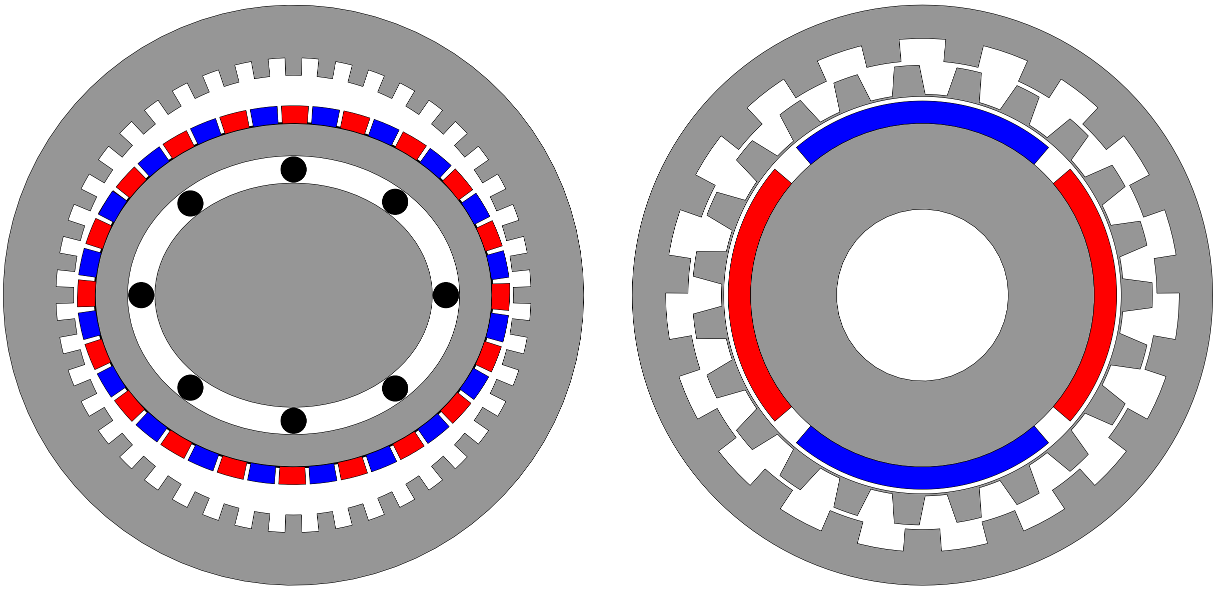

(c) Harmonic magnetic reluctance gear.

(d) Flux-modulated magnetic reluctance gear.

Figure 1.10: Magnetic reluctance gears.

Frank and Toliyat have studied methods of improving the mechanical robustness of these gears. [20]

The interesting possibility of using flux-modulated gears in contra-rotating turbine applications has been highlighted by Shah et al. [46]. It was shown that flux-modulated gears provide an especially simple way of transmitting power from two low-speed inputs to a single high-speed output.

Evans and Zhu have investigated the influence of several design parameters on the stall-torque of flux-modulated gears [47].

The dynamic performance of these gears has also been studied [21, 48, 31, 22]. This is one aspect in which mechanical gears may be preferred for their higher torsional stiffness. However, Montague et al. [49, 50, 51] have shown that flux-modulated gears can be used in servo applications if appropriate control strategies are employed.

Several prototype flux-modulated gears have been realized. Table 1.1 lists some examples, with their outer diameter (D_o), gear ratio (G_r) and active volume torque density (T/V_A) reported. Although it has been claimed that torque densities exceeding 100 kNm/m^3 can be achieved with this type of gear, the list of prototypes show that gears often fall short of this milestone. There are several factors that play a role in this, some of which will be dealt with later on in this work.

1.4 Magnetically geared machines

Gears can generally be used to increase the total system torque density of a drive train compared with a direct-drive solution, at the cost of additional complexity. Magnetic gears are not different from mechanical gears in this context. However, several interesting possibilities exist by which a magnetic gear can be integrated with an electrical machine into a single compact unit. In this way, the torque density can be raised beyond what can be achieved with a cascaded configuration. This type of integration is illustrated in Fig. 1.11. The flux-modulated magnetic gear is especially suited to this kind of integration due to its simple and balanced design.

The original idea can be traced to a patent by Razell and Cullen [56] (2004). A design of such a machine was first published by Chau et al. [57], but only in 2007. Fig. 1.12(a) shows a cross

Table 1.1: Prototype flux-modulated magnetic gears

Description	**D_o [mm]**	**G_r**	**T/V_A [kNm/m^3]**
Rasmussen et al. [52]	120	5.5	92
Atallah [53]	140	5.75	72
Shah et al. (dual input) [46]	120	5.5/6.5	47/56
Brönn et al. [33], Gerber and Wang [54]	150	10.5	62
Frank and Toliyat [20]	120	5.5	42
Fukuoka et al. [55]	156	10.3	49
Uppalapati et al. (Ferrite) [45]	112	4.25	33
Uppalapati et al. (Ferrite and NdFeB) [45]	112	4.25	66

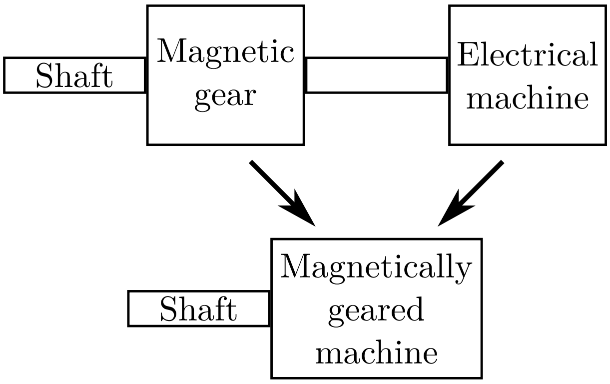

Figure 1.11: Cascaded and integrated magnetically geared drive trains.

section of the machine. The following year, Atallah et al. [58, 59] proposed a different topology, shown in Fig. 1.12(b). These two topologies have received the greatest interest, although other configurations do exist. It can be seen in Fig. 1.12 that these machines essentially contain a flux-modulated magnetic gear.

A list of published prototypes is given in Table 1.2. Note that the torque densities reported are not directly comparable, since different types of torque are used in the calculations. However, it is clear that the torque densities achieved by these machines are generally very high.

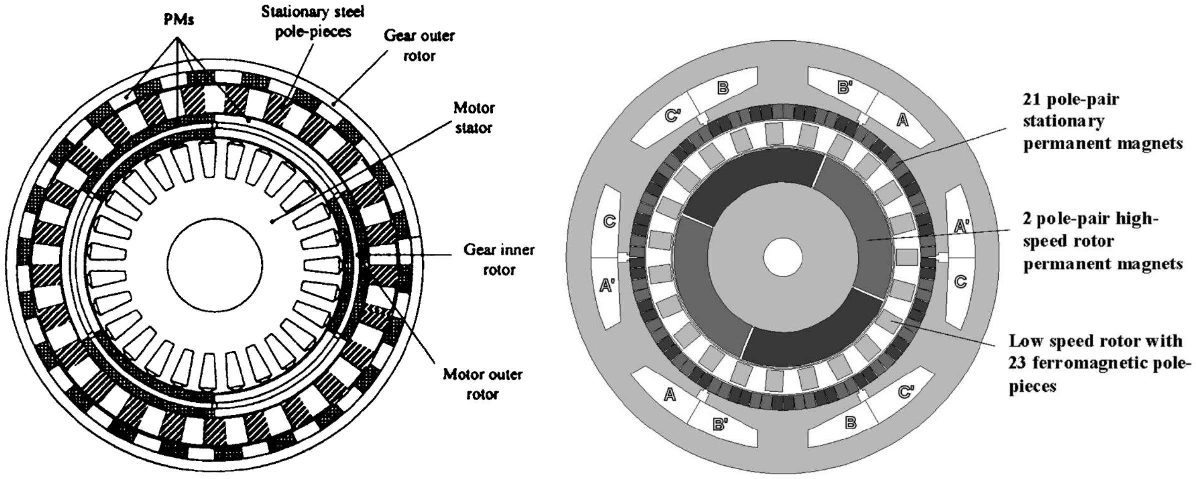

(a) An inner stator configuration. [57]

(b) An outer stator configuration. [59]

Figure 1.12: The two most prominent topologies of magnetically geared machines.

Table 1.2: Prototype magnetically geared machines

Description	D_o [mm]	G_r	T/V_A [kNm/m^3]
Atallah et al. [59]	178	11.5	>60 (measured continuous)
Jian et al. [60], Jiam et al. [61]	194	7.3	87 (simulated stall)
Rasmussen [62]	268.5	8.83	92 (measured stall)
Wang et al. [63]	320	6.6	105 (simulated stall, gear only)

1.5 Applications

The possible applications for magnetic gears and magnetically geared machines are numerous. Magnetic gears can replace mechanical gears in many applications due to the following advantages they hold:

Frictionless torque transfer Torque is transferred via magnetic forces, which means that magnetic gears do not suffer from wear and losses associated with meshing teeth.

Low maintenance The only parts in a magnetic gear which require lubrication are the bearings, for which the maintenance requirements are typically very low.

Overload protection Magnetic gears slip when their pull-out torque is exceeded, while mechanical gears may be damaged under overload conditions. This mechanism can also be used to protect other components in the drive train.

Reduced noise Magnetic gears are expected to be low-noise devices, due to smooth torque transfer characteristics and absence of tooth contact.

High-efficiency The mechanisms of power loss in magnetic gears are very different from those in mechanical gears. Magnetic gears can also achieve high efficiencies.

In the literature on magnetically geared machines, the focus has fallen on low-speed applications with stringent weight and/or volume constraints. Wind power generation, traction drives (especially for electric vehicles) and ship propulsion are examples of such applications.

In wind power generation, the maintenance requirements of mechanical gearboxes can be costly, especially in off-shore applications. Furthermore, the reliability of these gearboxes has been an issue and gearbox failures lead to significant down-time. On the other hand, direct-drive generators are typically very large and heavy. Magnetic gears and magnetically geared machines may provide a better solution for these applications.

1.6 Challenges

Magnetic gear technology can still be considered to be in its infancy and, as such, a number of challenges remain.

Design procedures that are accurate and fast are not well established, seeing that the technology is new. The design of magnetically geared machines poses an especially interesting problem, since it amounts to the design of two components which have to be well matched and meet the design specification.

The mechanical construction of magnetic gears can be a demanding task. Although the flux-modulated magnetic gear and machines derived from it are simpler than other types of magnetic gears, the assembly is nonetheless more complex than that of conventional electrical machines which typically consist of only two main components.

Magnetic gears are not as torsionally stiff as mechanical gears. This may limit their application in precision drive systems. More research is required in order to ascertain the viability of magnetic gears in such applications.

The availability and cost of permanent magnet material is a factor that will have a major impact on the feasibility of the technology for a large number of applications.

1.7 Research objectives and approach

This chapter has introduced the concept of magnetically geared machines, highlighted some of the key strengths of these machines and named some areas where additional development is required. Seeing that the concept is relatively new, there are numerous possibilities that remain to be investigated and many questions which have not been answered satisfactorily. The specific aims with this study are as follows:

- Formulate a general strategy for design optimization of magnetically geared machines.
- Construct and evaluate prototypes of different magnetically geared machines.
- Carry out a direct comparison between small magnetically geared machines and more conventional PM machines.

1.8 Dissertation layout

The remainder of this dissertation is organized as follows:

Chapter 2 The basic operating principles of flux-modulated magnetic gears are described. Simple analytical approximations are made and equations for the torque on the various components are derived. From these, the load angle is defined.

Chapter 3 Several different topologies of magnetically geared machines are presented and they are analyzed qualitatively.

Chapter 4 The design optimization process used in this work is described in detail and a method of analyzing the operating points of magnetically geared machines is presented.

Chapter 5 This chapter is dedicated to some computational aspects, with specific focus on 2D finite element analysis of magnetically geared machines.

Chapter 6 End-effects can have a significant impact on the performance of magnetic gears and magnetically geared machines. In this chapter it is explained why the end-effects are so significant in these machines. An optimization strategy is proposed which combines the computational efficiency of 2D FE analyses with the accuracy of 3D FE analyses.

Chapter 7 – 10 In these chapters the design, construction and evaluation of several prototypes are documented.

Chapter 11 A comparison between two magnetically geared machines, a vernier machine and a more conventional permanent magnet machine is presented.

Chapter 12 The original contributions made in this study are summarized, general conclusions are drawn and recommendations for future work are provided.

Chapter 2

Principles of operation

The flux-modulated magnetic gear (FMMG) has been identified as a high torque density device which is relatively simple to construct. Before delving into magnetically geared machines which contain such gears, the operating principles of these gears are discussed.

2.1 Relationship to planetary gears

FMMGs typically consist of three components, as illustrated in Fig. 2.1. The inner and outer magnet assemblies will be referred to as the sun gear and the ring gear. This naming convention highlights the relationship of these components with those of mechanical planetary gears, such

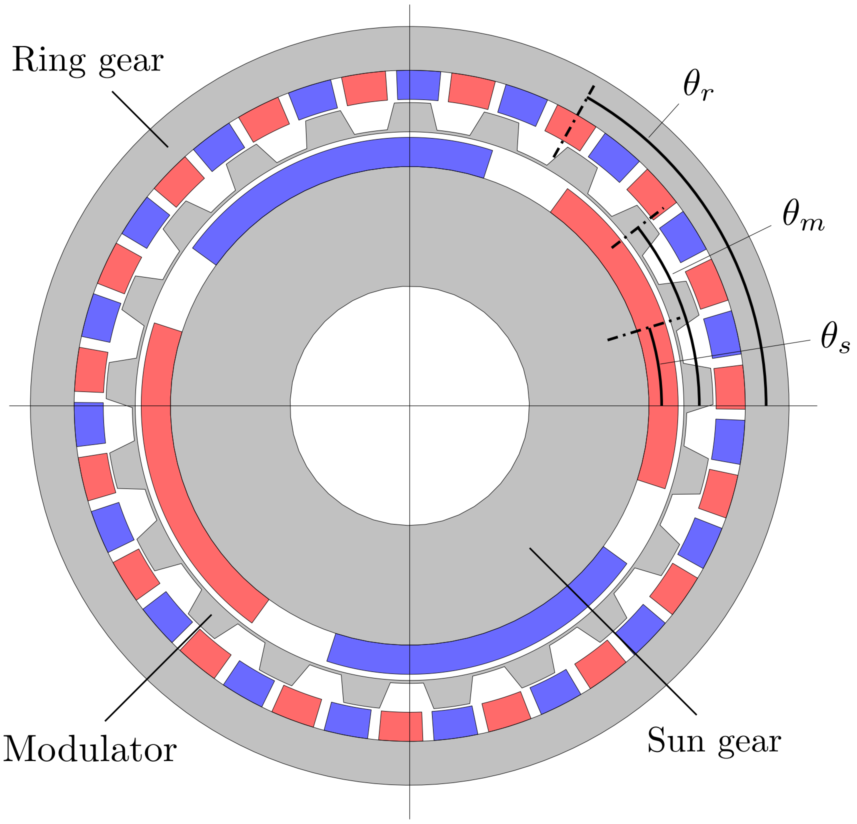

Figure 2.1: A typical flux-modulated magnetic gear.

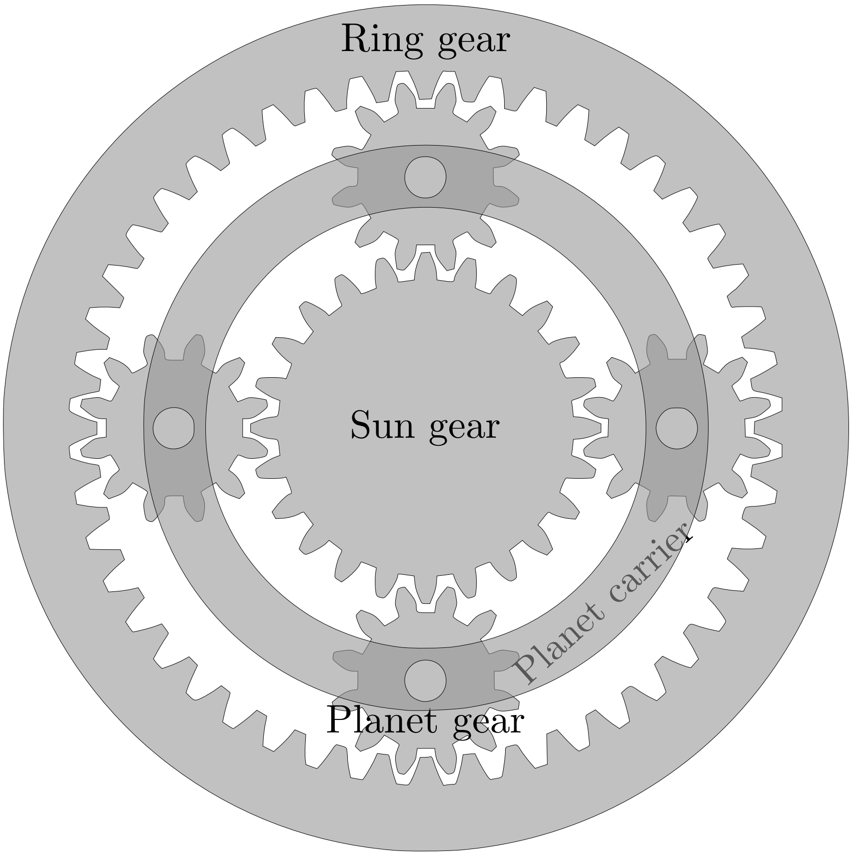

Figure 2.2: A mechanical planetary gear.

as the one illustrated in Fig. 2.2. [1]

In mechanical planetary gears, the relationship between the number of teeth on the sun gear (z_s), planet gears (z_p) and the ring gear (z_r) must obey [64]

$$z_r = z_s + 2z_p \tag{2.1}$$

in order to ensure that the circular pitches of the meshing gear teeth are equal. The relationship between the angular velocities of the sun gear, planet carrier and the ring gear can be expressed as

$$\omega_s z_s + \omega_r z_r = \omega_c(z_s + z_r) \tag{2.2}$$

In this chapter, similar formulae for flux-modulated magnetic gears will be derived which will show that the two devices are similar in many ways.

Although FMMGs and planetary gears share some characteristics, the mechanism of torque transfer is very different. While mechanical planetary gears transfer torque through the contact surfaces of meshing gear teeth and planetary magnetic gears through the direct interaction of magnetic poles, FMMGs transfer torque through the interaction of the fields produced by the sun and ring gear with modulated space harmonics produced by the opposite gear.

---

[1] This convention also avoids a contradiction which occurs when the outer component is called the low-speed rotor while the modulator acts as the low-speed component and the outer component is, in fact, stationary.

In this regard, FMMGs have the advantage that the area over which forces are transmitted is not limited to small contact surfaces, as is the case in mechanical planetary gears, or even to a subset of the magnets in the gear, as is the case in some magnetic gears. In FMMGs, all magnets simultaneously contribute to torque transfer. The following sections will provide a detailed analysis of the mechanism of torque transfer in FMMGs.

2.2 Basic principle of operation

The principle of operation of FMMGs will be discussed with reference to the gear shown in Fig. 2.1. The design variables describing the geometry of the FMMG are illustrated in Fig. 2.3, with the numerical values listed in Table 2.1. In planetary gears, the gear ratio is determined by the diameters of the various components, but in FMMGs, the gear ratio is determined by the number of pole pairs on the sun and ring gear and the number of modulator segments. The relationship between these three parameters will be derived in this chapter. The parameters listed in Table 2.2 will be referred to collectively as the gear's modulation set. Different gear ratios can be realized depending on which component is kept stationary. The table lists gear ratios for the case where the ring gear is stationary (G_{sm}) and for the case with a stationary modulator (G_{sr}). The notation G_{ab} denotes the speed of component a divided by the speed of component b. The sun gear can also be stationary, which usually results in the lowest gear ratio. In certain applications, it may even be appropriate to have all the components rotating. For example, when the modulator and ring gear are connected to contra-rotating turbine rotors, the power from the rotors can be multiplexed into the single high-speed output of the sun gear [46].

In the field of electrical machines, it is well understood that magnetic fields of the same space-harmonic order can interact to produce a stable torque. FMMGs operate by modulating the space-harmonics produced by the sun and ring gear's magnets in such a way that space-harmonics of the same order as those produced by the opposing component are generated. The flux density distributions in the gear, produced by the sun and ring gears respectively, are illustrated in Fig. 2.4. The radial flux density waveforms in the inner and outer air-gaps associated with Figs. 2.4(a) and 2.4(b) are plotted in Fig. 2.5. The spectra of these waveforms are shown in Fig. 2.6 and can provide especially important insight into the operation of FMMGs. In Fig. 2.6(a), the fundamental harmonic is the 2nd order harmonic. This harmonic is large on both sides of the

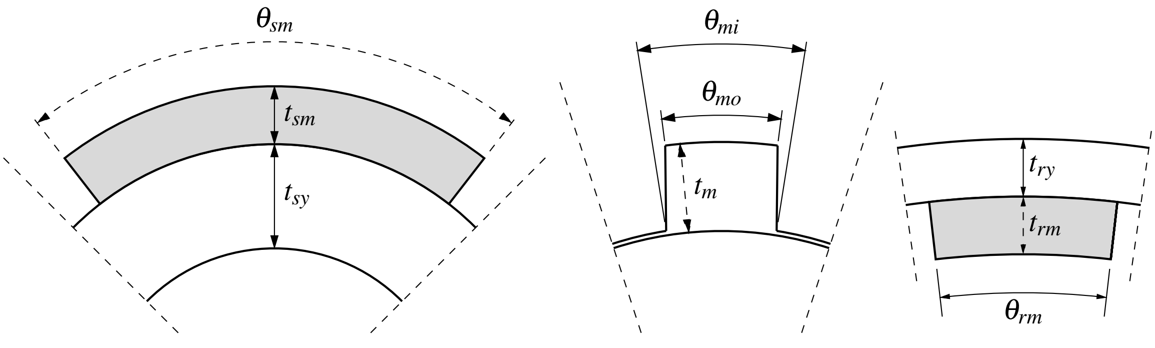

(a) Sun gear. (b) Modulator. (c) Ring gear.

Figure 2.3: Flux-modulated magnetic gear geometrical design variables.

Table 2.1: Flux-modulated magnet gear dimensions

Parameter	**Value**
θ_{sm}	0.9 [fraction of pole pitch]
θ_{rm}	0.9 [fraction of pole pitch]
θ_{mi}	0.6 [fraction of segment pitch]
θ_{mo}	0.4 [fraction of segment pitch]
t_{sy}	20 mm
t_{sm}	5 mm
t_{sg}	1 mm
t_m	7 mm
t_{rg}	1 mm
t_{rm}	5 mm
t_{ry}	7.5 mm
Outer diameter D	65 mm
Stack length L	40 mm

Table 2.2: Flux-modulated magnet gear modulation set

	Symbol	**Value**
Sun gear pole pairs	p_s	2
Ring gear pole pairs	p_r	21
Modulator segments/teeth	Q_m	23
Gear ratios		
$\lvert\omega_s/\omega_m\rvert$	G_{sm}	11.5
$\lvert\omega_s/\omega_r\rvert$	G_{sr}	10.5

modulator. The significant thing to note in this figure is that, while the amplitudes of almost all the harmonics are smaller on the ring gear side of the modulator, the 21st order harmonic is significantly stronger on the ring gear side. This harmonic results from the interaction of the fundamental component with the periodically varying reluctance of the modulator. Furthermore, this harmonic can interact with the large fundamental harmonic produced by the ring gear's magnets, shown in Fig. 2.6(b). In this figure, a similar effect can be seen where a significant 2nd order harmonic is introduced on the sun gear's side of the modulator due to the interaction of the ring gear's fundamental with the modulator's varying reluctance. This harmonic can interact with the fundamental of the sun gear to produce stable torque.

2.3 Simple model of the flux-modulated magnetic gear

In this section, a simple model of flux-modulated magnetic gears is presented. The purpose of the model is not to accurately predict the characteristics of FMMGs but to provide insight into the mechanism of torque transfer.

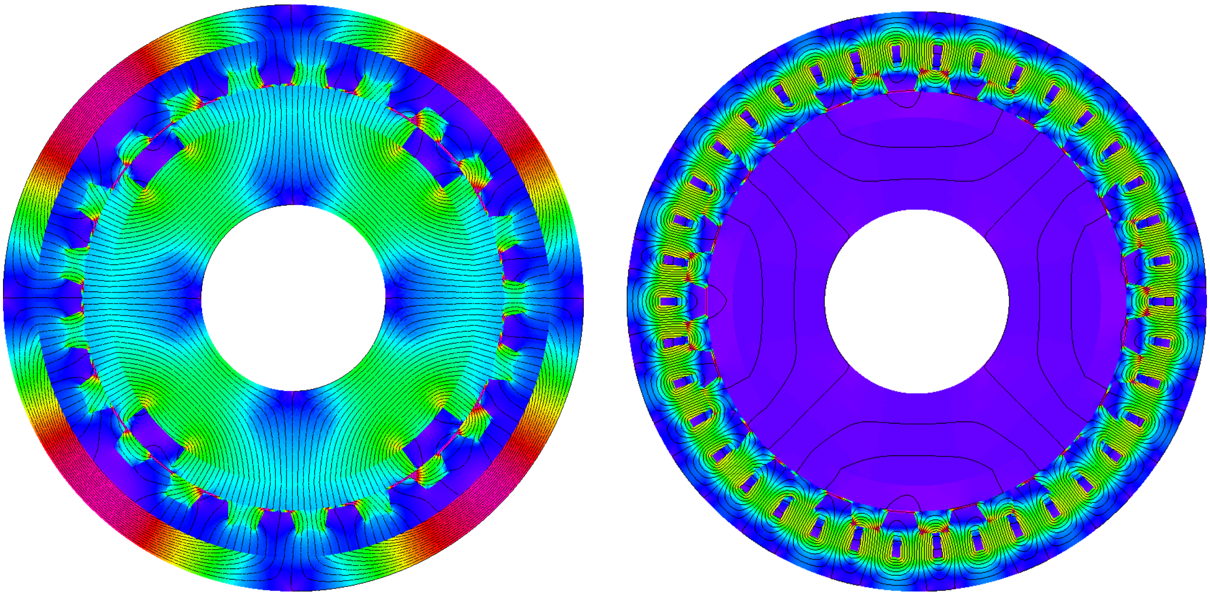

(a) Field produced by the sun gear.

(b) Field produced by the ring gear.

Figure 2.4: Flux density distribution in a flux-modulated magnetic gear.

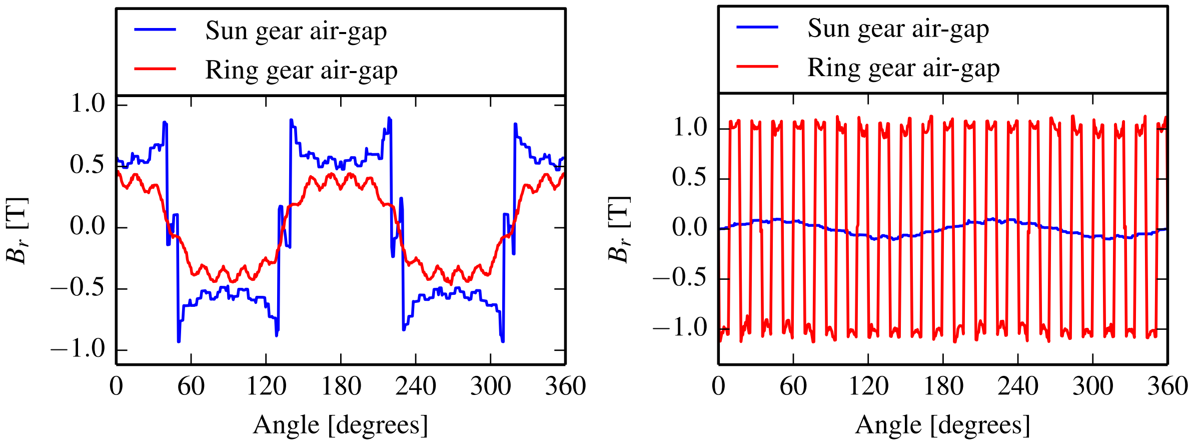

(a) Field produced by the sun gear.

(b) Field produced by the ring gear.

Figure 2.5: Radial Flux density in the air-gaps.

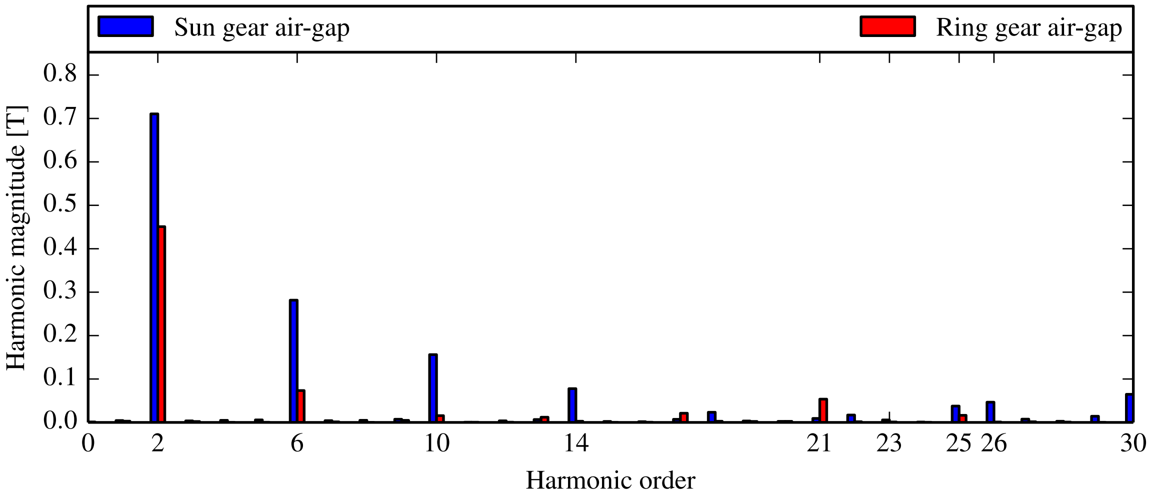

(a) Harmonics produced by the sun gear.

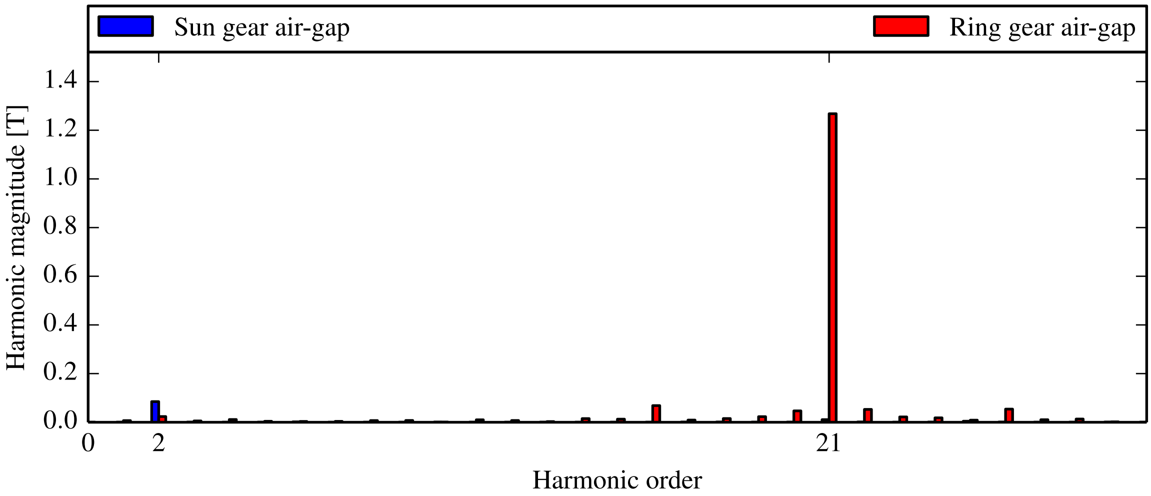

(b) Harmonics produced by the ring gear.

Figure 2.6: Space-harmonic flux density spectra in the air-gaps.

2.3.1 Ideal flux modulation

As the name suggests, flux-modulated magnetic gears rely on the principle of flux modulation. In this analysis, ideal flux modulation is defined as follows: Consider an MMF source,

$$\mathcal{F}_a = M_a \cos(p_a(\theta - \theta_a)) \tag{2.3}$$

with p_a the number of pole-pairs of the MMF source and θ_a an offset angle to one of the peaks of $\mathcal{F}_a$. The flux in the air-gap adjacent to the MMF source is

$$\phi_a = \mathcal{F}_a \mathcal{P}_{avg} \tag{2.4}$$

and the modulated flux in the opposite air-gap is

$$\phi_{am} = \mathcal{F}_a(\mathcal{P}_{avg} + \mathcal{P}_{mod} \cos(Q_m(\theta - \theta_m)) \tag{2.5}$$

with Q_m the number of modulator segments and θ_m an offset angle to one of the segment centers. The permeance, P_{avg} accounts for the reluctances of the magnets, yokes and the average reluctance of the modulator while the varying component, $\mathcal{P}_{mod}$, accounts for the difference in reluctance due to the modulator segments. Note that in this model, there is no leakage and that the continuity of magnetic flux is satisfied in the sense that

$$\int_0^{2\pi} |\phi_a| \mathrm{d}\theta = \int_0^{2\pi} |\phi_{am}| \mathrm{d}\theta \tag{2.6}$$

2.3.2 Flux harmonic analysis

In the following simplified analysis, the space harmonics of the sun and ring gears are assumed to be sinusoidal functions of the angular position.

$$\mathcal{F}_s = M_s \cos(p_s(\theta - \theta_s)) \tag{2.7}$$

$$\mathcal{F}_r = M_r \cos(p_r(\theta - \theta_r)) \tag{2.8}$$

The magnetic fluxes in the inner and outer air-gaps due to these MMF sources are obtained using (2.4) and (2.5).

$$\phi_s = M_s \mathcal{P}_{avg} \cos(p_s(\theta - \theta_s)) \tag{2.9}$$

$$\phi_r = M_r \mathcal{P}_{avg} \cos(p_r(\theta - \theta_r)) \tag{2.10}$$

$$\phi_{sm} = M_s \mathcal{P}_{avg} \cos(p_s(\theta - \theta_s)) + M_s \mathcal{P}_{mod} \cos(p_s(\theta - \theta_s)) \cos(Q_m(\theta - \theta_m)) \tag{2.11}$$

$$\phi_{rm} = M_r \mathcal{P}_{avg} \cos(p_r(\theta - \theta_r)) + M_r \mathcal{P}_{mod} \cos(p_r(\theta - \theta_r)) \cos(Q_m(\theta - \theta_m)) \tag{2.12}$$

The angles θ_s and θ_r represent the offset of the inner and outer magnetic-axes relative to a common reference angle. The angle θ_m represents the offset to the axis on the modulator with the highest permeance. These axes and their offset angles are illustrated in Fig. 2.7. The magnetic fluxes in (2.9) to (2.12) are plotted in Figs. 2.8 and 2.9, alongside the waveforms obtained from finite element analysis (FEA) for reference. The spectra are shown in Fig. 2.10.

Using the identity,

$$\cos A \cos B = \frac{1}{2} \left(\cos(A - B) + \cos(A + B) \right) \tag{2.13}$$

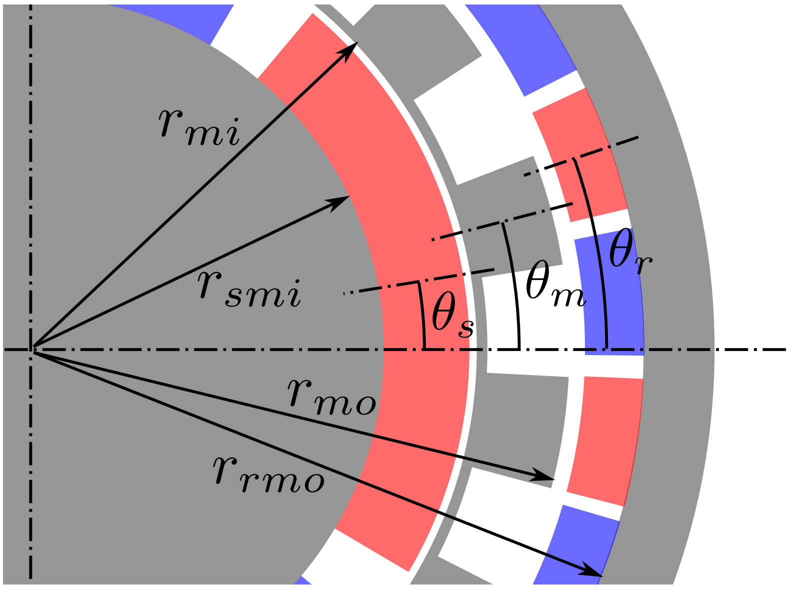

Figure 2.7: Offset angles and radius definitions in a flux-modulated magnetic gear.

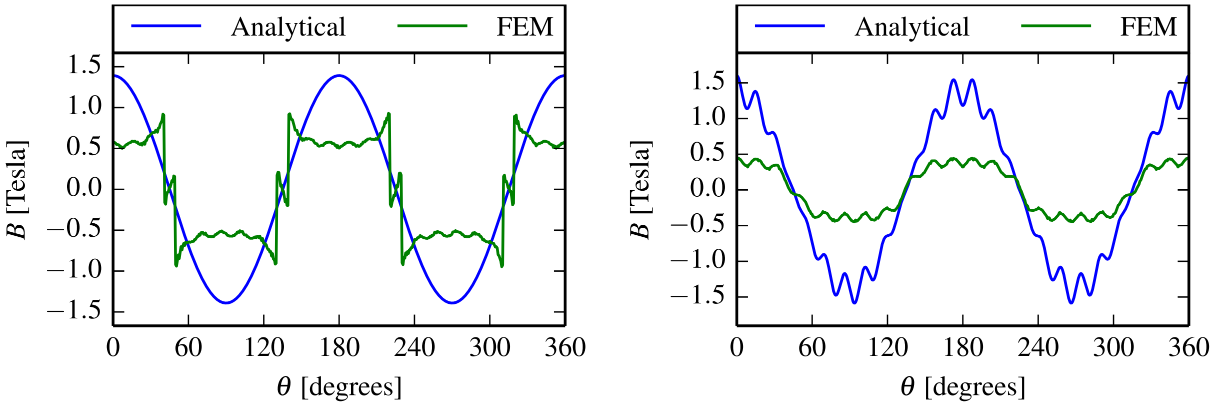

(a) Sun gear air-gap.

(b) Ring gear air-gap.

Figure 2.8: Air-gap flux densities due to the sun gear magnets.

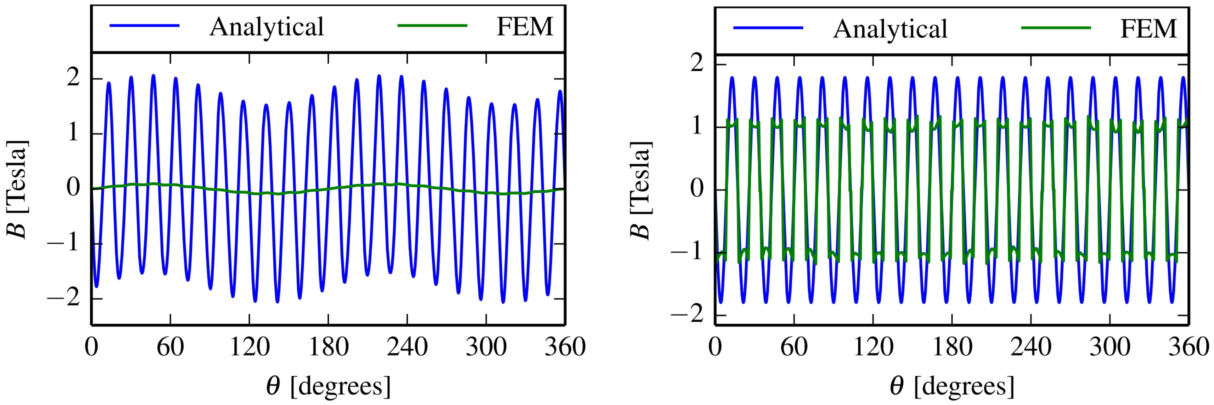

(a) Sun gear air-gap.

(b) Ring gear air-gap.

Figure 2.9: Air-gap flux densities due to the ring gear magnets.

(2.11) and (2.12) can be rewritten as

$$\begin{aligned}\phi_{sm} = & \underbrace{M_s\mathcal{P}_{avg}\cos(p_s(\theta-\theta_s))}_{\phi_{smf}} + \\ & \underbrace{\frac{M_s\mathcal{P}_{mod}}{2}\cos((Q_m-p_s)\theta+p_s\theta_s-Q_m\theta_m)}_{\phi_{sm-}} + \\ & \underbrace{\frac{M_s\mathcal{P}_{mod}}{2}\cos((Q_m+p_s)\theta-p_s\theta_s-Q_m\theta_m)}_{\phi_{sm+}}\end{aligned} \tag{2.14}$$

$$\begin{aligned}\phi_{rm} = & \underbrace{M_r\mathcal{P}_{avg}\cos(p_r(\theta-\theta_r))}_{\phi_{rmf}} + \\ & \underbrace{\frac{M_r\mathcal{P}_{mod}}{2}\cos((Q_m-p_r)\theta+p_r\theta_r-Q_m\theta_m)}_{\phi_{rm-}} + \\ & \underbrace{\frac{M_r\mathcal{P}_{mod}}{2}\cos((Q_m+p_r)\theta-p_r\theta_r-Q_m\theta_m)}_{\phi_{rm+}}\end{aligned} \tag{2.15}$$

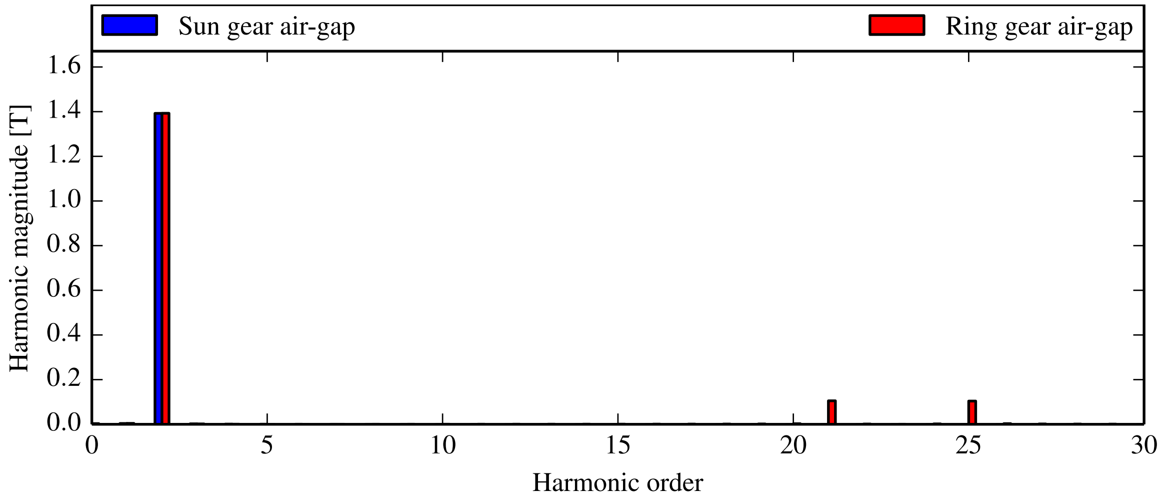

(a) Harmonics produced by the sun gear.

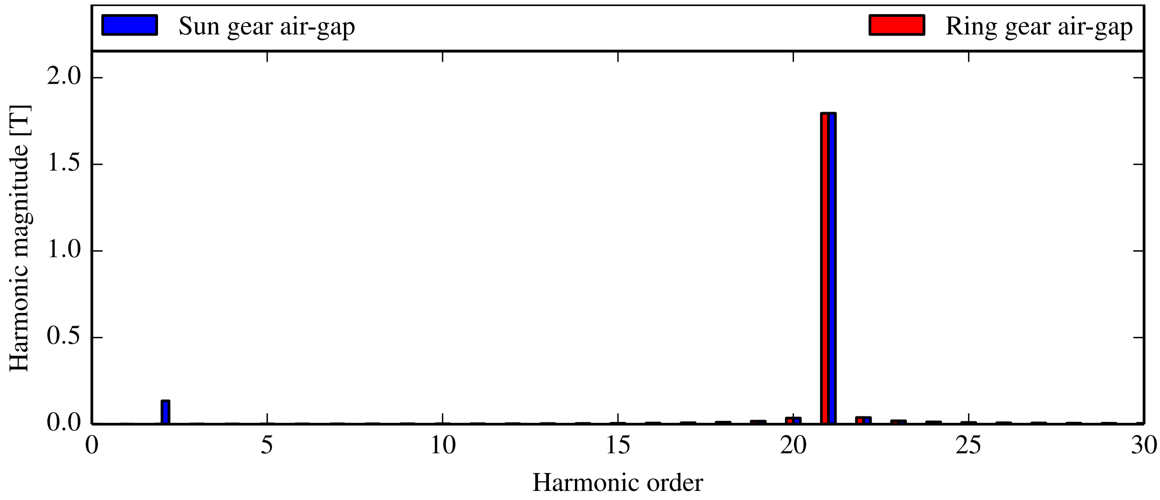

(b) Harmonics produced by the ring gear.

Figure 2.10: Space-harmonic flux density spectra in the air-gaps.

In (2.14) and (2.15), it is clear that the modulated fluxes have three components. The first (ϕ_{smf} and ϕ_{rmf}) are of the same order (fundamental) as the source MMF. The second and third components correspond to the two terms on the right-hand side of (2.13). In order for one of these modulated harmonics to interact usefully with the source harmonic from the opposite side, the order of the harmonics must be the same. This requirement can be stated as follows:

$$\text{Outer air-gap:} \quad p_r = |Q_m \mp p_s| \tag{2.16}$$

$$\text{Inner air-gap:} \quad p_s = |Q_m \mp p_r| \tag{2.17}$$

Upon further inspection, the choices can be reduced by disregarding the case where $p_s > p_r$ since this effectively reverses the roles of the sun and the ring gears. Thus, two choices which satisfy (2.16) and (2.17) remain:

$$p_r = Q_m - p_s \tag{2.18}$$

$$p_r = Q_m + p_s \tag{2.19}$$

Selecting (2.18) results in ϕ_{sm-} and ϕ_{rm-} acting as working modulated harmonics. Alternatively, using (2.19) results in ϕ_{sm+} and ϕ_{rm-} acting as working harmonics.

Although the choice of using (2.18) or (2.19) seems equally valid from this analysis, in practice, (2.18) results in significantly better performance.

2.3.3 Torque characteristics

Electromagnetic torque is produced in a magnetic gear when the energy stored in magnetic fields varies with rotation of the components. The torque on a component can be expressed as

$$T = \frac{\partial W'}{\partial \theta_c} \tag{2.20}$$

with W' the co-energy of the system and θ_c the angular position of the component on which the torque is calculated. In this analysis it is assumed that all the co-energy is stored in the air-gaps and the magnets. In these regions, the co-energy can be calculated as

$$W' = \frac{1}{2\mu_0} \int_V B^2 \mathrm{d}V \tag{2.21}$$

assuming that the permeability of the magnets is approximately equal to that of air (free space). The flux density, B, is calculated as

$$B(r,\theta) = \frac{\phi(\theta)}{2\pi r L} \tag{2.22}$$

where L is the stack length of the gear. Substituting (2.22) into (2.21) yields

$$W' = \frac{1}{2\mu_0} \int_\theta \int_r \int_z \frac{\phi^2}{(2\pi r L)^2} r \mathrm{d}z \mathrm{d}r \mathrm{d}\theta \tag{2.23}$$

$$= \underbrace{\frac{\ln r_o - \ln r_i}{8\mu_0 \pi^2 L}}_{C_g} \underbrace{\int_0^{2\pi} \phi^2 \mathrm{d}\theta}_{I_\phi} \tag{2.24}$$

with r_i and r_o the inner and outer radii of the volume of integration. The total flux in the inner and outer regions is

$$\phi_i = \phi_s + \phi_{rmf} + \phi_{rm-} + \phi_{rm+} \tag{2.25}$$

$$\phi_o = \phi_r + \phi_{smf} + \phi_{sm-} + \phi_{sm+} \tag{2.26}$$

The integral in (2.24) for the inner region is

$$I_{\phi i} = \int_0^{2\pi} \phi_i^2 \mathrm{d}\theta = \int_0^{2\pi} (\phi_s + \phi_{rmf} + \phi_{rm-} + \phi_{rm+})^2 \mathrm{d}\theta \tag{2.27}$$

Expanding the integrand results in 16 terms of the form $M\cos(a\theta + b)\cos(c\theta + d)$. According to (A.20), only the terms with $|a| = |c|$ make non-zero contributions to the integral. Two cases arise, depending on whether (2.18) or (2.19) holds.

In the case where $p_r = Q_m - p_s$, the integral becomes

$$I_{\phi i} = \int_0^{2\pi} (\phi_s^2 + 2\phi_s\phi_{rm-} + \phi_{rmf}^2 + \phi_{rm-}^2 + \phi_{rm+}^2) \mathrm{d}\theta \tag{2.28}$$

Similarly, the integral for the outer air-gap is

$$I_{\phi o} = \int_0^{2\pi} (\phi_r^2 + 2\phi_r\phi_{sm-} + \phi_{smf}^2 + \phi_{sm-}^2 + \phi_{sm+}^2)\mathrm{d}\theta \tag{2.29}$$

Note that the order of the harmonics ϕ_s and ϕ_{rm-} are equal. Similarly, the order of ϕ_r and ϕ_{sm-} are equal. Using (A.1) and (A.20) to evaluate the integrals results in

$$\begin{aligned} I_{\phi i} &= \pi M_s^2\mathcal{P}_{avg}^2 + M_sM_r\mathcal{P}_{avg}\mathcal{P}_{mod}\cos(-p_s\theta_s - p_r\theta_r + Q_m\theta_m) + \\ &\quad \pi M_r^2\mathcal{P}_{avg}^2 + \pi\frac{M_r^2\mathcal{P}_{mod}^2}{2} + \pi\frac{M_r^2\mathcal{P}_{mod}^2}{2} \\ &= \pi(\mathcal{P}_{avg}^2(M_s^2 + M_r^2) + \mathcal{P}_{mod}^2M_r^2) + M_sM_r\mathcal{P}_{avg}\mathcal{P}_{mod}\cos(-p_s\theta_s - p_r\theta_r + Q_m\theta_m) \end{aligned} \tag{2.30}$$

$$\begin{aligned} I_{\phi o} &= \pi M_r^2\mathcal{P}_{avg}^2 + M_sM_r\mathcal{P}_{avg}\mathcal{P}_{mod}\cos(-p_s\theta_s - p_r\theta_r + Q_m\theta_m) + \\ &\quad \pi M_s^2\mathcal{P}_{avg}^2 + \pi\frac{M_s^2\mathcal{P}_{mod}^2}{2} + \pi\frac{M_s^2\mathcal{P}_{mod}^2}{2} \\ &= \pi(\mathcal{P}_{avg}^2(M_s^2 + M_r^2) + \mathcal{P}_{mod}^2M_s^2) + M_sM_r\mathcal{P}_{avg}\mathcal{P}_{mod}\cos(-p_s\theta_s - p_r\theta_r + Q_m\theta_m) \end{aligned} \tag{2.31}$$

The co-energy in the inner and outer regions is given by

$$W_i' = \underbrace{\frac{\ln r_{mi} - \ln r_{smi}}{8\mu_0\pi^2L}}_{C_i} I_{\phi i} \tag{2.32}$$

$$W_o' = \underbrace{\frac{\ln r_{rmo} - \ln r_{mo}}{8\mu_0\pi^2L}}_{C_o} I_{\phi o} \tag{2.33}$$

The radii, r_{mi}, r_{smi}, r_{rmo} and r_{mo} are defined in Fig. 2.7. These represent the inner and outer radii of the inner and outer volumes of integration.

The torque on the ring gear is calculated as the change in co-energy in both air-gaps due to rotation of the ring gear:

$$T_r = \frac{\partial W_i'}{\partial\theta_r} + \frac{\partial W_o'}{\partial\theta_r} \tag{2.34}$$

$$= C_i\frac{\partial I_{\phi i}}{\partial\theta_r} + C_o\frac{\partial I_{\phi o}}{\partial\theta_r} \tag{2.35}$$

$$\frac{\partial I_{\phi i}}{\partial\theta_r} = \frac{\partial}{\partial\theta_r}\int_0^{2\pi} (\phi_s^2 + 2\phi_s\phi_{rm-} + \phi_{rmf}^2 + \phi_{rm-}^2 + \phi_{rm+}^2)\mathrm{d}\theta \tag{2.36}$$

$$\frac{\partial I_{\phi o}}{\partial\theta_r} = \frac{\partial}{\partial\theta_r}\int_0^{2\pi} (\phi_r^2 + 2\phi_r\phi_{sm-} + \phi_{smf}^2 + \phi_{sm-}^2 + \phi_{sm+}^2)\mathrm{d}\theta \tag{2.37}$$

In the above, the integrals of the quadratic terms are all independent of θ_r, and thus they do not contribute to the torque. From these equations it can be seen that only the modulated harmonics with the same order as those of the opposite source contribute to the torque.

$$\frac{\partial I_{\phi i}}{\partial\theta_r} = \frac{\partial}{\partial\theta_r}\int_0^{2\pi} (2\phi_s\phi_{rm-})\mathrm{d}\theta \tag{2.38}$$

$$\begin{aligned} &= \frac{\partial}{\partial\theta_r}\int_0^{2\pi} 2M_s\mathcal{P}_{avg}\cos(p_s\theta - p_s\theta_s)\cdot \\ &\quad \frac{M_r\mathcal{P}_{mod}}{2}\cos((Q_m - p_r)\theta + p_r\theta_r - Q_m\theta_m)\mathrm{d}\theta \end{aligned} \tag{2.39}$$

$$\frac{\partial I_{\phi o}}{\partial \theta_r} = \frac{\partial}{\partial \theta_r}\int_0^{2\pi} (2\phi_r\phi_{sm-})\mathrm{d}\theta \tag{2.40}$$

$$= \frac{\partial}{\partial \theta_r}\int_0^{2\pi} 2M_r\mathcal{P}_{avg}\cos(p_r\theta - p_r\theta_r)\cdot \tag{2.41}$$

$$\frac{M_s\mathcal{P}_{mod}}{2}\cos((Q_m - p_s)\theta + p_s\theta_s - Q_m\theta_m)\mathrm{d}\theta \tag{2.42}$$

When $p_s = Q_m - p_r$, the integrals can be evaluated using (A.20), giving

$$\frac{\partial I_{\phi i}}{\partial \theta_r} = \frac{\partial}{\partial \theta_r}\left(M_sM_r\mathcal{P}_{avg}\mathcal{P}_{mod}\cos(-p_s\theta_s - p_r\theta_r + Q_m\theta_m)\right) \tag{2.43}$$

$$= p_rM_sM_r\mathcal{P}_{avg}\mathcal{P}_{mod}\sin(-p_s\theta_s - p_r\theta_r + Q_m\theta_m) \tag{2.44}$$

$$\frac{\partial I_{\phi o}}{\partial \theta_r} = \frac{\partial}{\partial \theta_r}\left(M_sM_r\mathcal{P}_{avg}\mathcal{P}_{mod}\cos(-p_r\theta_r - p_s\theta_s + Q_m\theta_m)\right) \tag{2.45}$$

$$= p_rM_sM_r\mathcal{P}_{avg}\mathcal{P}_{mod}\sin(-p_r\theta_r - p_s\theta_s + Q_m\theta_m) \tag{2.46}$$

Note that according to this model, the amount of co-energy stored in the two working harmonics of order p_s and p_r are equal and that $\frac{\partial I_{\phi i}}{\partial \theta_r} = \frac{\partial I_{\phi o}}{\partial \theta_r}$. This means that the torque on any component is due to the variation in the co-energy stored in both working harmonics and that their contributions to torque are equal. Substituting (2.44) and (2.46) back into (2.35), the torque on the ring gear can be expressed as

$$T_r = (C_i + C_o)\,p_rM_sM_r\mathcal{P}_{avg}\mathcal{P}_{mod}\sin(-p_s\theta_s - p_r\theta_r + Q_m\theta_m) \tag{2.47}$$

$$T_r = \frac{\ln\frac{r_{mi}}{r_{smi}} + \ln\frac{r_{rmo}}{r_{mo}}}{8\mu_0\pi^2 L}p_rM_sM_r\mathcal{P}_{avg}\mathcal{P}_{mod}\sin(-p_s\theta_s - p_r\theta_r + Q_m\theta_m) \tag{2.48}$$

$$T_r = -\frac{p_rM_sM_r\mathcal{P}_{avg}\mathcal{P}_{mod}}{8\mu_0\pi^2 L}\left(\ln\frac{r_{mi}}{r_{smi}} + \ln\frac{r_{rmo}}{r_{mo}}\right)\sin(p_s\theta_s + p_r\theta_r - Q_m\theta_m) \tag{2.49}$$

The permeances, $\mathcal{P}_{avg}$ and $\mathcal{P}_{mod}$, can be expressed as quantities per unit of model depth or stack length:

$$\mathcal{P}_{avg} = L\mathcal{P}^l_{avg} \qquad\qquad \mathcal{P}_{mod} = L\mathcal{P}^l_{mod} \tag{2.50}$$

Substituting (2.50) into (2.49) yields

$$T_r = -\frac{p_rLM_sM_r\mathcal{P}^l_{avg}\mathcal{P}^l_{mod}}{8\mu_0\pi^2}\left(\ln\frac{r_{mi}}{r_{smi}} + \ln\frac{r_{rmo}}{r_{mo}}\right)\sin(p_s\theta_s + p_r\theta_r - Q_m\theta_m) \tag{2.51}$$

Similar formulae for the torque on the sun gear and the modulator can be derived. To summarize, the torque on the three components in a FMMG can be expressed as

$$T_s = -\frac{p_sLM_sM_r\mathcal{P}^l_{avg}\mathcal{P}^l_{mod}}{8\mu_0\pi^2}\left(\ln\frac{r_{mi}r_{rmo}}{r_{smi}r_{mo}}\right)\sin(p_s\theta_s + p_r\theta_r - Q_m\theta_m) \tag{2.52}$$

$$T_r = -\frac{p_rLM_sM_r\mathcal{P}^l_{avg}\mathcal{P}^l_{mod}}{8\mu_0\pi^2}\left(\ln\frac{r_{mi}r_{rmo}}{r_{smi}r_{mo}}\right)\sin(p_s\theta_s + p_r\theta_r - Q_m\theta_m) \tag{2.53}$$

$$T_m = \frac{Q_mLM_sM_r\mathcal{P}^l_{avg}\mathcal{P}^l_{mod}}{8\mu_0\pi^2}\left(\ln\frac{r_{mi}r_{rmo}}{r_{smi}r_{mo}}\right)\sin(p_s\theta_s + p_r\theta_r - Q_m\theta_m) \tag{2.54}$$

From these equations, it can be seen that

$$T_m = \frac{-Q_m}{p_s} T_s = -G_{sm} T_s \tag{2.55}$$

$$T_r = \frac{p_r}{p_s} T_s = G_{sr} T_s \tag{2.56}$$

The load angle in a FMMG is the argument of the sine function in (2.52), (2.53) and (2.54).

$$\delta_g = p_s\theta_s + p_r\theta_r - Q_m\theta_m \tag{2.57}$$

Using a similar approach, torque equations can also be derived for the case where $p_r = Q_m + p_s$. The complete derivation of these equations is given in appendix B. As mentioned previously, the modulation set is usually chosen so that $p_r = Q_m - p_s$ in which case (2.52) – (2.57) apply.

2.3.4 Speed characteristics

With an equation for the load angle (2.57) available, the relationship between the angular velocities of the three components can be derived. This is accomplished by taking the derivate of (2.57)

$$\frac{\mathrm{d}\delta_g}{\mathrm{d}t} = p_s\frac{\mathrm{d}\theta_s}{\mathrm{d}t} + p_r\frac{\mathrm{d}\theta_r}{\mathrm{d}t} - Q_m\frac{\mathrm{d}\theta_m}{\mathrm{d}t} \tag{2.58}$$

During steady-state operation, the load angle is constant and its derivative is zero. The remaining derivatives are the angular velocities of the components. Thus,

$$0 = p_s\omega_s + p_r\omega_r - Q_m\omega_m \tag{2.59}$$

$$p_s\omega_s + p_r\omega_r = Q_m\omega_m \tag{2.60}$$

$$\omega_s p_s + \omega_r p_r = \omega_m(p_s + p_r) \tag{2.61}$$

The above equation is in the exact same form as (2.2) for planetary gears.

2.3.5 Discussion

From equations (2.52) to (2.54), several observations can be made:

- The maximum torque on the sun and ring gear increases linearly with the number of pole-pairs. The maximum torque on the modulator increases linearly with the number of modulator segments.
- The torque has a linear dependence on the sun and ring gear MMFs, as well as the average and modulating permeances, $\mathcal{P}_{avg}$ and $\mathcal{P}_{mod}$.
- Naturally, the load angle is the same for all three components.
- The relationship between the angular velocities of the three components is the same as in planetary gears with the number of gear teeth substituted with pole pairs and modulator segments.

2.4 An alternative model

The primary purpose of the model in the previous section is that it allows the derivation of simple closed-form equations for the torque on the various components of a FMMG. However, it is unable to accurately model the harmonic content of the magnetic flux in various parts of the magnetic gear. An alternative model which is more accurate is presented in this section. The model is also based on equivalent magnetic circuits, but additional flux paths and smoothing effects are considered.

The MMFs are represented by square waves

$$\mathcal{F}_s = H_c t_{ms} f(p_s(\theta - \theta_s)) \tag{2.62}$$

$$\mathcal{F}_r = H_c t_{mr} f(p_r(\theta - \theta_r)) \tag{2.63}$$

$$\tag{2.64}$$

In the above equations, H_c is the coercive force of the magnets and t_{ms} and t_{mr} are the respective thicknesses of the sun and ring gear magnets. The function $f(p\theta)$ defines a square wave of order p with a value of either 1 or -1. The modulator reluctance is also represented by a square wave

$$\mathcal{R}_m = \frac{t_m}{2\mu_s L} + \left(\frac{t_m}{2\mu_0 L} - \frac{t_m}{2\mu_s L}\right) \cdot (1.1 - 0.9 f(Q_m(\theta - \theta_m))) \tag{2.65}$$

with t_m the thickness of the modulator and μ_s the permeability of the modulator lamination steel. This function is defined so that the reluctance varies between minima and maxima corresponding to positions aligned with the teeth and the slots respectively.

The reluctances associated with the magnets are

$$\mathcal{R}_s = \frac{t_{ms}}{\mu_m L} \tag{2.66}$$

$$\mathcal{R}_r = \frac{t_{mr}}{\mu_m L} \tag{2.67}$$

$$\tag{2.68}$$

for the sun and ring gear magnets, respectively, where μ_m is the permeability of the magnets.

For both the sun and ring gears, two flux paths are considered. These paths are illustrated in Figs. 2.11 and 2.12.

For the leakage paths, the horizontal reluctances are modeled as

$$\mathcal{R}_{sl} = \frac{\pi r_{mi}}{p_s \mu_0 L} \cdot |\cos(p_s(\theta - \theta_s))| \tag{2.69}$$

$$\mathcal{R}_{rl} = \frac{\pi r_{mo}}{p_r \mu_0 L} \cdot |\cos(p_r(\theta - \theta_r))| \tag{2.70}$$

In this model, the total flux in the air-gap adjacent to the source MMF is first calculated. The flux in the modulator and the opposing air-gap is then calculated based on two assumptions, i.e.

- The total flux is distributed, preferring paths of the highest permeance
- Filters are used to account for 2D flux paths

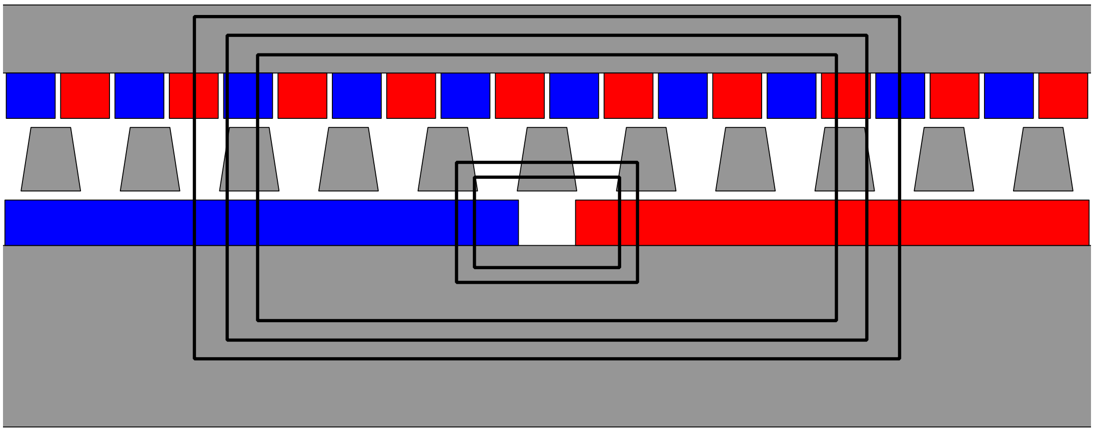

Figure 2.11: Flux paths for the sun gear.

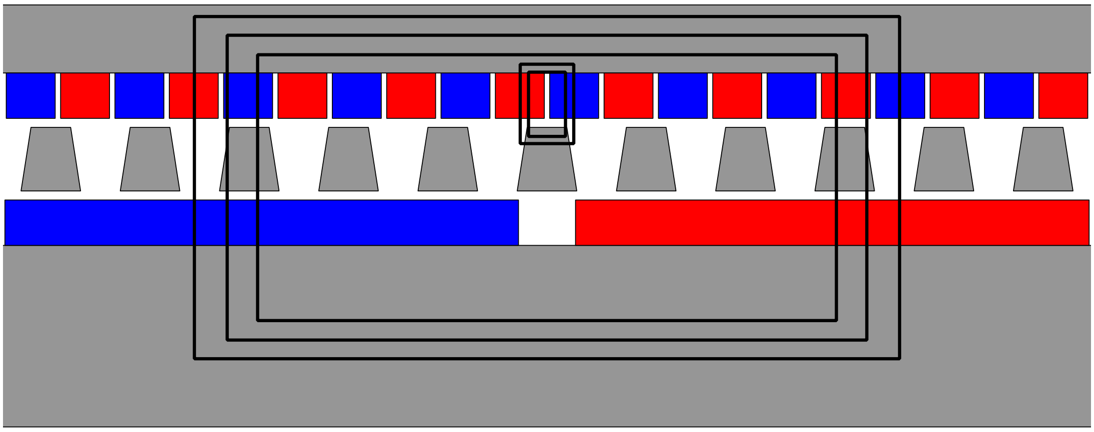

Figure 2.12: Flux paths for the ring gear.

2.4.1 Sun gear

The flux in the sun gear air-gap is divided into two components, the flux in the coupling and the leakage paths. For the coupling path, the flux is calculated as

$$\phi_{sc} = \frac{\mathcal{F}_s}{\mathcal{R}_s + \mathcal{R}_r + \mathcal{R}_m * w_s} \tag{2.71}$$

The term $\mathcal{R}_m * w_s$ denotes the convolution of $\mathcal{R}_m$ with a window function w_s. The effect is that the equivalent reluctance of the modulator seen in the sun gear air-gap is a smoothed (filtered) version of the modulator reluctance given by (2.65). The flux in the sun gear leakage path is calculated as

$$\phi_{sl} = \frac{\mathcal{F}_s}{\mathcal{R}_s + \mathcal{R}_{sl}} \tag{2.72}$$

in which the oscillating nature of the modulator reluctance is not considered. The total flux in the sun gear air-gap is then simply

$$\phi_s = \phi_{sc} + \phi_{sl} \tag{2.73}$$

The flux in the modulator is calculated using a "flux division" principle, analogous to current division in parallel circuit branches. Only ϕ_{sc} is considered as a source for the flux in the modulator. In its most basic form, the equation for the modulator flux is

$$\phi_{sm} = \phi_{sc} \cdot \frac{\frac{1}{\mathcal{R}_m}}{\left\langle \frac{1}{\mathcal{R}_m} \right\rangle} \tag{2.74}$$

Note that this differs from the usual current division equation in that the average value, $\left\langle \frac{1}{\mathcal{R}_m} \right\rangle$, is used as the denominator. This is because the source is also distributed. This equation is modified to account for the tangential flux which distorts the flux waveforms.

$$\phi_{sm} = (\phi_{sc} * w_s) \cdot \frac{\frac{1}{\mathcal{R}_m}}{\left\langle \frac{1}{\mathcal{R}_m} \right\rangle} \tag{2.75}$$

The flux in the ring gear air-gap is calculated by assuming that the modulator flux spreads out (fringes) as it enters the air-gap. This fringing is also modeled by applying the convolution operation to the calculated modulator flux

$$\phi_{smr} = \phi_{sm} * w_r \tag{2.76}$$

in which w_r is another window function.

The flux densities calculated for the gear described in Table 2.1 are plotted in Figs. 2.13 – 2.15. The waveforms obtained from a FEM simulation are also shown for reference.

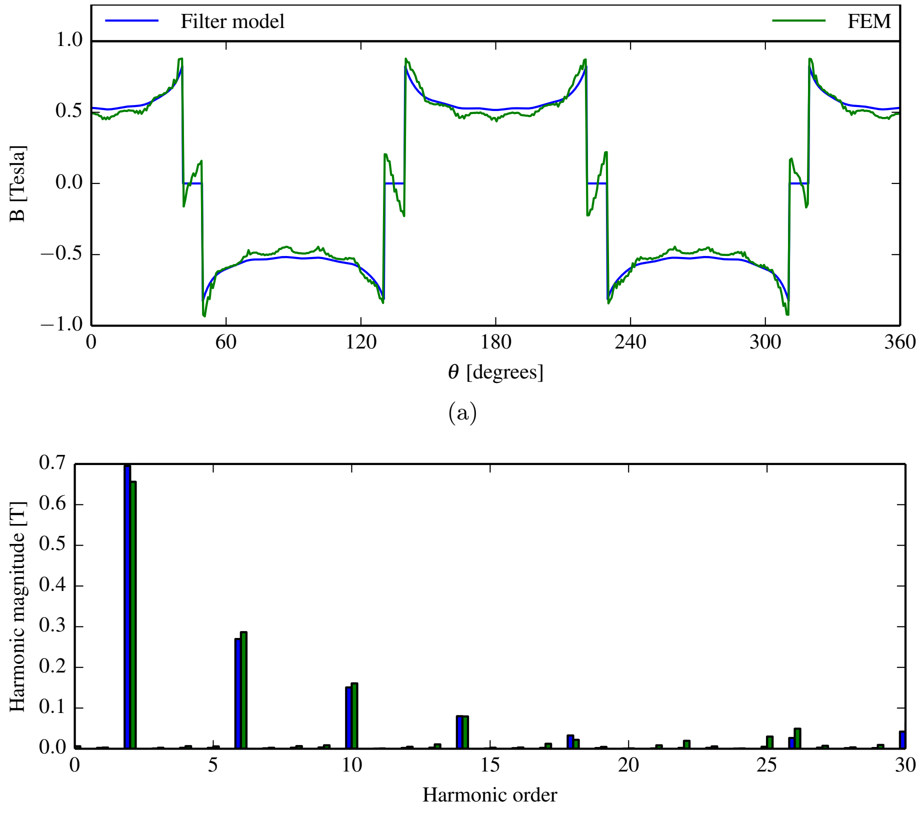

(a)

(b)

Figure 2.13: Flux density in the sun gear air-gap due to the sun gear magnets.

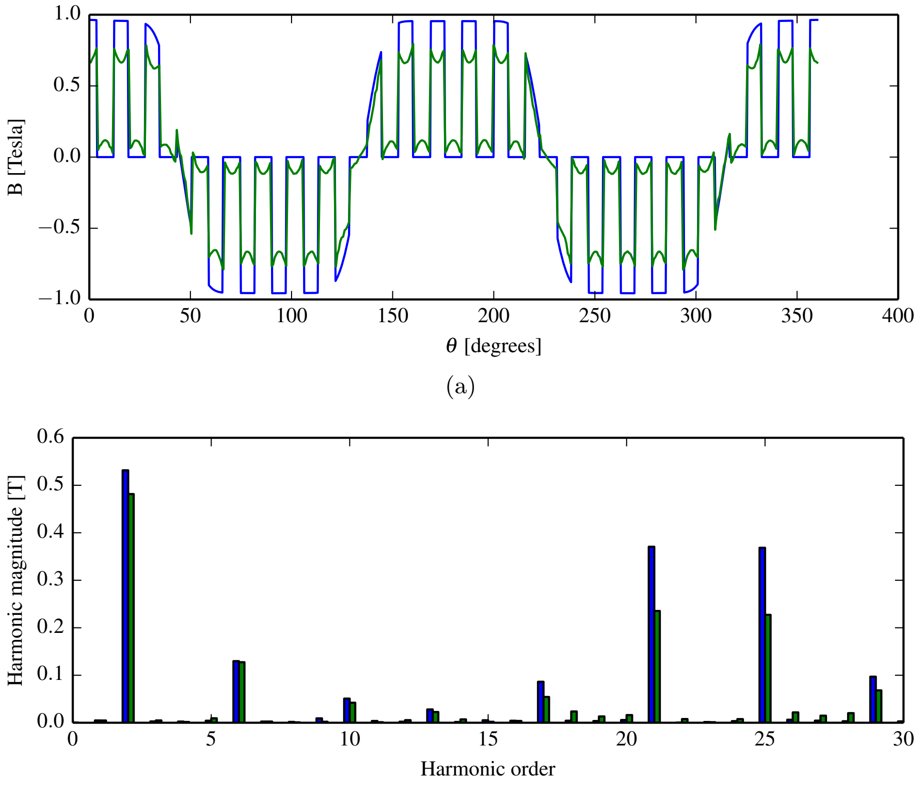

(a)

(b)

Figure 2.14: Flux density in the modulator due to the sun gear magnets.

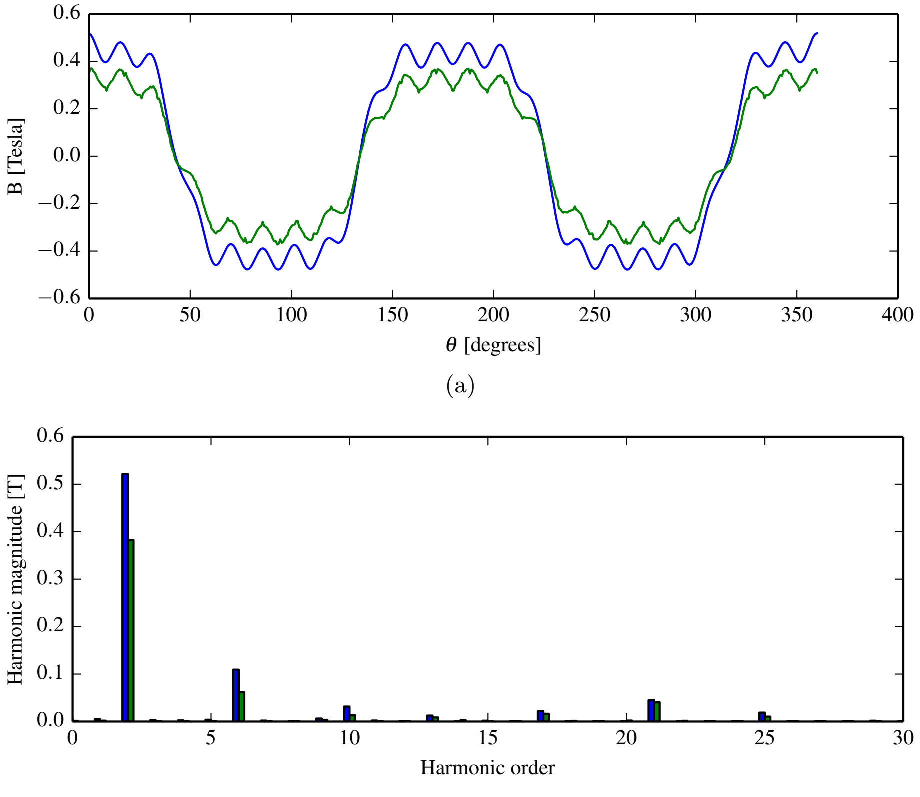

(a)

(b)

Figure 2.15: Flux density in the ring gear air-gap due to the sun gear magnets.

2.4.2 Ring gear

A similar approach is used when determining the fluxes generated by the ring gear.

The flux in the ring gear air-gap is given by

$$\phi_{rc} = \frac{\mathcal{F}_r}{\mathcal{R}_r + \mathcal{R}_s + \mathcal{R}_m * w_r} \tag{2.77}$$

$$\phi_{rl} = \frac{\mathcal{F}_r}{\mathcal{R}_r + \mathcal{R}_{rl}} \tag{2.78}$$

$$\phi_r = \phi_{rc} + \phi_{rl} \tag{2.79}$$

The flux in the modulator is then calculated as

$$\phi_{rm} = (\phi_{rc} * w_{r2}) \cdot \frac{\frac{1}{\mathcal{R}_m}}{\left\langle \frac{1}{\mathcal{R}_m} \right\rangle} \tag{2.80}$$

Note that the window function w_{r2} used in the above calculation differs from that in (2.77). This modification was found necessary in order to improve the accuracy of the model.

Finally, the flux in the sun gear air-gap is

$$\phi_{rms} = \phi_{rm} * w_s \tag{2.81}$$

The flux density waveforms generated by the ring gear magnets are shown in Figs. 2.16 – 2.18, once again with FEM waveforms for comparison.

2.4.3 Torque calculation

In this model, torque can also be calculated using (2.34). The only difference lies in the functions for the air-gap fluxes. Thus, using this model the different torque components can be expressed as

$$T_s = \frac{L(\ln r_{mi} - \ln r_{smi})}{8\mu_0\pi^2} \cdot \frac{\partial}{\partial\theta_s} \int_0^{2\pi} (\phi_s^l + \phi_{rms}^l)^2 \mathrm{d}\theta + \frac{L(\ln r_{rmo} - \ln r_{mo})}{8\mu_0\pi^2} \cdot \frac{\partial}{\partial\theta_s} \int_0^{2\pi} (\phi_r^l + \phi_{smr}^l)^2 \mathrm{d}\theta \tag{2.82}$$

$$T_r = \frac{L(\ln r_{mi} - \ln r_{smi})}{8\mu_0\pi^2} \cdot \frac{\partial}{\partial\theta_r} \int_0^{2\pi} (\phi_s^l + \phi_{rms}^l)^2 \mathrm{d}\theta + \frac{L(\ln r_{rmo} - \ln r_{mo})}{8\mu_0\pi^2} \cdot \frac{\partial}{\partial\theta_r} \int_0^{2\pi} (\phi_r^l + \phi_{smr}^l)^2 \mathrm{d}\theta \tag{2.83}$$

$$T_m = \frac{L(\ln r_{mi} - \ln r_{smi})}{8\mu_0\pi^2} \cdot \frac{\partial}{\partial\theta_m} \int_0^{2\pi} (\phi_s^l + \phi_{rms}^l)^2 \mathrm{d}\theta + \frac{L(\ln r_{rmo} - \ln r_{mo})}{8\mu_0\pi^2} \cdot \frac{\partial}{\partial\theta_m} \int_0^{2\pi} (\phi_r^l + \phi_{smr}^l)^2 \mathrm{d}\theta \tag{2.84}$$

In the above equations, the superscript l denotes values per unit of stack length. Unfortunately, the derivatives in the above expressions are not easily evaluated using analytical methods. However, numerical evaluation is simple and fast.

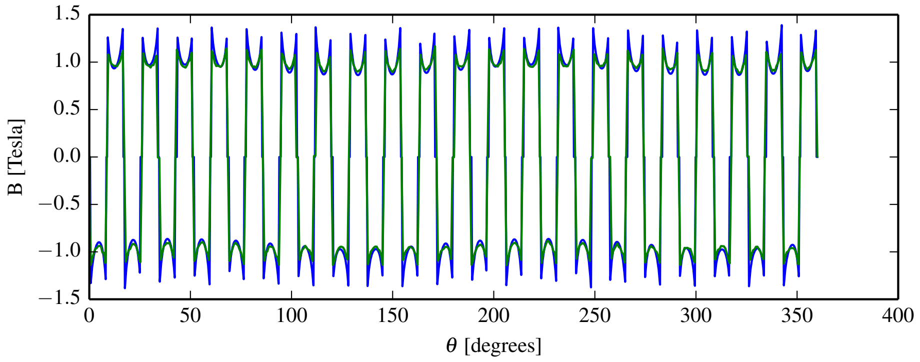

(a)

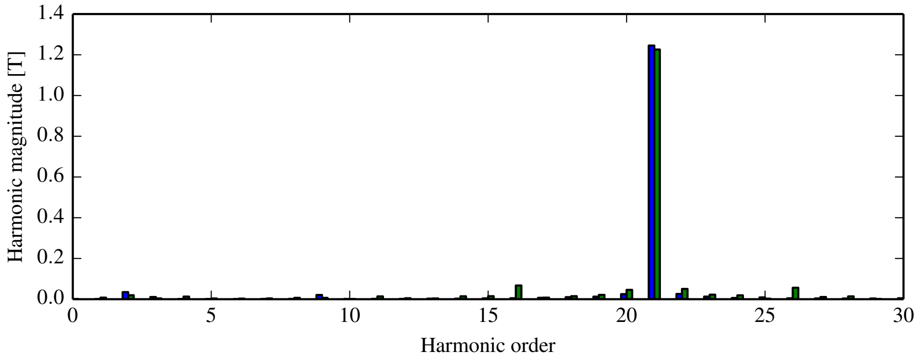

(b)

Figure 2.16: Flux density in the ring gear air-gap due to the ring gear magnets.

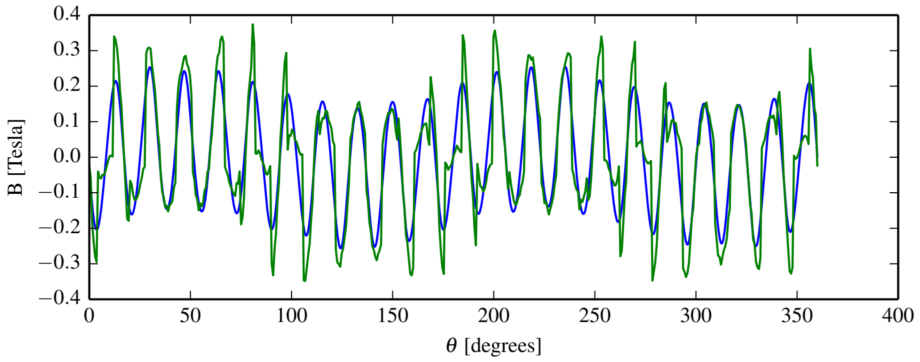

(a)

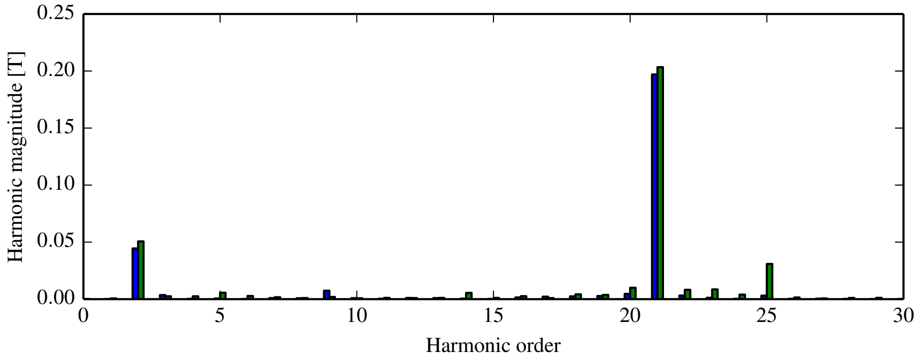

(b)

Figure 2.17: Flux density in the modulator due to the ring gear magnets.

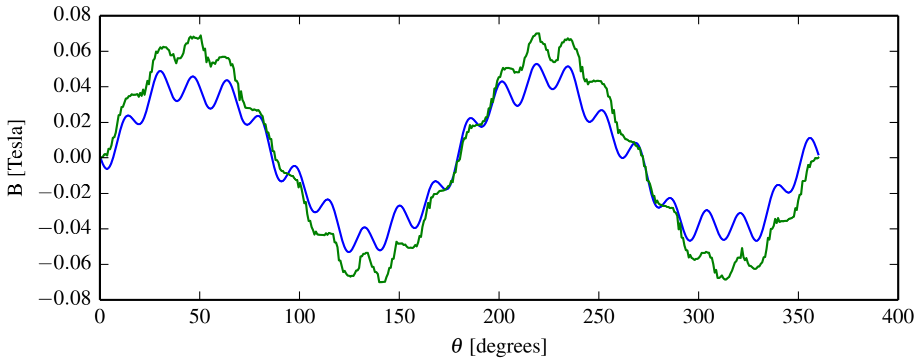

(a)

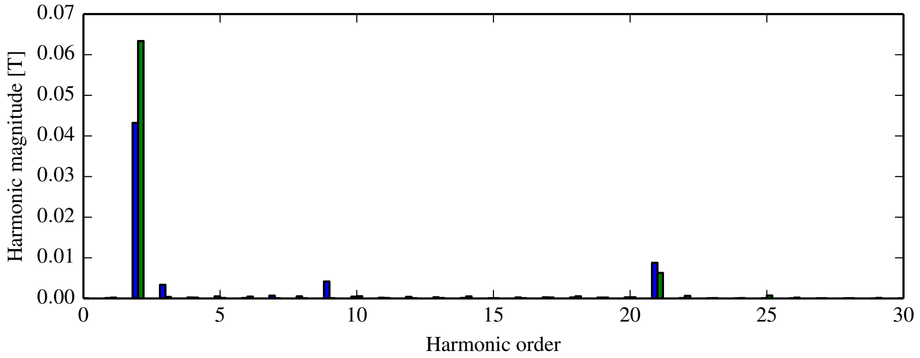

(b)

Figure 2.18: Flux density in the sun gear air-gap due to the ring gear magnets.

2.4.4 Discussion

It is clear from Figs. 2.13 – 2.18 that this model is capable of modeling the flux density harmonics to a relatively high accuracy. The drawbacks of this model are

- The model is sensitive to the window functions, which must be accurately estimated if correct results are to be obtained.
- The model assumes that the fluxes generated by the sun and ring gear can be superimposed to obtain the total flux. This is not correct because the reluctances change with higher saturation levels.
- In some aspects, the model lacks physical foundation and is merely a mathematical representation.

Despite these disadvantages, this model may be useful if the parameters of the model can be estimated accurately over a typical design space. However, the use of this model for design purposes was not pursued further in this work.

2.5 Other modeling methods

Although the models described in the previous sections are useful in the sense that they facilitate an understanding of FMMGs, they are not useful for general design purposes. The flux paths in

FMMGs are rather complex and there are many details which are not considered in the models. Another difficulty with these models lies in the estimation of the relevant model parameters.

Other models of FMMGs have been presented in literature. These include reluctance network models [31, 32], models employing winding function theory [20] and subdomain models [23, 65]. Some models are capable of including end-effects [32, 28], which can have a drastic impact on the performance of FMMGs, as will be illustrated in chapters 4 and 7. In general, a trade-off between simplicity and speed on the one hand and complexity and accuracy on the other hand has to be made. Some analytical models, such as the ones described in this chapter, also present an identification problem. It is not always easy to calculate model parameters based on the geometry of an FMMG.

In this work, only the finite element method was used for design analysis and optimization. The primary reasons for choosing this method are:

Ease of use: The method is the most flexible and allows vastly different topologies to be considered within the same framework.

Accuracy: The method can accurately model the geometry of the device under study with arbitrary variations in the topology. Furthermore, it can readily model saturation effects.

Speed: Although simulation times may be longer than with other methods, 2D FEM is sufficiently fast and the ease in which the model can be set up leads to time savings compared to other methods.

Chapter 3

Flux-modulated electrical machines

The operating principles of flux-modulated magnetic gears have been described. In this chapter, various topologies of electrical machines which rely on the flux modulation principle found in FMMGs will be discussed. An overview of the classification of electrical machines, as considered in this study, is shown in Fig. 3.1. As can be seen in the figure, the flux-modulated electrical machines are broadly divided into three categories:

Vernier machines These machines produce torque using a higher-order harmonic which is generated by the interaction of the stator's fundamental MMF harmonic with either the stator slots or an extra modulating component.

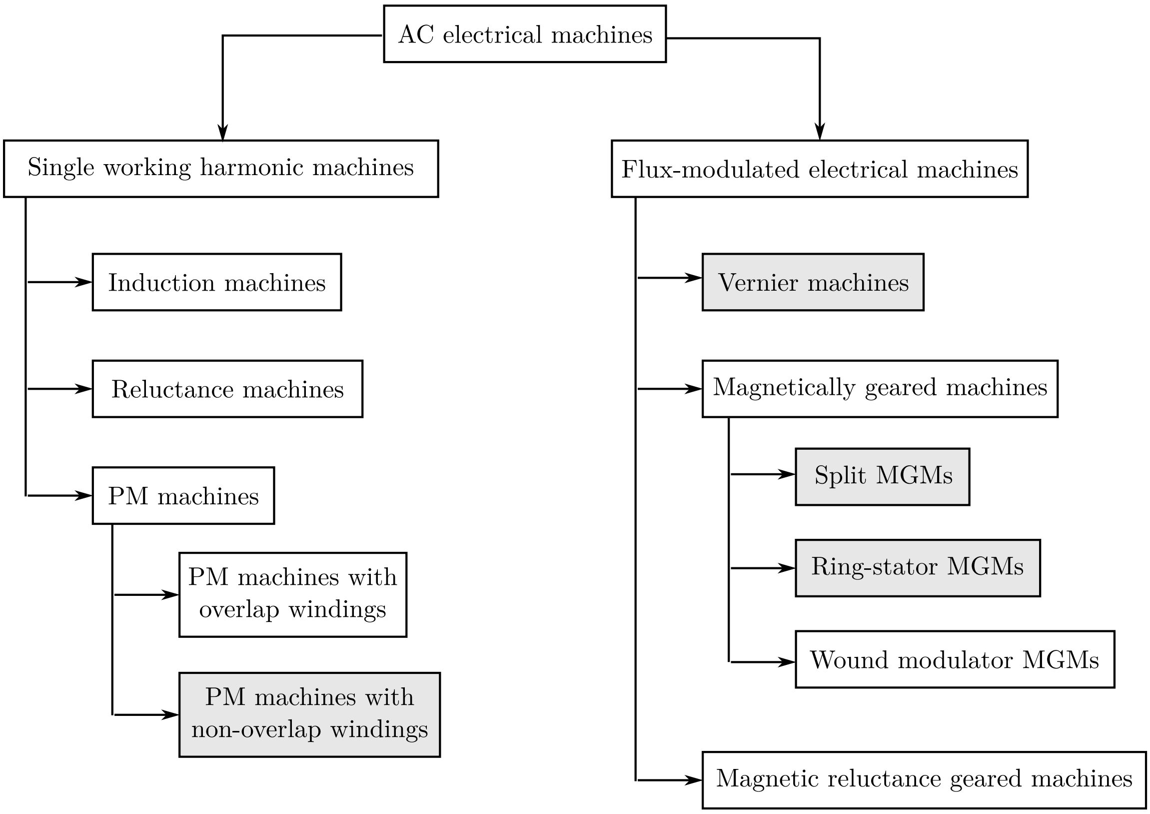

Figure 3.1: Classification of AC electrical machines. The four highlighted machines are given specific attention in this work and are compared in chapter 11.

Magnetically geared machines These topologies feature a full flux-modulated magnetic gear integrated with an electrical machine.

Magnetic reluctance geared machines These topologies feature a flux-modulated magnetic reluctance gear integrated with an electrical machine.

In this chapter, several variations of these machines will be described. Attention is given to the torque characteristics of magnetically geared machines, and equivalent circuit models are presented. Lastly, different operating modes of these special machines are discussed.

3.1 Split magnetically geared machines

Split magnetically geared machines consist of a separate flux-modulated magnetic gear and, typically, a permanent magnet machine. The defining characteristic is a shared high-speed rotor, adjacent to the modulator on one side and the stator on the other side. The rotor acts as both the sun gear and the machine's rotor. These machines typically have three air-gaps and can be configured as either magnetically decoupled, as illustrated in Fig. 3.2(a), or as magnetically coupled, shown in Fig. 3.2(b).

3.1.1 Decoupled configuration

Perhaps the simplest and most obvious method of integrating a flux-modulated magnetic gear and a permanent magnet machine is to fit the machine inside the gear and to share the sun gear yoke with the machine. In order to isolate the two components magnetically, the magnets on the inside and outside of the yoke should be of opposing polarity. In this way, the electrical machine and the gear can be magnetically decoupled. The disadvantage of the decoupled configuration

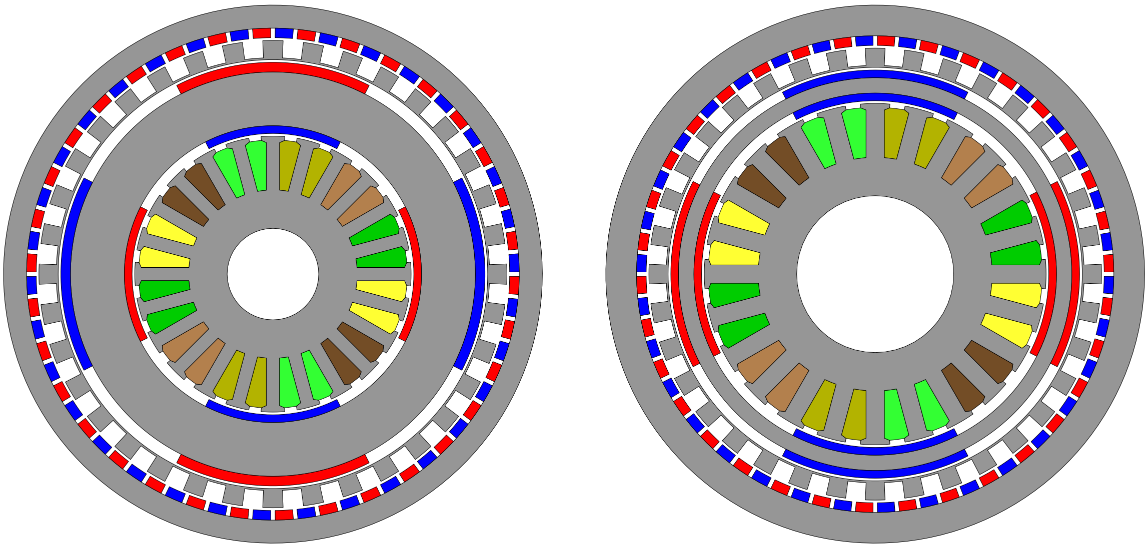

(a) Decoupled configuration (b) Coupled configuration

Figure 3.2: Split magnetically geared machines

is that a thick yoke is required for the shared rotor to separate the fluxes of the gear and the stator. On the other hand, the inductance of the machine in the decoupled configuration is usually higher than in a coupled machine. For this reason, the decoupled configuration may be better suited to applications such as traction drives.

3.1.2 Coupled configuration

The coupled configuration has the advantage that it requires no yoke for the sun gear. This allows a larger stator to be fitted inside the sun gear with a corresponding benefit in torque capability. One method of manufacturing the sun gear is to use a steel cylinder with surface mounted magnets on both sides, as shown in Fig. 3.2(b). A novel method which allows high torque densities to be realized, while reducing losses in the magnets, is presented in chapter 8.

3.1.3 Partially coupled configuration

In the design of magnetically geared machines, it is important to ensure that the magnetic gear and electrical machine contained in the design are well matched. In some circumstances, it may be desirable to have a coupled configuration, but with a higher portion of the sun gear's flux in the gear than in the stator. This can be achieved with the partially coupled configuration illustrated in Fig. 3.3. This topology also does not require a thick yoke, as with the decoupled configuration. The portion of flux penetrating the stator can be controlled by choosing an appropriate thickness for the sun gear yoke.

The flux paths in the decoupled, coupled and partially coupled configurations are shown in Fig. 3.4.

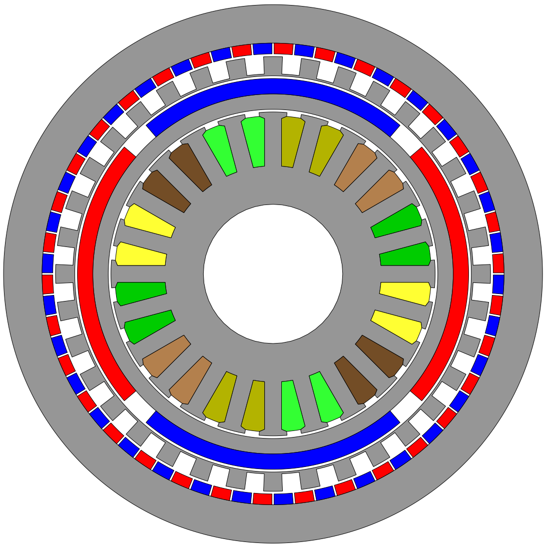

Figure 3.3: Split MGM: Partially coupled configuration.

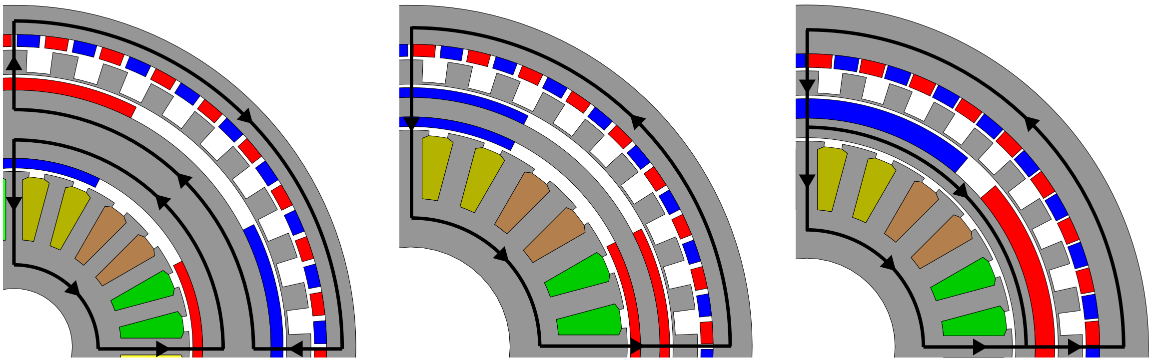

(a) Decoupled. (b) Coupled. (c) Partially coupled.

Figure 3.4: Flux paths in split MGM configurations.

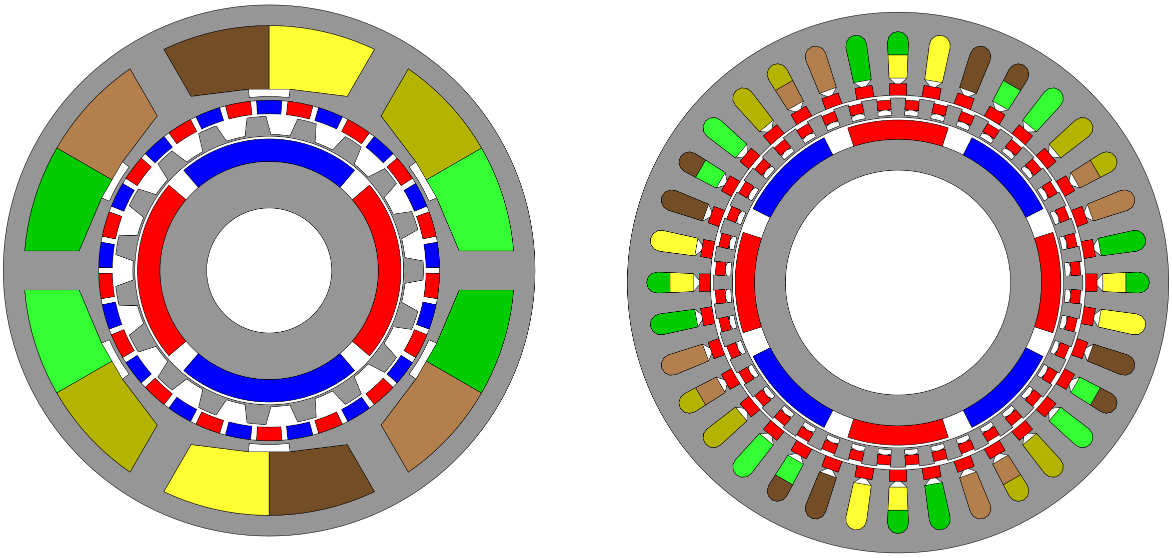

(a) Non-overlap winding, surface mounted magnets on inner stator periphery.

(b) Overlap winding, same polarity magnets between stator teeth and modulator segments.

Figure 3.5: Ring-stator magnetically geared machines.

3.2 Ring-stator magnetically geared machines

An alternative way of integrating a magnetic gear and a PM machine is to replace the ring gear yoke with a stator. In this way, one of the air-gaps required for split MGMs is eliminated. Ring-stator MGMs thus have only two air-gaps. This can be a significant advantage in terms of simplicity of construction. Ring-stator MGMs are also magnetically coupled machines in the sense that flux generated by the magnetic gear penetrates the stator.

Two examples of ring-stator machines are shown in Fig. 3.5. The first features a non-overlap winding with surface mounted magnets on the inner periphery of the stator, similar to the topology presented in [58, 59]. The second topology makes use of an overlap winding with a ring gear magnet arrangement alike to that found in some vernier machines [66]. Magnets of the same polarity are used, half are inserted in between the stator teeth and half between the modulator

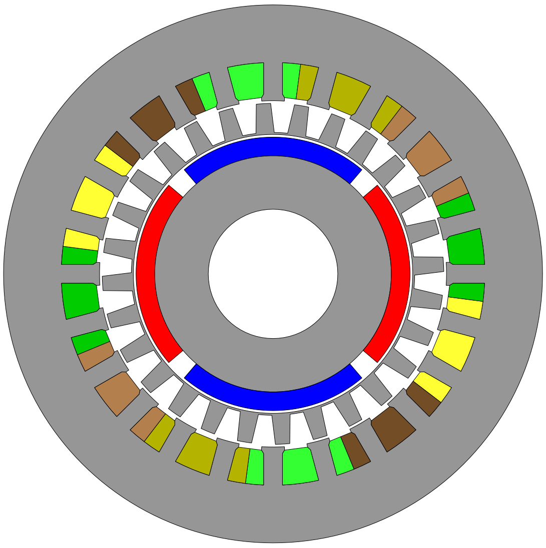

Figure 3.6: A ring stator machine with a magnetic reluctance gear.

segments. These two topologies are presented to give an appreciation of the multitude of options available when designing MGMs.

3.2.1 Reluctance gear variation

A possible variation of ring-stator machines is to omit the ring gear magnets. Such a machine has been presented in [67, 68]. This topology then consists of a flux-modulated magnetic reluctance gear with a stator winding inserted between the ring gear teeth. An example of this topology is shown in Fig. 3.6.

3.3 Wound modulator magnetically geared machines

Yet another method of integration is to insert a stator winding in the gaps between the modulator segments of a magnetic gear. Such a machine is illustrated in Fig. 3.7. The advantage of this configuration is that it utilizes the space occupied by the modulator much better. It also only requires three concentric components, with two air-gaps, as opposed to the four components and three air-gaps required by split MGMs. The disadvantage of this configuration is that the pole-pair combinations that can be employed is limited. Nevertheless, the wound modulator configuration is a good option in terms of space and active material utilization. Unfortunately, the mechanical construction of this topology is rather challenging. The wound modulator MGM is the topology which exhibits the strongest coupling between the flux generated by the magnetic gear and the stator.

3.4 Vernier machines

The similarity between magnetic gears and vernier machines has been pointed out in [69]. Essentially a vernier machine can be described as a permanent magnet machine in which the stator performs the function of both a sun gear and a modulator. A field similar to that produced by a sun gear is generated by the stator winding, whereas the stator slots modulate this field. Vernier machines share the high torque capability of magnetic gears to some extent, yet they are far simpler to manufacture than the other machines described in this chapter. An example of a vernier machine is shown in Fig. 3.8.

3.5 Magnetically geared machine torque characteristics

In conventional electrical machines with a single stator and a single rotor, there is only one torque to be investigated: the torque generated by the interaction of the stator and rotor fields and permeances. In the case of magnetically geared machines, there are generally three different sources of magnetomotive force, the stator, the sun gear and the ring gear. Typically, the modulator and the stator are slotted and so introduce permeance variations. Thus, in magnetically geared machines, the magnetic field interactions that produce torque are generally more complex than those in conventional machines. Furthermore, the magnitude and direction of the torque on the various components differ.

3.5.1 Component torques

MGMs in general, consist of four components, i.e. the stator, sun gear, modulator and ring gear. Depending on the topology, some of these components may be physically connected or integrated. In ring-stator machines, the stator and the ring gear form a single unit, whereas in wound modulator machines, the stator and the modulator are integrated. Nevertheless, in each case, the torque on the four distinct components can be defined.

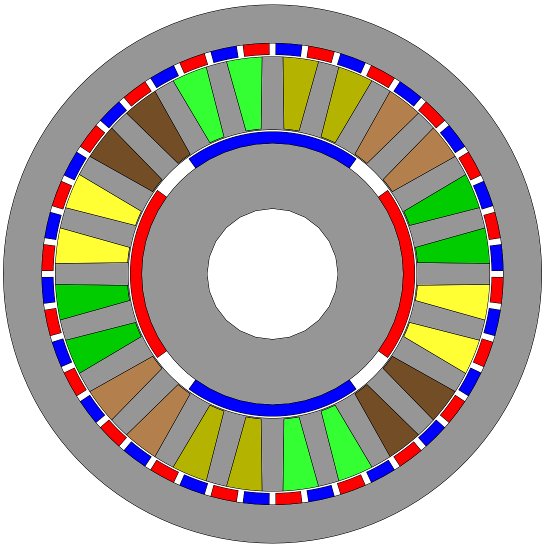

Figure 3.7: A Wound modulator magnetically geared machine.

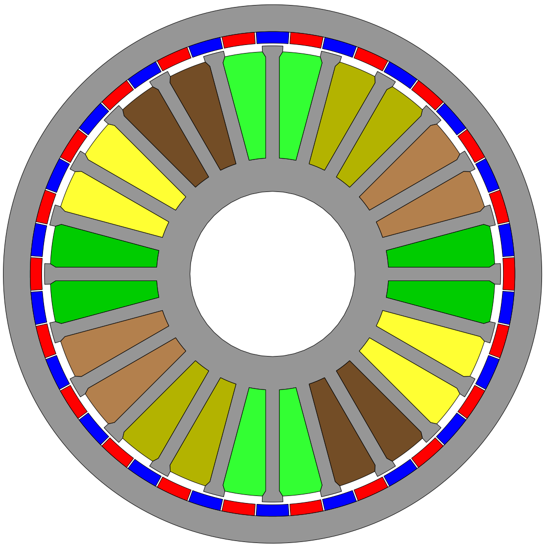

Figure 3.8: A Vernier machine.

For split MGMs, the torque on the four components is naturally defined as:

$$T_i = \frac{\partial W'}{\partial \theta_i} \qquad T_s = \frac{\partial W'}{\partial \theta_s} \tag{3.1}$$

$$T_m = \frac{\partial W'}{\partial \theta_m} \qquad T_r = \frac{\partial W'}{\partial \theta_r} \tag{3.2}$$

with θ_i defining the angular position of the stator. (The other angles have been defined in chapter 2.) In chapter 2, it was illustrated that the torque on the three components of a flux modulated magnetic gear is produced by the interaction of two space harmonics, one of order p_s and the other of order p_r. [1] In decoupled MGMs, the stator's field does not have an impact on the field in the magnetic gear and in this case, the stator torque is only produced by fields of order p_s, with the assumption that the stator is equipped with a p_s pole pair winding. However, in coupled MGMs, the stator's field does have an impact on the magnetic gear. The stator's field is modulated and thus, the stator torque is also produced by the two working harmonics in the machine. Furthermore, the stator's field can contribute to the torque on all the other components in an MGM, depending on the current angle and the magnetic gear's load angle.

The torque on the four components can also be expressed in terms of the air-gap torques T_1, T_2 and T_3. The air-gap torques define the torque transferred across the inner, center and outer air-gaps respectively. The orientation of these torques is defined such that a positive value corresponds to an anti-clockwise torque on the inner component and a clockwise torque on the outer component. The torques on the components, in terms of the air-gap torques are:

$$T_i = T_1 \tag{3.3}$$

$$T_s = T_2 - T_1 \tag{3.4}$$

$$T_m = T_3 - T_2 \tag{3.5}$$

$$T_r = -T_3 \tag{3.6}$$

By summing these equations, it is also clear that the following must hold:

$$T_i + T_s + T_m + T_r = 0 \tag{3.7}$$

In ring-stator and wound modulator machines, it is not as easy to define the torque on the four components in terms of their angular positions because two out of four components are physically integrated. However, with knowledge of the gear ratio, the torque on each of the four components can still be isolated.

For ring-stator machines, the torques on the sun gear and the modulator are defined as before:

$$T_s = \frac{\partial W'}{\partial \theta_s} = T_1 \qquad T_m = \frac{\partial W'}{\partial \theta_m} = T_2 - T_1 \tag{3.8}$$

Note the change in the air-gap number compared to the case of the split MGM. The torque on the outer component, the ring-stator, is equal to the outer air-gap torque,

$$T_{ri} = -T_2 \tag{3.9}$$

---

[1] This considers only the fundamental harmonics. In actual fact, higher order harmonics also contribute to the torque.

where the negative sign is required for the correct orientation of the air-gap torque defined earlier. The torques on the stator and the ring gear are then calculated as:

$$T_i = \frac{T_m}{-G_{sm}} - T_s \qquad\qquad T_r = T_{ri} - T_i \tag{3.10}$$

When defined in this way, (3.7) also holds for ring-stator machines.

In wound modulator machines, the torques can be defined as follows:

$$T_s = \frac{\partial W'}{\partial \theta_s} = T_1 \qquad\qquad T_r = \frac{\partial W'}{\partial \theta_r} = -T_2 \tag{3.11}$$

The torque on the integrated modulator and stator is

$$T_{mi} = T_2 - T_1 \tag{3.12}$$

which can be split into components using

$$T_i = \frac{T_r}{G_{sr}} - T_s \qquad\qquad T_m = T_{mi} - T_i \tag{3.13}$$

Once again, defining the torques in this way ensures that (3.7) is satisfied.

3.5.2 Average torque, cogging torque and torque ripple

Distinctions are often made between several kinds of torque, such as average torque, cogging torque and torque ripple. When discussing MGMs, it is necessary to be more elaborate when describing these different kinds of torque. In this section, these concepts are explored in the context of MGs and MGMs.

With the instantaneous torques on the four components defined in the previous section, the definition of the average component torque is obvious. However, this is not so for cogging torque and torque ripple. In conventional PM machines, cogging torque is defined as the torque on the rotor at standstill and zero current. This torque is a function of rotor position due to the variation in permeance caused by the stator slots. A similar definition could be made for MGMs if the machine is viewed as a unit with only a single shaft. However, it must be realized that an MGM has an additional degree of freedom, i.e. the sun gear's angular position. As mentioned, in conventional PM machines there is usually a single source of cogging torque, but in MGMs there are multiple sources. For example, cogging torque on the sun gear is generated as a result of the interaction between the sun gear's magnetic field and the stator slots, the modulator segments and the ring gear magnetic field. If an MGM's cogging torque is to be defined as for conventional machines, the criterion that the machine must be at standstill has interesting implications. If the sun gear is to be at standstill, the torque on this component must be zero. Consider the case of an MGM with the modulator acting as the low-speed rotor. According to the definition, the machine's cogging torque is the torque on the modulator versus its angular position at standstill and zero current. Cogging torque, defined in this manner, will be referred to as the *true cogging torque*:

$$\begin{aligned} &\text{True cogging torque} \equiv T_m(\theta_m) \\ &\text{with} \qquad \omega_m = 0 \qquad I = 0 \qquad T_s(\theta_s) = 0 \end{aligned} \tag{3.14}$$

The interesting thing here is that the solution to the condition $T_s(\theta_s) = 0$ occurs at non-zero load angles, except for points where the *synchronous cogging torque* (see below) on the sun gear is zero. This implies that the relationship between θ_m and θ_s in (3.14) is not linear. (See chapter 4 for an example.)

An alternative definition of cogging torque in an MGM can be referred to as the *synchronous cogging torque*. It can be defined for both rotors, as follows:

$$\text{Sun gear synchronous cogging torque} \equiv T_s(\theta_s) \tag{3.15}$$

$$\text{Modulator synchronous cogging torque} \equiv T_m(\theta_m) \tag{3.16}$$

$$\text{with} \qquad \omega_m = 0 \qquad \omega_s = 0 \qquad \delta_g = 0 \qquad I = 0 \tag{3.17}$$

The synchronous cogging torque is the torque on a rotor with no current in the machine and the gear's load angle equal to zero.

Torque ripple is defined as the variation in torque under loaded operating conditions. Similar principles apply to the definition of torque ripple as described for cogging torque. Variations in torque will result in variations in angular velocity and fluctuations in the load angle. However, it is far less critical to make the distinction between synchronous torque ripple and true torque ripple. The reason is that the frequency of the torque ripple is usually sufficiently high and the rotor inertia sufficiently large so that the torque ripple has little effect on the angular velocities of the rotors and the load angle. In MGMs, the torque on each of the four components will exhibit ripple under loaded conditions due to the interaction of various higher order harmonics present in the machine.

3.6 Equivalent circuit models

In this section equivalent circuit models of decoupled and coupled MGMs are presented. Decoupled MGMs can easily be modelled as a separate gear and electrical machine, employing a classical phasor diagram for the machine. For completeness' sake, a vector diagram of the current, flux linkage components and voltage of a decoupled MGM is shown in Fig. 3.9. This diagram is the same as for a conventional PM machine. Fig. 3.10 shows a per phase equivalent circuit model of a decoupled MGM.

Coupled MGMs have an additional source of flux, as illustrated in Fig. 3.11 which shows a vector diagram of the current, flux linkage components and voltage of a coupled MGM in the dq-plane. Note that the depicted flux linkage phasors represent the space harmonic of order p_s. A per phase equivalent circuit diagram is shown in Fig. 3.12. Since the inductances vary between the direct and quadrature axes, it is most convenient to employ dq-models with the d-axis aligned to the sun gear's magnetic axis. The direct and quadrature axis circuit models, derived from the vector diagram in Fig. 3.11, are shown in Fig. 3.13.

The flux linkage due to the stator currents, excluding the end-winding flux linkage, is given by

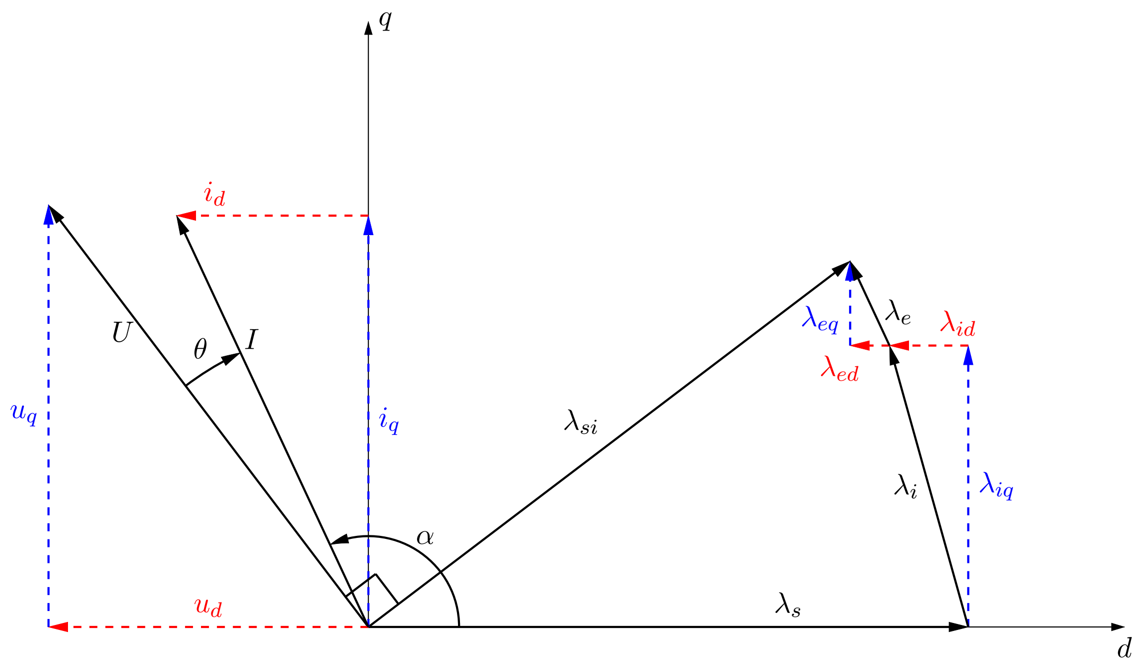

Figure 3.9: Vector diagram of a decoupled MGM.

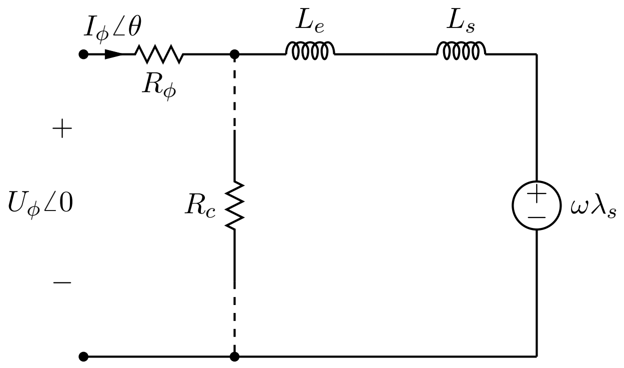

Figure 3.10: Equivalent per phase circuit model of a decoupled MGM.

λ_i. This flux can be separated into its dq components,

$$\lambda_{id} = \omega L_d i_d \tag{3.18}$$

$$\lambda_{iq} = \omega L_q i_q \tag{3.19}$$

$$\tag{3.20}$$

with L_d and L_q the dq inductances, excluding the end-winding inductance. The flux due to the end-windings is

$$\lambda_{ed} = \omega L_{ed} i_d \tag{3.21}$$

$$\lambda_{eq} = \omega L_{eq} i_q \tag{3.22}$$

It is often assumed that the dq end-winding inductances are equal, in which case λ_e is in phase with I. However, in this study the dq end-winding inductances were calculated separately and it was found that they can differ in magnitude.

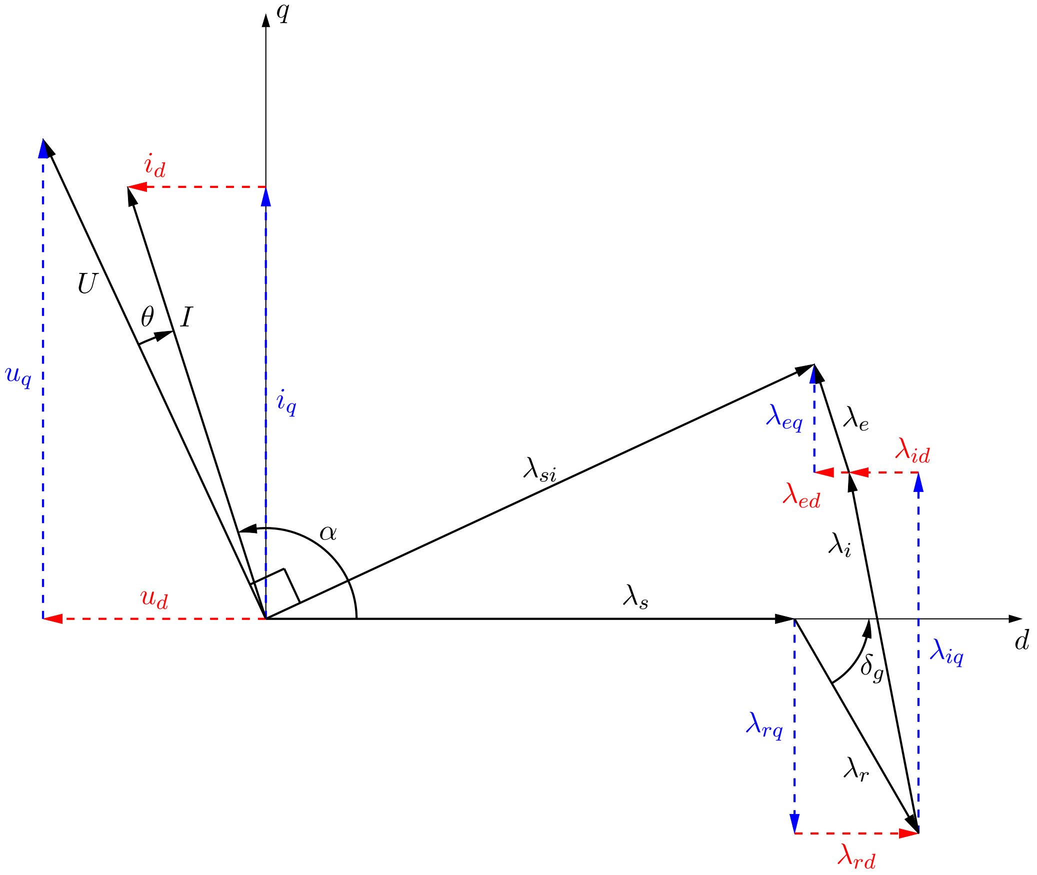

Figure 3.11: Vector diagram of a coupled MGM.

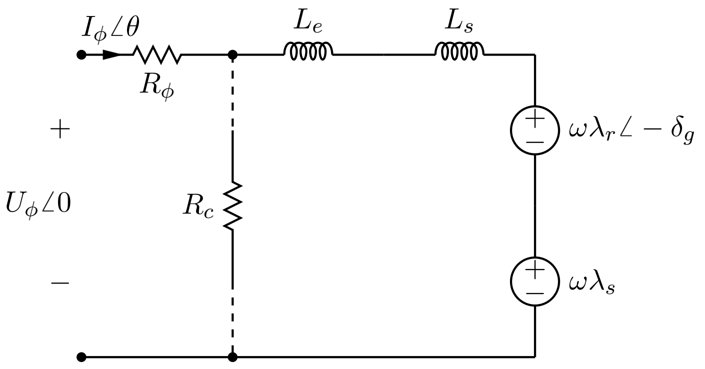

Figure 3.12: Equivalent per phase circuit model of a coupled MGM.

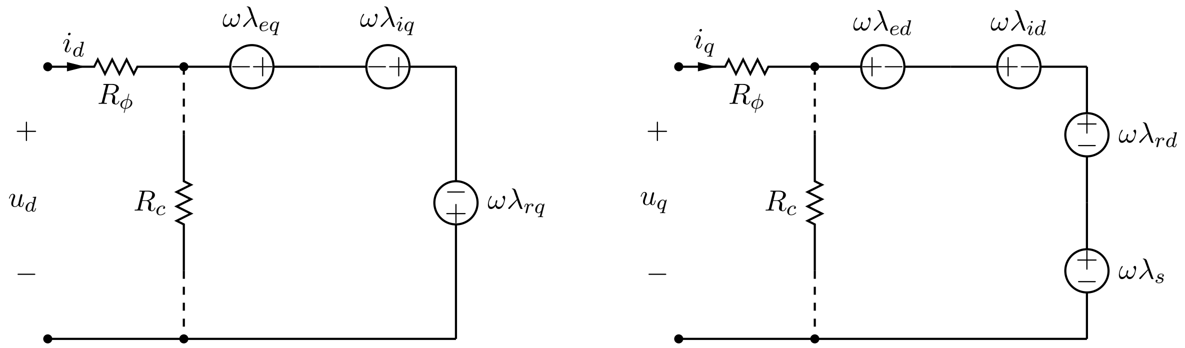

(a) Circuit model for the d-axis.

(b) Circuit model for the q-axis.

Figure 3.13: Equivalent dq circuit models of a coupled MGM.

The flux linkage λ_s is the flux linkage due to the sun gear magnets, and λ_r is due to the ring gear magnets. Note that the angle of λ_r is the load angle of the magnetic gear.

The dq terminal voltages are given by:

$$u_d = -\omega(\lambda_{rq} + \lambda_{iq} + \lambda_{eq}) + R_\phi i_d \tag{3.23}$$

$$u_q = \omega(\lambda_s + \lambda_{rd} + \lambda_{id} + \lambda_{ed}) + R_\phi i_q \tag{3.24}$$

3.7 Modes of operation

Magnetically geared machines have more than one rotor that can be used to transfer power to the machine. As such, the machine can be operated in several different modes, each characterized by a specific transformation of input to output power. The modes of operation are described here.

Geared machine An MGM can be said to operate as a geared machine when either the ring gear or the modulator is held stationary, the other component acts as a low-speed input/output, the sun gear is allowed to rotate freely and electrical power is absorbed/delivered to the stator. Power conversion is from purely electrical to purely mechanical, or vice versa. In this case, the average power transferred to the sun gear is zero, except under transient conditions when the speed of the machine changes. The primary focus of the design work presented in the remainder of this thesis is concerned with this mode of operation.

Gear Because an MGM contains a complete magnetic gear, the machine can be operated as a simple gear. In this case, the stator winding is simply not used and its terminals are left open. Again, either the ring gear or the modulator can be fixed and gear ratios as described in section 2.2 can be realized. Power conversion is from mechanical to mechanical. If the machine is to be operated in this mode, access to the sun gear is required. This can increase the complexity of the mechanical construction of the machine.

Power splitter This is a hybrid configuration where a portion of power is converted from electrical to mechanical and the remainder from mechanical to mechanical. In other words, in this mode the machine operates partly as a geared machine and partly as a gear.

CVT An MGM can be operated as a continuously variable transmission device. Power conversion is from mechanical to mechanical and electrical. Electrical power is used to regulate the gear ratio. One additional degree of freedom is required for this mode of operation.

In all modes, except the CVT mode, one member of the magnetic gear is kept stationary in order to take up the reaction torque. In the CVT mode, all members of the magnetic gear are rotating. In the context of MGMs where the stator winding produces a field with the same number of pole pairs as the sun gear, there is no use for the configuration with a stationary sun gear. Thus, a choice must be made between a stationary ring gear or modulator. A stationary ring gear results in the highest gear ratio. Considering the ring-stator topology, is also far more practical to have a stationary ring gear and stator, as it avoids the need for slip rings. The split MGM topology is more flexible in this regard. The ring gear can be allowed to rotate without the need for slip rings. Thus, the split MGM topology can also be used in applications requiring an outer rotor.

Chapter 4

Design analysis and methodology

This chapter is concerned with the design of magnetically geared machines (MGMs). In the first section, an overview of the design methodology employed in this study is given. In the remaining sections, the various steps of the design process are described in greater depth. This includes the numerical optimization process, as well as the finite element analyses used for design optimization and final performance verification. Special attention is paid to design aspects which are unique to MGMs, such as the calculation of the true cogging torque and optimal matching of the magnetic gear and electrical machine components of an MGM. In addition, a method of analyzing the operating points of MGMs is presented.

4.1 Overview of design methodology

An overview of the methodology employed in the design of magnetically geared machines is presented in Fig. 4.1. The first step consists of defining the topology, in terms of geometrical variables, and all other variables associated with the machine. Variables that are not of a geometrical nature include the current density, the properties of the permanent magnets, parameters related to the winding layout, the modulation set, etc. Not all of these variables are necessarily included in the numerical optimization procedure. Importantly, the variables associated with the modulation set are not included due to their discrete nature. However, several candidate modulation sets are identified, based on merit, and each design is then optimized numerically with the aid of finite element analyses. In the analyses used for optimization, some assumptions and simplifications are made in order to limit the computational cost. Once all the candidate modulation sets have been optimized, a design can be selected based on the optimization results. This design can be further refined if necessary. For example, special attention may be paid to the minimization of cogging torque. After the design refinement, it may be necessary to verify certain performance characteristics using analyses which are of a more comprehensive nature compared to the ones used for optimization. This then leads to a final design.

4.2 Modulation set selection

In chapter 2, the modulation set of a flux-modulated magnetic gear was defined as the parameter set (p_s, Q_m, p_r). In the context of MGMs, the modulation set will be defined so as to include the

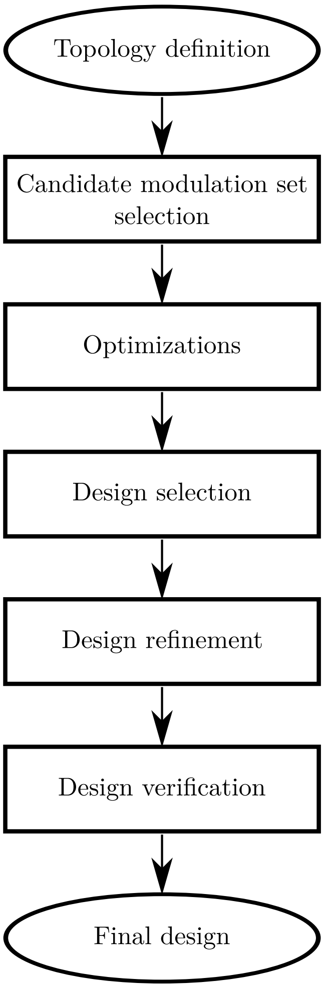

Figure 4.1: Overview of the design methodology employed in this study.

number of stator slots: (Q_s, p_s, Q_m, p_r). An important question in the design of MGMs is: How should the modulation set be chosen? The choice of modulation set has an impact on several aspects of the machine. The most important are:

Operating frequency Depending on which component acts as the low-speed rotor, either Q_m or p_r determines the fundamental operating frequency of the machine at a specific speed.

Cogging torque The choice of modulation set has a large impact on the cogging torque in MGMs.

Stall torque The stall torque of the magnetic gear is influenced by the modulation set. For a given volume, an optimal choice of the modulation set exists which maximizes the stall torque of the magnetic gear.

Gear ratio The gear ratio is determined by the modulation set. For a given input/output shaft rotational speed, the rotational speed of the sun gear is scaled by the gear ratio. Higher gear ratios result in higher sun gear speeds, with an associated increase in centrifugal forces and balancing requirements.

Note that the fundamental operating frequency is the same throughout an MGM. This is because, if the modulator acts as the low-speed rotor, it generates an electrical frequency given by

$$f_m = \frac{Q_m \omega_m}{2\pi} \tag{4.1}$$

Similarly, the sun gear generates an electrical frequency of

$$f_s = \frac{p_s \omega_s}{2\pi} \tag{4.2}$$

The rotational speeds of these two components are related by

$$\omega_s = \frac{Q_m}{p_s}\omega_m \tag{4.3}$$

which implies that $f_m = f_s$.

When choosing the modulation set, it is usually necessary to weigh these design options carefully. For example, it may be desirable to have a low operating frequency as it directly influences the losses in the machine, but a higher stall torque rating could be achieved with a higher Q_m or p_r, which implies a higher operating frequency.

Fig. 4.2 illustrates the variation in stall torque of two different MG designs. In both cases, an optimal area exists where the gear's stall torque peaks. From a loss perspective, it is always desirable to have a lower operating frequency, but the effect of the pole count on the stall torque should also be considered. It is recommended that p_r be chosen in the region up to the value which maximizes the stall torque. Selecting a p_r beyond this point, will decrease the stall torque and increase the losses and should be avoided.

The gear ratio of a magnetic gear has been shown to have an impact on the torque ripple in magnetic gears [18, 19]. MGs with fractional gear ratios were found to have lower torque ripple than MGs with integer gear ratios.

In [70], a cogging factor was introduced. This factor can also be used to obtain a rough estimate of the severity of the cogging torque in MGs. The cogging factor is defined as

$$f_c = \frac{2p_s Q_m}{\mathrm{LCM}(2p_s, Q_m)} \tag{4.4}$$

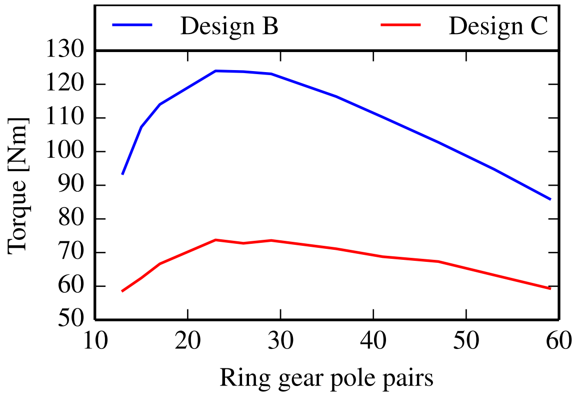

Figure 4.2: Variation in MG stall torque with number of ring gear pole pairs. (Data for Designs B & C in Fig. 6.5.)

with LCM(p_s, Q_m) denoting the lowest common multiple of p_s and Q_m. In general, the higher the cogging factor, the more severe the cogging torque. The best possible cogging factor is unity. Fig. 4.3 shows a plot of the cogging factor versus the gear ratio with a fixed number of sun gear pole pairs, $p_s = 3$. The plot also shows the increase in Q_m and p_r with the gear ratio. It can be seen that integer gear ratios produce higher cogging factors than fractional gear ratios. This supports the findings in [18, 19] that fractional gear ratios produce lower cogging torque. Thus, from a torque quality perspective, MGs and MGMs should generally be designed with fractional gear ratios.

Besides (2.18) which must be satisfied, Q_s and p_s should be chosen appropriately depending on the type of winding (overlap windings or non-overlap windings) that is employed.

4.3 Optimization

In this work, the design optimization of MGMs was carried out by employing numerical optimization algorithms coupled with parameterized finite element models. This process is illustrated in Fig. 4.4. The optimization algorithm is supplied with the problem definition and an initial design. The algorithm then repeatedly calls a finite element analysis to evaluate different designs, seeking an optimal solution. This process continues until an optimum is reached and the algorithm terminates.

4.3.1 Algorithm selection

Algorithms from the VisualDOC optimization suite were employed. The modified method of feasible directions (MMFD) [71] was applied most often. This is a single objective, gradient-based algorithm capable of handling multiple nonlinear inequality constraints. Other algorithms used include sequential quadratic programming (SQP), which is also a gradient-based algorithm, and particle swarm optimization (PSO), which is a non-gradient-based (global) method. Many

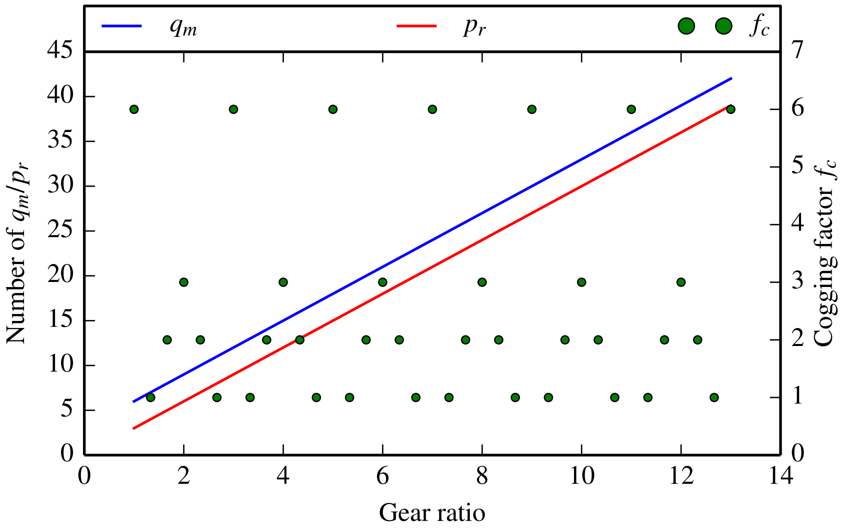

Figure 4.3: Cogging factor for magnetic gears with $p_s = 3$

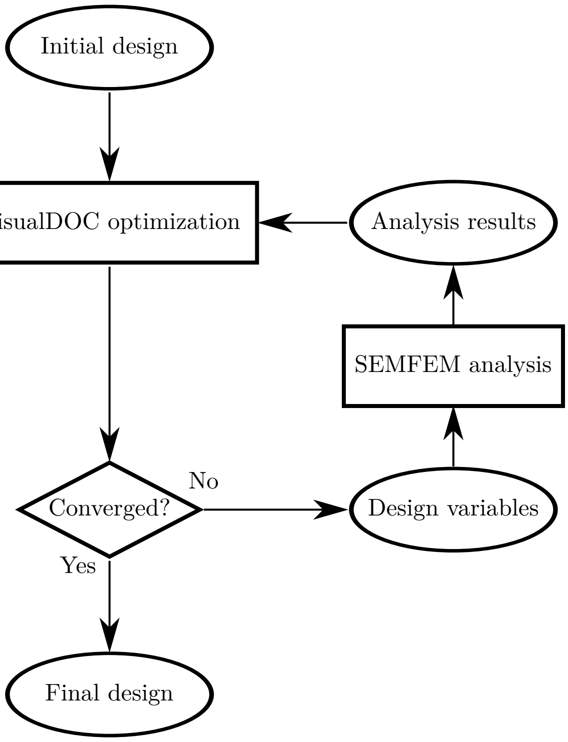

Figure 4.4: Overview of the optimization method used in this study.

different arguments can be made in favour of one optimization algorithm over another. The choice is not simple. In general, gradient-based algorithms are more efficient in solving problems where the objective function and constraints do not have many local extremities. In electrical machine design, optimizations problems which do not involve torque ripple generally do not contain many local extreme points. Because FEA was used in the analysis, a function evaluation is typically quite expensive and for this reason the efficiency of the optimization algorithm is an important factor. Based on these arguments, gradient-based algorithms were considered more suitable for the purpose of this study. The choice of the MMFD algorithm was a matter of past experience with the method.

4.3.2 Optimization problem formulation

Optimization problems are generally formulated as [72]

$$\text{Maximize:} \quad F(\boldsymbol{X}) \tag{4.5}$$

$$\text{Subject to:} \quad g_j(\boldsymbol{X}) \leq 0 \qquad j = 1, m \tag{4.6}$$

$$X_i^l \leq X_i \leq X_i^u \qquad i = 1, n \tag{4.7}$$

In the above, $\boldsymbol{X}$ is the set of design variables and (4.5) is the objective function. Constraints, which can be non-linear functions of the design variables, are defined by (4.6). The side constraints in (4.7) specify the minimum and maximum value of each design variable, thus defining the search space of the problem.

The side constraints are chosen appropriately such that any design within the search space can be manufactured. In this regard, the mechanical design of the machine is usually the limiting factor.

Constraints can be used in order to design for a specified efficiency or power factor. In this study, constraints were also employed to avoid permanent magnet demagnetization in some designs.

Some of the variables associated with the design of an electrical machine are discrete integers. Gradient-based optimizations algorithms generally do not handle problems involving discrete variables very well. This problem can be solved by running separate optimizations for each permutation of the discrete variables and selecting the best result. In this study, the variables associated with the modulation set of a gear or machine are discrete integers. The approach taken here, as shown in Fig. 4.1, was to identify several candidate modulation sets and to optimize each individually. The best design was then selected from the set of optimizations.

4.3.3 Matching of magnetic gear and electrical machine

The design of an MGM entails the design of two different torque transfer mechanisms, the magnetic gear and the electrical machine. Besides the standard quality measures of electrical machines such as efficiency, torque density, specific power, power factor, torque ripple, etc., a well designed MGM should ensure that the magnetic gear and electrical machine components are well matched. In this section, a method of assessing this balance is proposed and incorporated into the optimization process, allowing well matched designs to be obtained.

Consider an MGM with a fixed ring gear where the modulator is connected to the machine's shaft. If the terms for the stator torque and sun gear torque are grouped such that $T_{is} = T_i + T_s$, the modulator torque can be expressed as

$$\begin{aligned} T_m &= -G_{sm} T_{is} \quad (4.8) \\ &= -G_{sm}(T_i + T_s) \quad (4.9) \end{aligned}$$

Thus, the modulator torque is split between the sun gear and the stator. From this equation, it is easy to see that an MGM can be operated as a power splitting device. For example, if torque is applied to the modulator, a portion of the input power can be diverted to a high-speed output shaft connected to the sun gear and the remainder can be converted to electrical power. This study, however, is concerned with the design of MGMs which are to operate purely as electrical machines. This implies that, in steady-state operation, no power should be transferred to the sun gear and thus, the average torque on the sun gear must be zero. If a torque is applied to the modulator, the magnetic gear action transfers this torque to the sun gear. The stator must exert precisely the opposite torque on the sun gear, cancelling the torque from the magnetic gear side, if the machine is to operate in steady-state.

If the stator of an MGM is unable to exert a sufficiently large torque on the sun gear opposing the torque transferred by the magnetic gear, the maximum torque of the entire machine is limited by the stator. This is a poor design, since the magnetic gear is oversized. On the other hand, if the stator can generate a torque large enough to oppose the maximum torque transferred by the gear below its rated current, the design is also not optimal. Material could have been saved, reducing the torque capability of the stator, without affecting the machine's maximum torque. In a well designed MGM, the magnetic gear and the stator should be rated for the same operating point.

In this regard, it is useful to define the stator load factor of the machine as follows:

$$\gamma_i = -\frac{G_{sm}T_i'}{T_m'} \tag{4.10}$$

where G_{sm} is the gear ratio of the machine, considering a fixed ring gear. T_i' is the rated stator torque and T_m' is the stall torque of the modulator. The minus sign is required to make the factor positive, since T_i' and T_m' have opposite signs. The stator load factor is a measure of the balance between the maximum torque capability of the magnetic gear and the electrical machine components of an MGM. When $\gamma_i = 1$, the machine is rated to operate at the stall torque of the gear. For a well balanced design, the stator load factor should generally be less than one seeing that operating too close to the stall torque of the gear can lead to instability (slipping). Note that in coupled MGMs, the modulator stall torque T_m' is also influenced by the stator field, although the impact of the stator field is usually small.

The stator load factor can be used to assess the balance of the components in the machine without having to find an operating point satisfying $T_s = 0$. The rated torque of the machine can be determined and appropriate sizing of the stator can be ensured. This approach is applicable to all MGMs described in this work, including split MGMs, ring-stator MGMs and wound modulator MGMs.

In the optimization process, the stator load factor was constrained such that $\gamma_i > K_\gamma$ with K_γ the required stator load factor. Note that a successful optimization will drive the design to the constraint boundary where $\gamma_i = K_\gamma$. This can be understood considering that if a design does not lie on this constraint boundary, it will always be possible to achieve a better design which still satisfies the constraint. Thus, a design which does not lie on this constraint boundary, can not be optimal.

4.3.4 Single point analysis

As discussed in section 4.3.3, a necessary condition for steady-state operation of an MGM is that the net torque on the sun gear must be zero. Whenever this condition is not met, the simulated operating point can never be a steady-state operating point. Finding valid operating points would typically require multiple finite element solutions. This is different to the situation when simulating conventional PM machines, where the machine can operate in steady-state at any simulated current provided that the correct load is applied. Though this is interesting, it is not necessarily a problem when designing MGMs, even coupled MGMs. Usually, one is interested in the maximum ratings of an MGM, including the gear's stall torque and the rated stator torque or, alternatively, the stator load factor. In this study, both the gear's stall torque and the stator load factor were obtained from a single finite element simulation. This is achieved by simulating a point with the gear's load angle at a maximum and the rated current in the machine, with a current angle of 90°. The torques on the various components are then calculated as described in section 4.4.1.1 and the stator load factor is obtained from (4.10). The stall torque on the modulator and the ring gear correspond to the calculated values. The stator load factor indicates up to what percentage of the stall torque the machine would be able to operate.

These calculations can be performed using a time-stepped finite element simulation or from a single static solution. During optimization, a single static solution was often used in order to limit the computational cost of optimization. This approach worked well when the stator and sun gear torques were calculated using the dq flux-linkages and currents, as described in section 4.4.1.2.

4.3.5 Design variable selection

The selection of appropriate design variables is important when defining an optimization problem. For optimization problems where the machine's outer and inner diameters are fixed, a problem may arise if the thicknesses of components are selected as design variables. The sum of the thicknesses may be too large and thus, the components will not be able to fit in the available radial space. This issue can be overcome in several ways. One possibility is to fix the outer diameter of the machine and to constrain the inner diameter to the required value. The optimization algorithm should then ensure that the constraint is satisfied and that the machine fits in the available space. Alternatively, the inner diameter can be fixed and the outer diameter can be constrained. This ensures that unrealistic designs are not generated, but an extra constraint is still required and the obtained outer diameter will not match the specification exactly.

In this study, the optimization of component thicknesses within a specified outer and inner diameter, as illustrated in Fig. 4.5, was approached as follows: Instead of choosing the 5 thicknesses, t_1 to t_5, as the design variables, four auxiliary variables were used as design variables, labeled t_{p1} to t_{p4}. These variables specify what percentage of the available radial space a specific component occupies. The 5 thicknesses are then calculated based on these auxiliary variables:

$$r_1 = r_o - r_i \qquad t_1 = t_{p1} \cdot r_1 \tag{4.11}$$

$$r_2 = r_1 - t_1 \qquad t_2 = t_{p2} \cdot r_2 \tag{4.12}$$

$$r_3 = r_2 - t_2 \qquad t_3 = t_{p3} \cdot r_3 \tag{4.13}$$

$$r_4 = r_3 - t_3 \qquad t_4 = t_{p4} \cdot r_4 \tag{4.14}$$

$$t_5 = r_4 - t_4 \tag{4.15}$$

where r_k is the available space for the k^{th} component. This approach has several advantages over the methods which used the component thicknesses directly as design variables. Firstly, it is easy to define bounds on the design variables t_{p1} to t_{p4}. These variables must satisfy $0 < t_{pi} < 1$. Secondly, no additional constraints are required and the specifications of the inner and outer diameters are satisfied exactly. Finally, the number of required design variables is reduced by one, which reduces the computational cost of optimization.

In some cases, it is important to constrain the thickness of a specific component. For example, in the design of MGMs, the modulator thickness may need to be constrained to a minimum value in order to ensure manufacturability and mechanical integrity. The approach employing the auxiliary variables does not facilitate such constraints directly. In such cases, additional constraints can be added or a hybrid approach which only defines some thicknesses in terms of auxiliary variables, can be used.

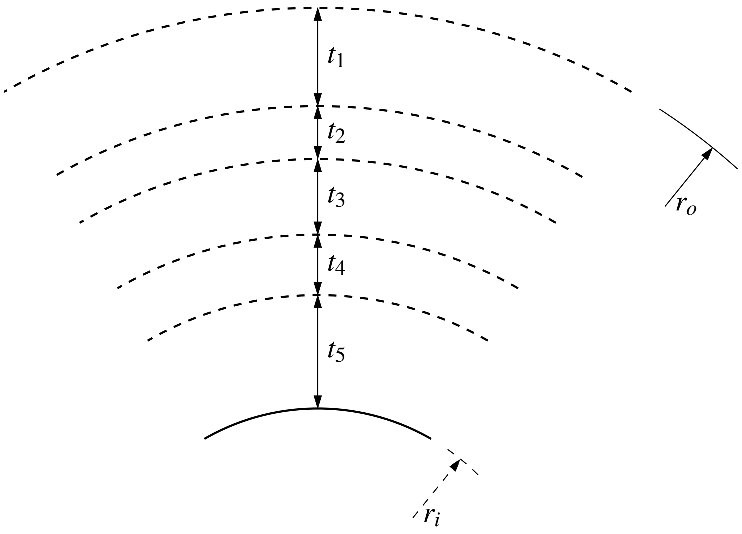

Figure 4.5: Component thicknesses to be optimized within a specified inner and outer diameter.

4.4 Finite element analysis

The finite element analyses employed in the optimization process were conducted using an in-house finite element simulation package called *SEMFEM*. This package can perform 2D static time-stepped FE simulations efficiently. The finite element analyses are responsible for the calculation of the objective function value, the constraints and all other performance characteristics of interest. This section describes the calculation of various performance measures in the finite element analysis program.

4.4.1 Torque calculations

4.4.1.1 Instantaneous torque

The instantaneous torques on the different components of an MGM have been described in the previous chapter. In this work, the torque on a specific component is calculated by summing the torques produced in each adjacent air-gap. The instantaneous air-gap torques are calculated using finite element analysis. In SEMFEM, either the Maxwell stress tensor method or Coulomb's virtual work method is employed, depending on the type of solver used. These methods are discussed in chapter 5.

The torque transferred by a well designed MG usually has a low ripple content, especially when a fractional gear ratio is selected [18, 19]. For this reason, a single instantaneous torque calculation can often be used as a good estimate of the average torque. However, this is not true of the torque produced by the stator, which can have a high ripple content.

4.4.1.2 Stator average torque

If the different torques in an MGM are to be calculated from a single point finite element simulation, it is better to calculate the stator torque using

$$\overline{T_i} = \frac{3}{2} p_s (\lambda_d i_q - \lambda_q i_d) \tag{4.16}$$

where λ_d, λ_q are the dq flux linkages and i_d, i_q are the dq currents. This formula gives a good estimate of the average stator torque. When calculating the stator torque in this way, the torque on the sun gear should be obtained as follows:

$$\overline{T_s} = -\frac{T_m}{G_r} - \overline{T_i} \tag{4.17}$$

In this way, the effect of the stator torque ripple on the sun gear can be eliminated while satisfying (3.7).

4.4.1.3 Cogging torque and torque ripple

In section 3.5.2, two kinds of cogging torque have been defined for MGs and MGMs. In practice, the synchronous cogging torque is much simpler to calculate than the true cogging torque, but the true cogging torque may be of more importance. For example, in wind power generators, it is the peak value of the true cogging torque that must be overcome in order for the turbine to start. On the other hand, when the machine is operated at speed, it is the synchronous cogging torque that contributes to the torque ripple.

The synchronous cogging torque can easily be calculated by time-stepped finite element analysis. The rotors of the machine or gear are rotated according to the applicable gear ratio at a constant load angle $\delta_g = 0$ and the different torque values are calculated. As an example, the synchronous cogging torque waveforms for the machine discussed in chapter 8 are shown in Fig. 4.6. This machine will be used as an example throughout this section.

The true cogging torque on the modulator can be determined in the following manner:

1. For each modulator position θ_m, obtain the curves $T_s(\theta_s)$ and $T_m(\theta_s)$ in a region around the synchronous point. An example of these curves for a specific modulator position is shown in Fig. 4.7.
2. Find the sun gear position θ_s^* such that $T_s(\theta_s^*) = 0$
3. Obtain the true cogging torque on the modulator by evaluating $T_m(\theta_s^*)$

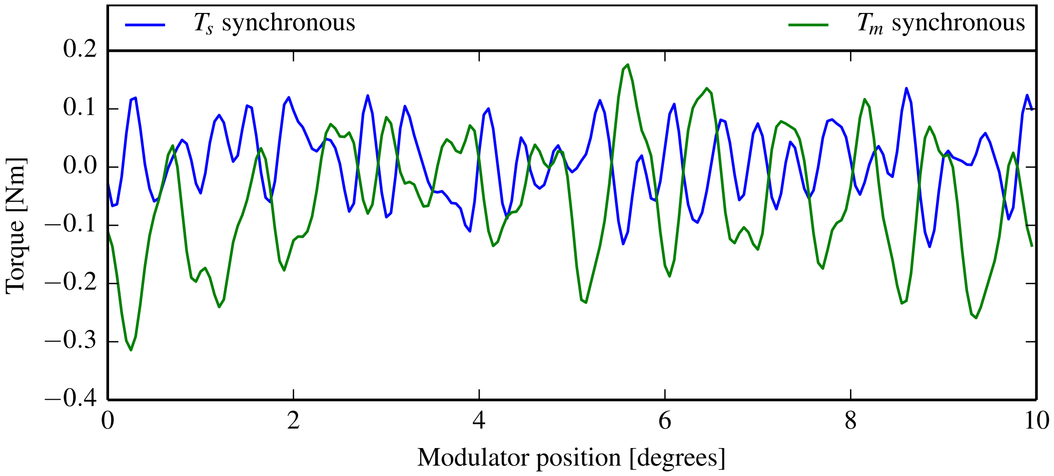

Figure 4.6: Synchronous cogging torque waveforms.

The true cogging torque obtained using this approach is plotted in Fig. 4.8, along with the synchronous cogging torque on the modulator. Clearly, the true cogging torque exhibits behaviour very different to the synchronous cogging torque. Importantly, the amplitude of the true cogging torque is much larger than that of the synchronous cogging torque.

The procedure for finding the true cogging torque, as described above, is cumbersome and requires more than one finite element solution per point on the true cogging torque waveform. However, this process can be greatly simplified if it is assumed that the curves in Fig. 4.7 are linear. It is clear from the figure that this is a very reasonable assumption. If it is also assumed that the gradients of the curves are related by

$$\frac{\mathrm{d}T_m}{\mathrm{d}\theta_s} = -G_{sm}\frac{\mathrm{d}T_s}{\mathrm{d}\theta_s} \tag{4.18}$$

then an approximation to the true cogging torque on the modulator can be obtained from the synchronous cogging torque waveforms:

$$T_m^{approx} = G_{sm}T_s^{sync} + T_m^{sync} \tag{4.19}$$

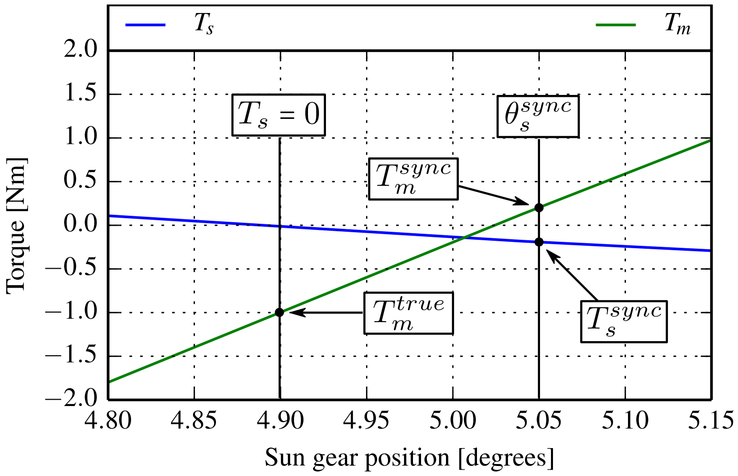

Figure 4.7: Variation in T_s and T_m about the synchronous cogging torque point.

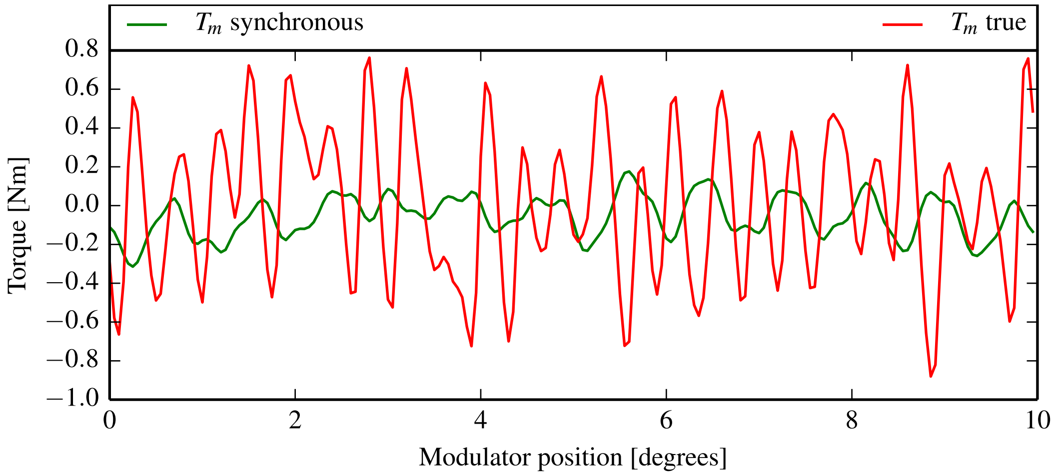

Figure 4.8: Comparison between the synchronous and true modulator cogging torque waveforms.

Fig. 4.9 shows a comparison between the true cogging torque, calculated using the detailed approach and the approximation of (4.19). The waveforms are in very good agreement. The differences are attributed to small nonlinearities in the curves of Fig. 4.7. Based on these results, it is suggested that (4.19) can be used to obtain the true cogging torque accurately and efficiently.

In this study, torque ripple calculations were performed without considering small oscillations in the load angle that may occur as a result of the torque pulsations. In other words, torque ripple was calculated assuming precise synchronism of the rotors, according to the gear ratio.

4.4.2 Voltage calculations

In SEMFEM, the voltage is calculated by fitting a cubic spline to the flux linkage waveform and taking the derivative of the spline.

$$E = \frac{\mathrm{d}\lambda}{\mathrm{d}t} \tag{4.20}$$

The per phase resistance of the winding, as well as the end-winding inductance should also be included in the model to obtain the correct terminal voltage, as explained in the previous chapter.

4.4.3 Losses and efficiency

Various forms of losses occur in the operation of magnetically geared machines, just like in other electrical machines. These losses can be categorized as follows:

Copper loss These losses are caused by currents flowing in the resistive winding of the machine. A distinction can be made between the DC copper loss which neglects skin-effects and AC copper loss which considers that current is not uniformly distributed in a conductor under AC excitation. Temperature also affects the resistance of the winding and thus, the losses generated.

Core loss Losses occur in the laminated cores of electrical machines when a time-varying magnetic field is applied. It is noted that, although it is common practice to separate these losses into hysteresis losses and eddy-current losses, there is no physical justification for this

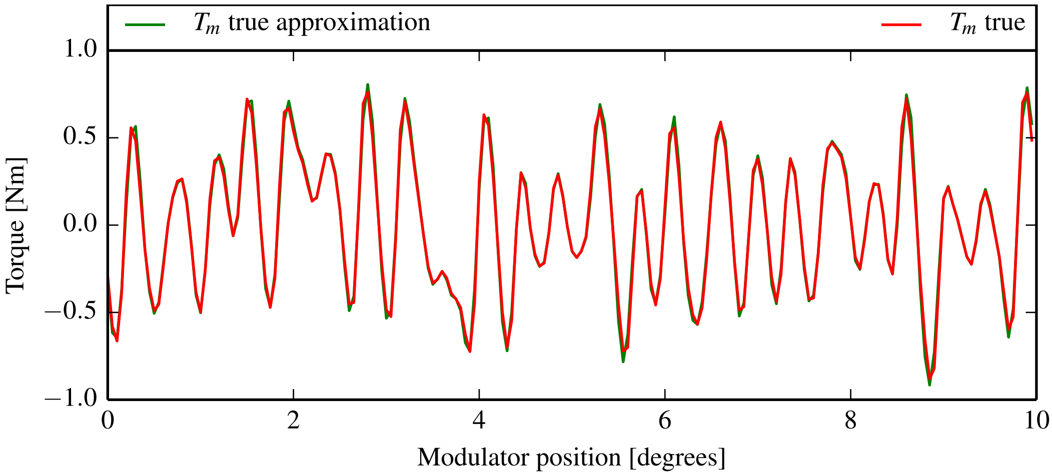

Figure 4.9: Comparison between the true cogging torque waveform and the approximation of (4.19).

separation. Reference [73] gives a good, brief discussion on the shortcomings of common loss models. It is clearly stated, “There is only one physical origin of remagnetization losses, namely, the damping of domain wall movement by eddy currents and spin relaxation.”

Magnet loss Many magnet materials are electrically conductive and thus, time-varying magnetic fields induce eddy-currents in the magnets which result in ohmic losses.

Windage loss The rotating components of a machine experience a drag force and cause air-flow in the machine which causes losses.

Bearing loss Losses occur in the bearings supporting the rotors of the machine.

Parasitic loss in the support structure The presence of conducting structural components in the vicinity of the active region of the machine can lead to eddy-currents if these components are subjected to a time-varying magnetic field. In this way, ohmic losses can also occur in the mechanical support structure.

In order to calculate the efficiency of the machine and to ensure that thermal constraints are satisfied, it is important to calculate these losses accurately. However, in a design environment it is also important to understand what simplifications can be made in order to reduce the computational cost of analyses. This is especially important when performing numerical design optimization and specifically in the calculation of losses because these calculations are potentially the most expensive in computational terms.

4.4.3.1 Calculation of copper loss

In this work, only the DC copper loss is considered. The instantaneous copper loss is calculated directly from the finite element mesh on a per element basis,

$$P_{cu}^{L} = \frac{J^2 k_f A^e L}{\sigma} \tag{4.21}$$

where J is the current density of the element, k_f is the copper fill factor for the specific coil, A^e is the cross sectional area of the element, L is the active stack length and σ is the conductivity of the material, usually copper or aluminium. The total copper loss is obtained by summing the contributions from all elements.

The calculation described above does not include the losses generated in the end-winding region. A simple way of including these losses is to multiply the loss of the active region by a factor which accounts for the additional conductor length,

$$P_{cu} = \frac{L + l_e}{L} P_{cu}^{L} \tag{4.22}$$

where l_e is the length of the end-winding on *one* side of the machine.

When the machine is supplied with balanced three-phase sinusoidal currents, the total copper loss is constant and thus, the instantaneous value from a single point simulation can be used. In general, the copper loss can be calculated very efficiently. In (4.21), only the area A^e requires calculation, the other parameters are supplied as input.

4.4.3.2 Calculation of core loss

A common approach to the calculation of core loss in electrical machines is to determine the amplitude of the fundamental component of the flux density in representative parts of the machine and to use this information to obtain the core loss,

$$P_{core} = M C_m f^{\alpha} \hat{B}^{\beta} \tag{4.23}$$

with M the mass of the considered part of the core, f the remagnetization frequency, $\hat{B}$ the peak flux density and C_m, α and β material specific parameters. This approach can also be used on a per element basis. There are, however, a number of problems with methods such as this, including the calculation of losses due to rotating flux and excitations consisting of multiple harmonics. In general, the principle of superposition cannot be applied to the calculation of losses due to multiple harmonic excitation, although this is frequently done in practice. The core loss is a nonlinear function of flux density.

Accurate calculation of core loss is very much an area of active research. Newer approaches which attempt to model BH loops accurately in finite element simulations were investigated. Although some good progress was made in this regard, this part of the project was stopped because it was realized that the amount of additional time required to achieve useful results in terms of the current project would be too great. Appendix C presents some of the work done in this regard and can serve as a good starting point for future research in this area.

In this study, core loss data for final designs was obtained by conducting 2D transient simulations with a commercial FE package, *MagNet* from *Infolytica Corporation*. Core loss calculations were not included as part of the analyses used for optimization. It was possible to ignore the core loss in the optimization stage because the core loss makes a relatively small contribution towards the total losses in the small machines considered here. When considering larger machines in which core losses have a significant impact, an approximation of the core losses will have to be included in the optimization stage. In order to keep the computational cost low, the core loss can be approximated by extracting flux densities in representative areas of the model from single point static finite element simulations and applying (4.23), assuming values for the frequency. Alternatively, static time-stepped simulations can be employed and the core loss can be calculated for each element as described in [73], where the flux density waveform is considered. This approach allows greater accuracy to be achieved but the computational cost is higher.

4.4.3.3 Calculation of magnet loss

Several methods can be employed to calculate the eddy-current losses in the magnets. These methods vary in terms of computational cost and accuracy. Analytical methods such as [74] are typically not as computationally expensive as transient finite element analysis, but also not as accurate. The most accurate method of calculating magnet loss is transient 3D finite element analysis, but this is prohibitively expensive for optimization purposes. The approach taken here was to neglect the magnet loss during optimization. The magnet loss of final designs was also investigated by conducting transient 2D simulations in *MagNet*.

4.4.3.4 Calculation of windage and bearing loss

Bearing manufacturers often provide in depth discussions on bearing loss calculations in their catalogues. Windage loss is highly dependent on the mechanical design of the machine. In this work, these losses were expected to be small compared to other loss components and were disregarded.

4.4.3.5 Calculation of losses in the supporting structure

These loss calculations are typically very expensive because they require transient 3D finite element simulations in order to calculate the eddy-currents in the supporting structure. Additional effort is also required to set up the model correctly. As such, these calculations are not included in the design optimization. A case where these losses contributed significantly to the poor performance of a prototype MG is presented in chapter 7.

4.4.3.6 Calculation of efficiency

The efficiency of an MG is calculated as the ratio of the input to output mechanical power. In the case of a speed increaser gear with a fixed ring gear, this is

$$\eta = \frac{P_{out}}{P_{in}} = \frac{\omega_s T_s}{\omega_m T_m} \tag{4.24}$$

In an MG, there is no copper loss and the other loss components are relatively more important. Note that when losses are considered, (2.55) and (2.56) are not strictly valid. Additional input torque is required to compensate for the effect of the losses. The relationship between the average rotational speeds of the input and output rotors hold because of the synchronous nature of MGs.

When considering MGMs, both the input and output power can either be electrical or mechanical, depending on whether the machine is operated as a motor or a generator. For generator operation, the efficiency is calculated as

$$\eta = \frac{P_{out}}{P_{in}} = \frac{3V_\phi I_\phi \cos\theta}{\omega_m T_m} \tag{4.25}$$

with V_ϕ and I_ϕ the RMS phase voltage and current and $\cos\theta$ the power factor of the machine. Care must be taken with this calculation to ensure that the condition for steady-state operation is satisfied.

4.4.4 Power factor

Magnetically geared machines typically have a good power factor, similar to conventional permanent magnet machines. In the time-stepped finite element simulations employed, the power factor is calculated as

$$\mathrm{PF} = \frac{P}{S} \tag{4.26}$$

with P the average real power delivered/absorbed by the machine and S the apparent power. The average real power is calculated as

$$P = \frac{1}{N}\sum_{\phi=1}^{3}\sum_{n=1}^{N} v[\phi,n]\cdot i[\phi,n] \tag{4.27}$$

where N is the number of time-steps, ϕ is the phase index and n is the sample index. The apparent power is calculated as

$$S = \sum_{\phi=1}^{3} V_{rms}[\phi] \cdot I_{rms}[\phi] \tag{4.28}$$

$$V_{rms} = \sqrt{\frac{1}{N}\sum_{n=1}^{N} v^2[\phi, n]} \tag{4.29}$$

$$I_{rms} = \sqrt{\frac{1}{N}\sum_{n=1}^{N} i^2[\phi, n]} \tag{4.30}$$

4.4.5 Thermal constraints

Generally, there are two factors which limit the maximum permissible current density in electrical machines. The one is efficiency constraints. As can be seen in (4.21), copper loss increases with the square of the current density. Thus, high current densities can easily compromise a machine's efficiency. The second limiting factor is thermal constraints. High current densities result in a lot of heat generated in the windings. The various materials used in the machine all have a temperature range within which they can perform their function. If the materials are subjected to temperatures outside of this range, the material characteristics will change, compromising the performance of the machine. High temperatures can also result in a shorter machine lifespan. Typically, the insulation of the windings is the material which fails first if subjected to excessively high temperatures. In PM machines, demagnetization of the magnets can also be an issue, especially at high temperatures.

The determination of the maximum permissible current density in a machine is a complex problem. As machines increase in power and torque density, the need for detailed thermal analysis becomes more crucial. In this study, thermal constraints were implemented by simply limiting the maximum permissible current density. Detailed thermal analysis is beyond the scope of this work.

4.5 Operating point analysis

For conventional machines, an operating point is uniquely defined by three parameters: (ω, i_d, i_q) with ω the angular frequency (speed), and i_d and i_q the dq-currents. In magnetically geared machines, these three parameters alone are not sufficient to define a unique operating point. The magnetic gear's load angle δ_g is also required. In decoupled MGMs, the load angle has no impact on the flux in the stator and so operating points of the machine (ω, i_d, i_q) and the gear (δ_g) can be determined separately. In this case, the machine's operating point can be determined using standard theory. In coupled MGMs, the situation is different. The flux in the stator is not only a function of the stator currents, but also of the magnetic gear's load angle and similarly the stator currents have an impact on the fields throughout the machine. This section delves into the analysis of operating points in coupled MGMs and presents a method of obtaining various important characteristics of the machine over its operational speed range.

A procedure for finding an operating point (i_d, i_q, δ_g) given ω and the load impedance, Z_L, can be outlined as follows:

1. Map λ_d, λ_q, T_s and T_m versus i_d, i_q and δ_g, giving

$$\begin{aligned} &\lambda_d(i_d, i_q, \delta_g), \quad \lambda_q(i_d, i_q, \delta_g) \\ &T_s(i_d, i_q, \delta_g), \quad T_m(i_d, i_q, \delta_g) \end{aligned} \tag{4.31}$$

2. Find i_d, i_q and δ_g such that

$$T_s(i_d, i_q, \delta_g) - \beta\frac{P_{rot}}{\omega_s} = 0 \tag{4.32}$$

$$-i_dR_L + i_qX_L = -\omega\lambda_q(i_d, i_q, \delta_g) + R_\phi i_d \tag{4.33}$$

$$-i_dX_L - i_qR_L = \omega\lambda_d(i_d, i_q, \delta_g) + R_\phi i_q \tag{4.34}$$

Equation 4.32 enforces the condition that the net torque on the sun gear is zero for steady state operation. The second term in (4.32) accounts for the rotational losses associated with the sun gear, including core loss, magnet loss and windage and friction loss. The total rotational loss is P_{rot} and β is a parameter between 0 and 1 which determines the distribution of the loss between the sun gear and the modulator. Using this model, the torque on the modulator is calculated as

$$T_m^l = T_m(i_d, i_q, \delta_g) + (1-\beta)\frac{P_{rot}}{\omega_m} \tag{4.35}$$

Equations 4.33 and 4.34 are derived from the dq equivalent circuits for the MGM, shown in Fig. 4.10 and from the relationship between the load and the machine's terminal voltages and currents:

$$R_L + jX_L = \frac{u_d + ju_q}{-(i_d + ji_q)} \tag{4.36}$$

In the equivalent circuits of Fig. 4.10, the flux-linkages λ_d and λ_q represent the total flux linkage, including contributions from the sun gear, the ring gear and the end-windings.

When generating the map, it is important that the power balance is maintained accurately. This can be verified by ensuring that (3.7) is satisfied. When single point simulations are used to construct the mapping, it is better to calculate the torque on the stator and the sun gear using (4.16) and (4.17). Using this approach, the average torque can be estimated from a single point even though cogging torque and torque ripple have an influence on the instantaneous torque at the simulated point.

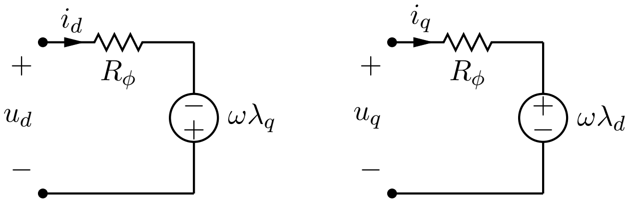

(a) d-axis (b) q-axis

Figure 4.10: Simplified equivalent circuit models.

The maps in (4.31) can be used to obtain various important characteristics of the machine over its operational range. For example, the maximum output power (generator operation) given a voltage and current limit can be found for the machine's operational speed range. This can be achieved by solving the following optimization problem over the required speed range:

$$\text{Maximize: } P(i_d, i_q, \delta_g) = \frac{3}{2}(i_d u_d + i_q u_q) \tag{4.37}$$

$$u_d = -\omega\lambda_q(i_d, i_q, \delta_g) + R_\phi i_d \tag{4.38}$$

$$u_q = \omega\lambda_d(i_d, i_q, \delta_g) + R_\phi i_q \tag{4.39}$$

$$\text{Subject to: } T_s(i_d, i_q, \delta_g) = 0 \tag{4.40}$$

$$I_\phi = \frac{1}{\sqrt{2}}\sqrt{i_d^2 + i_q^2} < I_{max} \tag{4.41}$$

$$U_\phi = \frac{1}{\sqrt{2}}\sqrt{u_d^2 + u_q^2} < U_{max} \tag{4.42}$$

In the formulation above, only copper loss is considered, but the method can be generalized to include other loss components.

The approach presented here was employed in later chapters to evaluate the performance of two MGMs for different loads, operational speeds and voltage and current limits.

A similar approach was applied to the analysis of a vernier machine and a more conventional PM machine. In these cases, the problem is simpler in the sense that there is no load angle that has to be determined. The problem of finding a maximum power point can be defined as follows:

Given mappings of the dq flux-linkages, $\lambda_d(i_d, i_q)$ and $\lambda_q(i_d, i_q)$,

$$\text{Maximize: } P(i_d, i_q) = \frac{3}{2}(i_d u_d + i_q u_q) \tag{4.43}$$

$$u_d = -\omega\lambda_q(i_d, i_q) + R_\phi i_d \tag{4.44}$$

$$u_q = \omega\lambda_d(i_d, i_q) + R_\phi i_q \tag{4.45}$$

$$\text{Subject to: } I_\phi = \frac{1}{\sqrt{2}}\sqrt{i_d^2 + i_q^2} < I_{max} \tag{4.46}$$

$$U_\phi = \frac{1}{\sqrt{2}}\sqrt{u_d^2 + u_q^2} < U_{max} \tag{4.47}$$

Chapter 5

Movement facilitation in 2D FEM analyses

5.1 Introduction

Analyzing magnetically geared machines using the finite element method is very demanding for two reasons: Firstly, the lack of periodicity often necessitates modeling of the full machine. Secondly, the machines have multiple air-gaps (typically two or three) which increase the problem complexity when movement has to be considered. The result is that the computational cost of FEA can be an important issue when using this method in the design of MGMs, especially when performing numerical design optimization.

In this chapter, two methods that facilitate movement in finite element meshes are applied to the simulation of the MGM illustrated in Fig. 5.1 and evaluated in terms of accuracy and computational efficiency. The methods considered are the air-gap element (AGE) and the moving band (MB).

5.2 Movement facilitating techniques

The methods to be evaluated are briefly described in this section. Although, in the present context, the methods are applied in static time-stepped simulations, they are just as applicable to transient analyses such as presented in [75].

5.2.1 Air-gap Element

The air-gap element [76] is a technique whereby the field in the entire air-gap region is calculated analytically using a Fourier series expansion of the vector potential. The field representation must satisfy the boundary conditions derived from the adjoining meshed regions. The vector potential in the air-gap takes the form

$$A(x,y) = \sum_i \alpha_i(x,y)u_i \tag{5.1}$$

where the α_i, expressed as Fourier series, fulfill the role of shape functions and the u_i are the nodal values of the vector potential on the AGE boundary. Movement is accomplished by a simple

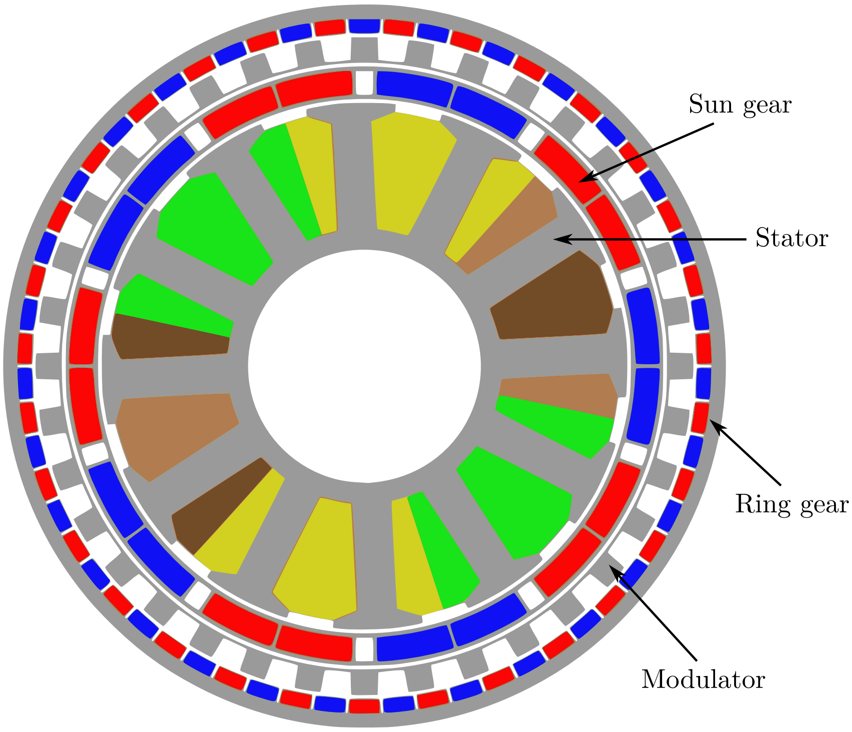

Figure 5.1: An example of an MGM with an inner stator.

recalculation of the α_i without any modification to the mesh structure, resulting in simple and efficient time-stepping [77].

Considering (5.1), it is clear that all the air-gap nodes are connected, and thus this method results in a dense block appearing in the final system matrix which can have a drastic impact on the computational time required to obtain a solution. An advantage of the air-gap element technique is that the results can be very accurate because of the high order of the field representation in the air-gap region.

The Fourier series representation of the vector potential can be used directly to calculate the torque using the Maxwell stress tensor method,

$$T = \frac{L}{\mu_0} \int_{\theta_1}^{\theta_2} r^2 B_r B_\theta \mathrm{d}\theta \tag{5.2}$$

with L the machine's stack length. As described in [78], this calculation can be implemented as

$$T = \frac{L}{\mu_0} \mathbf{A_e}^T \mathbf{F} \mathbf{A_e} \tag{5.3}$$

with $\mathbf{A_e}$ a vector of nodal values of the vector potential along the boundary of the air-gap element and $\mathbf{F}$ derived from the Fourier coefficients of the α_i in (5.1)

$$F_{ij} = r \int_{\theta_1}^{\theta_2} \frac{\partial \alpha_i}{\partial r} \frac{\partial \alpha_j}{\partial \theta} \mathrm{d}\theta \tag{5.4}$$

Recently, this method has been applied in optimization, where it was used to accurately calculate the gradient of the torque with respect to geometric model parameters [79].

5.2.2 Moving Band

This technique was first proposed in [80]. It has several advantages over other movement facilitating methods. It employs no special elements or coupling techniques, no dense blocks are generated in the system matrix and the system dimension is not increased. For these reasons, the moving band technique should be superior in terms of computational speed. However, there are difficulties with this method as well: Remeshing the air-gap region is inevitable and thus the numbering as well as the number of nodes in the mesh does not stay constant. For this reason, the conditioning of the system matrix is not maintained and preconditioning routines must be rerun when the mesh changes. Also, because the elements in the air-gap are geometrically distorted or remeshed to accommodate arbitrary movement, the results obtained using this method often have an oscillating error component. It has been shown that this problem can be drastically reduced by using higher-order elements in the moving band [81].

There are a few options for calculating torque in the moving band [82]. The Maxwell stress tensor method can also be applied, but in this study Coulomb's virtual work method [83] was used for torque calculation in the moving band:

$$T = \frac{L}{\mu_0} \sum_{e=1}^{N_{mb}} \int_{\Omega_e} \left(-\mathbf{B}^T \mathbf{G}^{-1} \frac{\partial \mathbf{G}}{\partial \theta} + \frac{1}{2} \frac{B^2}{|\mathbf{G}|} \frac{\partial |\mathbf{G}|}{\partial \theta} \right) \mathrm{d}\Omega \tag{5.5}$$

with $\mathbf{B} = [B_x, B_y]$, $B = ||\mathbf{B}||$, $\mathbf{G}$ the Jacobian matrix of the global nodal coordinates with respect to local element coordinates, and $|\mathbf{G}|$ the determinant of $\mathbf{G}$.

5.3 Finite element implementation

The finite element code used in this study is an in-house implementation called *SEMFEM*. The main library is written in Fortran and C and compiled, with optimization, using the GNU compilers *gfortran* and *gcc*.[1] In this section, some details regarding the implementation are discussed.

5.3.1 General

First order triangular elements were used. This is not because any of the methods are restricted to first order elements, but simply because of the ease of implementation.

A direct method of solving systems of linear equations was used. The implementation is the subprogram ACTCOL listed in [84]. The conditioning of the system is improved prior to solving using the algorithm proposed in [85]. Newton-Raphson iterations were performed to solve the nonlinear system.

5.3.2 Solver Implementations

Flowcharts describing the working of the two solvers are depicted in Fig. 5.2. Both solvers comprise a serial section and a parallel section.

---

[1] Compiler version: gcc 4.8.1, optimization flags: -O2/-O3 -fopenmp

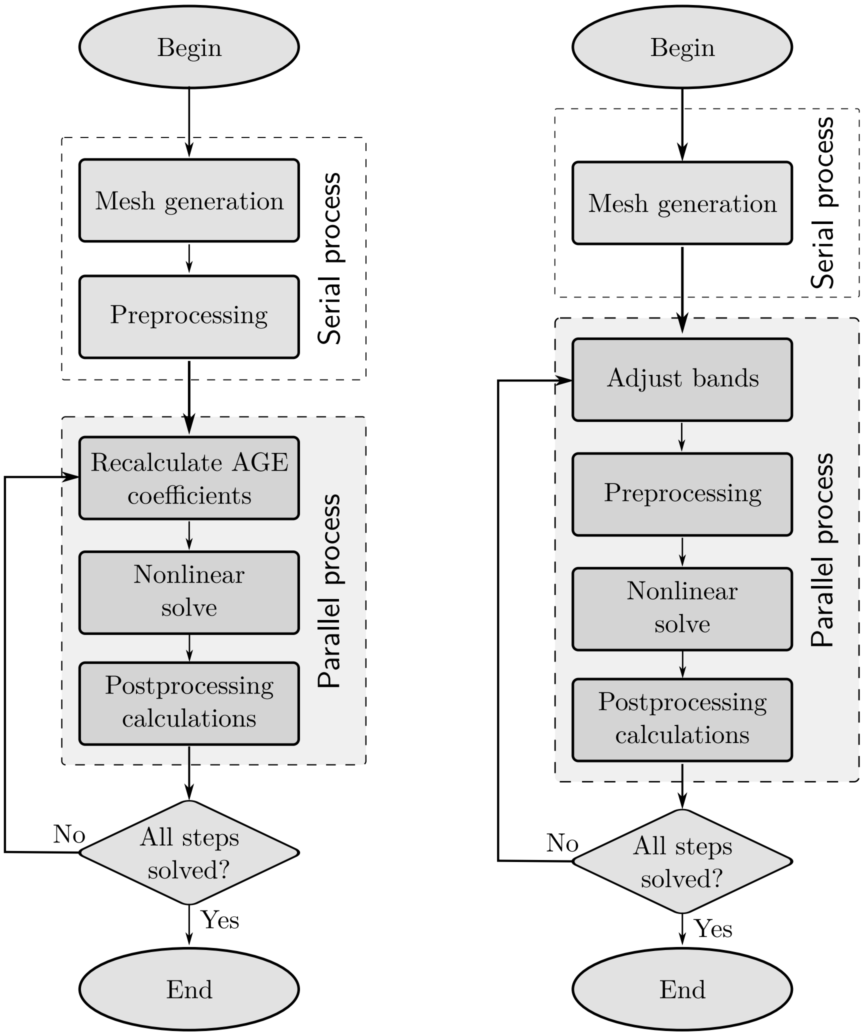

(a) Air-gap element (AGE) (b) Moving band (MB)

Figure 5.2: Flowcharts of different movement facilitating solvers.

The AGE solver utilizes exactly the same mesh for all time-steps, allowing the preprocessing step, which includes profile reduction, to be executed only once. Movement is accomplished by a simple recalculation of some coefficients and updating the entries in the system matrix. On the other hand, the moving band solver has to perform the preprocessing step for every time-step, since the connections between nodes in the air-gap region change.

In both methods, the total number of time-steps to be solved are distributed between several parallel sections, implemented using OpenMP [86]. This is a powerful method of parallelization, since it is introduced at a high level. It exploits the fact that time-steps can be solved independently in static time-stepped simulations. As shown in Fig. 5.2, the nonlinear solver and all postprocessing calculations, including the torque calculation, are executed in parallel.

5.4 Evaluation

The MGM shown in Fig. 5.1 was analyzed using both the AGE and the MB. Static time-stepped simulations consisting of 300 time-steps were performed for three different meshes, varying in

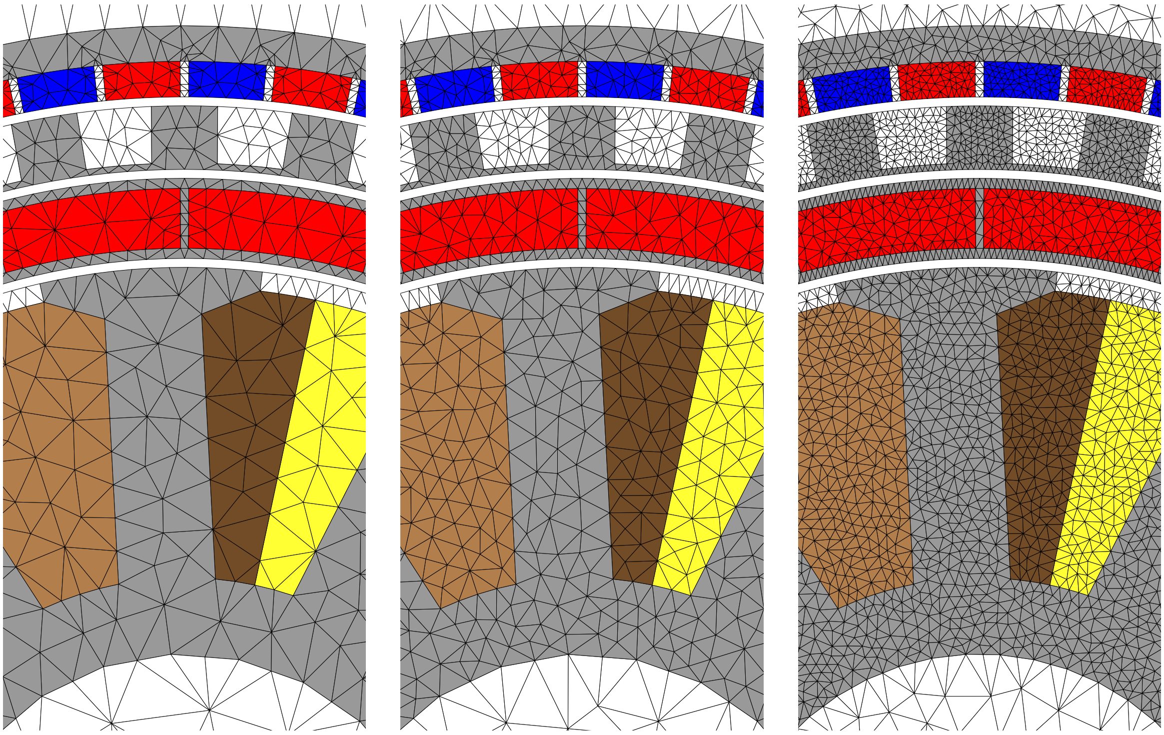

(a) Mesh 1 (b) Mesh 2 (c) Mesh 3

Figure 5.3: Three different meshes used for comparison.

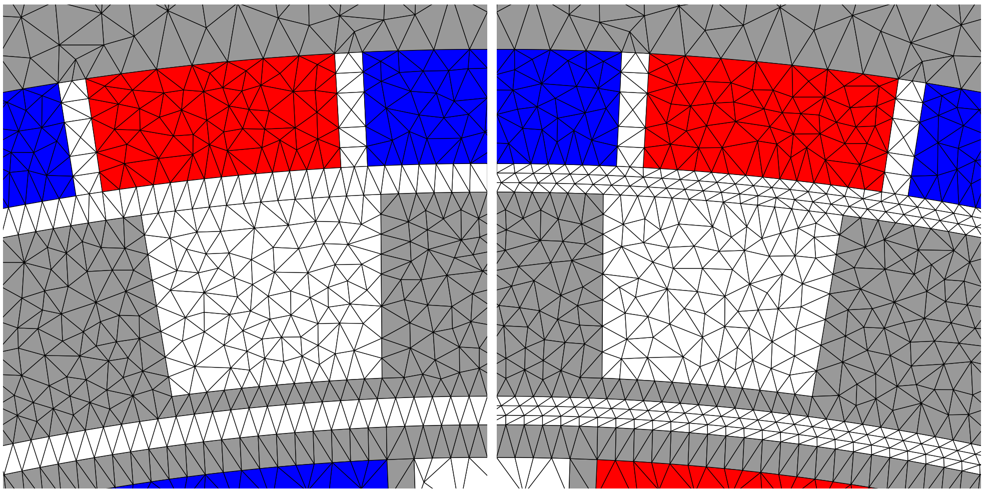

(a) Single layer: MB1 (b) Single layer: MB1

Figure 5.4: Variants of the moving band technique used with Mesh 3.

terms of the density of elements. The meshes are shown in Fig. 5.3. For Mesh 1 and 2, the MB was set up with a single layer of elements (MB1). For Mesh 3, an additional variant of the MB was used with three layers (MB3). Fig. 5.4 illustrates the two variants of the MB used with Mesh 3. The MB with three layers was not used for Mesh 1 and 2 because the coarseness of these meshes, together with thin layers in the air-gap, results in elements with very poor aspect ratios. Of course, this problem can be avoided by simply refining the air-gap regions, but such refinements are not applied in this comparison.

Thus, a total of 7 simulations is considered. The simulations were performed at the maximum load angle of the magnetic gear and rated conditions of the stator. Further details regarding the simulated operating point can be found in [87] where the design of the MGM is described.

The simulations were conducted on a Linux platform using an Intel Core i7 CPU @ 3.5 GHz with 4 cores (8 virtual cores).

5.4.1 Comparison of Accuracy

The torques calculated in the three air-gaps for all 7 simulations are plotted in Fig. 5.5. The torques in the inner, center and outer air-gaps are labeled T_1, T_2 and T_3 respectively. From this figure, it is apparent that the average torques calculated using the different methods and meshes match reasonably well, if not perfectly. However, when one considers the torque ripple, the results from the AGE and the MB differ significantly. In Fig. 5.5, it can be seen that the largest deviation between the calculated torques occurs in T_2 and T_3. Close-up views of T_2 and T_3 are shown in Figs. 5.6 and 5.7. The figures share the legend of Fig. 5.6.

In the case of T_2 (Fig. 5.6), the MB with a single layer (MB1) produces a high frequency ripple even with the fine mesh (Mesh 3). This is a good example of the problem mentioned in section 5.2.2. The deformation and remeshing of the elements result in discontinuities in the problem between the different time-steps. This causes oscillations in the calculated torque. Using the three-layer MB (MB3), these oscillations are dramatically reduced because of the improved smoothness of the solution in the air-gap region. The results show very good agreement between the AGE and MB3 for Mesh 3.

In Fig. 5.7, the torque ripple calculated using the MB decreases with increasing mesh density. In the case of Mesh 3, the results from the AGE, MB1 and MB3 are in close agreement.

From Figs. 5.6 and 5.7, it can be observed that the results from the different methods tend to converge as the mesh density is increased. The variation in average torque is due to the refinement of the mesh in the entire problem domain, not just the air-gap regions.

The three-phase voltages calculated for all simulations are plotted in Fig. 5.8. The figure contains 7 sets of plots which are indistinguishable from each other in this figure. Fig. 5.9, which also uses the legend of Fig. 5.6, shows a close-up view of the voltage waveforms. The figure highlights an area where the difference between the simulations is relatively large. The three groupings of results correspond to the three different meshes. Only in the case of Mesh 1 is there a notable difference between the results from the AGE and the MB. From these results, it can be concluded that the voltage computation is less sensitive to the movement handling scheme than the torque

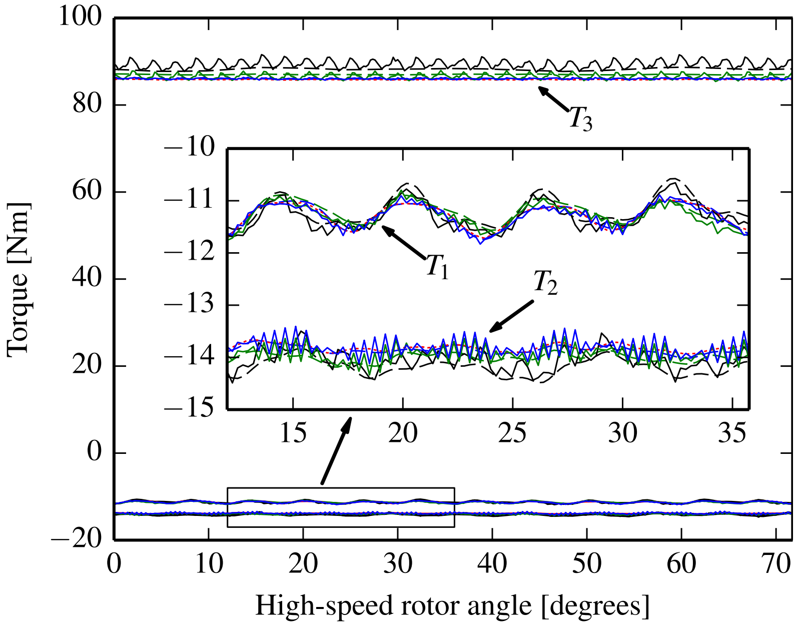

Figure 5.5: Comparison of calculated air-gap torques for all simulations.

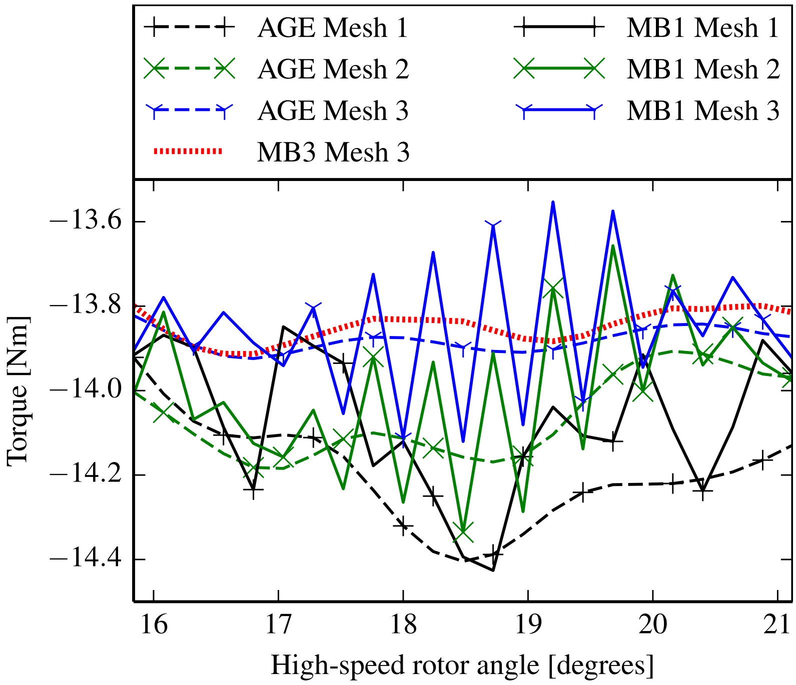

Figure 5.6: Close-up view of T_2 calculated using different methods.

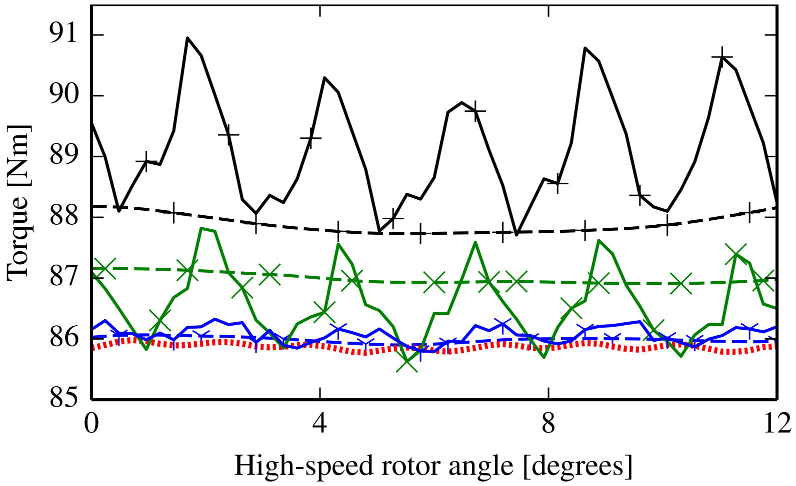

Figure 5.7: Close-up view of T_3 calculated using different methods. (See Fig. 5.6 for legend.)

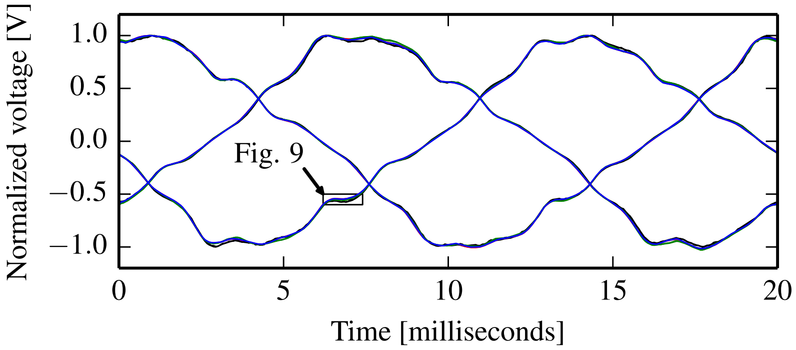

Figure 5.8: Comparison of calculated phase voltages for all simulations.

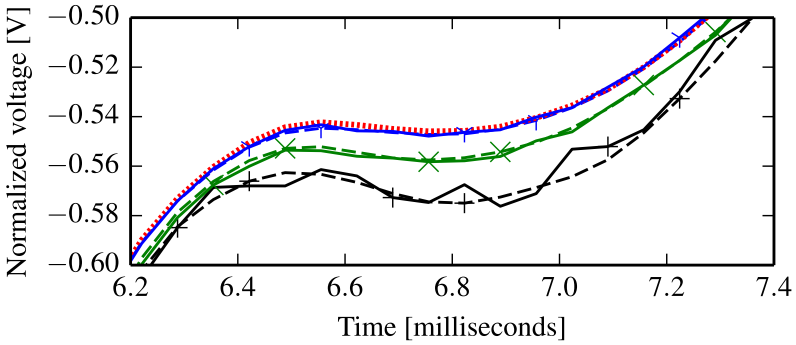

Figure 5.9: Close-up view of calculated phase voltages for all simulations. (See Fig. 5.6 for legend.)

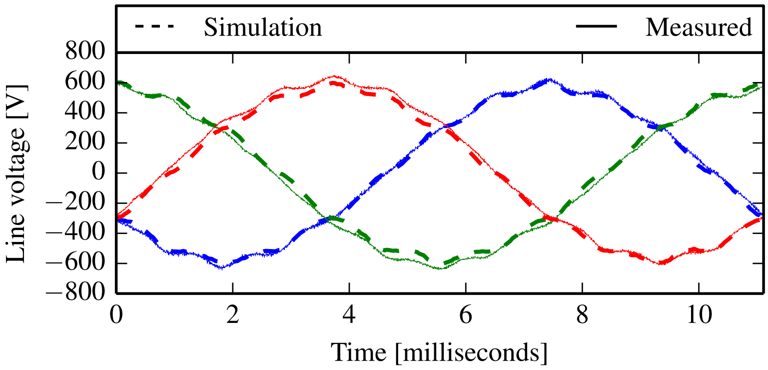

Figure 5.10: Comparison of simulated (MB1, Mesh 1) and measured no-load line voltages.

computation. All the methods provide good accuracy in the calculation of flux linkage and voltage.

A comparison of simulated and measured no-load line voltages with the machine's modulator rotating at 150 rpm is shown in Fig. 5.10. The simulated results were obtained using Mesh 1 with MB1. Despite some inaccuracies in the manufacturing of the prototype, these results agree fairly well.

5.4.2 Comparison of Performance

The calculation times for the different simulations are given in Table 5.1. The table lists times using a single thread (no parallelism) as well as times for 8 threads, which fully exploit the available CPU cores. The calculation times for the MB simulations are consistently reduced by a factor 4 using parallelism. The same speed-up is not quite achieved for the AGE simulations due to the relatively high cost of the preprocessing step, which is not performed in parallel. This effect becomes greater as the mesh density is increased.

Clearly, the MB is much faster than the AGE. Note also that as the number of nodes in the mesh increases, the margin that the MB has over the AGE increases rapidly. In the simulation

Table 5.1: Performance comparison of movement methods

Mesh	**Calculation times*** [seconds]		
	AGE	**MB1**	**MB3**
Mesh 1	1 026.3	99.8	-
(5 722 nodes)	**334.3**	**24.6**	-
Mesh 2	3 095.6	305.6	-
(9 860 nodes)	**1 266.8**	**74.7**	-
Mesh 3	33 351.5	2 339.4	3 259.2
(28 391 nodes†)	**19 143.5**	**579.6**	**818.9**

* Normal type: 1 thread, bold type: 8 threads
Platform: Linux, Intel Core i7 CPU @ 3.5 GHz, 8 virtual cores
† Excluding additional nodes in the air-gap region using MB 3

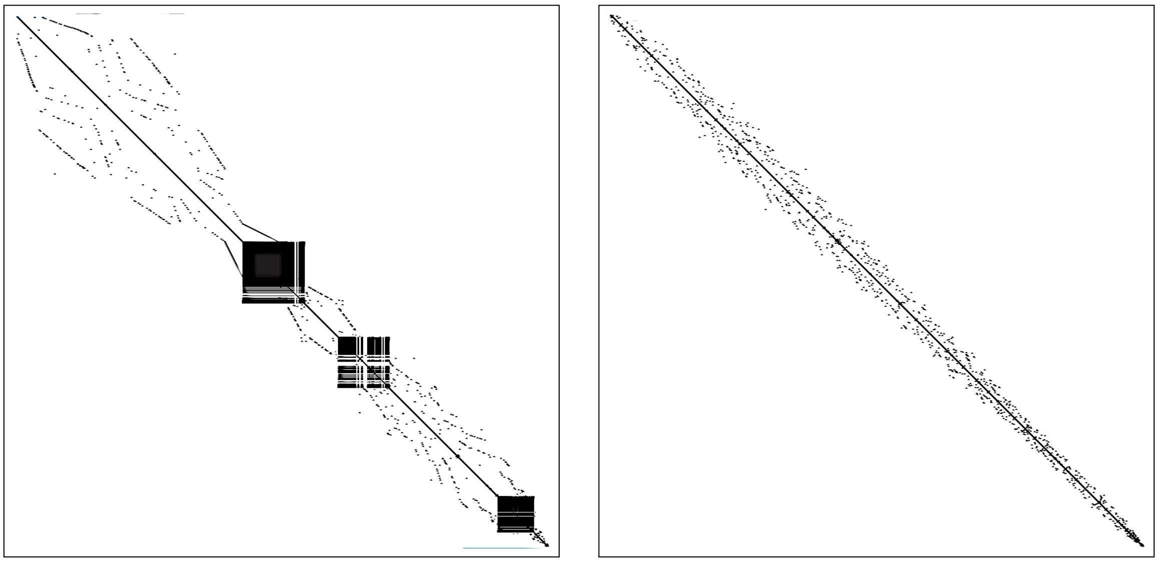

(a) Air-gap element (b) Moving band

Figure 5.11: Matrices generated by FEM.

of Mesh 1, the MB was roughly 14 times faster, while in the case of Mesh 3, MB1 and MB3 were 33 and 23 times faster, respectively.

The difference in performance between the two methods can be several times greater than in the simulation of more conventional single air-gap machines, as has been shown in [88]. In order to explain why the MB is so much faster than the AGE when simulating MGMs, Fig. 5.11 illustrates the structure of final system matrices obtained using the AGE and the MB. The contribution of the three air-gap elements are clearly present in the AGE matrix in the form of the three dense blocks. The MB matrix can be solved efficiently using the direct method employed in *SEMFEM*, but the higher profile and density of the AGE matrix has a great impact on the computational effort required to solve the system. The AGE is especially costly when simulating MGMs because the number of dense blocks are equal to the number of air-gaps. Furthermore, the dimensions of the blocks are related to the number of air-gap nodes, which is typically very high in an MGM without periodicity.

5.5 Conclusions

In this chapter, two methods of simulating movement in magnetically geared machines using the finite element method have been evaluated. Both methods can be executed in parallel, resulting in an appreciable increase in performance. If only the average torque is required as a simulation output, the advantage of using the moving band is significant and the accuracy is likely to be sufficient.

The air-gap element does not suffer from noise associated with distorted elements and for this reason, it may be preferred for torque ripple calculations. The disadvantage of the air-gap element is its high computational cost. In the case of magnetically geared machines, this cost can be prohibitively high due to the high number of air-gaps and lack of periodicity. When accurate torque ripple calculations are required, using the moving band with 3 layers is a good choice.

Chapter 6

Analysis of end-effects

One common problem in the design of MGs and MGMs that has been regularly reported in literature [89, 90, 91, 92, 93, 94] is the relatively large discrepancy between results obtained using 2D finite element analysis (FEA) and 3D FEA or practical measurements. Researchers have generally ascribed this to the so-called end-effects which can be especially significant in these machines.

In this chapter, the end-effects in MGs and MGMs are investigated in detail. The purpose is to identify the origins of these effects and to clarify why the impact is relatively large in magnetic gears and magnetically geared machines. Simulation studies are conducted in order to determine to what extent 2D FEA can be utilized in the design of MGs and MGMs.

6.1 Limitation of 2D FE modeling

Owing to the nature of 2D FE modeling, the end-effects are disregarded in 2D FEA, which leads to an overoptimistic prediction of machine performance. This discrepancy is usually acceptable for conventional electrical machines because the end-effects are either insignificant or can be accounted for by using simple analytical approximations. However, for magnetic gears and magnetically geared machines, the results obtained using 2D FEA overestimate the performance of the machine by a significant margin.

In order to quantify the severity of the end-effects and determine the extent of the correlation between 2D and 3D FE results, an end-effect ratio E_T is introduced, which is defined as the stall torque ratio between 2D and 3D FE results.

$$E_T = \frac{T'_{m3D}}{T'_{m2D}} \tag{6.1}$$

The end-effect ratio is used throughout this chapter as a measure of the severity of the end-effects. Its theoretical limit, $E_T = 1$, is achieved when the gear's stack length is infinitely long. An end-effect ratio close to unity indicates that end-effects do not have a serious negative impact on the torque capability of the gear.

The extent of the problem with 2D FE modeling is evident in literature where several authors [89, 90, 92, 91, 93, 94] have reported 2D FE modeling errors ranging between 20% and 40%.

Table 6.1 lists prototypes, their gear ratios and the end-effect ratios reported, the worst cases having $E_T \approx 0.6$. In [90, 91], the magnitude of the error is ascribed to the large saliency in the air-gap, which is known to cause large end-effects.

Clearly, the error made by 2D FE modeling is too large to be ignored. It can also be seen that a large variation in the error magnitude exists. In this chapter, an attempt is made to provide insight into the mechanisms that cause these large end-effects by conducting detailed 3D FEA of a magnetic gear. The design parameters of the magnetic gear under study are given in Table 6.2.

6.2 Modeling of electrical laminations

In this investigation, special attention was given to the modeling of the electrical lamination material used to construct the modulator and the ring gear yoke. Electrical laminations have significantly different BH-curves between directions parallel and perpendicular to the lamination plane. This difference can be taken into account by using an anisotropic lamination material model in 3D FEA.

Given a BH-curve, $B(H)$, for a uniform sample of steel, the BH-curves in the plane of the laminations, $B_{xy}(H)$, and perpendicular to this plane, $B_z(H)$, can be deduced from the following relations [95]:

$$B_{xy}(H) = \kappa B(H) + (1-\kappa)\mu_0 H \tag{6.2}$$

$$H_z(B) = \kappa H(B) + (1-\kappa)\frac{B}{\mu_0} \tag{6.3}$$

with κ the stacking factor, taken as 0.95 in this study.

The difference between a simple isotropic model and an anisotropic model of the laminated material is illustrated in Fig. 6.1, which shows the axial component of the flux density in the modulator for the model with the supporting casing described in the following section. This axial component of flux is not accounted for in 2D simulations.

In all 3D simulations performed and described in this chapter, such anisotropic models were used. The difference in these results compared to results obtained using isotropic models were found to be small.

In one simulation, a fictitious material was used for the modulator. The material had normal characteristics in the plane of the laminations, but the permeability of the material perpendicular

Table 6.1: End-effect ratios reported in literature

Prototype description	G_r	E_T
Magnetic gear [89]	5.75	70 %
Magnetic gear [90]	5.5	60 %
Magnetic gear [92]	5.5	65 %
Magnetically geared machine [91]	8.83	81 %
Magnetic gear[93]	10.5	62 %
Magnetic gear[94]	10.5	70 %

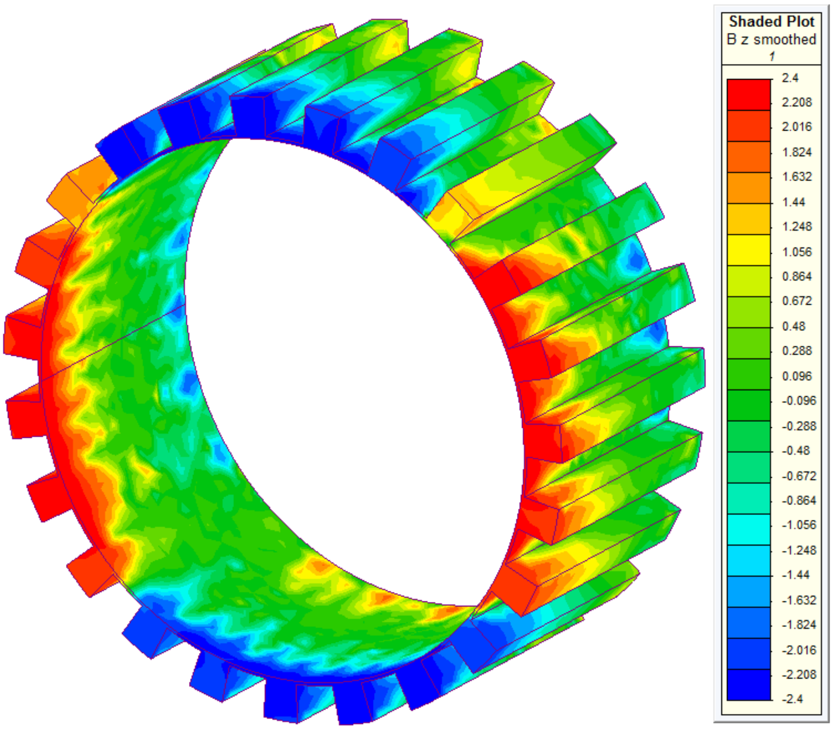

(a) Isotropic BH-curve.

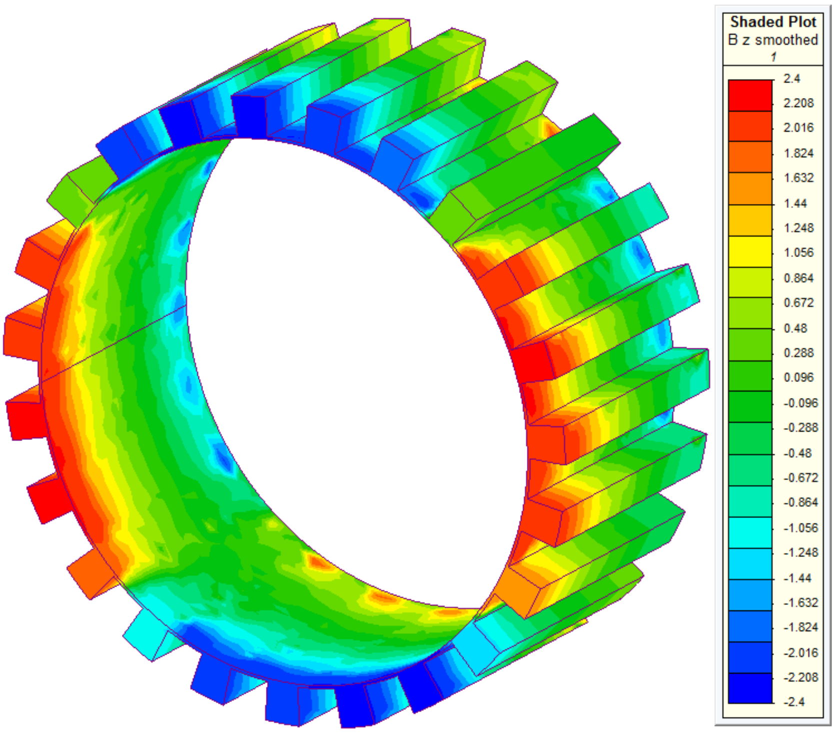

(b) Anisotropic BH-curve.

Figure 6.1: Flux density color map of B_z in the modulator of a magnetic gear.

Table 6.2: Flux-modulated magnetic gear design parameters

Parameter	**Value**
Sun gear magnet pitch [fraction of pole pitch]	0.9
Ring gear magnet pitch [fraction of pole pitch]	0.8
Inner modulator tooth pitch [fraction of segment pitch]	0.6
Outer modulator tooth pitch [fraction of segment pitch]	0.4
Sun gear yoke thickness t_{sy} [mm]	15
Sun gear magnet thickness [mm]	4.5
Sun gear air-gap length [mm]	0.7
Modulator thickness [mm]	7
Modulator bridge thickness [mm]	0.5
Ring gear air-gap length [mm]	0.7
Ring gear magnet thickness [mm]	4
Ring gear yoke thickness t_{ry} [mm]	6
Ring gear yoke outer diameter r_{ry} [mm]	140
Stack length L [mm]	50
Magnet remanent flux density [T]	1.39
Magnet relative recoil permeability	1.05
Number of sun gear pole pairs p_s	3
Number of modulator segments Q_m	27
Number of ring gear pole pairs p_r	24
Gear ratio G_r	9

to the lamination plane was defined as a constant $2u_0$. The purpose was to investigate how much the end-effects can be reduced by using a modulator which does not readily permit axial flux. The gear's stall torque increased by 4% using the fictitious material compared to the normal anisotropic material.

6.3 End-effect origins

In this section, three discernible end-effect phenomena are identified which are responsible for the difference between 2D and 3D FE results. The first two are *leakage* and *fringing*. Fig. 6.2 shows a plot of the axial magnetic flux density (B_z) in a slice through an MG where only sun gear magnets are considered. It can be seen that some of the flux coupling to the modulator does not penetrate through it, but returns outside the stack to the sun gear yoke. This is termed *leakage*. Secondly, flux coupling to the ring gear is not confined to the area in the gear stack but also couples through the air region outside the stack. This is termed *fringing*. While these two effects are present in all electrical machines, their impact may be larger in MGs and MGMs because of

- large equivalent air-gaps

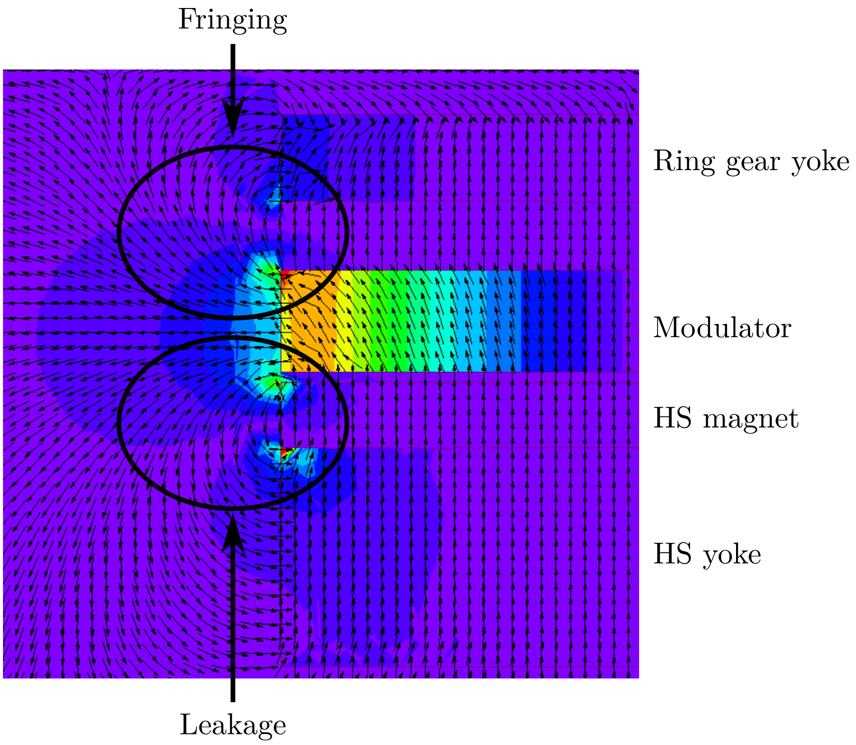

Figure 6.2: Leakage and fringing in a magnetic gear. The plot shows the axial component of magnetic flux density, B_z.

- modulator saliency
- inherent sandwiched structure

Large equivalent air-gaps are conducive to leakage because the relative difference in reluctance between the intended (2D) flux path and the leakage paths in the end-region is smaller. Saliency can increase fringing fields because concentrated flux, due to saliency, is more prone to fringing. The structure of magnetic gears is such that a ferromagnetic component is sandwiched between two layers of magnets. It can be seen in Fig. 6.2 that a significant axial flux component is present in the modulator. This inherent structure of MGs contributes to leakage and fringing.

A third end-effect mechanism exists in magnetic gears. Unlike in conventional electrical machines, the torque produced in a magnetic gear can be split into two components, i.e. the torque due to attractive and to repulsive magnetic forces. Fig. 6.3 illustrates an MG with the magnets contributing to the attractive and repulsive torques respectively. Note that half the magnets on the outer ring contribute to attractive torque and the other half to repulsive torque. These

Table 6.3: Torque production in a magnetic gear

Simulation	**2D FE torque**	**3D FE torque**	**E_T**
Repulsive	24.0 Nm	19.4 Nm	80.8 %
Attractive	31.6 Nm	29.6 Nm	93.7 %
(Repulsive + Attractive)	55.6 Nm	49.0 Nm	88.1 %
Full model	57.3 Nm	51.2 Nm	89.4 %

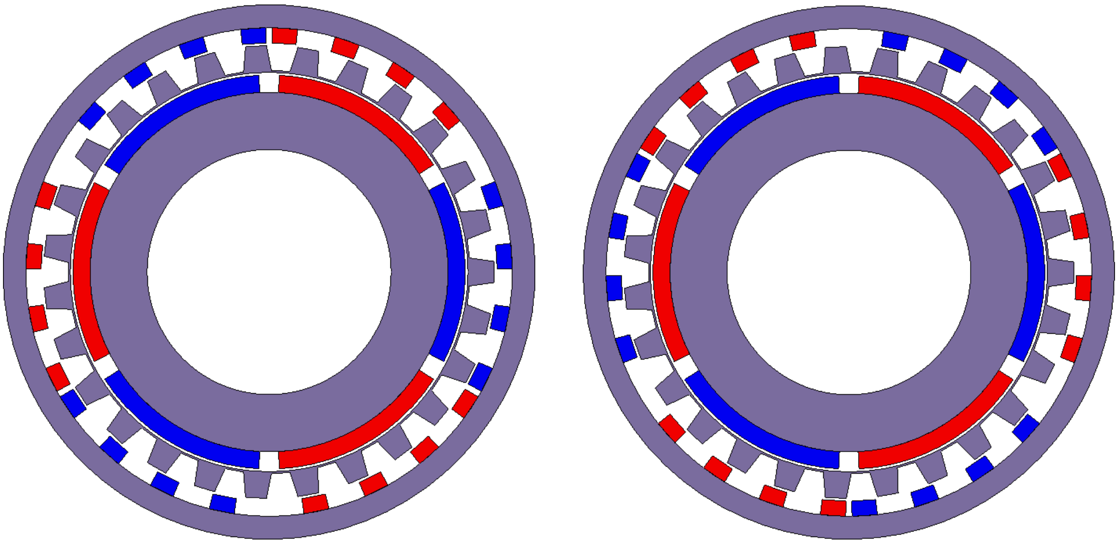

(a) Attractive torque.

(b) Repulsive torque.

Figure 6.3: Magnetic gear illustrating magnets responsible for different torque components.

two models have been simulated using both 2D and 3D FEA. The results are given in Table. 6.3. The *full model* simulation is the normal case with both attractive and repulsive torques acting. The full model case corresponds fairly well with the superimposed attractive and repulsive components. It is interesting to note that the attractive torque component drops by less than 7% from 2D to 3D whereas the repulsive component drops by almost 20%. The large drop in the repulsive component is due to an effect which will be termed *escaping* and can be defined as the phenomenon that opposing magnetic poles tend to force flux in the z-direction in the end-region. It can also be viewed as a special, severe case of leakage resulting from the flux focussing effect of opposing magnetomotive forces. This effect is illustrated in Fig. 6.4 which shows the *axial* flux density on a slice placed 1 mm beyond the end of the gear stack. In other words, it shows axial flux just outside the gear. In the figure, the three ellipses highlight the areas where *escaping* occurs corresponding to the areas where repulsive torque is produced. It can be clearly seen that the axial flux outside the gear stack is higher over the repulsive magnets than the attractive ones. This effect is unique to machines based on magnetic gearing principles and contributes to the severity of end-effects in magnetic gears compared to other electrical machines.

6.4 Parameters affecting end-effects

In this section, the influence that several design parameters have on the torque capability of MGs will be investigated. Three different designs with an outer diameter $D = 140$ mm, as depicted in Fig. 6.5, are evaluated in this section. A prior study was reported in [96], but it was based on only 2D FEA. Special attention is paid to the difference between 2D and 3D FE results in this investigation.

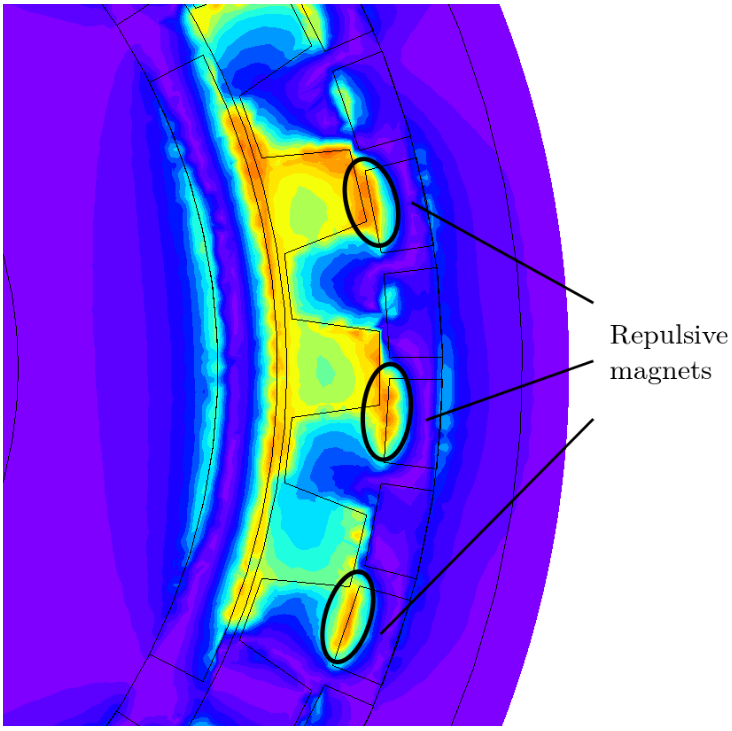

Figure 6.4: Escaping occurring over the repulsive magnets.

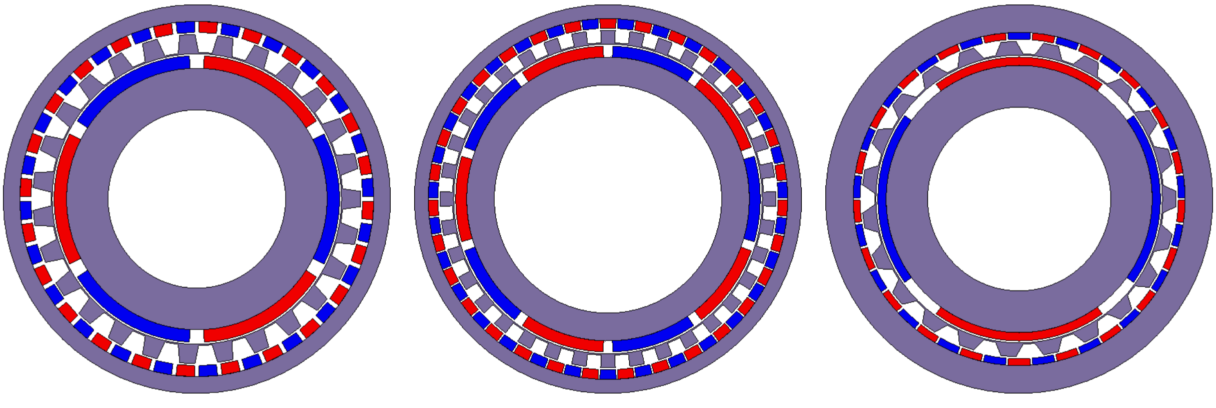

(a) $p_h = 3$, $Q_m = 27$, $p_r = 24$ (b) $p_h = 5$, $Q_m = 36$, $p_r = 31$ (c) $p_h = 2$, $Q_m = 23$, $p_r = 21$

Figure 6.5: Cross sectional views of three magnetic gear designs with an outer diameter of 140 mm. Design A corresponds to the gear investigated in section 6.3.

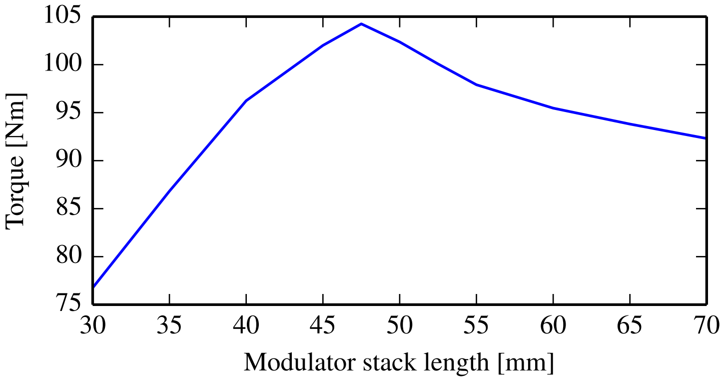

Figure 6.6: Effect of the modulator stack length on the performance of a magnetic gear. (The stack length of the gear is 50 mm.)

6.4.1 Effect of modulator stack length

Since the modulator contains the main leakage and escaping flux paths, it is sensible to evaluate its impact on the end-effects. Fig. 6.6 shows the effect of the modulator stack length on the stall torque of design A with a stack length of 50 mm. Perhaps somewhat counter-intuitively, the MG performs better with a modulator stack length that is slightly shorter than the gear's stack length.

6.4.2 Effect of modulator thickness

The effect that the modulator thickness has on the maximum torque of design A is shown in Fig. 6.7. It shows that for a modulator with an inner bridge, an optimum thickness exists which maximizes the stall torque of the gear. It appears that both 2D and 3D FE results show the same tendency. Fig. 6.8 demonstrates the effect of the modulator thickness on E_T. The end-effect ratio decreases with increasing modulator thickness which means that the 2D modeling error becomes larger.

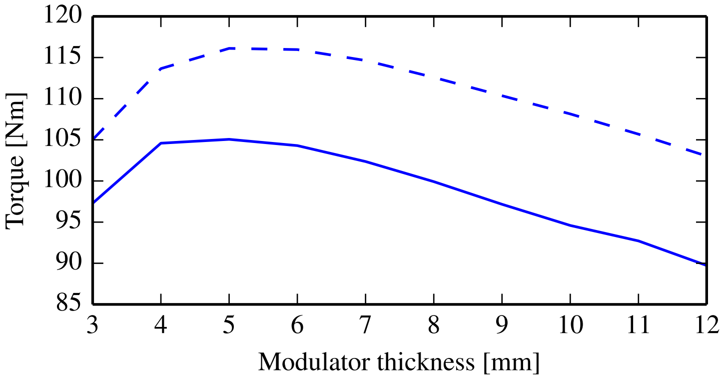

Figure 6.7: Variation of the stall torque with the modulator thickness.
(2D: dashed, 3D: solid)

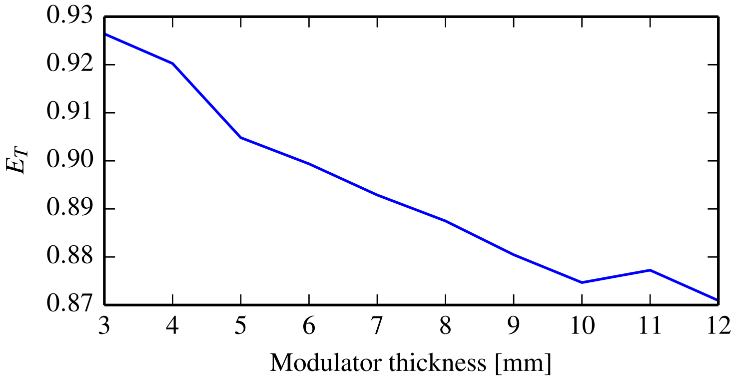

Figure 6.8: Variation of the torque end-effect ratio with the modulator thickness.

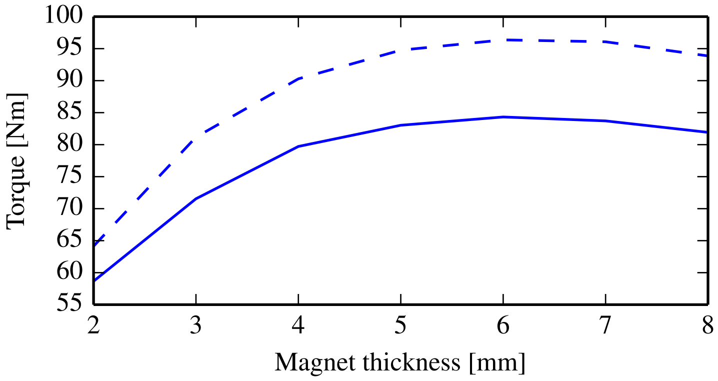

Figure 6.9: Variation of the stall torque with magnet thickness.
(2D: dashed, 3D: solid)

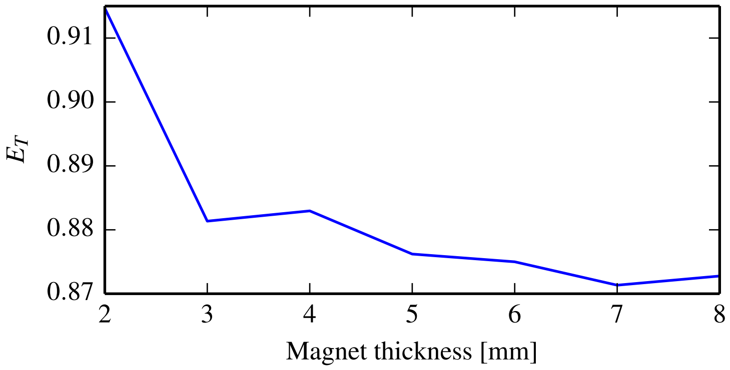

Figure 6.10: Variation of the torque end-effect ratio with magnet thickness.

6.4.3 Effect of magnet thickness

The effect of the magnet thickness on the maximum torque and E_T is illustrated in Figs. 6.9 and 6.10. In the simulated model of design A, the magnets on the sun gear and the outer ring gear were of the same thickness. The thicknesses of the inner and outer yokes were increased to avoid excessive saturation, but the inner diameter of the outer yoke was kept constant. The modulator thickness was also kept constant while the thickness of the magnets were varied as shown in the graphs. A better end-effect ratio is achieved with thinner magnets. Fig. 6.11 also shows that the torque per magnet thickness decreases with increasing magnet thickness. 2D and

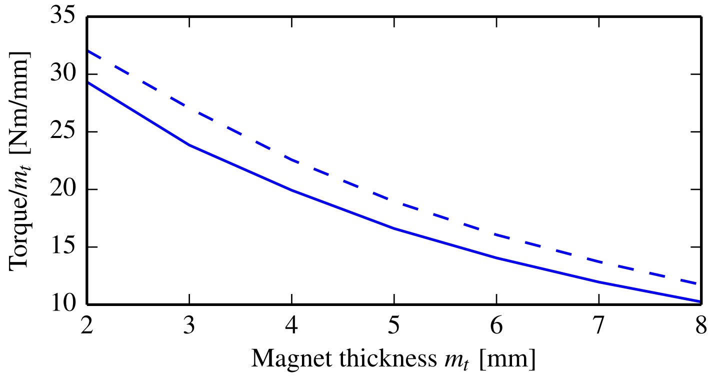

Figure 6.11: Variation of the torque per magnet thickness with magnet thickness. (2D: dashed, 3D: solid)

3D FE results show reasonable correlation. Considering the high cost of magnet material, it is also beneficial from a cost perspective to use thinner magnets.

6.4.4 Effect of pole count and gear ratio

Two magnetic gears (designs B and C) with different numbers of pole pairs on the sun gear have been simulated with a varying number of pole pairs on the ring gear. Again, the thicknesses of the inner and outer yokes were increased so that the impacts of saturation can be disregarded,

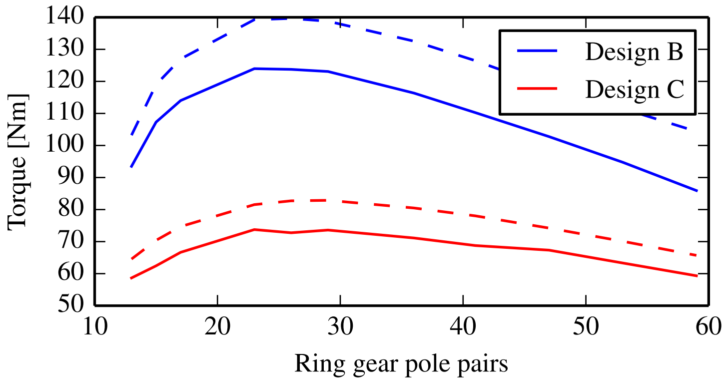

Figure 6.12: Variation of the stall torque with the number of pole pairs on the ring gear. (2D: dashed, 3D: solid)

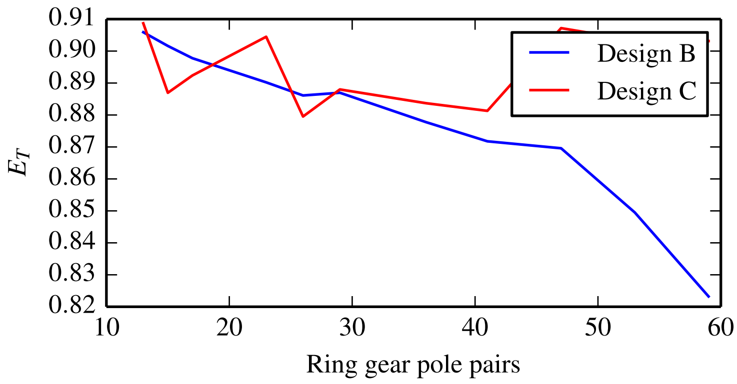

Figure 6.13: Variation of the torque end-effect ratio with the number of pole pairs on the ring gear.

but the air-gap diameters were kept constant. The variation of the stall torque with the number of pole pairs on the ring gear is shown in Fig. 6.12. It can be seen that for both designs the stall torque is maximized for a certain ring gear pole count and this number does not vary significantly between the 2D and 3D FE analyses. A plot of the end-effect ratio is shown in Fig. 6.13. In the case of design B, E_T decreases with increasing ring gear pole pairs. In the case of design C, this trend is not clear. This is attributed to the sensitivity of the end-effect ratio to the torque calculation and the fact that the torque curves are relatively flat in the case of design C.

6.4.5 Effect of the stack length

All three designs in Fig. 6.5 were evaluated with different stack lengths. In each case the stack length was varied between $L = 10$ mm and $L = 140$ mm which corresponds to an aspect ratio, $a = L/D$ of about 0.07 to 1. The three designs have significantly different stall torque versus aspect ratio curves, as shown in Fig. 6.14. However, the torque end-effect ratio, shown in Fig. 6.15, exhibits similar behaviour for all three designs. As expected, the aspect ratio of the gear has a strong influence on the impact of the end-effects. For all the designs evaluated, E_T was above 80% for aspect ratios greater than 0.2.

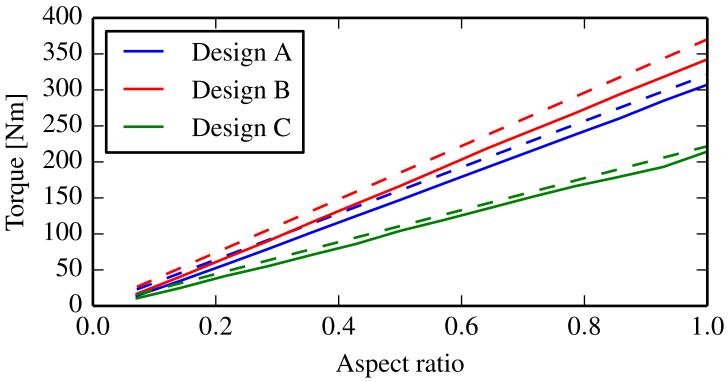

Figure 6.14: Stall torque versus aspect ratio for three different MG designs. (2D: dashed, 3D: solid)

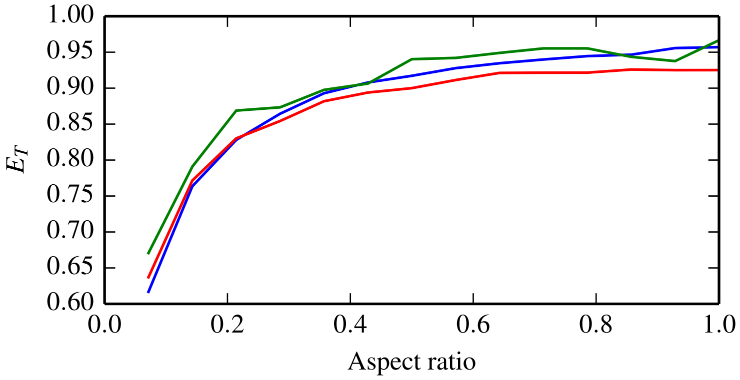

Figure 6.15: Torque end-effect ratio versus aspect ratio for three different MG designs.

6.4.6 Effect of the supporting structure

The three types of end-effect, leakage, fringing and escaping are inherent to MGs and MGMs and cannot be easily remedied. However, if the mechanical supporting structure is not well designed and ferromagnetic materials are used in close proximity to the gear stack, the impact of the end-effects can be significantly greater. In an investigation of a prototype magnetic gear, presented in the following chapter, it was found that the supporting structure was largely responsible for the severity of the end-effects and thus the inferior torque performance.

6.5 Magnetically geared machines

The end-effects described in section 6.3 are just as relevant in magnetically geared machines as in magnetic gears. It has been shown in the previous section that end-effects can have a significant impact on the stall torque of an MG, T'_m. The stator torque T'_i, however, is not generated by a magnetic gearing action, and thus it may not be impacted in the same way that T'_m is. This has interesting implications for the stator load factor, defined in section 4.3.3 as

$$\gamma_i = -\frac{G_{sm} T'_i}{T'_m} \tag{6.4}$$

If the relative difference between 2D and 3D FE results for T'_m is larger than the difference for T'_i, the true stator load factor will actually be higher than that calculated using 2D simulations. An end-effect ratio can be defined for the stator load factor, in a similar way as in (6.1)

$$E_{\gamma_i} = \frac{\gamma_{i_{3D}}}{\gamma_{i_{2D}}} \tag{6.5}$$

The machines displayed in Figs. 6.16(a) and 6.16(b) have outer diameters of 140 mm. Simulations for stack lengths ranging from 10 mm to 140 mm were performed, corresponding to aspect ratios of 0.07 - 1. Fig. 6.17 shows the variation of the 2D and 3D modulator torques while Fig. 6.18

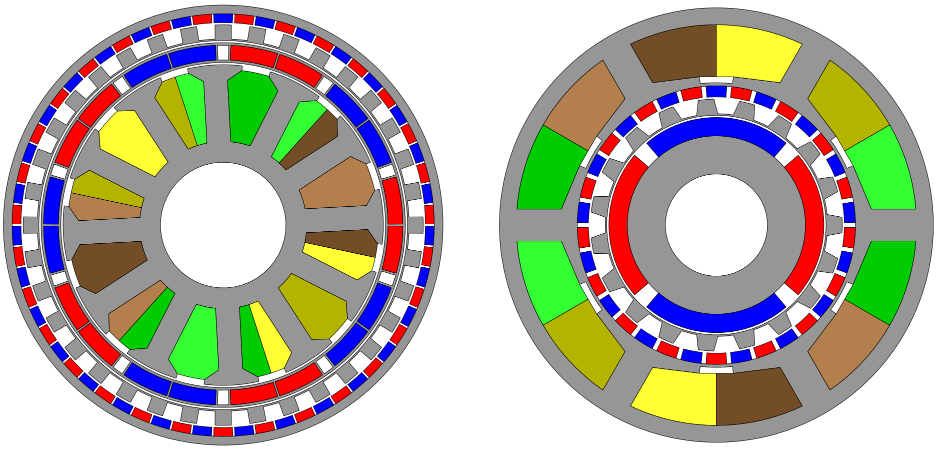

(a) Split MGM.

(b) Ring-stator MGM.

Figure 6.16: Two magnetically geared machines.

shows the variation of the stator torques. Note that the difference between the 2D and 3D FE results are more pronounced for the modulator torque. Fig. 6.19 shows the variation of the calculated stator load factors. The stator load factor is a constant in the 2D case. In contrast to the stall torque which is always lower in the 3D case, the stator load factor is actually higher in 3D than in 2D for both the split MGM and the ring-stator MGM. This is due to the stator torque not being as sensitive to end-effects as the modulator torque, as explained. For the designs studied here, the stator load factor of the split MGM calculated in 3D does not converge to the 2D value as quickly as that of the ring-stator topology.

A comparison between the torque end-effect ratio, E_T, and the stator load factor end-effect ratio, E_{γ_i}, is shown in Fig. 6.20. The opposing trends are clear. The result is that an MGM designed for a given stator load factor using 2D FEA is likely to have a lower than calculated stall torque but a better stator load factor when end-effects are considered.

6.6 Application in design optimization

In this section, a design optimization strategy for flux-modulated magnetic gears is demonstrated. The proposed method is depicted in Fig. 6.21. It starts with an initial design which is optimized using 2D FEA. A curve of the end-effect ratio E_T versus the stack length L at the optimum design point is then generated using 3D FEA. A second 2D optimization is then run with a

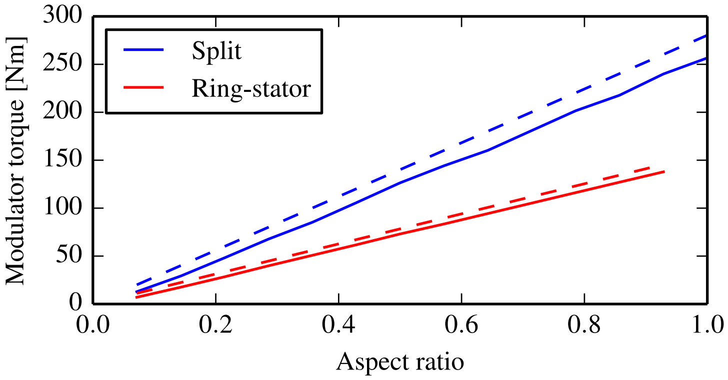

Figure 6.17: Stall torque versus stack length for two MGMs. (2D: dashed, 3D: solid)

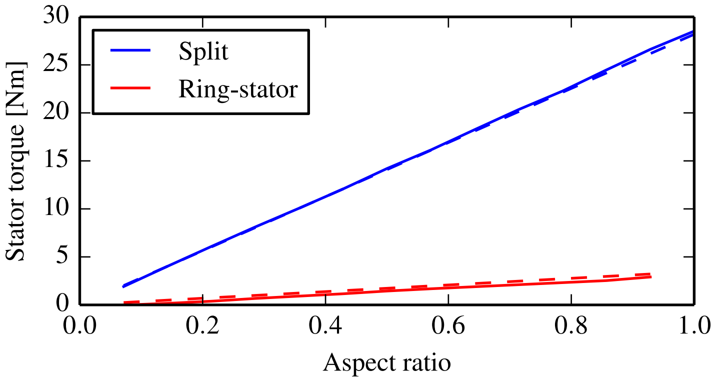

Figure 6.18: Stator torque versus stack length for two MGMs. (2D: dashed, 3D: solid)

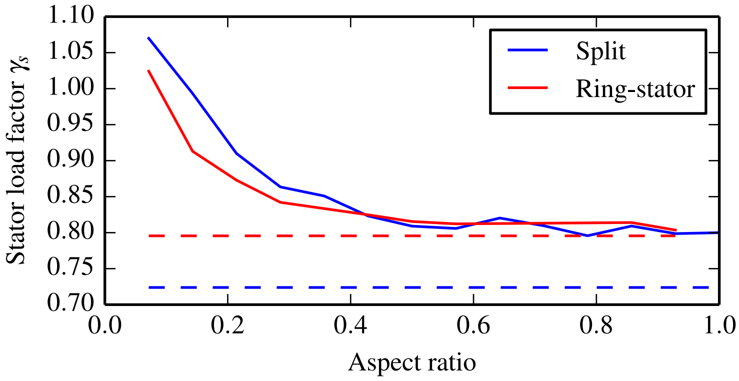

Figure 6.19: Stator load factor versus stack length for two MGMs. (2D: dashed, 3D: solid)

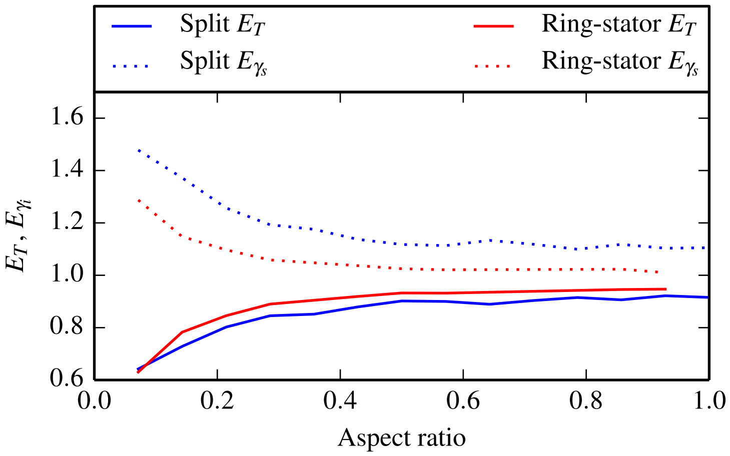

Figure 6.20: Different behaviours of end-effect ratios in MGMs.

compensated torque calculation:

$$T = E_T(L) \cdot T_{2D} \tag{6.6}$$

where E_T is a function of the stack length L. This second optimization leads to the final design which can be verified using 3D FEA.

The proposed optimization strategy is applied to the design of a flux-modulated magnetic gear with a stall torque of 200 Nm. The gear in Table 6.2 is used as the initial design. The objective of the optimization is to minimize the total active mass. In this example, the design variables are limited to only four variables, but of course many more can be chosen. The design variables are the yoke thicknesses of the sun gear and the ring gear, t_{sy} and t_{ry}, the outer radius, r_{ry}, and the stack length, L. The air-gap lengths were increased to 1 mm. Table 6.4 lists the design variables, the constraint (modulator stall torque T'_m) and the objective (active mass M) for the initial design, the 2D optimum and the final design. The curve of the end-effect ratio versus the stack length at the 2D optimum is shown in Fig. 6.22. In this case, the curve is relatively flat in the region of the 2D optimum design point. The final design's stall torque has been verified with 3D FEM, the result was $T'_m = 202.2$ Nm.

The main advantage of this optimization strategy is that it makes use of a very limited number of 3D FEM solutions, yet the influence of end-effects can be accounted for with good accuracy.

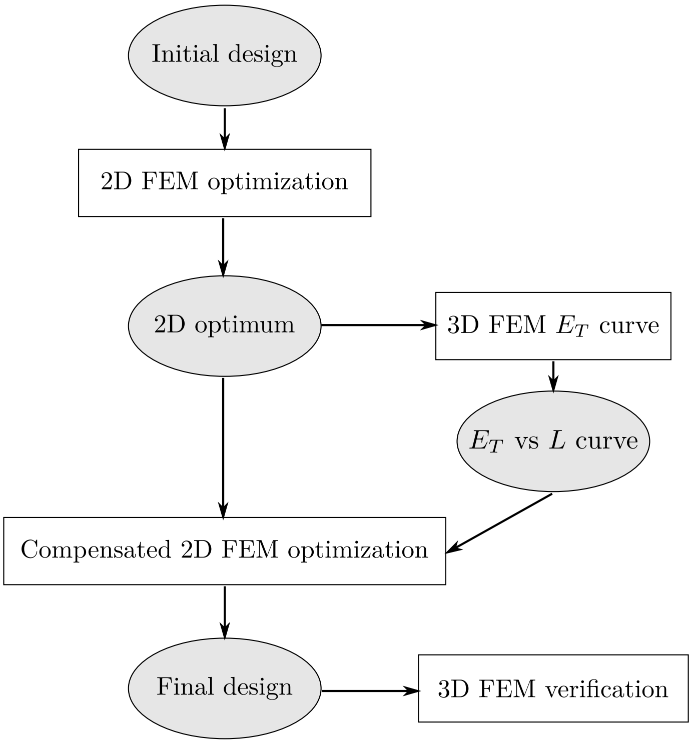

Figure 6.21: Proposed optimization strategy for flux-modulated magnetic gears.

Table 6.4: Optimization designs

Design	$\mathbf{t_{sy}}$ *	$\mathbf{t_{ry}}$ *	$\mathbf{r_{ry}}$ *	**L** *	$\mathbf{T'_m}$ **[Nm]**	**M [kg]**
Initial design	15	6	70	50	107.1 †	3.78
2D optimum	8.6	5.7	95.3	57.3	199.5 †	5.42
Final design	8.5	5	105.5	58.2	199.5 ‡	6.08

* Dimensions given in [mm]
† Calculated with 2D FEA
‡ Calculated using (6.6)

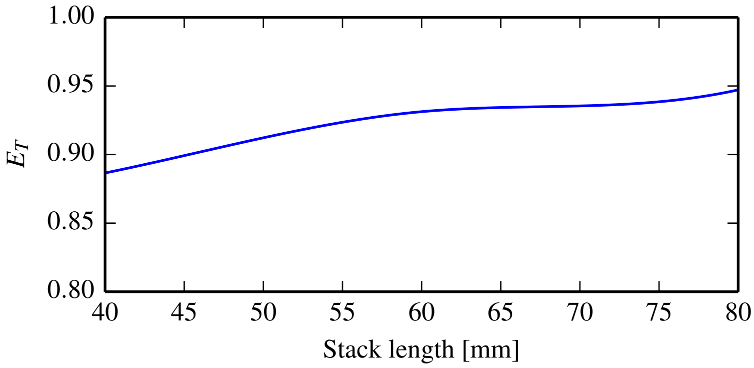

Figure 6.22: End-effect ratio versus stack length at the 2D optimum.

Furthermore, optima achieved with this strategy will be close to the true optimum.

Although, the focus of this example is on magnetic gears, this strategy can also be applied to magnetically geared machines by compensating for both E_T and E_{γ_s}. The torque is compensated as before using (6.6). The stator load factor can be calculated using the compensated stall torque and the 2D stator torque. The 2D stator torque has been shown to be sufficiently accurate. (See Fig. 6.18.)

6.7 Discussion

It has been shown in literature and demonstrated here that end-effects can have a great impact on the performance of magnetic gears and magnetically geared machines. Three-dimensional finite element analysis is necessary for accurate performance calculations.

Three types of end-effect have been identified: *leakage*, *fringing* and *escaping*. The term *escaping* is used to describe a phenomenon which is unique to machines based on the magnetic gearing principle and which is partly responsible for the relatively large impact of end-effects in magnetic gears.

Although various parameters have an effect on the end-effect ratio, it has been shown that the aspect ratio of the machine has by far the greatest impact. Thus it is possible to estimate true performance by using 2D results together with the knowledge of the behaviour of the end-effect ratio versus the aspect ratio or stack length of the machine. An optimization strategy based on these observations which makes minimal use of 3D FEM simulations has been demonstrated.

Interestingly, it has been shown that the stator load factor of a magnetically geared machine improves when end-effects have a negative impact on the machine's stall torque. This may result in an oversized stator when 2D finite element analysis is used to perform matching between the gear and electrical machine components of a magnetically geared machine.

Chapter 7

Evaluation of a magnetic gear

In this chapter, the design of a prototype flux-modulated magnetic gear, first presented in [97], is critically examined. The effect of the modulator bridges on the air-gap flux density harmonics and the performance in terms of torque, as well as efficiency, is analyzed. The magnetic design of the gear was done by using 2D FE analysis. It was, however, found that the practical measurement results in terms of peak torque capability (stall torque) and efficiency fell far short of the predicted ones. The intrinsic end-effects of MGs and MGMs have been described in the previous chapter. This chapter presents a detailed investigation of the end-effects in the prototype. Measures that could be taken to alleviate the negative impact of these effects are then proposed. Based on the findings, design changes are made and implemented in a new prototype. The improvements in the measured performance of the new prototype confirms the validity of the analyses and highlights the importance of the avoiding secondary end-effects due to mechanical design.

7.1 The prototype magnetic gear

In this section, the electromagnetic design, the mechanical layout and the predicted and measured performance characteristics of the prototype magnetic gear are discussed.

7.1.1 Magnetic design

Fig. 7.1 shows a cross-sectional view of the prototype magnetic gear. The design was not fully optimized. In this design, the modulator is kept stationary while the sun gear and ring gear assemblies rotate. For this configuration, the gear ratio is:

$$G_{sr} = \frac{p_r}{p_s} \tag{7.1}$$

The detailed dimensions of the prototype magnetic gear are given in Table 7.1. The type of permanent magnets used in the prototype is N35 grade NdFeB magnets. The modulator and the ring gear yoke were fabricated using 0.5 mm, M-19 electrical laminations. In order to ease the construction and increase the torsional stiffness of the flux modulator, the segments were connected with thin bridges on the sun gear side. The modulator was constructed by placing stainless steel rods in the slots between the modulator segments and filling these slots with epoxy

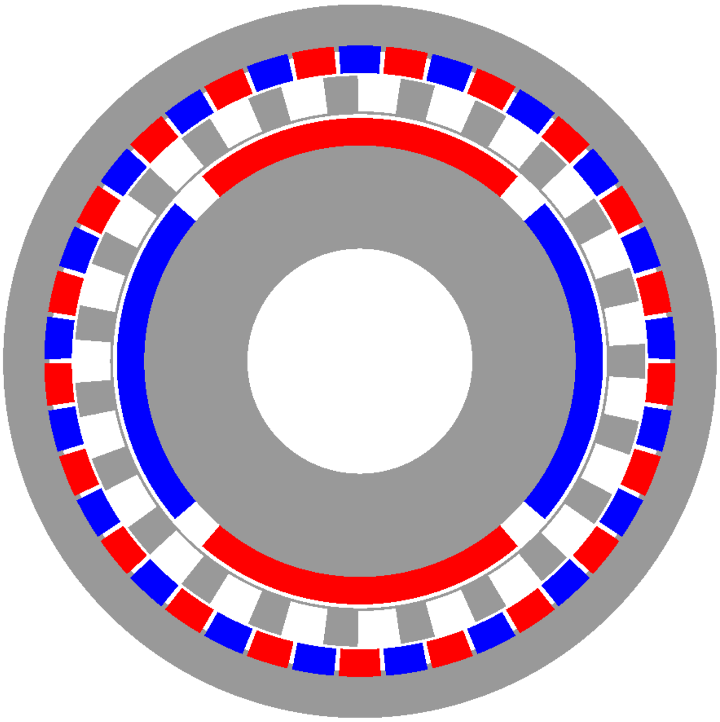

Figure 7.1: Cross-sectional view of the prototype magnetic gear.

resin. The sun gear yoke was made of solid mild steel and integrated with the shaft as shown in Fig. 7.2. The figure also shows the ring gear shaft and the modulator, which is supported by the casing.

The flux density distribution of the magnetic gear at its maximum torque position obtained using 2D FE analysis is shown in Fig. 7.3. According to the 2D FE analysis, the ring gear stall torque is 53.6 Nm. This results in a torque density of 101 kNm/m^3 based on the active material volume. Bearing in mind that N35 magnets are a low grade of Neodymium magnets nowadays, this result seems to verify that stall torque densities exceeding 100 kNm/m^3 are practically achievable.

7.1.2 Effect of the modulator bridges

Fig. 7.4 shows the modulator of the magnetic gear without bridges and with bridges added. The radial flux density distribution in the sun gear air-gap due to sun gear magnets and ring gear magnets respectively are displayed in Fig. 7.5. Figs. 7.6 and 7.7 show the radial air-gap flux density spectra in the sun and ring gear air-gaps respectively. It can be observed from Fig. 7.6 that the bridges can suppress the undesired higher order harmonics (e.g. 21st and 25th harmonics) in the sun gear air-gap, which helps to minimize unwanted losses in the sun gear magnets and solid yoke.

The fundamental harmonic (2nd) in the sun gear air-gap due to the sun gear magnets is actually slightly stronger with bridges. However, this harmonic due to the ring gear magnets is slightly weaker. From Fig. 7.7 it is clear that the bridges have very little impact on the harmonics in the ring gear air-gap due to either the sun or ring gear magnets.

In order to illustrate the benefits of reducing higher order harmonics in the sun gear air-gap,

Table 7.1: Prototype design parameters

Parameter	**Value**
Sun gear magnet pitch [fraction of pole pitch]	0.9
Ring gear magnet pitch [fraction of pole pitch]	0.897
Modulator tooth pitch [fraction of segment pitch]	0.447
Sun gear yoke inner diameter [mm]	41
Sun gear yoke thickness [mm]	18.8
Sun gear magnet thickness [mm]	5
Sun gear air-gap length [mm]	0.7
Modulator thickness [mm]	7
Modulator bridge thickness [mm]	0.5
Ring gear air-gap length [mm]	0.5
Ring gear magnet thickness [mm]	5
Ring gear yoke thickness [mm]	7.5
Ring gear yoke outer diameter [mm]	130
Stack length [mm]	40
Number of sun gear pole pairs	2
Number of ring pole pairs	21
Gear ratio	10.5

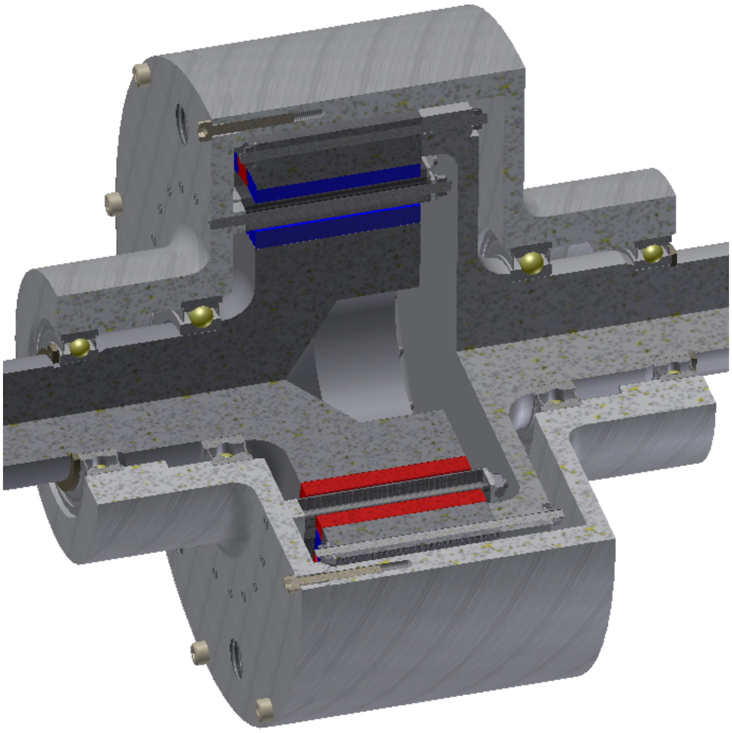

Figure 7.2: Three-quarter section view of the prototype magnetic gear showing mechanical support structure, sun gear and ring gear shafts.

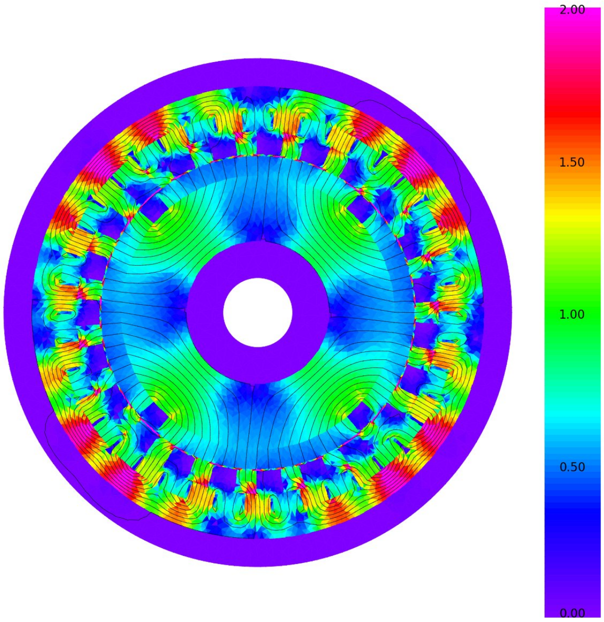

Figure 7.3: Flux density distribution of the prototype magnetic gear obtained using 2D FE analysis.

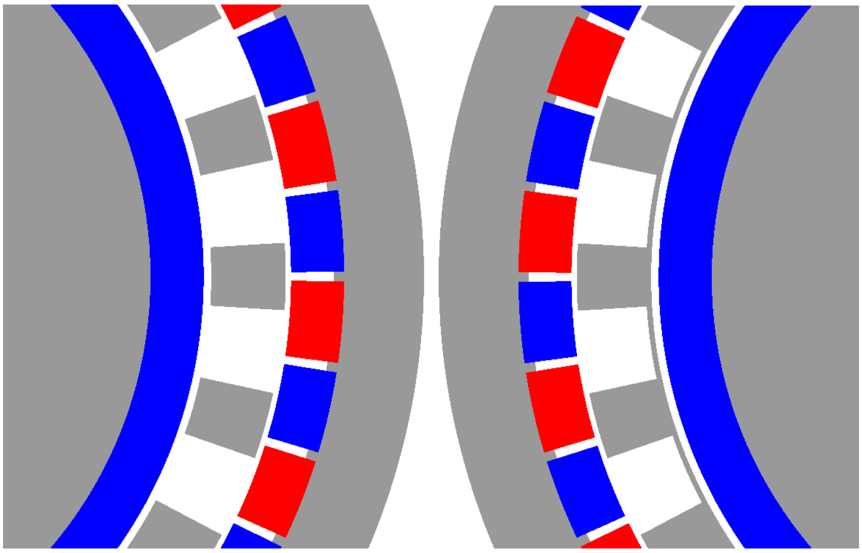

(a) No bridges on the modulator

(b) Bridges added on the sun gear side of the modulator

Figure 7.4: Close-up view of the magnetic gear

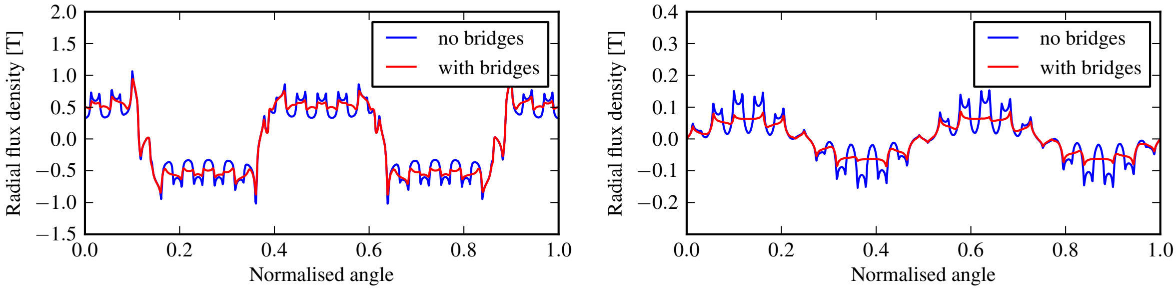

(a) Due to sun gear magnets

(b) Due to ring gear magnets

Figure 7.5: Radial flux density waveform in the sun gear air-gap.

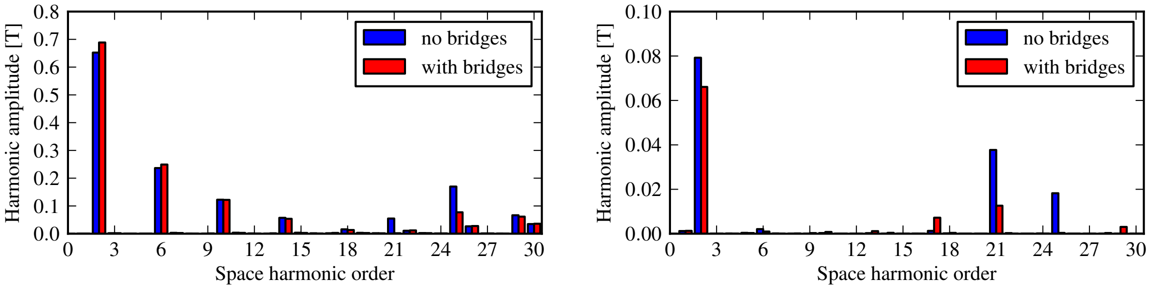

(a) Due to the sun gear magnets.

(b) Due to the ring gear magnets.

Figure 7.6: Space harmonics present in the sun gear air-gap.

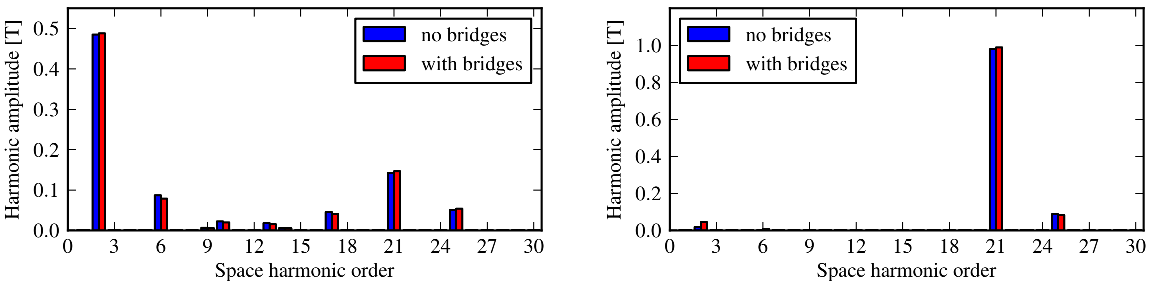

(a) Due to the sun gear magnets.

(b) Due to the ring gear magnets.

Figure 7.7: Space harmonics present in the ring gear air-gap.

simulations of the gear with the sun gear operating at a speed of 12 000 rpm were performed. Fig. 7.8 shows a comparison of the ohmic losses in the sun gear magnets. The losses are almost four times smaller in the case of the bridged modulator. The advantages in terms of torque ripple on the sun gear rotor are illustrated in Fig. 7.9.

Two-dimensional FE analysis indicates that the stall torque of the gear is 52 Nm without bridges and 53.4 Nm with bridges. Fig. 7.10 shows a plot of the torque on the ring gear as a function of the sun gear position. These results agree well with those presented in [92], which also indicate that bridges on the sun gear side of the modulator do not have a significant impact on the stall

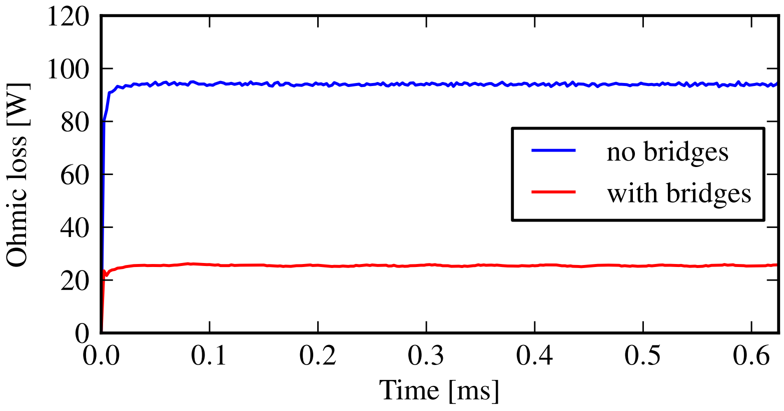

Figure 7.8: Total ohmic losses in the sun gear magnets with the sun gear rotating at 12 000 rpm.

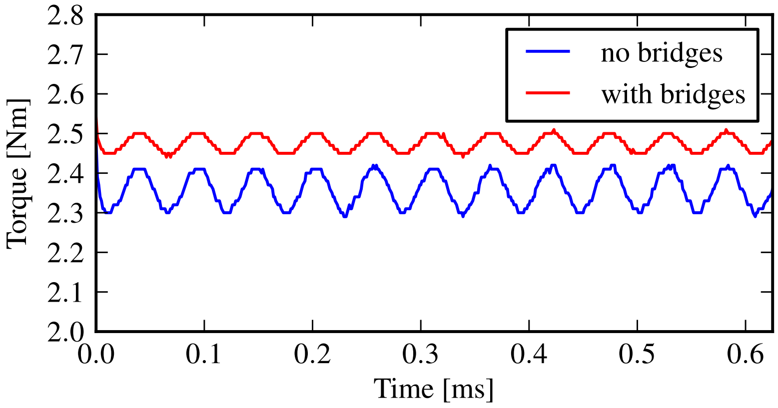

Figure 7.9: Torque on the sun gear operating at a speed of 12 000 rpm.

torque.

Thus, in the case of this prototype, the bridged modulator shows not only the benefits of simplified mechanical construction, but also the distinct advantage of suppressing unwanted high order flux harmonics in the sun gear air-gap with little impact on the flux harmonics in the ring gear air-gap and the stall torque of the gear. This is an important advantage for high-speed operation.

7.1.3 Predicted versus measured results

The experimental setup used to test the prototype is shown in Fig. 7.11. The measured ring gear stall torque was only 33 Nm which amounts to a 38% reduction when compared with that of 2D FE predicted results. Furthermore, the prototype suffered significantly from rotational losses as can be seen in Fig. 7.12(a) which shows the no-load losses of the gear as a function of the rotational speed. To identify the regions in the gear where the losses are concentrated, Thermax temperature indicators were placed at various parts of the prototype. A significant temperature rise was found on the side of the casing supporting the modulator during high-speed operation, which was caused by the time-varying end leakage flux in the casing. These losses decreased the

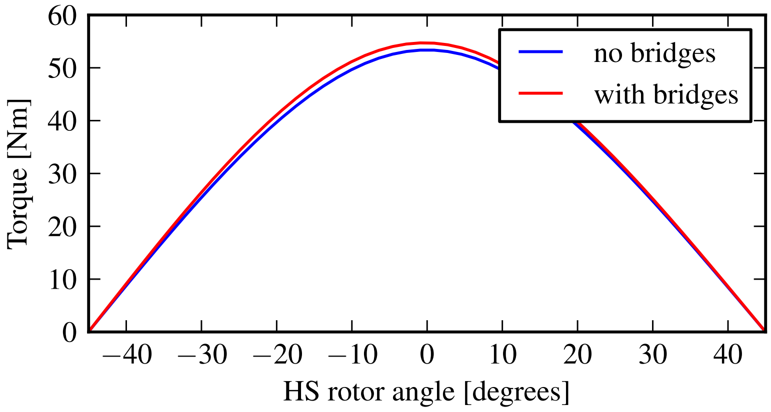

Figure 7.10: Torque on the ring gear vs. position of the sun gear. The ring gear is kept at a fixed position. The position at 0° corresponds to the maximum torque position in Fig. 7.3

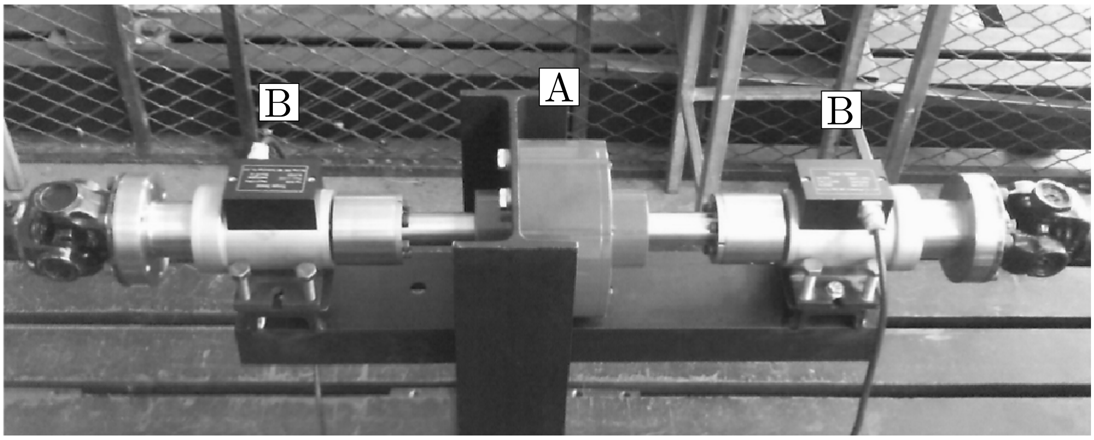

Figure 7.11: Experimental setup used to test the prototype magnetic gear. (A: Prototype, B: torque transducer)

efficiency of the prototype gear substantially, especially at higher speeds. Fig. 7.12(b) shows the efficiency of the gear at a constant load of 20 Nm.

7.2 Analysis of end-effects

In this section, detailed 3D FE modeling of the prototype magnetic gear is presented. The purpose of this analysis is to determine the causes of the large difference between the results

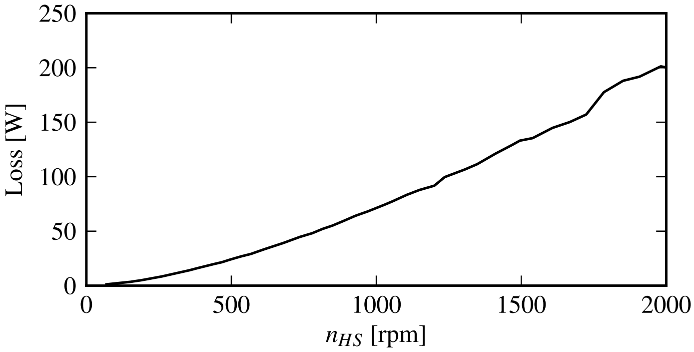

(a) Total no-load losses vs. sun gear speed.

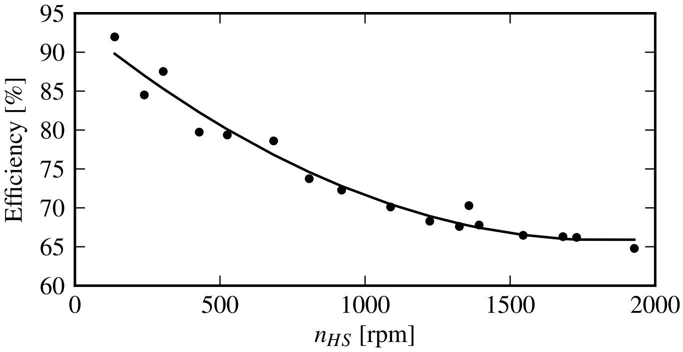

(b) Efficiency vs. sun gear speed at a constant load of 20 Nm.

Figure 7.12: Measured results of the original prototype.

from 2D FE analysis and measurements. Simulations were performed using *MagNet 7* from *Infolytica Corporation*.

The results of the simulations in this section are summarized in Fig. 7.14, to which reference will be made in each case.

The first step taken in the analysis of the end-effects was to do a 3D simulation of the ideal gear, i.e. without any structural parts in the model. The stall torque obtained in this way should be less than in a 2D simulation because of the various end-effects described in the previous chapter. The stall torque obtained from the 3D simulation was 46.6 Nm (Fig. 7.14: *3D, ideal case*), a drop of only 13% compared to the 2D value. From this, it appears that the torque reduction is not only caused by the unavoidable end-effects associated with the finite stack length, but also by the surrounding structural components which have an impact on the flux distribution in the gear.

One difference between the prototype and the ideal 3D model was that the modulator in the prototype was slightly extended. This was done in the belief that this would enhance the coupling between the sun and ring gears. Taking this extension of the modulator into account in the 3D model actually yielded a 5% lower stall torque of 44.2 Nm (Fig. 7.14: *3D, extended modulator*). While it is true that the extended modulator increases the total flux linkage of the magnets, the assumption that this improves the torque capability of the gear is incorrect. What is important to the torque capability is the coupling of the appropriate harmonics between the sun and ring gear. Extending the modulator reduces the reluctance of the leakage path, exacerbating the end-effects.

In order to determine the cause of the additional drop in stall torque, a 3D simulation including all the relevant structural components in the model was done. This simulation reported a stall torque of only 35.9 Nm (Fig. 7.14: *3D, support structure*). A flux density distribution plot produced by this simulation is shown in Fig. 7.13. It can be seen that flux leaks into the surrounding casing, especially where the modulator is supported.

Even with almost all the structural components included in the model, the simulated stall torque is still 9% higher than the measured result. This discrepancy is due to manufacturing tolerances, specifically the dimensions of the magnets, which are slightly smaller and unintentional skewing of the modulator. A simulation with the magnets within the tolerance specified and skewing the modulator by 10° electrical results in a stall torque of 33.5 Nm (Fig. 7.14: *3D, tolerances applied*), which is very close to the measured results.

7.3 Design improvements

The simplest modification that can be made to the design that will significantly reduce the end-effects is to replace the connecting ring of the modulator with a nonmagnetic one. Making only this modification results in a stall torque of 41.5 Nm (Fig. 7.14: *3D, modified 1*). Alternatively, if the supporting plate on the side connected to the modulator is replaced with a nonmagnetic one, the stall torque is 40.7 Nm (Fig. 7.14: *3D, modified 2*). In both cases, however, the stall

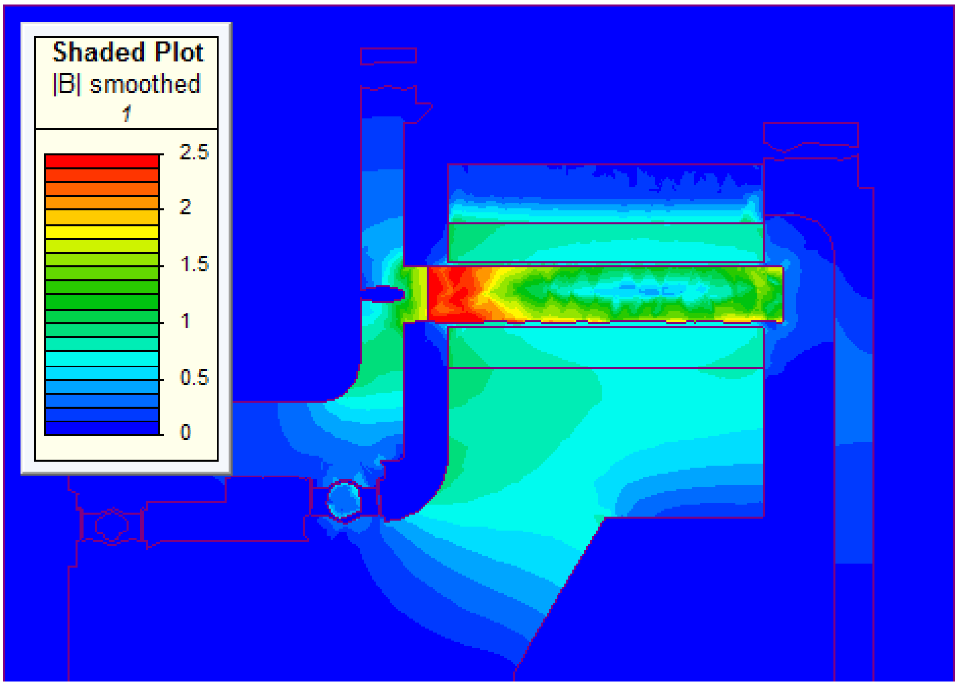

Figure 7.13: Flux density distribution plot clearly showing the severe leakage through the modulator supporting structure.

torque is still significantly lower than the ideal 3D case and it could be considered worthwhile to construct most of the casing from nonmagnetic material or to move the supporting casing further away from the active parts of the gear.

Based on the analysis, the prototype's casing and modulator were redesigned. The new casing was made from aluminium and the modulator was separated from the casing using a vesconite support ring. The improved modulator assembly is shown in Fig. 7.15.

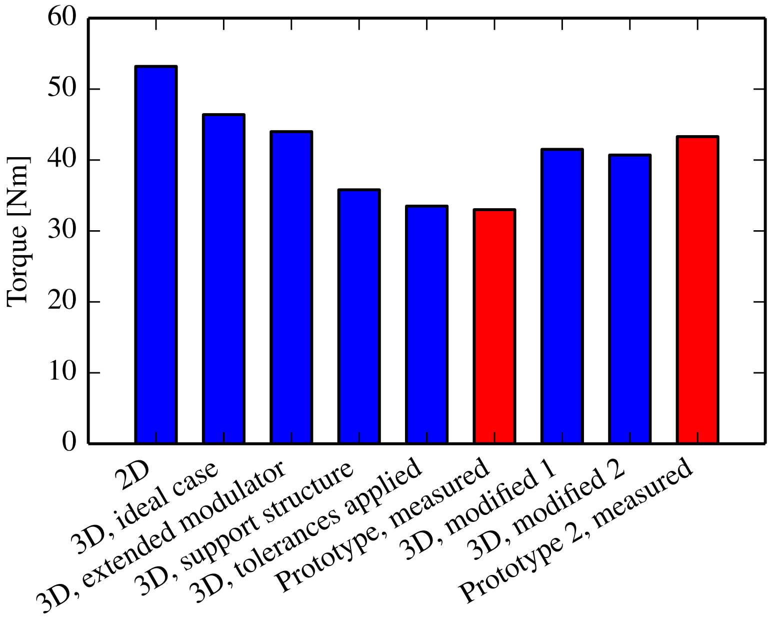

Figure 7.14: Stall torque of the ring gear from different simulations.

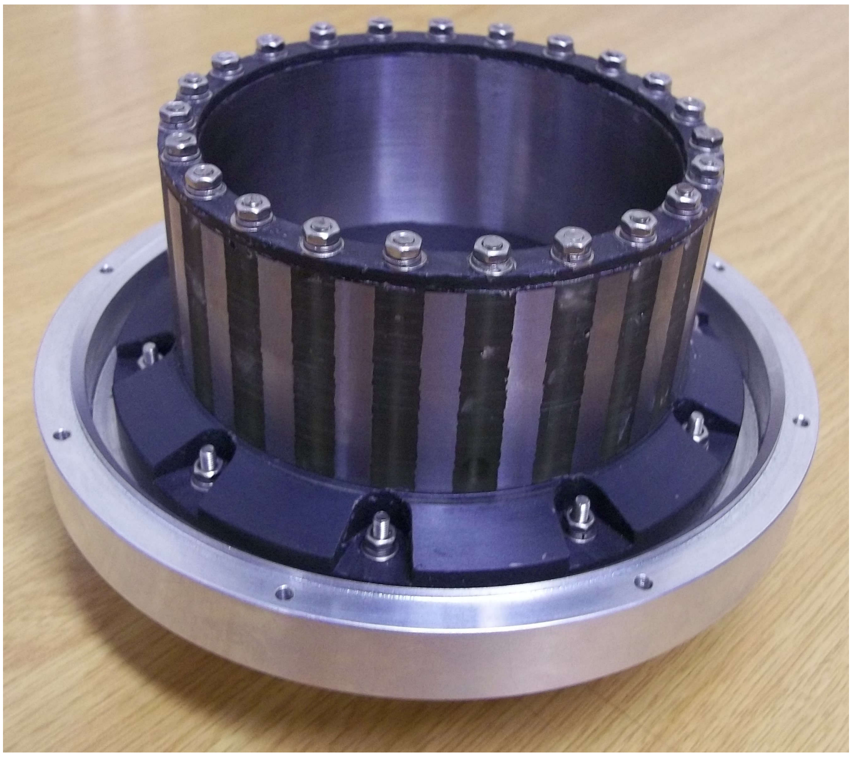

Figure 7.15: Improved modulator assembly with aluminium casing and vesconite support ring.

The new mechanical design resulted in a dramatic reduction in the losses generated in the gear. Fig. 7.16 shows a comparison of the no-load losses of the original and improved designs. The improved prototype's stall torque was measured as 43.3 Nm, compared to the original 33 Nm. These results confirm the findings that the casing and especially the modulator support structure were responsible for the poor performance of the original prototype.

An efficiency map of the gear is shown in Fig. 7.17. At high load, the gear achieved an efficiency above 94 % up to a speed of 1600 rpm on the high-speed side. Testing at higher speeds was not possible because of vibrations in the test bench.

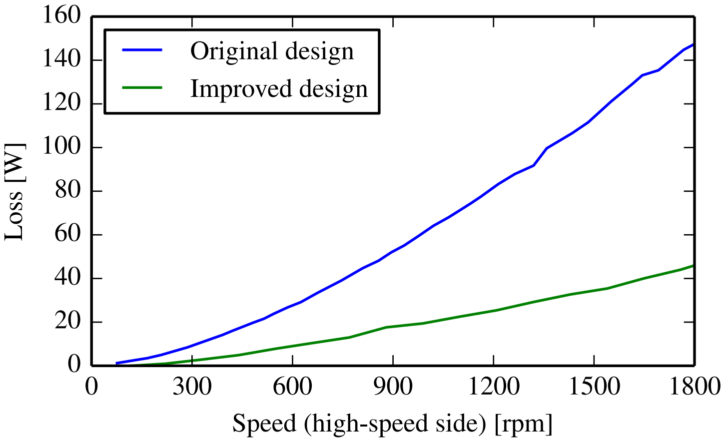

Figure 7.16: Reduction in no-load losses due to improvements in mechanical design.

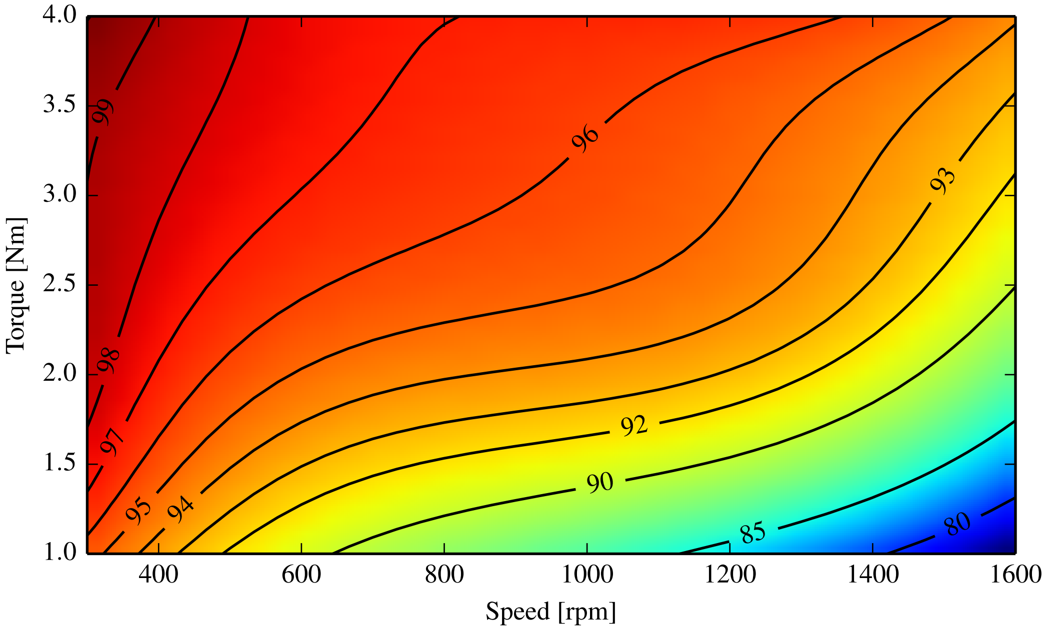

Figure 7.17: Efficiency map of the improved prototype.

7.4 Discussion

The evaluation of the design and end-effects of a prototype magnetic gear has been presented in this chapter. Introducing connecting bridges on the flux modulator helps simplify the construction and also dampens some potentially harmful harmonics in the sun gear air-gap.

Two-dimensional FE analysis promises very good performance and indicates that torque densities exceeding 100 $\mathrm{kNm/m^3}$ are practically achievable. However, end-effects have a significant detrimental impact on the stall torque capability of flux-modulated magnetic gears and must be taken into consideration if accurate performance estimates are to be obtained.

For flux-modulated magnetic gears it is vitally important that the flux modulator is magnetically insulated. It must be kept in place by components with low permeability, e.g. austenitic stainless steel, aluminium, epoxy or plastics. Materials with a low conductivity are also preferred because this limits the losses which can occur at higher speeds if any flux couples to the casing. Poor casing design can result in significant leakage flux. The leakage flux not only reduces the torque capability of the gear, but will also reduce the efficiency of the gear depending on the conductivity of the surrounding structural parts as well as the speed of operation. The vast improvement in the measured performance of the new prototype validates these findings. The design of a proper casing for a magnetic gear is not necessarily difficult or more costly, but care must be taken in the selection of materials to mitigate the impact of end-effects.

Chapter 8

Evaluation of a split MGM

In this chapter, the design and evaluation of a small split MGM is presented. The analysis and optimization methodology discussed in chapter 4 is employed to investigate several candidate designs. A thorough comparison between a coupled topology and a decoupled topology is made by comparing designs with several different stator slot and sun gear pole pair numbers, each optimized according to the specifications. A novel coupled topology is proposed which features a special structure for the sun gear. The structure reduces the magnet losses in this component and has an improved manufacturability for small machines. This novel coupled topology was also compared with a common coupled topology with PMs surface-mounted on the sun gear.

Based on the set of initial optimizations, a design was selected and attention was paid to the minimization of cogging torque. Torque ripple and voltage quality were also analyzed. A prototype was manufactured and experimentally evaluated. In general, the measured results are in good agreement with the simulations. However, the no-load losses are considerably higher than expected. The mechanical design of this prototype is identified as an area where further improvements are required.

8.1 Design constraints

The design constraints of the machine are listed in Table 8.1. These were chosen, not with a specific application in mind, but as a convenient set of specifications which can be used for the comparison of different machines. The outer diameter and stack length were chosen in order to limit the cost of prototyping. The air-gap length was fixed at a value which is practically achievable. The current density in the machine was fixed at $5\,\mathrm{A/mm^2}$ so that only natural air-cooling is required. A winding fill factor of 0.55 was assumed.

In addition, it was assumed that the machine would be controlled by a power electronic converter which allows some freedom in the choice of operating frequency.

8.2 Selection of the modulation set

For this design, it was decided to use a fixed (stationary) ring gear. In this case, the modulator is connected to the machine's shaft and the relationship between its angular velocity and the fundamental electrical operating frequency is

$$f_e = \frac{Q_m \omega_m}{2\pi} = \frac{Q_m n_{\text{rpm}}}{60} \tag{8.1}$$

with ω_m and n_{rpm} the mechanical angular velocity in [rad/s] and [rev/min] respectively. Note that this operating frequency is valid throughout the entire machine, although different components have different numbers of pole pairs and rotate at different speeds. From (8.1) it is clear that the operating frequency depends only on the number of modulator segments and the mechanical operating speed. Thus, for a given n_{rpm}, the frequency can be adjusted by an appropriate choice of Q_m, just as in conventional machines the frequency at a specific speed is determined by the number of poles. A compromise must be made between low operating frequency associated with low Q_m and high torque capability associated with high Q_m. Lower operating frequencies are desirable in terms of reduced core losses in the machine as well as less demanding specifications for power electronic converters used in the drive system.

The number of modulator segments was chosen as 36, which results in an operating frequency of 60 Hz at 100 rpm.

With Q_m fixed, the choice of the number of sun gear pole pairs p_s and the number of stator slots Q_s remain. These were not included in the optimization process because this would dramatically increase the computational cost of an optimization. A few possible combinations were investigated, based on the following criteria

- High torque density
- Short end-windings
- Low cogging torque between the stator and the sun gear

Short end-windings are highly desirable, not only in terms of copper loss but also because of the impact on the mechanical design of this machine, as discussed in section 8.5. One way in which the length of the end-windings can be minimized is by using a double-layer non-overlap winding together with a high number of slots.

It was shown in [96] that, for a given Q_m, a value of p_s exists which maximizes the torque capability of the magnetic gear. In the case of magnetically geared machines, p_s also has an influence on the stator torque requirement.

Table 8.1: Design specifications

Parameter	**Value**
Outer diameter	140 mm
Stack length	50 mm
Air-gap length	0.7 mm
Current density	5 A/mm^2
Winding fill factor	0.55

Taking the above arguments into consideration, the selected pole/slot combinations with winding factors [98] listed in Table 8.2 were evaluated for both the coupled and decoupled configurations. Sun gear pole counts below 10 were not considered because of the higher cogging torque and longer end-windings. Designs with 12 poles on the sun gear were also not considered due to two undesirable attributes of this design. Firstly, the cogging torque of this combination was expected to be higher due to the lower LCM between the number of poles and slots. Secondly, the torque ripple in the magnetic gear was expected to be higher because 6 poles on the sun gear would result in an integer gear ratio. It was shown in [99] that fractional gear ratios offer superior torque quality.

8.3 Design optimization

8.3.1 Methodology

With Q_m fixed and possible combinations of sun gear poles and stator slots identified, the optimization of the machine was carried out. The optimization problem was formulated as a constrained optimization

$$\text{Maximize:} \quad F(\mathbf{X}) = \text{Torque } T_m/\text{active mass} \tag{8.2}$$

$$\text{Subject to:} \quad t_{rm} > 0.6t_{sm} \quad \text{or} \quad t_{rm} > 0.6t_{smo} \tag{8.3}$$

$$\gamma_i > 0.8 \tag{8.4}$$

with t_{sm} and t_{smo} the thickness of the sun gear magnets for the coupled and decoupled configurations respectively and t_{rm} the thickness of the ring gear magnets. Constraint (8.3) is enforced to mitigate the risk of demagnetizing the ring gear magnets due to a highly uneven distribution of magnetic material [96].

The constraint (8.4) states that the stator load factor (defined in section 4.3.3) must be greater than 0.8. This choice leaves a 20 % operational margin between the gear's rated operating torque and its stall torque. It implies that the stator will be rated to operate up to 80 % of the gear's stall torque.

The analysis used in the optimization is based on a single point FE analysis where the torque transferred by the gear is at its maximum and the current angle is 90°. For a detailed description of the calculation of the various performance measures, see chapter 4.

Table 8.2: Winding factors for the candidate pole slot combinations

Slots/Poles	10	14	16
12	0.933	0.933	0.866
18	-	0.902	0.945
21	-	0.866	0.89

8.3.2 Design variables

The design variables used in the optimizations are illustrated in Fig. 8.1. The only difference between the coupled and the decoupled configurations is the structure of the sun gear. For all other parts, the design variables used for optimization are the same. In the final optimization, the modulator thickness t_m was restricted to a minimum of 5 mm, as explained in section 8.5.

8.3.3 Optimum designs

The optimal torque per active mass achieved for different pole/slot combinations is given in Tables 8.3 and 8.4 for the coupled and decoupled configurations respectively. It is worth noting that the winding factor alone does not give an accurate indication of which pole/slot combinations perform best. Although a higher number of poles generally results in a higher torque capability of the electrical machine component of an MGM, the torque required to achieve a specific stator load factor also increases, sometimes more than the electrical machine's torque capability. This can explain why most designs with lower pole counts performed better. Also, in both the coupled and the decoupled cases, the $p_s = 8$, $Q_s = 12$ combination performed better than the $p_s = 8$, $Q_s = 18$ combination, despite the latter having a significantly better winding factor. These results support the finding in [100] that the winding factor does not always give an accurate indication of machine performance.

In both configurations, the best results were obtained with $p_s = 5$ and $Q_s = 12$. The layouts of these designs are illustrated in Fig. 8.2. The coupled configuration was selected for further design refinement because it obtained the highest torque per active mass.

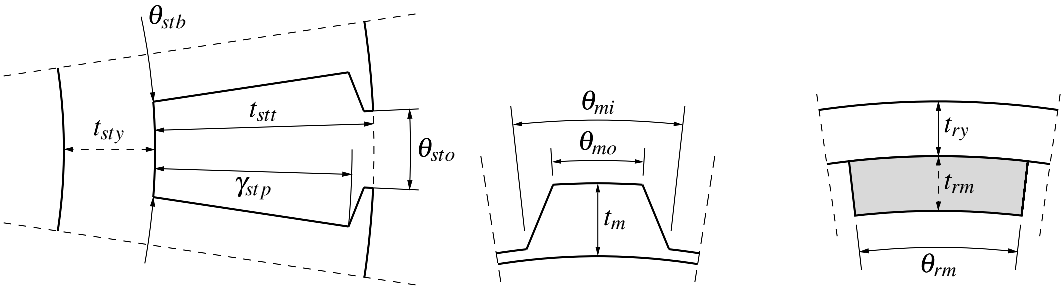

(a) Stator. (b) Modulator. (c) Ring gear.

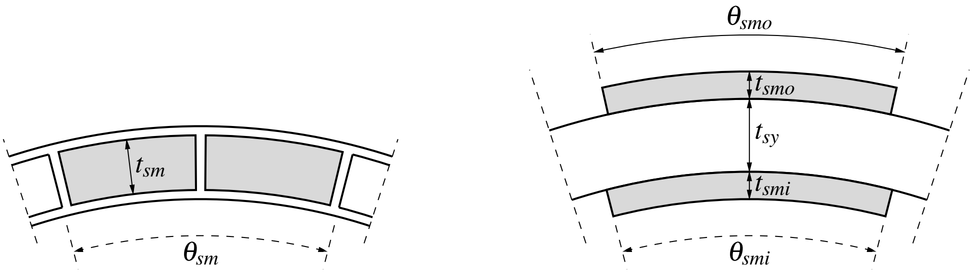

(d) Sun gear with laminated magnet carrier. (e) Sun gear with surface mounted magnets.

Figure 8.1: Design variables for various components of the magnetically geared PM machine.

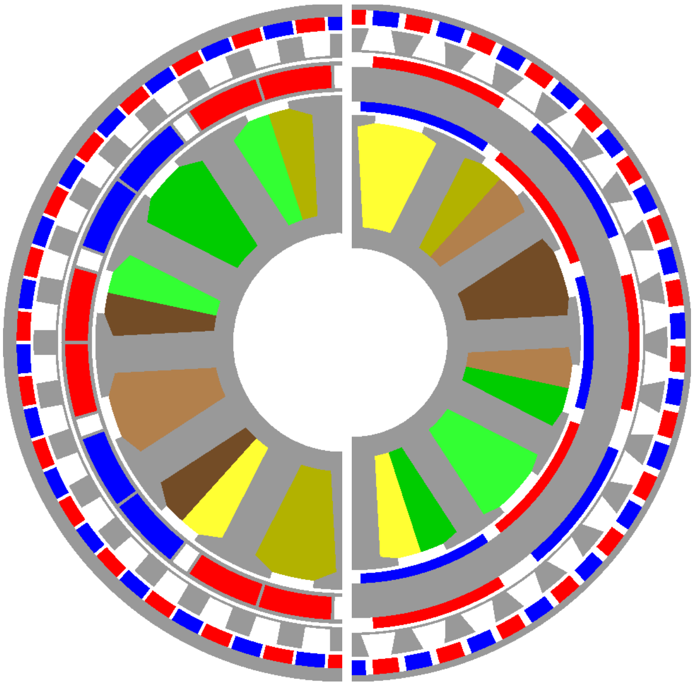

(a) Coupled (b) Decoupled

Figure 8.2: Layouts of the optimal designs.

Table 8.3: Optimal torque per active mass: coupled configuration

Slots/Pole pairs	5	7	8
12	**21.2**	19.5	17.2
18	-	16.6	15.6
21	-	15.5	14.4

* Values given in [Nm/kg]

Table 8.4: Optimal torque per active mass: decoupled configuration

Slots/Pole pairs	5	7	8
12	17.9	17.9	16.3
18	-	13.8	14.3
21	-	13.4	12.8

* Values given in [Nm/kg]

8.3.4 Cogging torque minimization

Cogging torque is undesirable because it is a source of noise and vibration in electric machinery. In some applications, for example wind energy, it can also have an effect on the self-starting capability of a wind turbine. For a magnetically geared machine, it is especially important from a start-up perspective to minimize the synchronous cogging torque on the sun gear, since the true cogging torque is easily dominated by the first term in (4.19).

In order to minimize cogging torque, several techniques can be applied [101]. For this particular design, it was possible to reduce the cogging effects to a satisfactory level by merely varying the slot opening pitch.

Fig. 8.3 shows the effect that the slot opening has on the amplitude of the sun gear synchronous cogging torque. The sun gear synchronous cogging torque waveform can be seen in Fig. 8.4. The true cogging torque is shown in Fig. 8.5. Note that the true cogging torque waveform is basically the sun gear synchronous cogging torque scaled by the gear ratio.

8.3.5 Comparison with surface mounted design

In addition to the coupled topology with the magnet carrier, a coupled topology with double sided surface mounted magnets was also investigated. The two coupled topologies are illustrated in Fig. 8.6. The surface mounted topology was also optimized for the case with $p_s = 5$ and

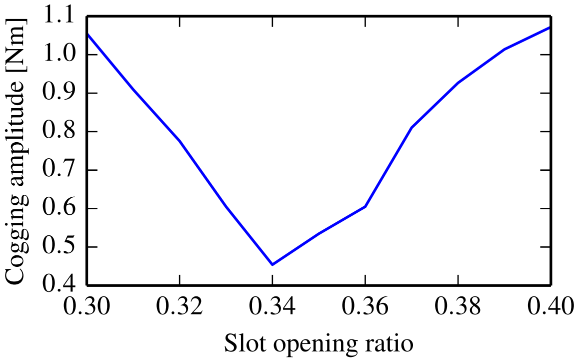

Figure 8.3: Effect of the slot opening on the amplitude of the cogging torque.

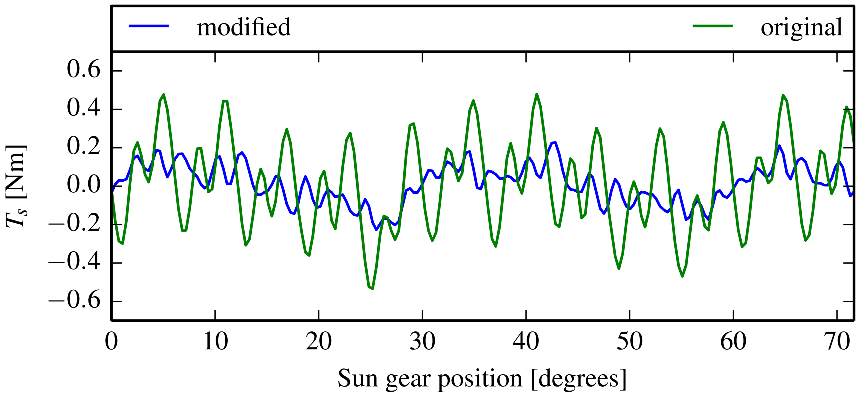

Figure 8.4: Comparison of the original and reduced synchronous cogging torque on the sun gear.

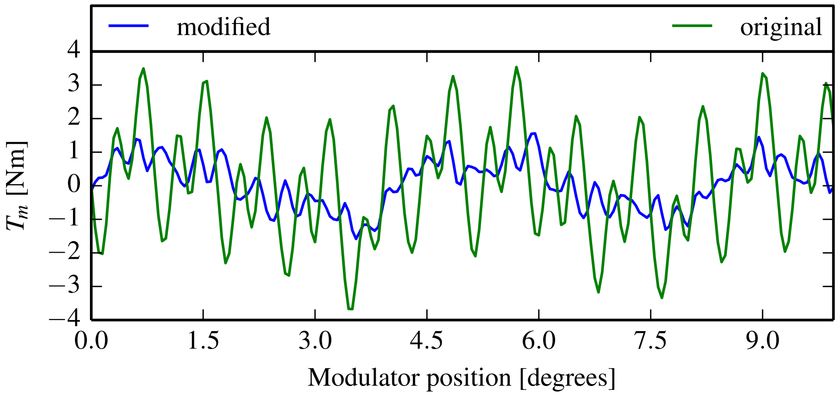

Figure 8.5: Comparison of the original and reduced true cogging torque on the modulator.

$Q_m = 12$, using an approach similar to the one described in section 8.3.1.

In Table 8.5 a few important differences between the two optimum designs are listed. The losses were calculated using transient 2D FEA, with the machine operating at rated current and 200 rpm (modulator speed), corresponding to an operating frequency of 120 Hz. The eddy current loss generated in the sun gear magnets is significantly higher in the surface mounted case. Note that the stator winding generates a strong sub-harmonic which contributes to these losses, along with slotting effects. The majority of the losses occur in the inner magnets (stator side) of the surface mounted configuration. The magnet carrier effectively shields the sun gear magnets from harmful flux pulsations. The core loss in the sun gear laminations is slightly higher in the configuration with the magnet carrier, but the impact is small compared to the difference

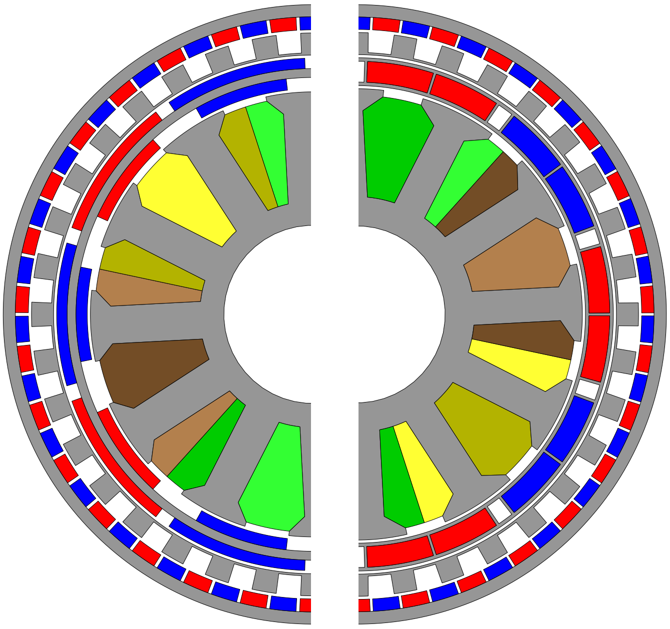

(a) Yoke with surface mounted magnets on both sides.

(b) Laminated carrier securing magnets in cavities.

Figure 8.6: Cross section of two coupled MGMs with different sun gear configurations.

in the magnet eddy current loss. The surface mounted configuration achieved a slightly higher stall torque (calculated with 3D FEA). Note that the configuration with the surface mounted magnets is idealized in the sense that no provision is made for a retaining can, which may be required for the outer magnets on the sun gear. This could lead to a drop in the achievable stall torque for the surface mounted configuration. The magnet carrier eliminates the need for any additional retaining cans or magnet fixtures.

In this case, another issue with the surface mounted design was that the manufacturer could not supply magnets thin enough for the design. If thicker magnets are used, the space available for the stator is reduced and the machine's performance is compromised. Although this was an important consideration for the present design, this issue should not present itself in larger machines.

8.3.6 Final design

The dimensions of the final design are given in Table 8.6. These were slightly modified from the optimal values given by the optimization without having a significant impact on performance. The final design was also evaluated using 3D FE analysis since it has been shown that 3D effects can be significant in magnetic gears [89, 90, 92, 91, 102]. In Table 8.7, the torque capability results from 3D FE analysis as well as the active mass of the various materials used are listed. The machine's rated torque is calculated as 85 % of the machine's stall torque. This leaves a 15 % operational margin. The purpose of this margin is to prevent the gear from slipping under load fluctuations. The required margin is very application specific and could in practice be optimized for specific load characteristics.

8.4 Performance analysis

In this section, the torque quality and the voltage quality of the final design are analyzed and discussed.

8.4.1 Torque quality

Fig. 8.7 shows the waveform of T_m over one electrical period with the machine operating at rated torque. Clearly, the torque on this component is very smooth.

Table 8.5: Comparison between different sun gear topologies

Parameter	**Magnet carrier**	**Surface mounted magnets**
Sun gear magnet loss	2.45 W	26.91 W
Sun gear core loss*	3.14 W	1.28 W
Total loss	88.7 W	112.7 W
Stall torque	88.2 Nm	94.4 Nm

* Assuming a laminated carrier and a laminated yoke in the surface mounted configuration.

Table 8.6: Optimal machine design parameters

Parameter	**Value**
Sun gear magnet pitch	0.9 [fraction of pole pitch]
Ring gear magnet pitch	0.9 [fraction of pole pitch]
Inner modulator pitch θ_{mi}	0.5 [fraction of segment pitch]
Outer modulator pitch θ_{mo}	0.47 [fraction of segment pitch]
Stator yoke thickness	6.6 mm
Stator tooth thickness	24.4 mm
Sun gear magnet thickness t_{sm}	4.7 mm
Sun gear ring thickness	0.8 mm
Sun gear rib thickness	0.6 mm
Modulator thickness t_m	5 mm
Modulator bridge thickness	0.5 mm
Ring gear magnet thickness t_{rm}	2.8 mm
Ring gear yoke thickness	2.8 mm
Slot base angle θ_{stb}	0.45 [fraction of slot pitch]
Slot opening angle θ_{sto}	0.34 [fraction of slot pitch]
Slot tip γ_{stp}	0.85 [fraction of tooth thickness]
Number of sun gear pole pairs p_s	5
Number of modulator segments Q_m	36
Number of ring gear pole pairs p_r	31
Number of slots Q_s	12
Gear ratio	7.2

Table 8.7: Optimal machine design characteristics

Parameter	**Value**
Gear stall torque	88.2 Nm
Rated torque	75 Nm
Rated stator torque	10.4 Nm
Torque density* (stall torque)	114.6 kNm/m^3
Torque density* (rated torque)	97.5 kNm/m^3
Rated copper loss†	55 W
Magnet mass	0.90 kg
Copper mass†	1.17 kg
Steel mass	2.44 kg
Total mass	4.51 kg
Rated torque per active mass	16.6 Nm/kg

* Excluding end-winding region

† Including end-winding region

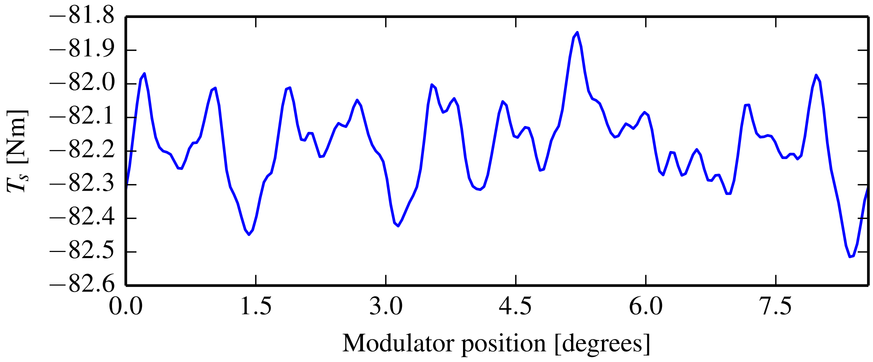

Figure 8.7: Torque ripple on the modulator at rated operating point.

Fig. 8.8 shows the torque ripple on the sun gear over one electrical period, also at the machine's rated operating torque. Note that the average torque on the sun gear is zero, resulting in steady-state operation. The torque ripple on the sun gear is relatively large at about 10% of rated T_i.

8.4.2 Voltage quality

Fig. 8.9 shows the simulated no load phase and line voltage waveforms respectively, assuming sinusoidal currents. Fig 8.10 shows the harmonics present in the voltages under no load and full load conditions. From Fig 8.10, it is clear that a large third harmonic, as well as a ninth harmonic, is present. These harmonics are effectively cancelled when line to line voltages are used. It can also be seen that under full load conditions, a 13th order harmonic is present. This is due to the use of the non-overlap winding layout. Considering line voltages, the total harmonic distortion under no load and full load conditions is 2% and 3.3% respectively.

8.5 Mechanical design

8.5.1 Conceptual design

The machine under discussion has four concentric parts, of which two rotate at different speeds. Thus, it is relatively complex to construct compared to more conventional electric machines. The structural mass will be larger compared to that of a conventional PM machine of similar size.

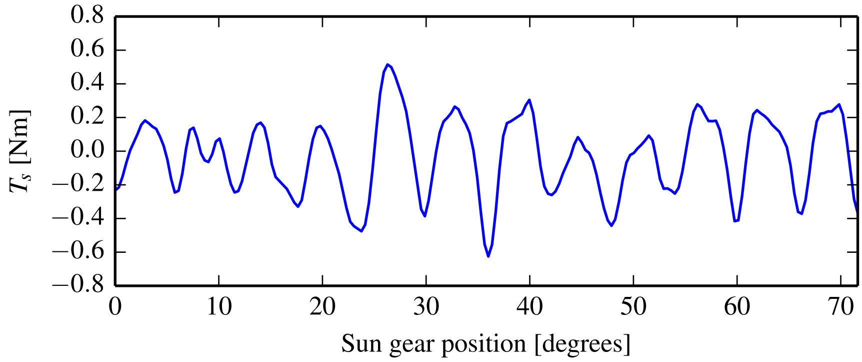

Figure 8.8: Torque ripple on the sun gear at rated operating point.

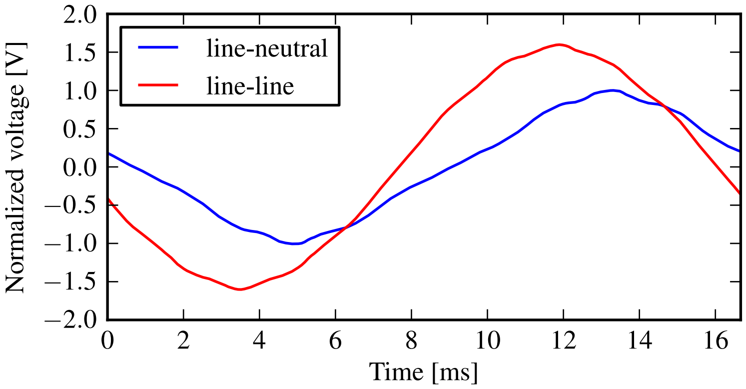

Figure 8.9: Normalized terminal voltages.

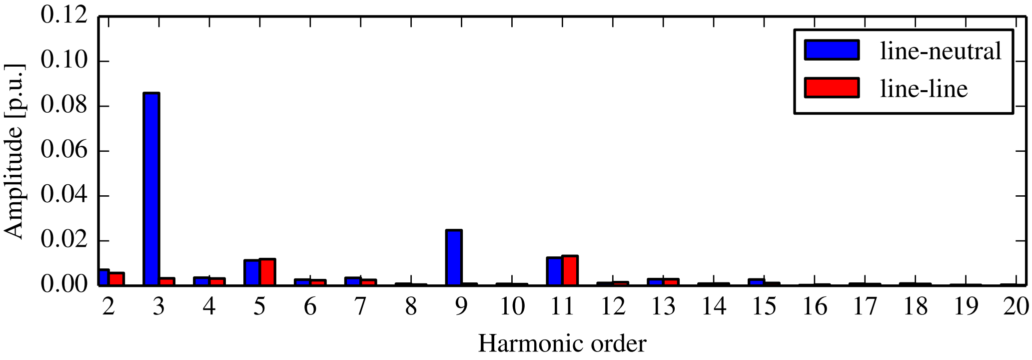

(a) No load

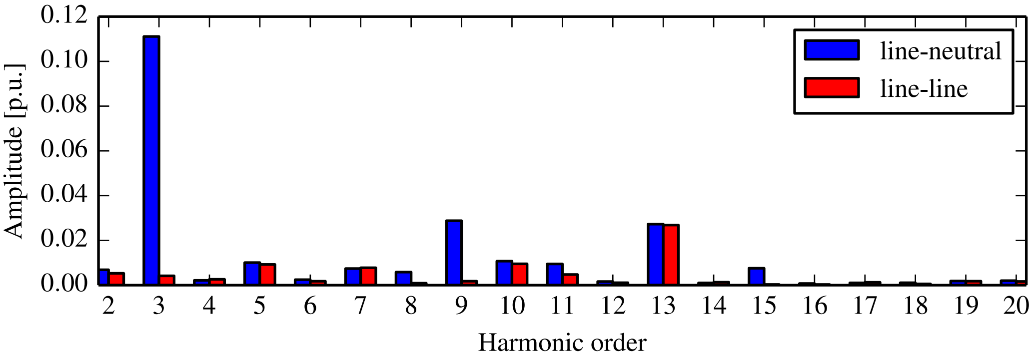

(b) Full load

Figure 8.10: Voltage harmonics.

However, this additional complexity is not necessarily prohibitive. In this section, a complete mechanical design which is relatively simple and requires only a little increase in structural mass will be discussed.

Fig. 8.11 illustrates simplified longitudinal section diagrams of the supporting structure of a conventional fractional slot PM machine and the proposed structure of the magnetically geared PM machine under discussion. The magnetically geared machine requires two additional bearings and one additional supporting plate assembly for the sun gear. The stator requires virtually no additional support structure because it can be mounted directly on the central hub.

All the supporting plates must be spaced away from the main stack in order to leave room for the end-windings. This is illustrated in Fig. 8.12 which shows a detailed longitudinal section view of the mechanical design of the machine. For this reason, the space required for the end-windings should be minimized.

Both the modulator and the sun gear are supported on threaded stainless steel rods which are glued in place using epoxy resin. This construction technique requires that these components be thick enough in order for rods of sufficient diameter to be inserted. The sun gear, modulator and ring gear are only supported on one side, which requires that the supporting structure, as well as the components themselves, be stiff. In the present case, the minimum modulator thickness was restricted to 5 mm in order to allow 3 mm supporting rods to be fitted in the slots. Finite-element analysis indicated that higher torque capability could be realized with a thinner modulator, consistent with the findings presented in [96].

The construction of the surface mounted configuration differs only with respect to the sun gear. It may be possible to use a solid (non-laminated) yoke for the sun gear, which simplifies the structure, but this will result in higher losses. Whether the yoke is laminated or not, its thickness is likely to be limited by mechanical constraints, not electromagnetic design.

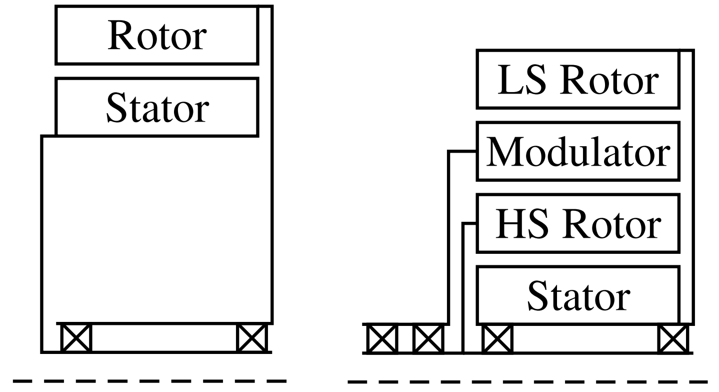

(a) Conventional fractional slot machine

(b) Magnetically geared machine with an inner stator

Figure 8.11: Simplified representations of the mechanical support structure.

8.5.2 Prototype fabrication

Fig. 8.12 shows a detailed longitudinal section view of the original mechanical design of the prototype. The design was modified at a later stage in order to increase the stiffness of the various component assemblies. Some stages of manufacturing process are illustrated in Fig. 8.13. The stator's non-overlap winding was wound directly onto the teeth – a tedious process. The design could also have been realized with a stator constructed using a separate teeth and yoke structure. A winding fill factor of 0.49 was achieved, which is slightly lower than the value used during the optimization. Information related to the winding is given in Table 8.8

The sun gear was manufactured using a laminated carrier into which magnets were inserted. This assembly was fixed to a supporting plate by stainless steel rods that were inserted in mounting channels between the magnets. Once the rods were inserted, these channels were filled with resin. The modulator was constructed using a similar approach. Rods connected to a side plate were inserted in the slots between the modulator teeth, and the cavities were filled with resin. The ring gear magnets were accurately located by small protrusion on the inner surface of the ring gear yoke and glued in place. All laminations were laser-cut, the material used was M470-50A silicon steel.

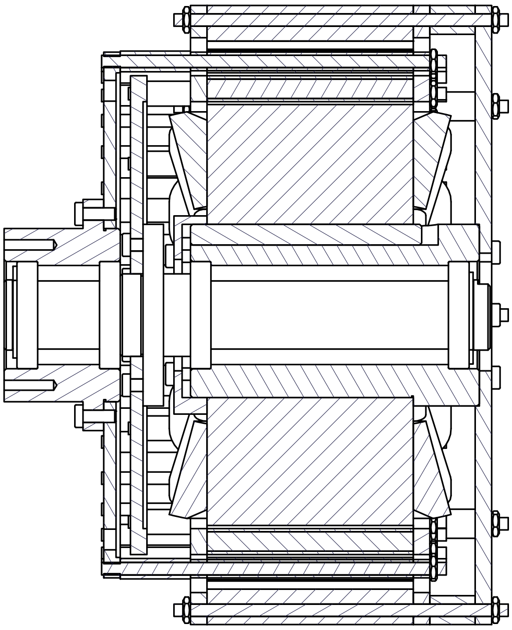

Figure 8.12: Longitudinal section view of the original mechanical design.

Table 8.8: Winding information

Parameter	Value
Wire diameter	0.63 mm
Phase resistance R_ϕ	6.3 Ω
Number of turns per coil	212
Fill factor	0.49

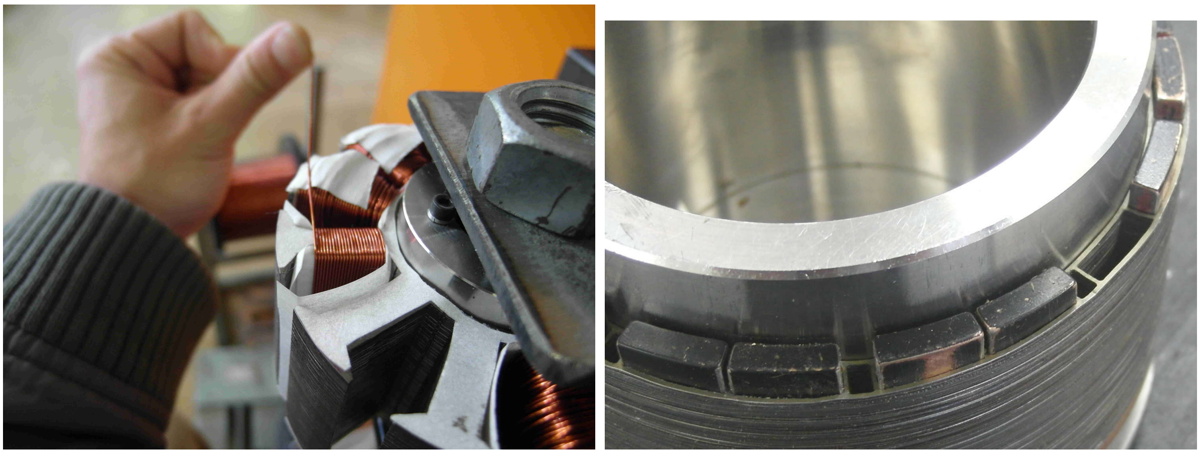

(a) Winding process.

(b) Partially completed sun gear on the mould. Empty mounting channels, magnets and an empty magnet slot are visible.

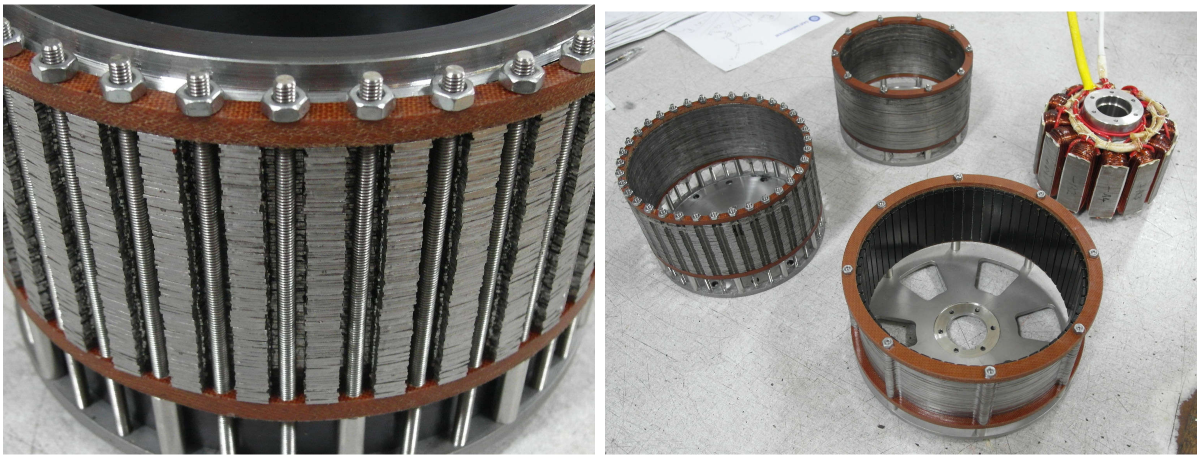

(c) Modulator support rods. Cavities to be filled with epoxy.

(d) Completed components ready for assembly.

Figure 8.13: Fabrication of the prototype.

Some problems were experienced in the manufacturing process and the prototype's rotors run with noticeably eccentricity. At certain angular positions, the sun gear makes light contact with the stator. The mechanical design of the prototype and the manufacturing process are areas where significant improvements can be made in future.

8.6 Performance evaluation

Fig. 8.14 shows the machine on the test bench. A servo motor connected to a gearbox was used to drive the prototype which operated as a generator. The prototype was connected to a resistive load through an autotransformer, which provided a simple method of adjusting the load. A torque sensor measured the input power delivered to the modulator. The generated output power was measured with an oscilloscope as well as two wattmeters.

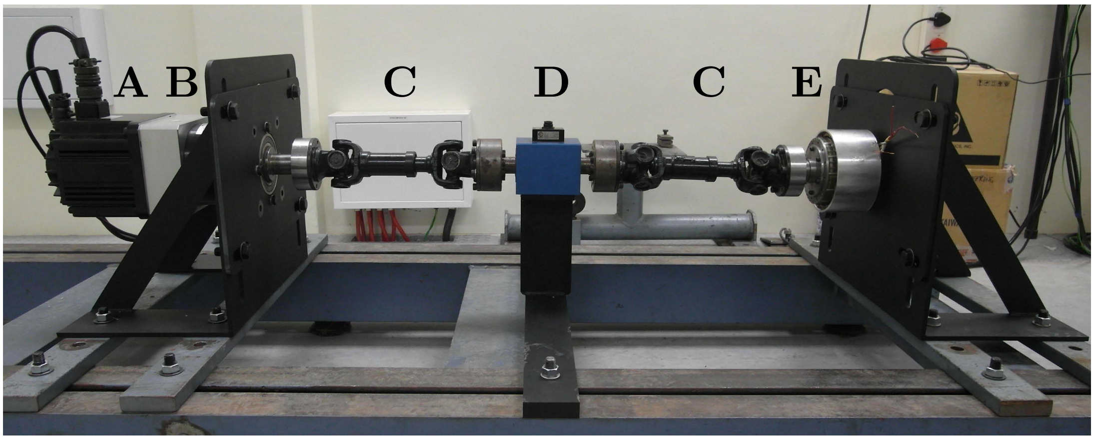

Figure 8.14: Setup used to test the prototype. A: servo motor, B: gearbox, C: prop shaft, D: torque sensor, E: MGM prototype

8.6.1 Stall torque test

The gear's stall torque was evaluated by locking the sun gear and rotating the modulator slowly. Fig. 8.15 shows a waveform of the torque on the modulator during this test. The peak measured torque was 82 Nm (107 kNm/m^3) whilst the simulated stall torque was 88 Nm (115 kNm/m^3). The prototype achieved 93 % of its designed stall torque rating.

8.6.2 No-load tests

Fig. 8.16 shows a comparison of the magnitude of the simulated and measured no-load line voltages up to a speed of 200 rpm. The measured voltage is about 7 % lower than predicted by the 3D finite element model.

A comparison of the simulated (2D FEA) and measured no-load voltage waveforms at 150 rpm (modulator shaft) is shown in Fig. 8.17. Besides the small difference in amplitude, the waveforms are in excellent agreement.

The measured no-load losses are shown in Fig. 8.18, along with results from transient 2D FEA. The total loss at 150 rpm is almost 100 W, while the loss calculated with transient 2D FEA was only 30 W. The simulated loss does not include losses generated by windage and bearing

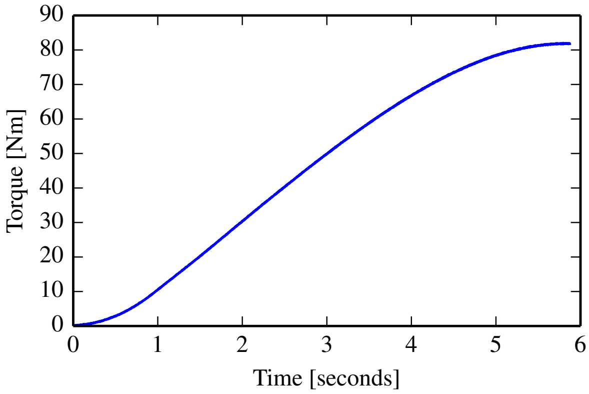

Figure 8.15: Measurement of the stall torque.

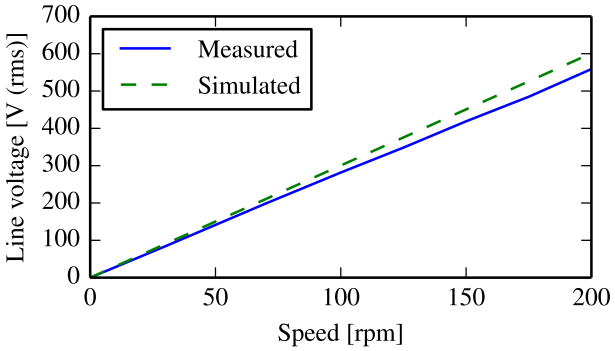

Figure 8.16: Measured no-load line voltage versus speed.

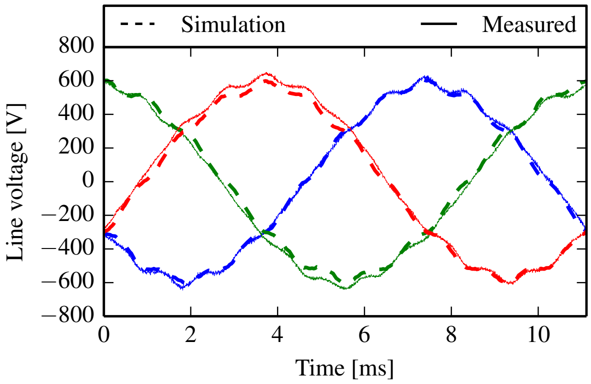

Figure 8.17: Comparison of simulated and measured no-load line voltage waveforms.

friction. Although core loss is frequently underestimated by FEA, the high measured loss is largely attributed to factors which are not accounted for in the simulation. As mentioned in section 8.5, the sun gear makes contact with the stator periodically, generating excess friction. Some additional eddy currents can be generated in the stainless steel rods supporting the sun gear and the modulator, even though care was taken to isolate the rods from each other. The rods were not included in the finite element model. Flux leaking to the supporting structure can also cause eddy current losses, but the design was made to limit this. Non-ferrous materials were used for the supporting structure and non-conducting spacers were used in areas in close proximity to the active stack. Despite the efforts to limit all these losses, the impact on the performance of the machine is clearly significant. However, these results need not be discouraging, as it is expected that the no-load losses can be greatly reduced through refinements in the design, especially on the mechanical side. Furthermore, the no-load losses were not considered in the optimization process.

8.6.3 Load tests

The machine was tested in generator mode over a speed range of 30 – 175 rpm with an input torque ranging between 10 and 60 Nm. The speed was accurately controlled by the driving servo motor. The load on the machine was varied by adjusting the voltage applied to a resistor bank using an autotransformer, which was fed by the machine. An efficiency map of the machine over this operating range is illustrated in Fig. 8.19. An efficiency above 85 % is achieved over a wide

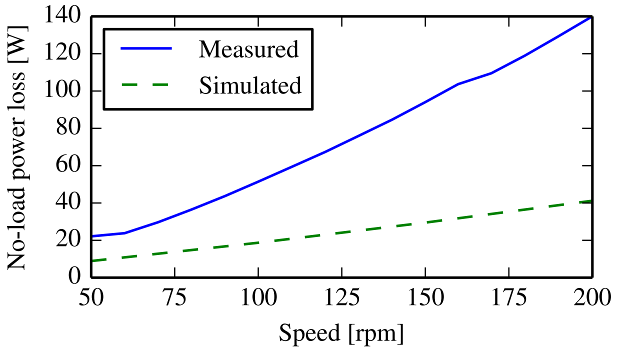

Figure 8.18: No load loss curve.

operational range. Considering the extra losses incurred due to manufacturing problems, the result is satisfactory. All tests were conducted at a power factor of 0.9 and above.

8.6.4 Operating point analysis

In order to verify that the machine's operating points can be simulated accurately, a specific operating point was analyzed in greater depth. Measurements at the considered operating point are listed in Table 8.9. The voltage, current and power factor uniquely define the load. The load angle of the magnetic gear δ_g could not be measured. This measurement would require two position sensors, one for the modulator and one for the sun gear.

The predicted values in the table were obtained using the method described in section 4.5. The mappings of the flux linkages and torques were calculated using 3D FEA. A reasonable level of accuracy was achieved, considering the number of stages at which errors were introduced.

The prototype's maximum operational range with a line voltage limit of 600 V and a phase current limit of 1.3 A is shown in Fig. 8.20. Plots such as these can aid in the selection of

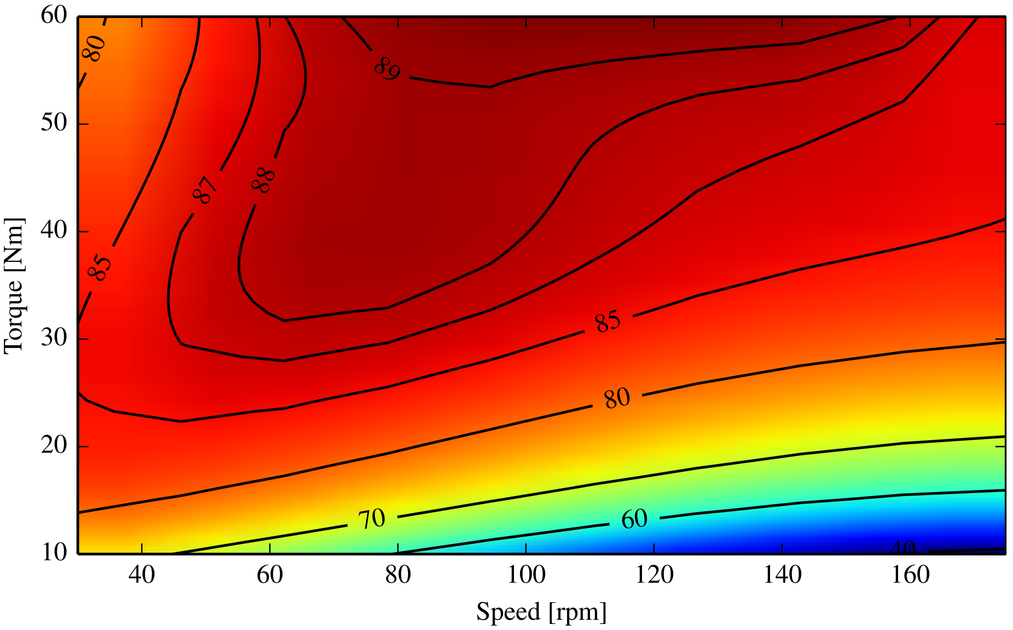

Figure 8.19: Efficiency map of the prototype operating in generator mode at a power factor ≥ 0.9.

Table 8.9: Comparison of measured and predicted operating point

	Measured	**Predicted**	**Error [%]**
Torque T_m	59.9 Nm	65.1 Nm	8.7
Speed n_m	150 rpm	150 rpm	0
Line voltage	357 V	374 V	4.8
Phase current	1.43 A	1.50 A	4.9
Input power	940 W	1 023 W	8.8
Output power	835 W	915 W	9.6
Power factor	0.94	0.94	0
Load	$136 + j48\,\Omega$	$136 + j48\,\Omega$	0
Efficiency	88.9 %	89.4 %	0.6
Load angle δ_g	n.a.	-55.5°	n.a.

appropriate ratings for an inverter used to control the machine.

8.7 Discussion

In this chapter, the design and evaluation of prototype magnetically geared machine with a novel structure for the sun gear were discussed. The analysis and optimization methodology described in chapter 4 was employed with good success.

Although some difficulties were experienced in the manufacturing process, the prototype shows good performance and achieved 93 % of its stall torque rating, corresponding to an active volume torque density of 107 kNm/m^3. The mechanical construction of the magnetically geared machine,

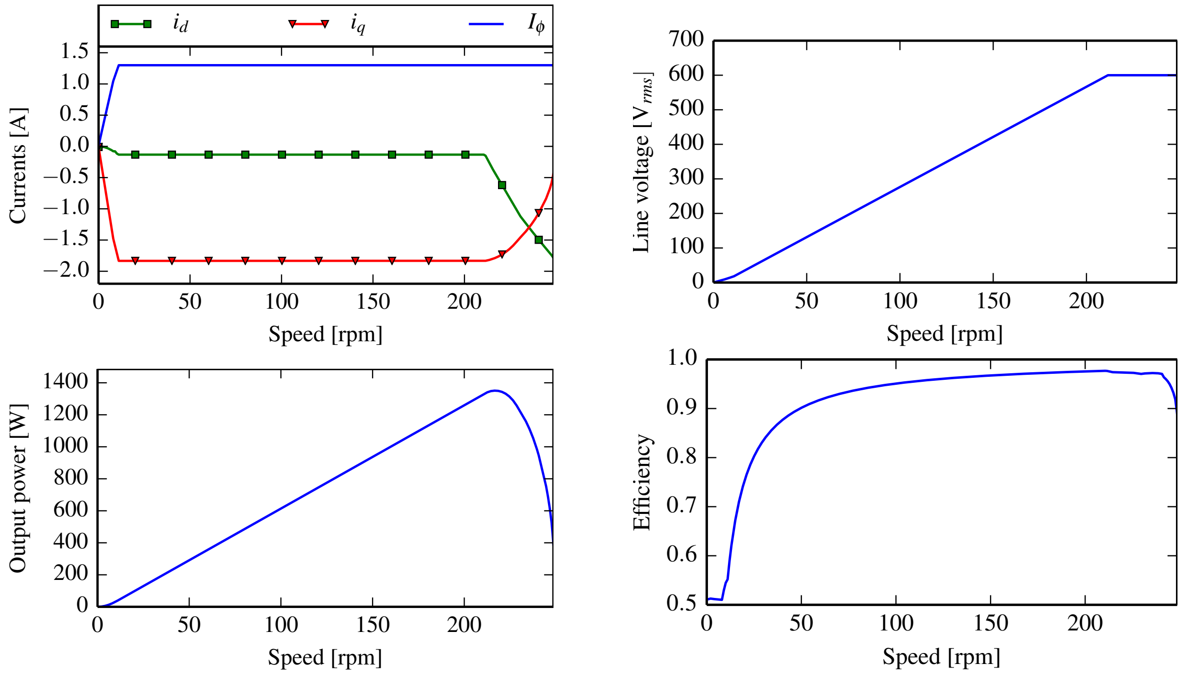

Figure 8.20: Maximum output power characteristics with a line voltage limit of 600 V and a phase current limit of 1.3 A.

although more complex than that of conventional machines, is not an insurmountable obstacle.

It is expected that a reduction in the no-load losses can be achieved with improvements in the mechanical design of the machine. The calculation of these losses can also be included in the optimization process in future work, leading to further improvements in the design.

The work described in this chapter supports existing claims of the exceptionally high torque density that can be achieved with magnetically geared machines. These machines have great potential in low-speed, high-torque applications.

Chapter 9

Evaluation of a ring-stator MGM

In this chapter, a second magnetically geared machine is evaluated. This machine can be classified as a ring-stator machine, described in chapter 3. As mentioned, the primary difference between this machine and the machine from chapter 8 is that the stator is placed on the outer periphery and that the ring gear magnets are mounted on the inner surface of the stator. This reduces the number of air-gaps from three to two while still retaining the operating principles of a magnetically geared machine.

The specifications for this machine were chosen with the aim of allowing a reasonable comparison with the split MGM from the previous chapter to be made. A similar approach to the design was taken, as reported in this chapter. A more thorough description of the design and evaluation of this machine can be found in [103].

9.1 Design constraints

The constraints placed on the split MGM were also applied to the ring-stator MGM. These constraints are listed in Table 8.1.

In this machine, the windings are situated close to the outer periphery of the machine, which enhances the heat dissipation of the machine. However, the ring gear magnets are surface mounted on the inner periphery of the stator, in close proximity to the windings. Care must be taken that the heat generated in the winding does not raise the temperature of the magnets to the extent that they become prone to demagnetization. Detailed thermal analysis is beyond the scope of this project, but it is noted that the thermal effects on the magnets due to the windings can be of great importance in this machine. In this study, the current density was limited to $5\,\mathrm{A/mm^2}$, as for the split MGM.

9.2 Design optimization

A cross section of the exact ring-stator topology is shown in Fig. 9.1. Closed slots are used for the stator. This provides a solid yoke-like surface onto which the ring gear magnets can be glued. The geometric design variables for the machine are illustrated in Fig. 9.2.

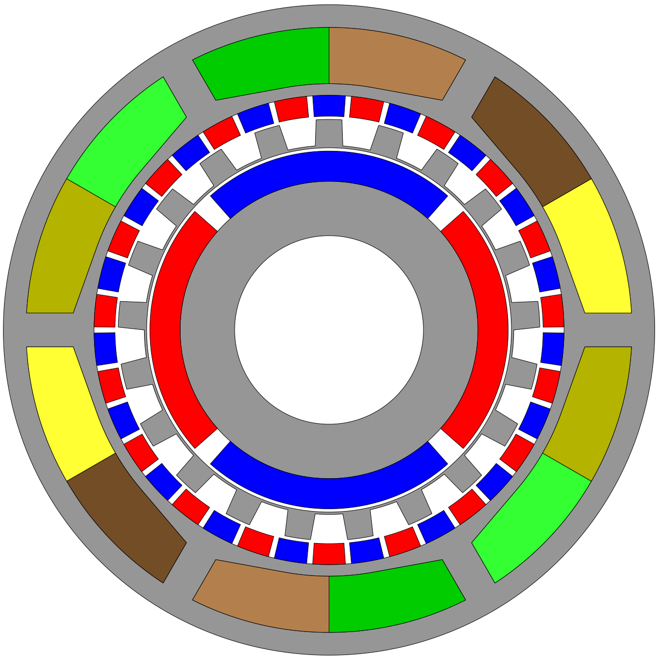

Figure 9.1: Cross section of the optimized ring-stator MGM topology.

The optimization problem was formulated as

$$\text{Maximize:} \quad F(\mathbf{X}) = \text{Torque } T_m/\text{active mass} \tag{9.1}$$

$$\text{Subject to:} \quad t_{sm} < 1.5t_{rm} \tag{9.2}$$

$$\gamma_i > 0.8 \tag{9.3}$$

with t_{sm} and t_{rm} the thicknesses of the sun and ring gear magnets, respectively. The first constraint was enforced in order to protect the ring gear magnets from demagnetization. The second constraint enforces the same stator load factor (see section 4.3.3) as for the split MGM.

9.3 Winding, pole and slot number selection

The ring-stator magnetically geared machines can make use of several possible winding configurations, including overlap and non-overlap windings. For this design a non-overlap winding was selected because these windings are generally easier to manufacture. The next step was to select the machine's modulation set. Given the size of the machine, the number of sun gear pole pairs can not be too high. It must also be considered that the modulator, being sandwiched between the stator and the sun gear, results in a large gap between the stator and the sun gear. This means that flux can easily leak between adjacent poles. This effect can be limited by choosing a low sun gear pole count. Another aspect which must be considered when selecting the modulation set is the impact on cogging torque.

With these considerations in mind, two sun gear pole and stator slot combinations were investigated, with a wide variation in the number of modulator segments. Each combination was optimized using 2D FEA, considering the design variables described in the previous section. All

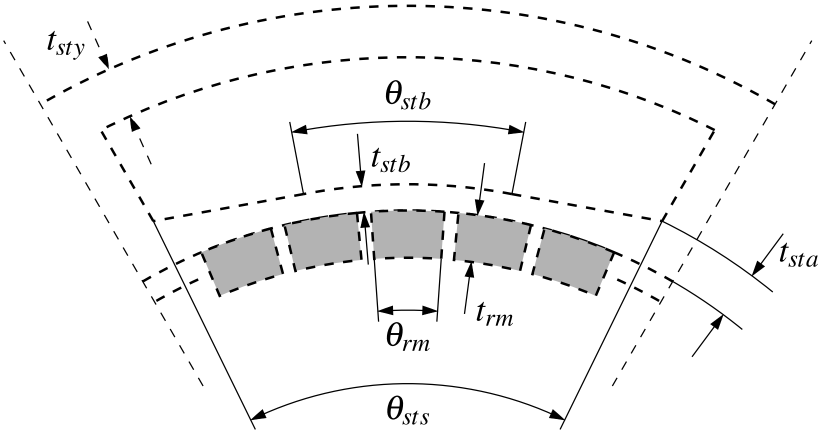

(a) Ring-stator.

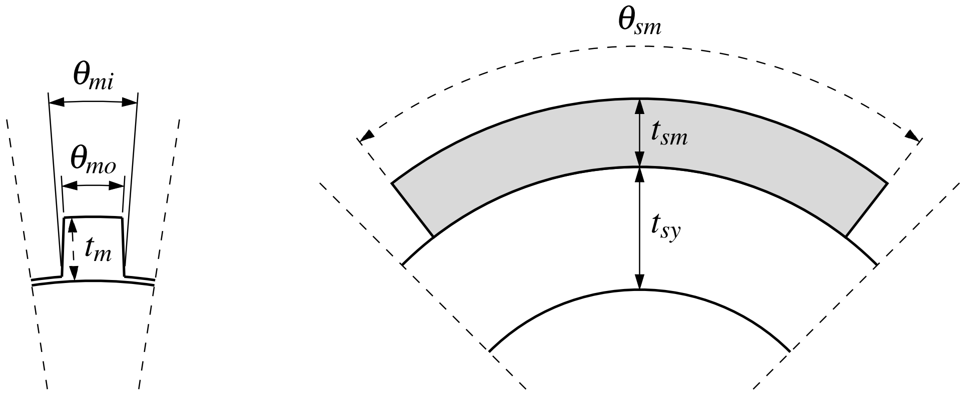

(b) Modulator.

(c) Sun gear.

Figure 9.2: Geometrical design variables used in the optimization of the ring-stator MGM.

optimum designs were evaluated with 3D FEA. The results are shown in Fig. 9.3. In the figure, the blue lines represent a machine with 4 poles ($p_s = 2$) and 6 stator slots. The red lines represent a machine with 6 poles ($p_s = 3$) and 9 stator slots. It is clear that the 4/6 combination performs better than the 6/9 option. Machines with $p_s > 3$ perform even worse. Thus, $p_s = 2$ and $Q_s = 6$ were selected. The graph in Fig. 9.3 shows that the stall torque initially increases rapidly with the number of modulator segments. The curve flattens as Q_m increases further. It can be argued that a good choice for Q_m would lie in the region where the stall torque is close to the maximum value, but if Q_m is too large, it would unnecessarily increase the machine's operating frequency. Based on the data in Fig. 9.3, $Q_m = 21$ was selected.

9.4 Final design

The final design parameters are listed in Table 9.1. The machine's torque ratings, calculated with 3D FEA, as well as the mass of the various active materials are summarized in Table 9.2. The rated torque is again calculated as 85 % of the machine's stall torque, as for the split MGM.

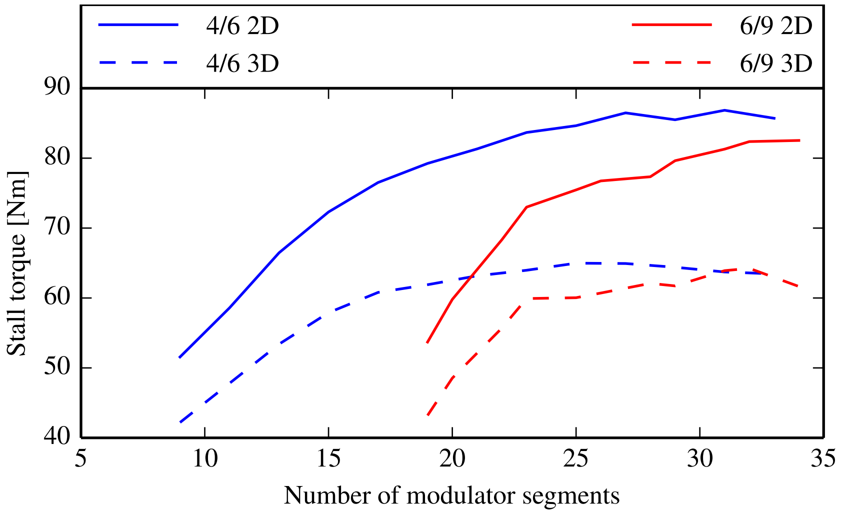

Figure 9.3: Optimized stall torque as a function of the number of modulator segments.

Table 9.1: Optimal machine design parameters

Parameter	**Value**
Sun gear magnet pitch	0.92 [fraction of pole pitch]
Ring gear magnet pitch	0.84 [fraction of pole pitch]
Inner modulator pitch θ_{mi}	0.5 [fraction of segment pitch]
Outer modulator pitch θ_{mo}	0.41 [fraction of segment pitch]
Sun gear yoke thickness t_{sy}	11.7 mm
Sun gear magnet thickness t_{sm}	6.5 mm
Modulator thickness t_m	6.1 mm
Modulator bridge thickness	0.5 mm
Ring gear magnet thickness	4.5 mm
Stator base thickness	2.5 mm
Stator additional thickness	4.6 mm
Stator yoke thickness	4.9 mm
Slot base angle θ_{stb}	0.36 [fraction of slot pitch]
Slot width angle θ_{sts}	0.874 [fraction of slot pitch]
Number of sun gear pole pairs p_s	2
Number of modulator segments Q_m	21
Number of ring gear pole pairs p_r	19
Number of slots Q_s	6
Gear ratio	10.5

Table 9.2: Optimal machine design characteristics

Parameter	**Value**
Gear stall torque	76 Nm
Rated torque	64.6 Nm
Rated stator torque	6.15 Nm
Torque density* (stall torque)	98.7 kNm/m^3
Torque density* (rated torque)	83.9 kNm/m^3
Rated copper loss†	94 W
Magnet mass	0.93 kg
Copper mass†	1.94 kg
Steel mass	2.38 kg
Total mass	5.25 kg
Rated torque per active mass	12.3 Nm/kg

* Excluding end-winding region
† Including end-winding region

9.5 Mechanical construction

The layout of the ring-stator MGM lends itself to a more elegant design of the mechanical support structure, compared to the split MGM. The crucial factors in this regard are the reduced number of air-gaps and the fact that the stator's winding is conveniently located on the outer component of the machine. A simplified schematic of the mechanical design is shown in Fig. 9.4. In the case of this machine, all the components are supported on both sides of the active stack. This reduces the required stiffness of the components. It may also allow slightly greater dimensional and geometrical tolerances of some of the parts, which could lead to lower manufacturing costs. The design requires four bearings, just like the split MGM design in the previous chapter.

The sun gear was fabricated from a solid mild steel cylinder. The magnets were glued in place without any additional restraining mechanisms. This may be an acceptable practice for a prototype, but not necessarily a viable option for machines with an expected lifespan in the order of 20 years.

The manufacturing process of the modulator was improved significantly with experience gained

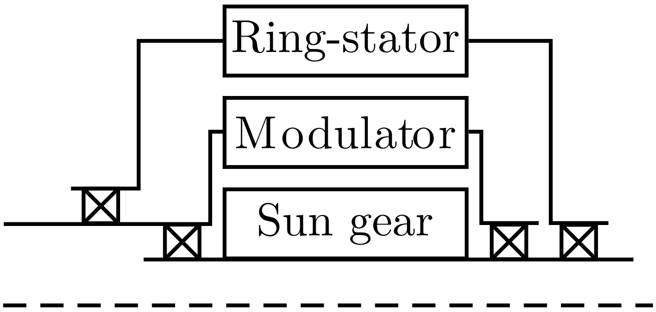

Figure 9.4: Simplified representation of the mechanical support structure.

from the manufacture of the split MGM's modulator. Instead of laser-cutting the laminations to the required final dimensions, a lamination is cut with a thick inner bridge and extended teeth. The thick inner bridge allows a lamination to maintain rigidity in the assembly of the stack on a mould. It also allows a key-way to be used for accurate location, thus leading to the modulator teeth being perfectly aligned. Once the modulator stack has been assembled, stainless steel rods are inserted and the cavities are filled with epoxy. After the curing process, the mould is removed and the modulator is machined on a lathe to the required dimensions, leaving a thin steel bridge on the inner periphery. This process simplifies the assembly of the modulator stack on the mould. In addition, the modulator can be manufactured more accurately since the machining process allows finer tolerances to be achieved than the casting process.

The modulator assembly, ready for epoxy casting, is shown in Fig. 9.5(a). The completed cast is shown in Fig. 9.5(b), with the inner mould still inside. The key way and the thick inner bridge can be seen in Fig. 9.5(c).

The realization of the stator winding was a difficult task. With closed slots, the winding had to be inserted using a thread and needle approach. A poorer than anticipated fill factor resulted from this process. Better results could likely have been achieved by cutting separate yoke and tooth laminations for the ring-stator which would allow preformed coils to be inserted. Information on the prototype's winding is given in Table 9.3.

9.6 Performance evaluation

The machine was evaluated using the same testing setup used for the split MGM.

9.6.1 Stall torque test

The simulated and measured modulator torque vs. modulator position with a locked sun gear is shown in Fig. 9.6. The simulated (3D FEA) stall torque was 61.8 Nm while the measured value was 59.2 Nm. The prototype achieved 95.8 % of the simulated stall torque.

9.6.2 No-load tests

A comparison of the magnitudes of the simulated and measured no-load line voltages are shown in Fig. 9.7. The simulated values were obtained from time-stepped 2D FEA. However, in this case, the magnitude of the voltage obtained from 3D FEA match the 2D results closely. The measured voltage is almost 10 % lower than the simulated voltage. This may be due to several

Table 9.3: Winding information

Parameter	**Value**
Wire diameter	0.65 mm
Phase resistance R_ϕ	7.3 Ω
Number of turns per coil	370
Fill factor	0.359

(a) Modulator assembly ready for casting.

(b) Completed cast, outer diameter machined.

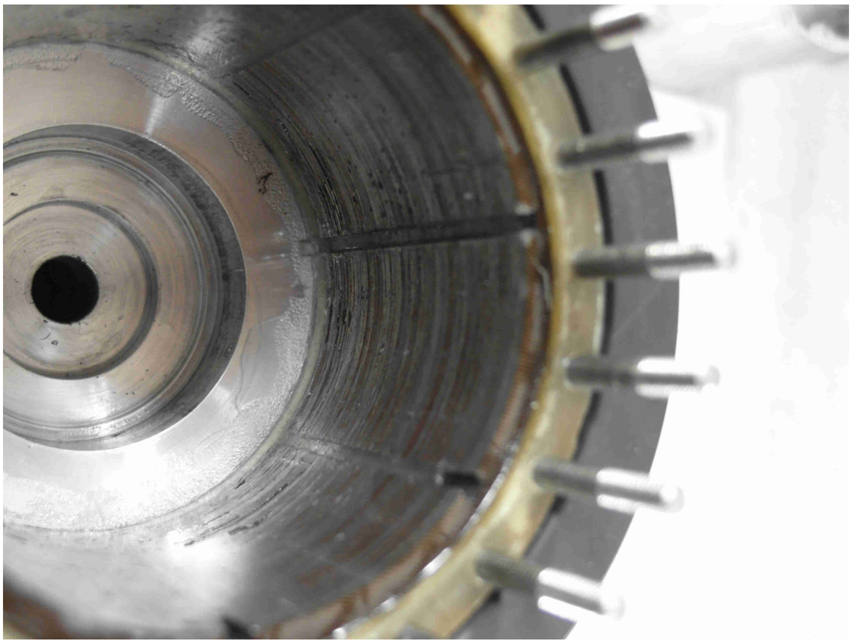

(c) Thick inner bridge and key way visible before machining of the inner diameter.

Figure 9.5: Improved modulator fabrication process.

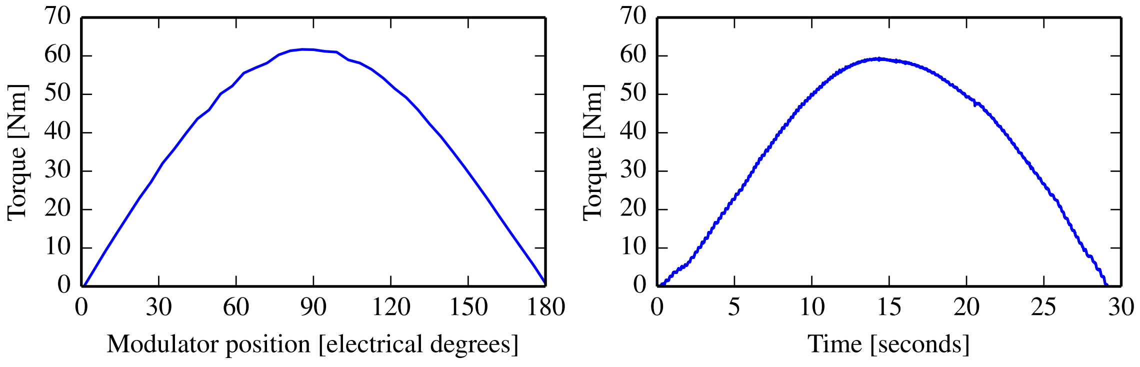

(a) Simulated.

(b) Measured.

Figure 9.6: Simulated and measured modulator stall torque.

factors. The material characteristics used in the FE models may not reflect the true material characteristics. The BH curve of the lamination steel and the magnets' characteristics (coercivity, relative permeability) are the important characteristics which affect the flux density in the machine, and thus the voltage magnitude. Dimensional inaccuracies can also play a role. The precise cause of this discrepancy has not been identified.

In Fig. 9.8, the simulated and measured no-load phase voltage waveforms are plotted, with the modulator rotating at 150 rpm. The shape of the waveforms match well, but as mentioned, the measured voltage is lower than expected.

A comparison between measured and simulated no-load power loss curves is shown in Fig. 9.9. The simulated data was obtained from transient 2D FEA and only includes core loss in the laminated components and eddy-current losses in the solid active components (magnets and sun gear yoke). The additional measured loss is attributed to other factors. Due to the machining on the inner periphery of the modulator, a conductive surface was created which allows eddy-currents to flow. These eddy-currents cause additional losses. Eddy-current losses can also be generated in the structural components fabricated from aluminium and stainless steel. Finally, losses are generated in the bearings. It was found that the total no-load loss varies significantly with the amount of preload placed on the bearings and that the losses in the bearings made an unexpectedly large contribution to the no-load losses in the machine. More detailed analysis of the losses in the machine is given in [104].

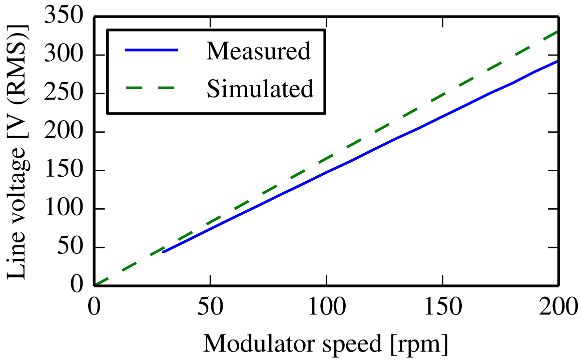

Figure 9.7: Comparison of no-load line voltage magnitudes vs. speed.

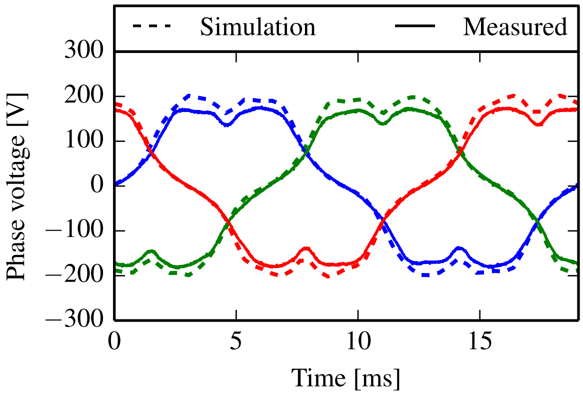

Figure 9.8: Comparison of no-load phase voltage waveforms at 150 rpm.

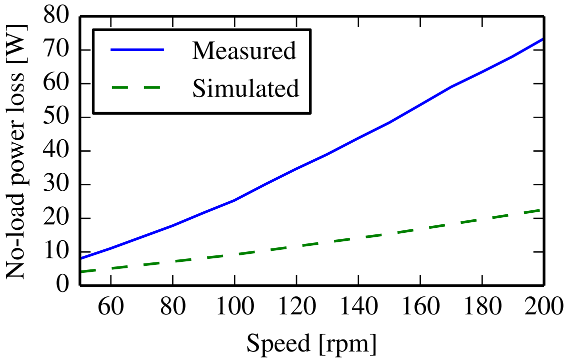

Figure 9.9: Comparison of simulated and measured no-load loss.

9.6.3 Load tests

An efficiency map of the machine operating in generator mode over an operational range up to 200 rpm and 45 Nm is shown in Fig. 9.10. Due to the high no-load loss and the poorer than anticipated slot fill factor, the efficiency of the machine is not high. With better manufacturing methods, a significant improvement in the efficiency is to be expected.

9.6.4 Operating point analysis

The method of calculating the operating points of an MGM described in section 4.5 was also applied to the analysis of the ring-stator MGM. In this case, data from 2D FEA was used, due to the high cost of the 3D FEA simulations. The dq flux maps were constructed using the following equations:

$$\lambda_d(i_d, i_q, \delta_g) = \lambda_{dm}(i_q, \delta_g) + i_d(L_d(i_d, i_q, \delta_g) + L_{ed}) \tag{9.4}$$

$$\lambda_q(i_d, i_q, \delta_g) = \lambda_{qm}(i_d, \delta_g) + i_q(L_q(i_d, i_q, \delta_g) + L_{eq}) \tag{9.5}$$

In the above, λ_{dm} and λ_{qm} are the dq flux linkages due to the permanent magnets on both the sun and the ring gear. In conventional PM machines, $\lambda_{qm} = 0$ since there is only one set of permanent magnets which are aligned to the d-axis. In coupled MGMs the ring gear magnets contribute to the q-axis flux linkage at non-zero load angles. The dq inductances (excluding the end-winding contribution) are functions of the dq currents and the MG load angle.

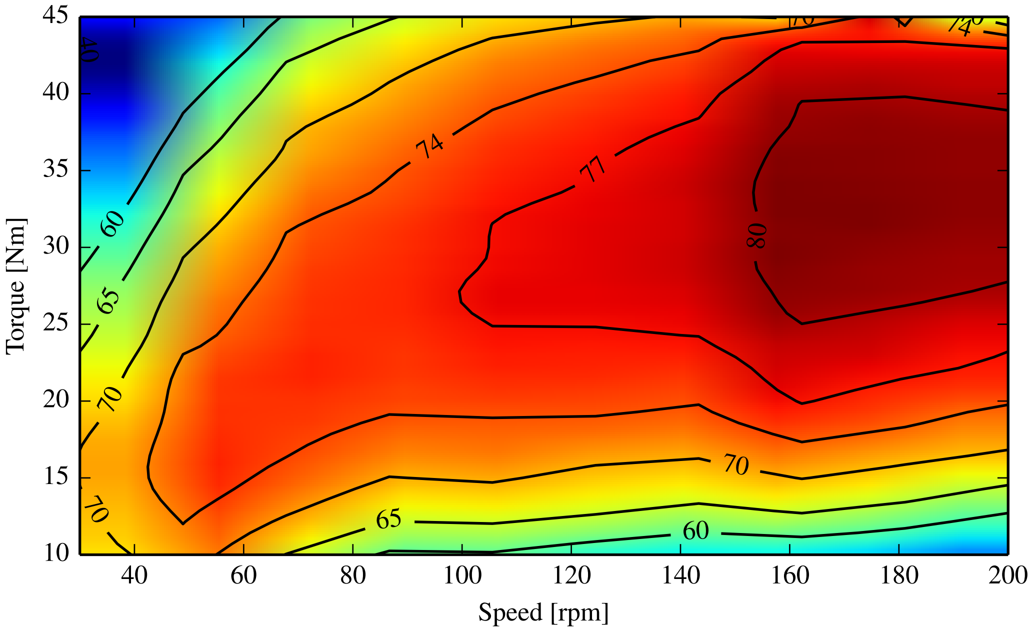

Figure 9.10: Efficiency map of the prototype ring-stator MGM.

The end-winding inductances, L_{ed} and L_{eq}, were calculated by subtracting the inductances calculated using 2D FEA from that calculated with 3D FEA at a single current value. It was assumed that the end-winding inductances can be modeled as constants, limiting the number of required 3D FE simulations.

Seeing as it was known from measurements that the no-load voltage of the machine was about 10 % lower than simulations predicted, the value of λ_{dm} was multiplied by a factor 0.9 in order to compensate for this discrepancy. Calculations and measurements for a specific operating point are compared in Table 9.4. The predicted values were calculated as described in section 4.5, using the measured load impedance. The measured and predicted values agree well.

Traces of the machine's maximum power output (generator operation) with a voltage limit of 400 V and current limit of 2.5 A were obtained using the approach described in chapter 4. These

Table 9.4: Comparison of measured and predicted operating point

	Measured	**Predicted**	**Error [%]**
Torque T_m	40.8 Nm	43.2 Nm	6.0
Speed n_m	150 rpm	150 rpm	0
Line voltage	156 V	163 V	4.4
Phase current	1.87 A	1.95 A	4.4
Input power	640 W	679 W	6.0
Output power	488 W	532 W	8.9
Power factor	0.964	0.966	0.1
Load	$46.4 + j12.5\,\Omega$	$46.4 + j12.5, \Omega$	0
Efficiency	76.3 %	78.5 %	2.9
Load angle δ_g	n.a.	-44.9°	n.a.

traces are shown in Fig. 9.11. The same code was used to obtain these traces for both the split MGM and the ring-stator MGM. This shows that the method can be successfully applied in the analysis of different kinds of MGMs.

9.7 Discussion

This chapter has presented the design and evaluation of a ring-stator magnetically geared machine. The prototype performed well in terms of its stall torque, achieving 95.8 % of the design value of 61.8 Nm. In terms of efficiency, the machine did not perform as well as expected. This is due to the poor winding fill factor and the higher than expected no-load rotational loss in the machine. The high no-load loss is attributed to losses in the bearings, with poor alignment leading to high bearing loads, eddy-currents generated in the conductive inner surface of the modulator, and parasitic losses in structural components.

With some modifications in the mechanical design, notably a separate stator yoke, this machine should compare favourably with the split MGM in terms of ease of construction. One important concern is the proximity of the ring gear magnets to the stator winding. The heat generated in the winding can make the ring gear magnets more prone to demagnetization. This should be considered when calculating the machine's thermal current limit.

As mentioned in chapter 3, many variations of specific MGM topologies can be realized. For example, the ring-stator topology could be implemented with a non-overlap winding stator. Thus, it is noted that the possibilities investigated in this design are far from exhaustive.

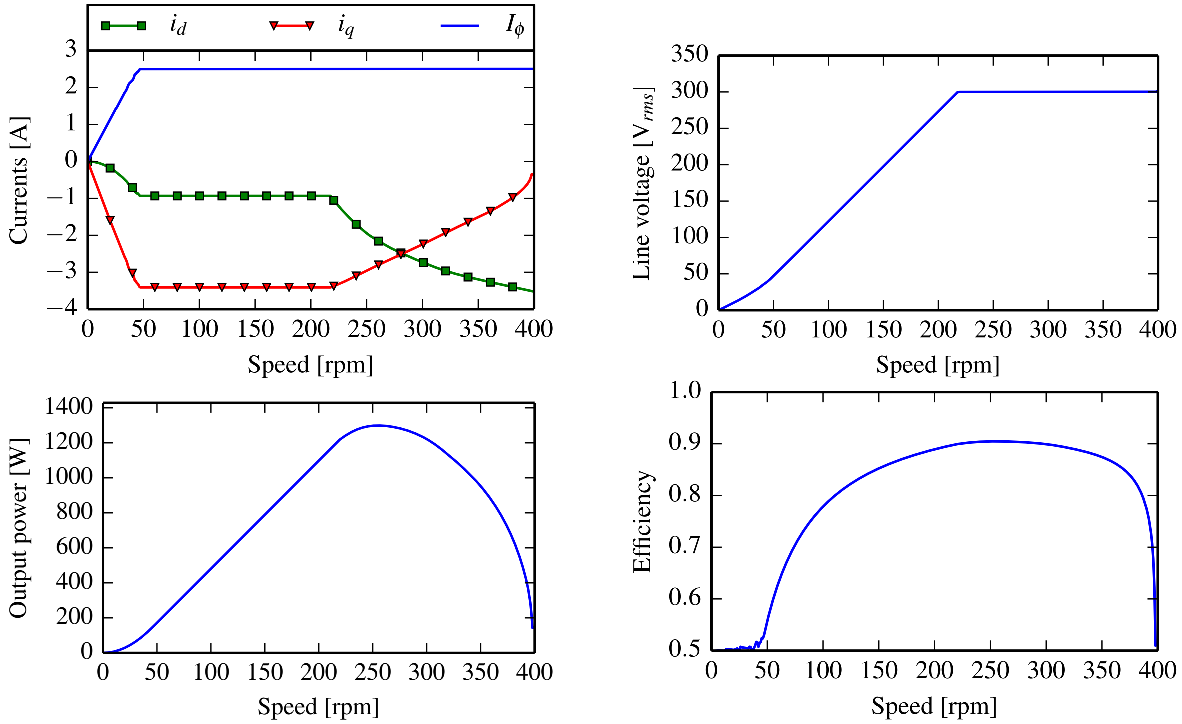

Figure 9.11: Maximum output power characteristics with a line voltage limit of 400 V and a phase current limit of 2.5 A.

Chapter 10

Evaluation of a vernier machine

In this chapter, the design and evaluation of a vernier machine is described. The machine was designed with the same active volume constraints as the two magnetically geared machines presented in the previous chapters. Vernier machines also operate on the flux modulation principle, although they are not classified as magnetically geared machines in this work, as explained in chapter 3. These machines also have attractive characteristics for direct-drive applications, primarily high torque density and excellent torque quality. The realization and evaluation of this prototype allows a more meaningful comparison to be made between the candidate machines.

Vernier machines and flux modulated magnetic gears are very similar in terms of their operating principles. The relationship between these machines have been described in [105]. In a vernier machine, the relationship between the number of rotor pole pairs p_r, the number of stator teeth Q_s and the number of winding pole pairs p_s is

$$p_r = Q_s - p_s \tag{10.1}$$

This equation corresponds exactly to (2.18). In vernier machines, the winding generates a low order space harmonic field with p_s pole pairs and the stator teeth perform the modulating function. The rotor magnets generate a high order space harmonic field with p_r pole pairs which interacts with the modulated space harmonic of the same order to generate useful torque.

10.1 Design specifications

For the design of the machine, an outer rotor configuration was selected. This choice maximizes the air-gap diameter and results in thinner magnets with a larger pole arc relative to the inner rotor configuration. This minimizes flux leakage.

A conventional double-layer overlap winding was employed. Neodymium Iron Boron magnets, grade N48H, were used in the design.

The constraints on the active volume of the machine and other parameters are listed in Table 10.1. These constraints correspond to the ones used throughout this work for the design of small prototypes, allowing good comparisons to be made. The machine's outer diameter, stack length and air-gap length are fixed. The maximum current density is constrained such that the machine can be naturally cooled. A slot fill factor of 0.4 was assumed in the design. This value is lower than that used for the machines with non-overlap windings. The reasoning was that a lower fill factor would likely result from the in-house fabrication of the overlap winding, compared with the non-overlap windings. The fill factor is calculated as the ratio of the area in a slot containing conductive material (copper) to the total slot area.

10.2 Pole and slot number selection

The first step in the design process was to select several candidate modulation sets. Compared to magnetically geared machines, the choice of the modulation set for vernier machines is more limited: The number of stator teeth, which perform the modulating function, must be a multiple of the number of phases.

Modulation sets with the number of winding pole-pairs ranging from 1 to 4 were investigated, with a few different slot numbers in each case. The candidate modulation sets that were investigated are listed in Table 10.2, along with the number of slots per pole per phase, q, for each case.

10.3 Design optimization

Having identified several candidate modulation sets, the next step in the design process was to perform design optimizations for each modulation set. Once again, the optimization was con-

Table 10.1: Vernier machine design constraints

Parameter	**Value**
Outer diameter	140 mm
Stack length	50 mm
Air-gap length	0.7 mm
Maximum current density	5 A/mm^2
Slot fill factor	0.4

Table 10.2: Candidate vernier machine modulation sets

p_s	Q_s	p_r	q
1	24	23	4
1	30	29	5
1	36	35	6
2	24	22	2
2	30	28	2.5
2	36	34	3
3	27	24	1.5
3	36	33	2
4	24	20	1
4	36	32	1.5

ducted using SEMFEM analyses coupled with the VisualDOC optimization suite, as illustrated in Fig. 4.4. A gradient-based optimization algorithm, the modified method of feasible directions (MMFD) [71], was used. The geometrical design variables are illustrated in Fig. 10.1. These variables, along with the current density in the slots, form the complete list of variables to be optimized.

The optimization problems were formulated as follows:

$$\text{Maximize:} \quad F(\mathbf{X}) = \text{Torque } T_r \tag{10.2}$$

$$\text{Subject to:} \quad \eta > 0.8 \tag{10.3}$$

$$\text{PF} > 0.7 \tag{10.4}$$

$$J < 5\text{A/mm}^2 \tag{10.5}$$

with η the machine's efficiency, PF the power factor, and J the RMS current density. The machine's efficiency is calculated considering only copper loss with the machine operating at 100 rpm. At this speed, other forms of losses are expected to be quite small due to the relatively low operating frequency. This includes core loss in the stator core and rotor yoke as well as eddy current loss in the magnets. The copper loss generated in the end-windings were approximated using a simple analytical approach. This is important because the length of the end-windings differ considerably between the various pole/slot combinations. For the purpose of the optimizations, the power factor was calculated without considering the effect of end-winding inductance, which implies that the power factor of the final machine will be lower than the constrained value in (10.4).

The results from these optimizations are tabulated in Table 10.3. A couple of observations can be made based on this data. Generally, the configurations with lower slot numbers achieved higher torque for a fixed number of winding pole pairs. The combinations with $p_s = 1$ performed significantly worse than the other combinations. The best options were the combinations with p_s/Q equal to 2/24, 3/27 and 4/24. From these, the 2/24 combination was selected for further analysis and prototyping because of its higher efficiency.

In general, vernier machines are known to have a relatively low power factor. This is because modulation of the rotor's magnetic field results in low PM flux linkage in the stator. As such,

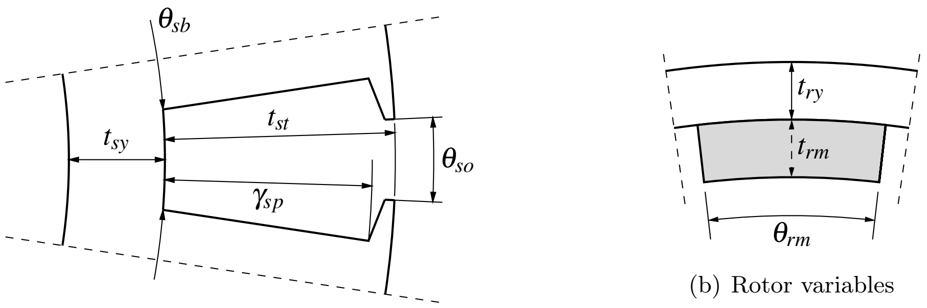

(a) Stator variables

(b) Rotor variables

Figure 10.1: Geometrical design variables of the vernier machine.

Table 10.3: Optimization results for different pole/slot combinations

p_s	Q	T	PF	η
1	24	24.9	0.70	0.80
1	30	20.3	0.71	0.80
1	36	12.6	0.70	0.80
2	**24**	**39.3**	**0.70**	**0.85**
2	30	31.9	0.70	0.83
2	36	18.0	0.70	0.81
3	27	40.9	0.70	0.82
3	36	31.3	0.70	0.83
4	24	38.3	0.78	0.80
4	36	33.4	0.70	0.83

the power factor is an important aspect to consider in the design. Within the defined design constraints, it was found that a trade-off exists between torque capacity and power factor. In order to make a good choice between these two aspects, the specific requirements of the application should generally be considered. In the present case, the machine is not intended for a specific application.

Further design optimizations were performed in a manner such that the pareto front of the machine's torque capability versus its power factor could be obtained. This allows a well informed choice to be made, where the cost of torque capability in terms of lower power factor is clearly quantified.

The pareto front was generated by performing several optimizations, all at a speed of 150 rpm and with the efficiency constrained such that $\eta > 0.85$. First, the torque was maximized with no constraint on the power factor. The power factor at the achieved optimum defines the start of the curve. Subsequent optimizations were performed with an ever more stringent constraint on the power factor. In this way, the pareto front, shown in Fig. 10.2, is traced. The maximum torque that could be achieved is 50 Nm at a power factor of 0.57. If the machine is to achieve a power factor of 0.9, the rated torque drops to 20 Nm. From this curve, the best design point can be selected, considering the needs of the application.

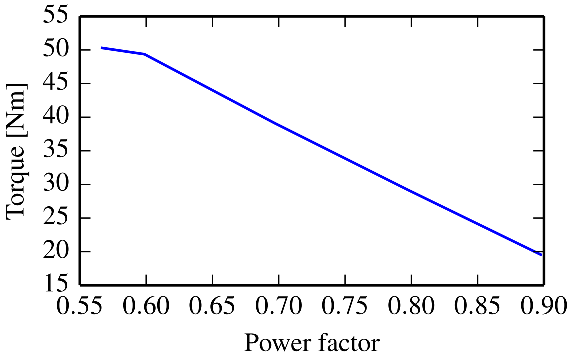

Figure 10.2: Pareto front of the rated torque versus power factor.

Based on the curve of Fig. 10.2, the final design was selected with a rated torque of 40 Nm and a power factor of 0.69. The final design's dimensions and calculated performance measures are listed in Table 10.4. A cross section of the design is shown in Fig. 10.3.

10.4 Mechanical construction

The various components of the prototype machine are shown in Fig. 10.4. A hollow mild steel shaft supports the stator of the machine and is used for mounting purposes. The rotor casing is fabricated from aluminium. These parts are shown in Fig. 10.4(a). The stator core laminations are shown in Fig. 10.4(b).

Some difficulties were experienced with the manufacturing of the winding. Initially, this process was attempted in-house. The casing's design was such that limited space was available for the end-windings. Together with a lack of expertise in winding fabrication, this lead to a failure to achieve the desired slot fill factor. The problem was rectified by making modifications to the casing and employing a professional winding service. The coil-span was also reduced to 5 slot pitches instead of the design value of 6 slot pitches (full pitch winding). The final stator, with its overlap-winding and external connections protruding from the shaft can be seen in Fig. 10.4(c). Detailed winding information is given in Table 10.5.

The rotor, with surface mounted magnets glued in place, is shown in Fig. 10.4(d).

Table 10.4: Final design parameters

Parameter	Value
t_{sy}	10 mm
t_{st}	29.3 mm
θ_{sb} (Fraction of slot pitch)	0.552
θ_{so} (Fraction of slot pitch)	0.651
γ_{sp} (Fraction of t_{st})	0.9
t_{ry}	7 mm
t_{rm}	3 mm
θ_{rm} (Fraction of pole pitch)	0.95
Rated torque	40 Nm
Torque density*	52.0 kNm/m^3
Rated current density	3.89 A/mm^2
Rated copper loss	67 W
Rated power factor	0.69
Efficiency @ 150 rpm	89 %

* Excluding end-winding region

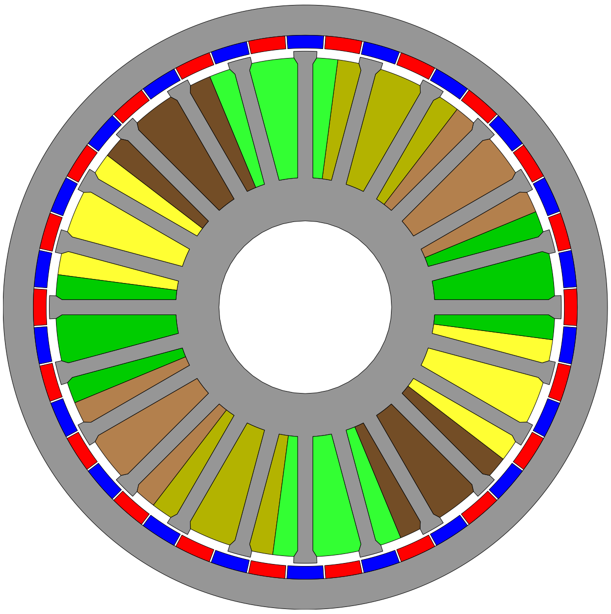

Figure 10.3: Cross sectional view of the vernier machine.

Table 10.5: Vernier machine winding information.

Parameter	**Value**
Wire diameter	0.63 mm
Phase resistance	4 Ω
Number of turns	60
Number of parallel circuits	1
Coil-span	5
Fill factor	0.34

10.5 Performance evaluation

The completed machine, mounted on the test bench, and the measurement setup are shown in Fig. 10.5. A servo motor with a gearbox is used to drive the prototype at the desired speed. The input torque and speed are measured by a torque sensor. The prototype is electrically loaded by a resistor bank and a capacitor bank connected through separate autotransformers. This allows both the active and reactive power to be adjusted. The output power is measured using the two-wattmeter method and with an oscilloscope.

10.5.1 No-load tests

A comparison of the magnitudes of the simulated and measured no-load line voltages are shown in Fig. 10.6. The measured voltage is 7 % lower than the simulated voltage. Considering that the simulated results is from a two-dimensional finite element analysis, the results are acceptable. The no-load line voltage waveforms are shown in Fig. 10.7. These waveforms show very little harmonic distortion. The simulated and measured waveforms are in good agreement.

The no-load power loss was measured up to a speed of 250 rpm. As shown in Fig. 10.8, the

(a) Casing and shaft. (b) Stator core.

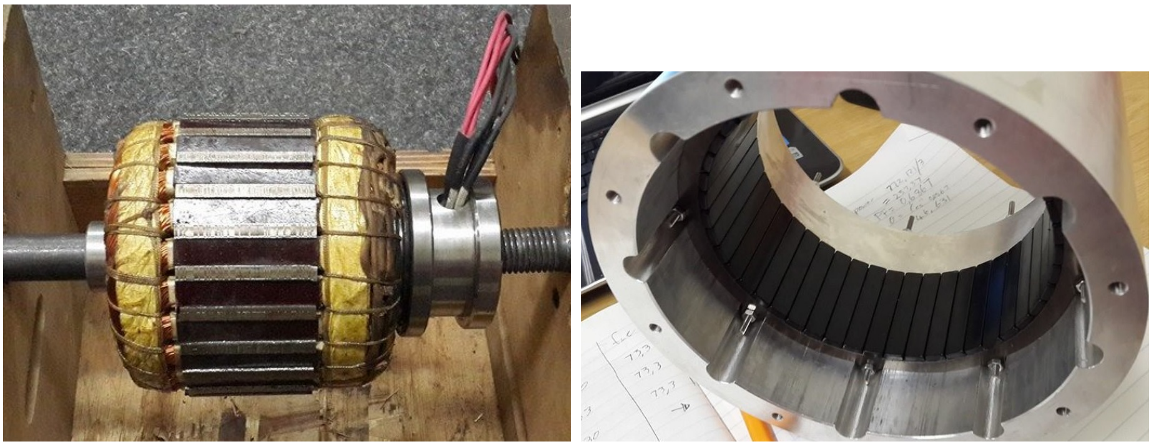

(c) Stator with windings. (d) Rotor.

Figure 10.4: Fabrication of the vernier machine prototype.

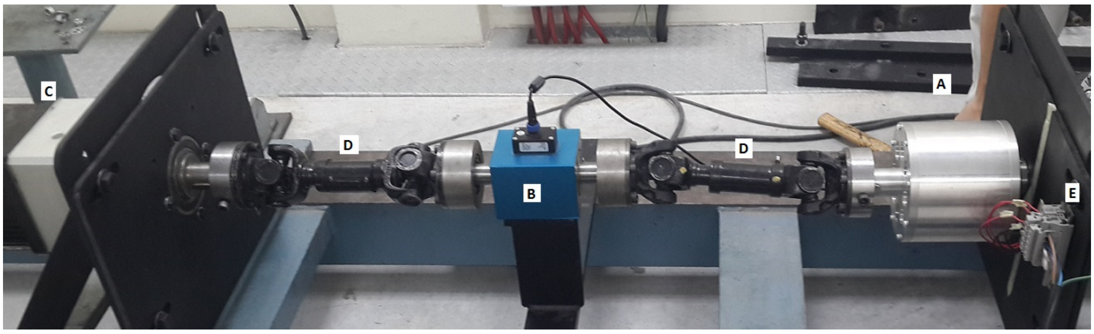

(a) Machine on the test bench.

(b) Load and measuring equipment.

Figure 10.5: Testing of the vernier machine.

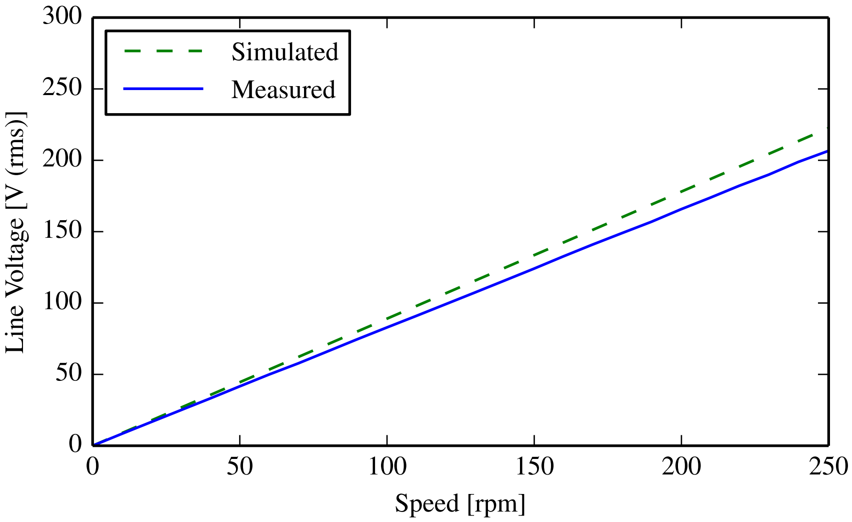

Figure 10.6: No-load line voltage.

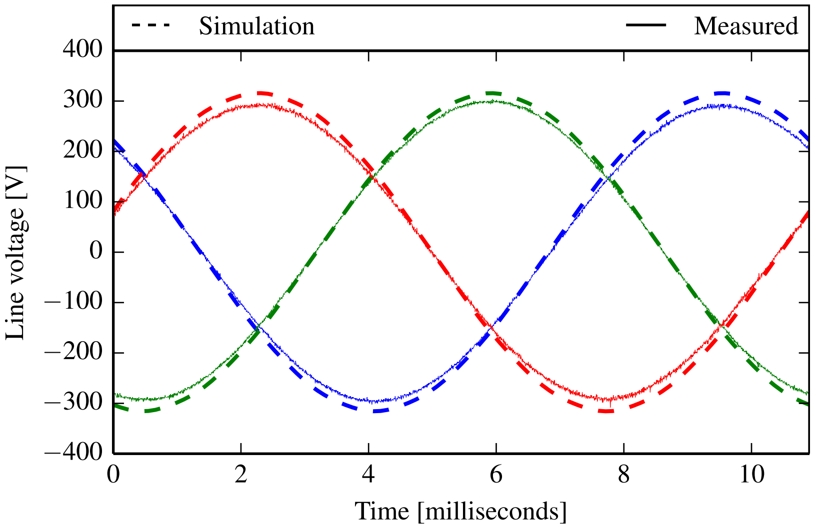

Figure 10.7: No-load line voltage waveforms.

no-load loss is very low. This is due to the fact that, under no-load conditions, the excitation in the machine is low.

10.5.2 Load tests

The efficiency of the machine was measured over the operational range shown in Fig. 10.9. The machine's efficiency drops as the load increases. As the speed increases, the machine's efficiency improves significantly. This is due to the low core and magnet losses in the machine.

10.5.3 Operating point analysis

The operating points of the machine were analyzed based on the equivalent circuit models shown Fig. 10.10. The dq flux linkages can be expressed as follows:

$$\lambda_d(i_d, i_q) = \lambda_{dm}(i_q) + i_d(L_d(i_d, i_q) + L_{ed}) \tag{10.6}$$

$$\lambda_q(i_d, i_q) = i_q(L_q(i_d, i_q) + L_{eq}) \tag{10.7}$$

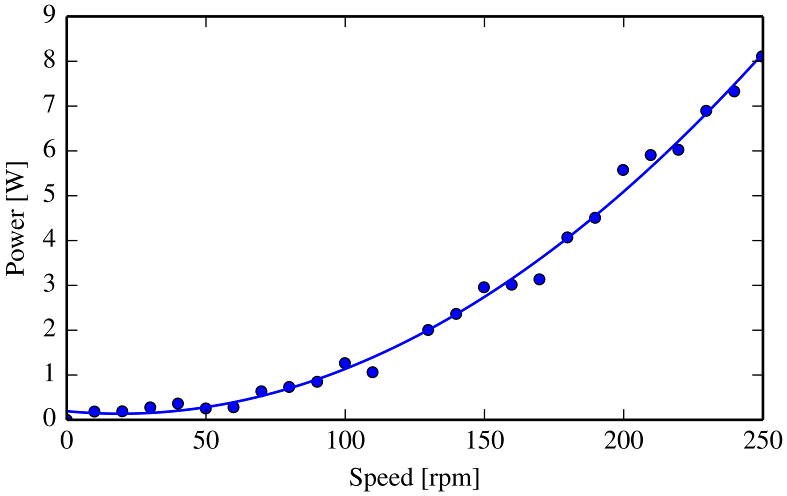

Figure 10.8: Measured no-load power loss.

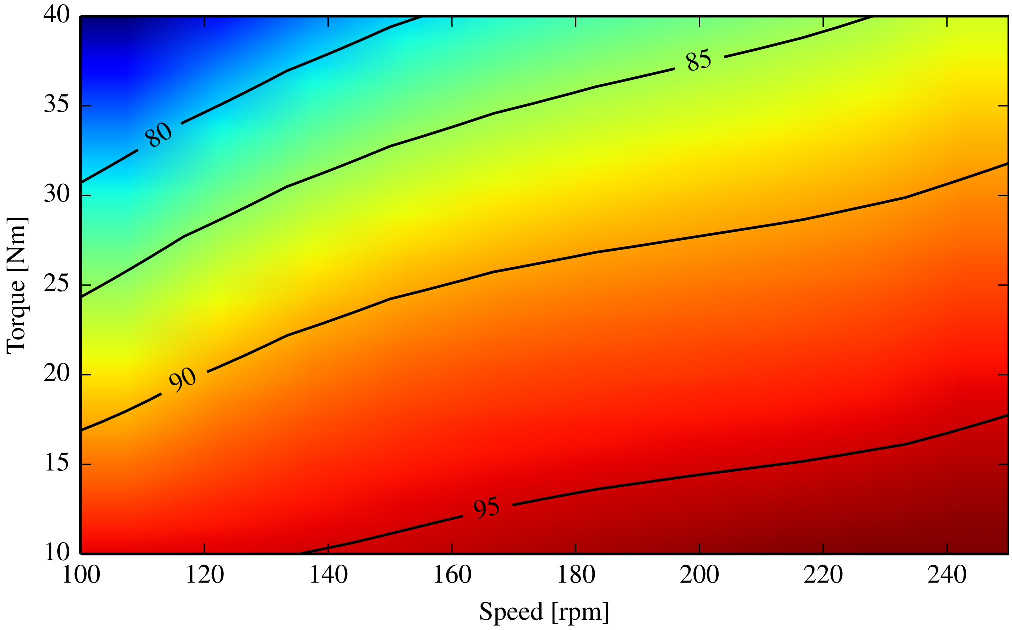

Figure 10.9: Efficiency map of the vernier machine.

where λ_{dm} is the d-axis flux linkage due to the permanent magnets, L_d and L_q are the inductances modeled in 2D, and L_{ed} and L_{eq} are the end-winding inductances. Note that these are the standard equations where the flux linkages are only dependent on the currents. There is no load angle, as in magnetically geared machines. It was assumed that the end-winding inductances can be modeled as constants.

From the equivalent circuit models, the following equations can then be derived:

$$-i_dR_L + i_qX_L = -\omega(i_q(L_q(i_d, i_q) + L_{eq})) + R_\phi i_d \tag{10.8}$$

$$-i_dX_L - i_qR_L = \omega(\lambda_{dm}(i_q) + i_d(L_d(i_d, i_q) + L_{ed})) + R_\phi i_q \tag{10.9}$$

Table 10.6 shows a comparison between a measured operating point and simulated results for the given load. In the calculation of the predicted operating point, the PM flux linkage was reduced by 7 % in accordance with the no-load voltage measurement. The end-winding inductances were calculated based on the differences between 2D and 3D finite element simulations. The measured and predicted results are in very close agreement.

Traces of the vernier machine's maximum output power in generator operation with a line voltage limit of 300 V and a phase current limit of 4 A are shown in Fig. 10.11. Only copper loss was

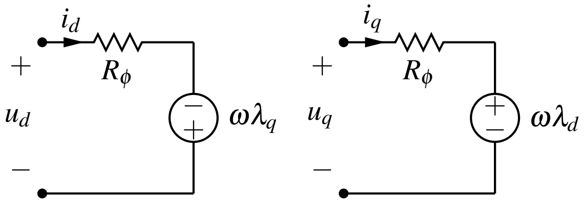

(a) d-axis. (b) q-axis.

Figure 10.10: Equivalent circuit models.

Table 10.6: Comparison of measured and predicted operating point

	Measured	**Predicted**	**Error [%]**
Torque T_m	39.5 Nm	39.0 Nm	-1.33
Speed n_m	150 rpm	150 rpm	0
Line voltage	175 V	174 V	-0.89
Phase current	3.22 A	3.19 A	-0.89
Input power	620 W	612 W	-1.23
Output power	495 W	486 W	-1.77
Power factor	0.51	0.51	-0.54
Load	$15.9 - j27.1\,\Omega$	$15.9 - j27.1\,\Omega$	0
Efficiency	79.9 %	79.2 %	-0.90

considered in the calculations. From the figure, it is clear that the vernier machine has the potential to operate over a wide speed range.

10.6 Discussion

Vernier machines can be a good alternative for direct-drive applications. Although their torque density is lower than magnetically geared machines, they still have high torque capability. Their simplicity, in mechanical terms, can be a significant advantage. Their great weakness is their poor power factor. In variable speed applications, this implies that a vernier machine will likely require a power electronic converter with a higher VA-rating than machines with a higher power factor. Nevertheless, their high torque capacity could outweigh the disadvantages associated with a lower power factor.

Vernier machines have the potential to be used in applications requiring a wide constant power speed range. Together with their high torque density at low speeds, this could make vernier machines an attractive choice for traction applications.

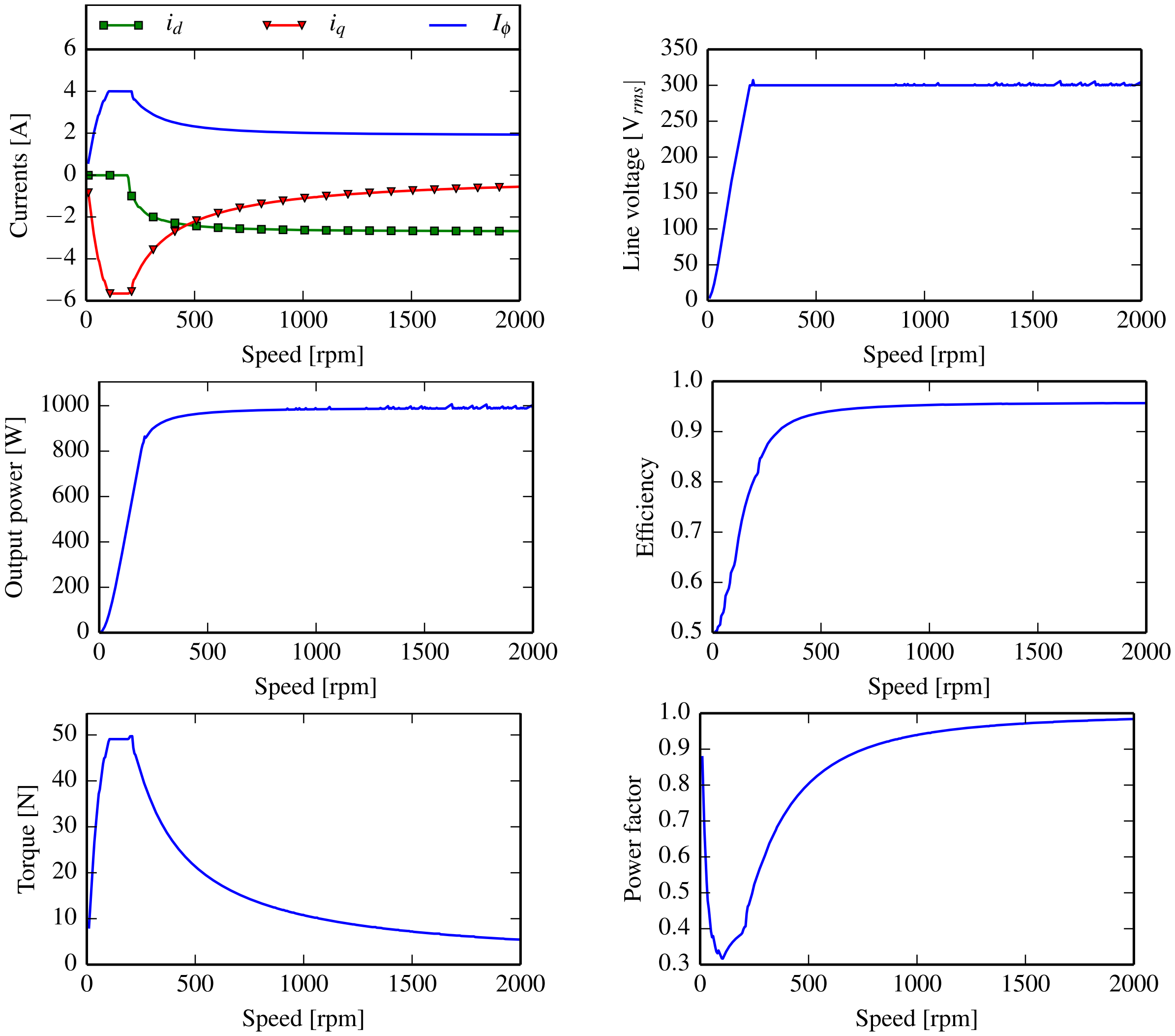

Figure 10.11: Maximum output power characteristics with a line voltage limit of 300 V and a phase current limit of 4 A.

Chapter 11

Comparison of topologies

In this chapter, the prototypes that have been constructed are compared in detail. A small PM machine with a non-overlap winding is also designed and used as a reference machine in the comparison. The aim is to compare the performances, material requirements and practical aspects of these machines, and in so doing, outline their respective advantages and disadvantages.

11.1 Reference machine

The topology selected for a reference machine is shown in Fig. 11.1. This is a fractional-slot PM machine with a non-overlap winding and will be referred to as the direct-drive machine (DDM). This type of machine is often proposed as a good candidate for low-speed, high-torque applications such as wind power generation and traction drives. The machine was optimized, subject to the constraints in Table 8.1. In this case, the optimization problem was formulated as an unconstrained problem:

$$\text{Maximize:} \quad F(\mathbf{X}) = \text{Torque } T/\text{active mass } M \tag{11.1}$$

No consideration was given to demagnetization as the risk is not as high as in magnetically geared machines. The geometrical design variables are identical to those used for the vernier machine, as illustrated in Fig. 10.1. In fact, the only difference between the DDM and the vernier machine lies in the winding arrangement.

Several pole/slot combinations were optimized. Table 11.1 lists the combinations investigated, along with their fundamental winding factors (k_w), and optimization results for each case. From the table it can be seen that the torque per active mass does not increase significantly with higher pole counts over the investigated set. This indicates that, within the specified volume, the DDM reaches its maximum torque at lower pole counts than the MGMs and the vernier machine. From Table 11.1, the combination with $p = 17$ and $Q = 27$ was selected because of its lower operating frequency and lower slot count, which makes the machine more practical to manufacture. A cross section of this design is shown in Fig. 11.1. The machine has a rated torque of 27.9 Nm. The machine's torque ripple and line voltage waveforms are shown in Fig. 11.2 and Fig. 11.3 respectively.

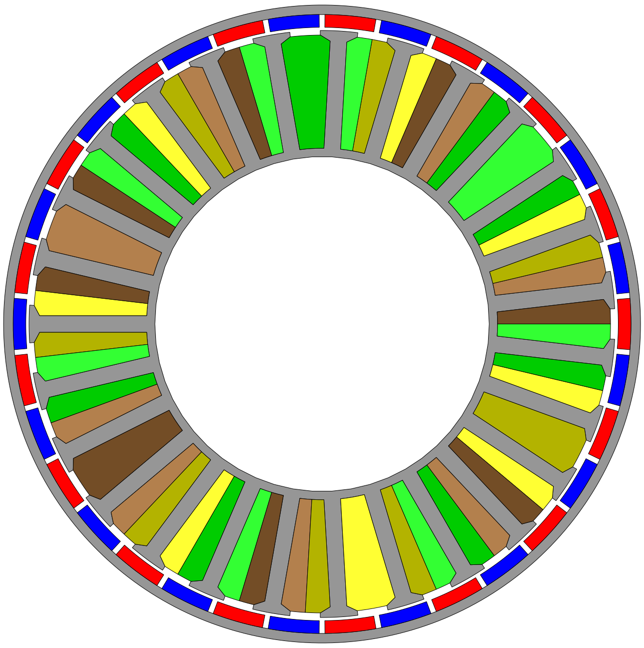

Figure 11.1: A fractional-slot permanent magnet machine with a non-overlap winding.

Table 11.1: Investigated pole/slot combinations for the PM machine.

p_s	Q	$\mathrm{k_w}^*$	$\eta^\dagger$	PF	T/M [kNm/kg]
14	24	0.933	82 %	0.96	8.32
17	**27**	**0.877**	**82 %**	**0.94**	**8.48**
19	36	0.953	82 %	0.93	7.95
21	36	0.933	83 %	0.94	8.39
23	36	0.867	83 %	0.94	8.49
26	39	0.866	84 %	0.92	8.78
31	51	0.901	84 %	0.91	8.39

[*] Values obtained from [98].

[†] Considering only copper loss, including estimation of the end-winding loss.

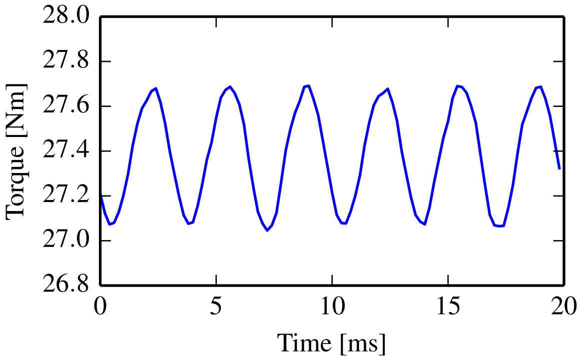

Figure 11.2: Direct-drive machine full load torque ripple.

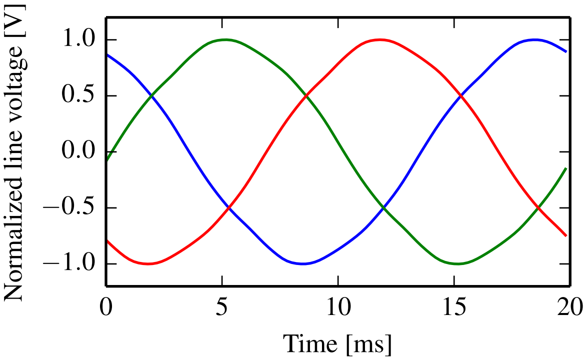

Figure 11.3: Direct-drive machine full load line voltage.

11.2 Comparison

Table 11.2 shows a comparison of the various designs considered in this study, including the split MGM (SMGM), the ring-stator MGM (RSMGM) and the vernier machine (VM). The prototypes of these machines are shown in Fig. 11.4. The results for the reference direct-drive machine (DDM) are also included in the table.

For the MGMs, the stall torque was obtained from 3D FEA. The table also lists the end-effect ratio, defined in chapter 6. All other calculations, including the MGM stator torques and the torque of the DDM and the VM are based on 2D simulation data, together with parameters that account for the end-windings. The dq end-winding inductances were calculated by subtracting the inductance calculated with 2D FEA from that calculated with 3D FEA. The calculated copper loss includes the contribution of the end-winding and is based on a copper fill factor of 0.55 for all machines. In the table, the end-winding factor indicates the length of the end-windings relative to the stack length, for each machine. Magnet loss and core loss data are based on transient 2D FEA.

The SMGM achieved the highest rated torque, torque density and torque per active mass. Its rated torque density is 2.7 times higher than the DDM. The RSMGM also has a very high torque density. Although the VM's torque per active mass is lower than that of the DDM, its torque per volume is almost 1.5 times higher.

The rated copper loss of the SMGM is the lowest. Even though the rated stator torque of the RSMGM is the lowest, its rated copper loss is similar to that of the DDM and the VM. The copper loss in the DDM is very high, considering that its rated torque is lower than that of the other machines. This is despite the fact that the DDM has the shortest end-windings. Despite the long end-windings of the VM, its copper loss is not excessively high.

In all the machines, the losses generated in the magnets are small compared to the copper loss and the core loss. The DDM has very low magnet loss. The magnet loss of the two MGMs are the highest. Note that the magnet loss of the SMGM would have been much higher if not for the magnet carrier design employed for the sun gear, as described in chapter 8.

The core loss of the DDM is the lowest, whereas the SMGM has the highest core loss. The RSMGM and the VM also have low core loss. The reason for the high core loss in the SMGM is its high operating frequency, compared to the other machines. This machine's operating frequency is higher than the other machines' because it was the only machine that benefited from a higher pole count within the specified volume. For the other machines, a higher pole count did not result in a significant increase in maximum torque.

The efficiency of the SMGM is the highest. The reference DDM has a poor efficiency due to its high copper loss and relatively low torque.

Among these machines, the VM is the only one with a poor power factor.

The MGMs used more than double the amount of permanent magnet material compared to the DDM and the VM. However, the rated torque per kilogram of magnet material of the DDM, SMGM and RSMGM are more comparable. The VM achieved the highest torque per kilogram of magnet material, almost double that of the RSMGM.

The SMGM used the least amount of copper, followed by the DDM. The VM used the most copper, due to its use of overlap windings.

Fig. 11.5 compares the maximum output power characteristics of these machines over an operational speed range of 0 – 600 rpm. In this comparison, only copper loss is considered.

The number of turns of each machine was scaled such that the voltage limit of 400 V was reached at 150 rpm, as can be seen in Fig. 11.5(a). The maximum copper loss was set to 100 W. This limit determines the current limit for each machine, indicated by the dashed lines in Fig. 11.5(b). The current limits also indicate the relative VA-ratings of the drives of the respective machines, since the voltage limits are equal.

The superior torque capability of split MGM at low speeds can clearly be seen in Fig. 11.5(c). The RSMGM and the VM deliver similar torques at low speed, but the VM can operate within

Table 11.2: Comparison of machines.

Parameter	**DDM**	**SMGM**	**RSMGM**	**VM**	**Unit**
Gear stall torque	-	88.2	61.8	-	Nm
E_T	-	0.87	0.82	-	-
Rated torque [*]	27.7	75.1	52.8	41.1	Nm
Rated stator torque	27.7	10.4	5.03	41.1	Nm
Stall torque density	-	114.6	80.3	-	kNm/m^3
Rated torque density	36.0	97.6	68.6	53.4	kNm/m^3
Gear ratio	-	7.2	10.5	11	-
End-winding factor	0.24	0.41	1.24	2.00	-
Rated copper loss	77.7	42.9	72.9	60.5	W
Magnet loss [†]	0.29	5.00	6.04	1.10	W
Core loss [†]	6.6	21.4	10.0	10.2	W
Total loss [†]	84.6	69.3	88.9	71.8	W
Frequency @ 150 rpm	42.5	90	52.5	55	Hz
Efficiency @ 150 rpm	80.6	94.2	89.3	88.9	%
Power factor	0.90	0.94	0.90	0.58	-
Magnet mass	0.40	0.90	0.93	0.41	kg
Copper mass	1.61	1.14	2.12	3.91	kg
Steel mass	1.55	2.44	2.38	2.69	kg
Total active mass	3.56	4.48	5.43	7.01	kg
Rated T/M_m	69.3	83.4	56.8	100.2	Nm/kg
Rated T/M	7.78	16.8	9.72	5.86	Nm/kg

[*] The rated torques of the two MGMs are based on a load angle $\delta_g = 60°$.

[†] Based on 2D simulation data at 150 rpm and rated conditions

the specified maximum voltage over a very wide speed range. The DDM can operate over a slightly wider speed range than the MGMs, but its torque and power capability is much lower than that of the other machines at low speeds.

The maximum output power of each machine, considering generator operation, is shown in Fig. 11.5(d). The peak power of the split MGM is very high. This graph shows that the vernier machine can deliver a relatively high constant power over a very wide speed range.

The efficiency of the MGMs, especially the split MGM, compare favourably with that of the VM and the DDM over the operational range of the MGMs. This analysis also shows that the VM can achieve high efficiency at higher speeds.

The power factor of the four machines are compared in Fig. 11.5(f). The shape of these curves deserves an explanation. Consider, for example, the curve for the DDM: In the first part of the curve the current increases until it reaches a maximum value. As the current increases, the power factor drops. Then, in the second part of the curve, the current stays constant while the voltage increases up to its maximum value. In this section of the curve, the power factor increases due to improving efficiency. In the final section of the curve, both the voltage and current magnitudes stay constant at their maximum values. Initially, the output power and efficiency increases with a corresponding increase in power factor, but then the ouput power decreases and the power factor drops. The curves show that the two MGMs and the DDM can operate at high power factors over the major parts of their respective speed ranges. The VM has a poor power factor in the speed range where it delivers its maximum torque, but its power factor increases steadily until it reaches a high value at higher speeds.

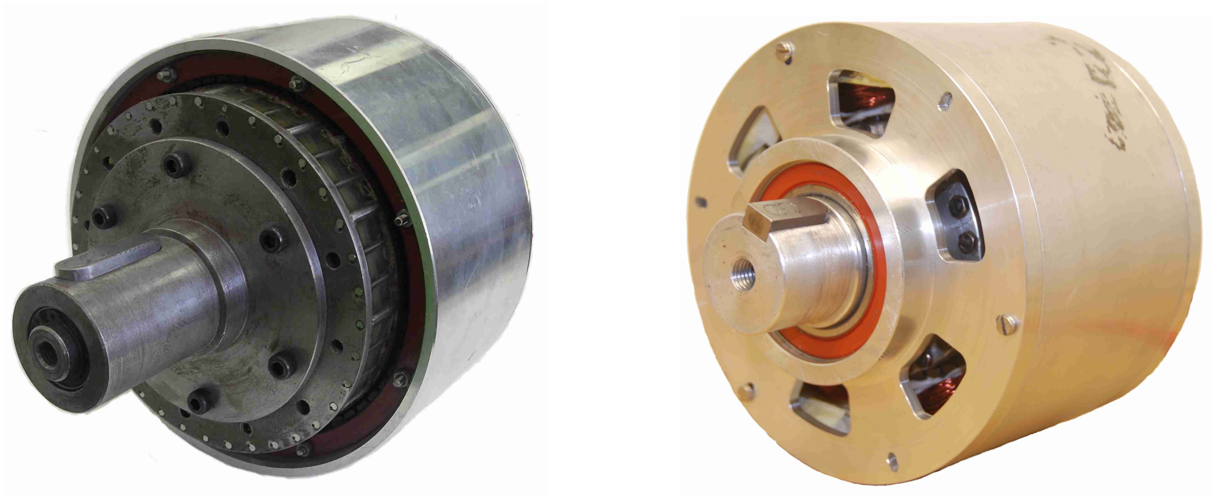

(a) Split MGM (b) Ring-stator MGM

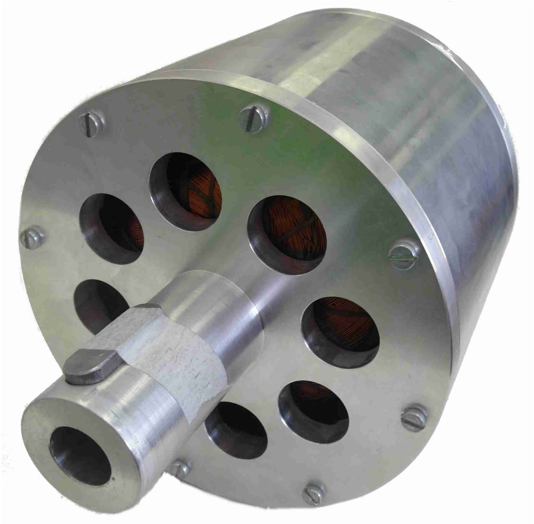

(c) Vernier machine

Figure 11.4: Three prototype flux-modulated electrical machines.

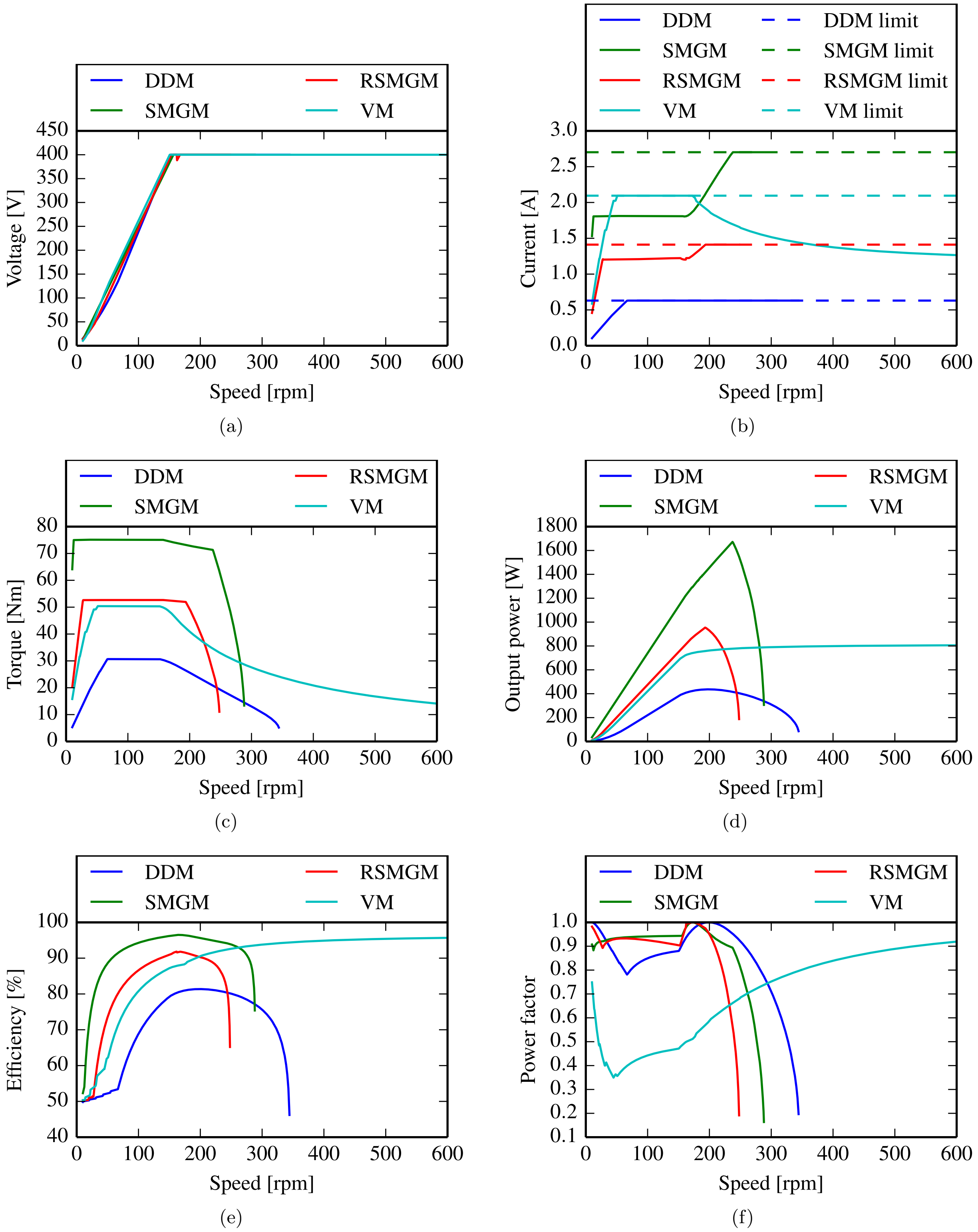

(a) (b)

(c) (d)

(e) (f)

Figure 11.5: Comparison of maximum output power characteristics.

Chapter 12

Conclusions and recommendations

This chapter concludes by summarizing the findings of this study. The first section highlights the original work presented in this dissertation, while the remaining sections comment on the various topics covered in this study.

12.1 Original work

The original contributions made in this study are listed below.

- Various literatures have reported large discrepancies between the expected performance of magnetic gears (MGs) and magnetically geared machines (MGMs) calculated with two-dimensional (2D) finite element analysis (FEA) and measured results or three-dimensional (3D) FEA. A detailed investigation into the end-effects that cause these discrepancies has been presented. The reason for the relatively large errors made by 2D FEA compared with more conventional electrical machines has been clarified.

- A design optimization methodology for magnetically geared machines has been proposed. The method makes use of the stator load factor which is a measure of the relative torque capability of the magnetic gear and electrical machine components of an MGM. The stator load factor is constrained in a numerical design optimization. This procedure ensures that designs are realized in which the electrical machine and magnetic gear components are well matched. Given the fact that 2D FEA results can be inaccurate, an extension to this method has been proposed which has the advantage of low computational cost associated with 2D FEA while still providing the high accuracy associated with 3D FEA.

- A method of analyzing the operating points of coupled MGMs has been presented. The method requires that the dq flux linkages, the sun gear torque and the modulator torque be mapped versus the dq currents and the magnetic gear's load angle. Once the mapping is obtained, operating points can be found within various constraints.

- The simulation of MGMs using FEA can be exceptionally time-consuming when movement has to be considered. This is due to the lack of periodicity often present in these machines and their multiple air-gap topologies. A comparison of two different movement facilitating methods in 2D FEA has been presented. It has been shown that the air-gap element can be prohibitively expensive for these machines and that moving band implementations with multiple layers in the air-gap can provide good accuracy at significantly reduced computational cost.

- The aforementioned design optimization methodology has been applied in the design of two different MGMs, of which prototypes have been constructed. In particular, a split MGM with a novel structure for the sun gear has been designed and experimentally evaluated. Test results agreed well with performance calculations from FEA.

- A distinction has been made between the *synchronous cogging torque* and the *true cogging torque* in MGs and MGMs. A simple method of approximating the true cogging torque, given the synchronous cogging torque, has been presented. This method is useful since it is much simpler to calculate the synchronous cogging torque in practice.

- A comparison of a conventional PM machine, a split MGM, a ring-stator MGM and a vernier machine has been presented. These machines were designed using the same optimization strategy. Prototypes of both MGMs and the vernier machine were constructed and tested.

- The nomenclature used when describing magnetic gears and magnetically geared electrical machines is not well established in literature. As a result, some confusion and contradictions may arise. In this dissertation, it has been attempted to make a clear distinction between different kinds of magnetic gears. The nomenclature used when describing flux-modulated magnetic gears, which was the type of gear considered in this work, accurately reflects their function and highlights the similarities with existing mechanical planetary gears for which naming conventions are well established.

12.2 Features of magnetically geared machines

MGs and MGMs have several attractive features which warrant interest in these devices. Their frictionless torque transfer capability imply that these devices have the potential to have long service lives with little maintenance requirements. The absence of friction also allows these devices to operate quietly.

Another important feature is the overload protection inherent to these devices. A magnetic gear which is overloaded slips without damaging the gear. This feature can be used to protect an entire drive train from overload conditions, reducing the required safety factors for other components.

In this study, it has been demonstrated that MGs and MGMs can achieve significantly higher torque densities than more conventional PM machines. This feature makes these devices attractive in applications were space is limited.

12.3 Design and analysis of magnetically geared machines

12.3.1 End-effects

End-effects have a significant impact on the stall torque capability of magnetic gears and magnetically geared machines. An in depth analysis has shown that the exceptionally large impact of end-effects can partially be attributed to a phenomena termed *escaping*. The large impact of end-effects necessitates the use of 3D modeling for accurate performance computation. However, due to the high computational cost of the 3D modeling, it is proposed that optimization is performed using mainly 2D FEM analyses.

Due to the end-effects present in MGs and MGMs, it has been found that poor casing design can seriously compromise the performance of these devices in terms of stall torque and efficiency. When designing casings for MGs and MGMs, non-ferrous materials should be used and/or it must be ensured that the spacing around the active stack is sufficiently large that leakage flux does not couple to the casing. An investigation into a prototype magnetic gear which failed to achieve its design specifications validates these findings. By redesigning the prototype's casing alone, the stall torque was increased by 30 % while the losses in the gear was reduced by roughly 70 %.

12.3.2 Optimal component matching in magnetically geared machines

The stator load factor has been presented as a useful measure of the balance between the magnetic gear and electrical machine components of an MGM. A method of designing well balanced MGMs through numerical optimization with a constraint on the stator load factor has been demonstrated. In addition, it has been shown that these optimizations can be performed using only single point 2D finite element simulations in the analysis. This limits the computational cost of optimizing MGMs.

The selection of the stator load factor depends on the nature of the application, but the value should be below unity in order to make efficient use of the stator. In applications with high peak loads, a value much lower than unity may be appropriate if the stator can be temporarily overloaded.

12.3.3 Computational aspects

In general, analysis of magnetically geared machines can be computationally expensive. The lack of periodicity often present in these machines implies that full model simulations are required. For this reason, special attention has been given to the simulation of movement in 2D finite element analyses. The efficiency of the movement facilitating method is of great importance for magnetically geared machines because up to three air-gaps are present in these machines. It has been shown that the air-gap element can be prohibitively expensive for MGMs. A moving band solver has successfully been implemented which has been shown to be significantly faster. When used with three layers, the moving band technique can also provide high accuracy.

12.3.4 Operating point analysis

A method of finding operating points for magnetically coupled MGMs has been presented. The method employs four dimensional mappings of the dq flux linkages as well as the sun gear torque and the ring gear or modulator torque. Using this method, operating points defined by the triple (i_d, i_q, δ_g) can be found, given the load impedance. Alternatively, the method can be used to trace various operating limits of the machine or to find the maximum torque per ampere trajectories. This method has been demonstrated for the two MGM prototypes realized in this study.

12.4 Evaluation of different flux-modulated electrical machines

12.4.1 Prototype machines

Three prototype flux-modulated electrical machines have been realized, two magnetically geared machines and one vernier machine.

The prototype split MGM achieved an active volume stall torque density of $114\,\mathrm{kNm/m^3}$, which is far higher than conventional PM machines of similar size. A novel structure for the sun gear has been employed which has been shown to reduce the magnet losses in this component considerably, while allowing a high torque density to be achieved.

A prototype ring-stator MGM has been realized for comparative purposes. Compared with the split MGM, this topology has two important advantages. Firstly, the number of air-gaps is reduced to two, which simplifies the mechanical construction of these machines. Secondly, the stator is located on outer periphery of the machine, which is better for heat dissipation seeing as the majority of the losses are generated in this component. On the other hand, the ring gear magnets are located close to the dominant heat source, the winding. This means that care must be taken in order to prevent these magnets from demagnetization. In this study, the ring-stator MGM did not perform as well as the split MGM.

A vernier machine with an outer rotor and surface mounted permanent magnets has been designed and experimentally evaluated. In mechanical terms, this machine is the simplest of the three flux-modulated machines. The prototype exhibited very low cogging torque. Experimental results agreed well with the simulations, although the efficiency was lower than the design value due to a lower slot fill factor. A significant disadvantage of the vernier machine is its low power factor.

12.4.2 Comparison of machines

Considering the data in the Table 11.2, the split MGM appears to be the most attractive option for small direct-drive applications, seeing as it achieved the highest torque per active mass, torque density, power factor and efficiency. The ring-stator MGM also achieved almost twice the torque per active mass compared to the benchmark direct-drive machine within the specified volume.

The vernier machine also achieved a higher torque density than the conventional PM machine. However, its torque per active mass was slightly lower. Interestingly, the vernier machine achieved the highest torque per kilogram of magnet material. Thus, if the cost of permanent magnets is high, vernier machines may be a very attractive option for direct-drive applications. However, due to the low power factor of vernier machines, the additional cost associated with a larger power electronic converter will also have to be considered.

Although the machines were not specifically designed for a wide constant power speed range, it is worth noting that the designed vernier machine has a wide operational speed range.

The mechanical complexity of the machines is an important factor to consider in the comparison. The split MGM, which performed best, is also the most complex in mechanical terms seeing that it has three air-gaps. The ring-stator MGM is simpler than the split MGM because it has only two air-gaps, but still significantly more complex than the vernier machine and the conventional PM machine with only a single air-gap. Nevertheless, the mechanical complexity of the MGMs is not considered to be a prohibitive problem in the light of their appreciable advantages.

12.5 Potential applications

The cost of permanent magnets will likely be an important factor in determining whether magnetic gears and magnetically geared machines are adopted widely in industry. Interestingly, the results in Table 11.2 show that MGMs can be competitive in terms of torque per magnet volume.

Two very attractive aspects of magnetic gears are their low maintenance requirements and the inherent overload protection that they offer. These advantages can be very important in the wind power industry where tower-top maintenance is difficult to perform, especially in off-shore applications. If a magnetic gear is used as the first stage of wind turbine drive-train, the entire drive-train can be protected from dangerous torque pulsations caused by gusty winds. The wind power industry, however, is by no means the only industry that can benefit from this technology. It is envisaged that savings in maintenance costs can make magnetic gears a viable alternative in many applications, even if the initial capital costs are higher.

Based on the simulation data, the experimental data gathered in this study and other sources, it can be concluded that magnetically geared machines are worth considering for low-speed applications despite the disadvantages in terms of mechanical complexity. Their torque density far surpasses that of conventional PM machines and they can achieve high efficiencies.

Vernier machines may be a very attractive option for traction applications. The machines have high torque capability at low speeds and a wide operational speed range.

12.6 Future work

As shown in chapter 3, magnetically geared machines with various other topologies than those analyzed in this study can be realized. It is specifically recommended that the wound modulator MGM and the partially coupled split MGM be investigated in future work.

In this study, core and magnet losses were not accounted for during design optimization. This was done in order to limit the computational cost of optimization. It was also assumed that copper loss would be the dominating loss component due to the relatively low operating frequencies and the small size of the machines considered. This assumption proved to be accurate. However, this may not always be the case, especially when larger machines or machines with higher operating frequencies are considered. Accurate loss calculations can be incorporated into the optimization process under these circumstances or when stringent efficiency constraints have to be met.

Several optimizations of magnetic gears performed in this study revealed that designs with the highest stall torque may be prone to demagnetization. This supports the findings in [47] that for designs with a high PM volume, a constraint on the distribution of PM material between the sun gear and the ring gear has to be enforced in order to avoid demagnetization. Alternatively, a demagnetization analysis can be included as part of the analysis used for optimization. In this regard, it is also concluded that thermal analyses may be of high importance in order to determine exactly when demagnetization will occur and to allow design constraints to be specified accordingly.

The comparative results presented in this study apply to small machines. The comparison should be repeated at higher power levels seeing as the machines may not scale equally well.

Cost effective and robust mechanical design of MGs and MGMs is an area where significant improvements can be made. Specifically, methods of manufacturing modulators and the sun gear in split MGMs are not well established. The torque capability of MGs and MGMs can increase dramatically with a reduction in the air-gap clearances. Mechanical designs which allow thinner air-gap regions to be used can be highly advantageous.

References

[1] C. G. Armstrong, “Power transmitting device,” US Pat. 687 292, 1901.

[2] H. T. Faus, “Magnet gearing,” US Pat. 2 243 555, 1941.

[3] S. Rand, “Magnetic transmission system,” US Pat. 3 523 204, 1970.

[4] M. Hetzel, “Low friction miniature gear drive for transmitting small forces, and method of making same,” US Pat. 3 792 578, 1974.

[5] K. Ikuta, S. Makita and S. Arimoto, “Non-contact magnetic gear for micro transmission mechanism,” in *Micro Electro Mechanical Systems, Proc. An Investigation of Micro Structures, Sensors, Actuators, Machines & Robots. IEEE*, 1991, pp. 125–130.

[6] E. Furlani, “A two-dimensional analysis for the coupling of magnetic gears,” *IEEE Trans. Magn.*, vol. 33, no. 3, pp. 2317–2321, 1997.

[7] Y. Yao, D. Huang, C. C. Hsieh, D. Chiang and S. Wang, “Simulation study of the magnetic coupling between radial magnetic gears,” *IEEE Trans. Magn.*, vol. 33, no. 2, pp. 2203–2206, 1997.

[8] Y. Yao, D. Huang, C. Lee, S. Wang, D. Chiang and T. Ying, “Magnetic coupling studies between radial magnetic gears,” *IEEE Trans. Magn.*, vol. 33, no. 5, pp. 4236–4238, 1997.

[9] S. Kikuchi and K. Tsurumoto, “Design and characteristics of a new magnetic worm gear using permanent magnet,” *IEEE Trans. Magn.*, vol. 29, no. 6, pp. 2923–2925, 1993.

[10] A. H. Neuland, “Apparatus for transmitting power,” US Patent US1 171 351, 2 8, 1916.

[11] G. A. Reese, “Magnetic gearing arrangement,” US Patent US3 301 091, 1 31, 1967.

[12] T. B. Martin, “Magnetic transmission,” US Pat. 3 378 710, 1968.

[13] N. Laing, “Magnetic transmission,” US Pat. 3 645 650, 1972.

[14] ——, “Centrifugal pump with magnetic drive,” US Pat. 3 762 839, 1973.

[15] B. Ackermann and L. Honds, “Magnetic drive arrangement comprising a plurality of magnetically cooperating parts which are movable relative to one another,” US Pat. 5 633 555, 1997.

[16] B. Ackermann, “Magnetic drive arrangement,” US Pat. 5 994 809, 1999.

[17] K. Atallah and D. Howe, "A novel high-performance magnetic gear," *IEEE Trans. Magn.*, vol. 37, no. 4, pp. 2844–2846, 2001.

[18] N. Frank and H. Toliyat, "Gearing ratios of a magnetic gear for marine applications," in *Proc. of IEEE Electr. Ship Technologies Symp. (ESTS)*, 2009, pp. 477–481.

[19] ——, "Gearing ratios of a magnetic gear for wind turbines," in *IEEE Int. Electr. Machines & Drives Conf.*, 2009, pp. 1224–1230.

[20] ——, "Analysis of the concentric planetary magnetic gear with strengthened stator and interior PM inner rotor," in *IEEE Energy Conv. Congress and Exposition (ECCE)*, 2010, pp. 2977–2984.

[21] N. Frank, S. Pakdelian and H. Toliyat, "Passive suppression of transient oscillations in the concentric planetary magnetic gear," *IEEE T-EC*, vol. 26, no. 3, pp. 933–939, 2011.

[22] S. Pakdelian, N. Frank and H. Toliyat, "Damper windings for the magnetic gear," in *IEEE Energy Conv. Congress & Expo. (ECCE)*, 2011, pp. 3974–3981.

[23] L. Jian and K. Chau, "Analytical calculation of magnetic field distribution in coaxial magnetic gears," *Prog. In Electromagn. Res.*, vol. 92, pp. 1–16, 2009.

[24] L. Jian, K. Chau, Y. Gong, J. Jiang, C. Yu and W. Li, "Comparison of coaxial magnetic gears with different topologies," *IEEE Trans. Magn.*, vol. 45, no. 10, pp. 4526–4529, 2009.

[25] L. Jian and K. Chau, "A coaxial magnetic gear with halbach permanent-magnet arrays," *IEEE T-EC*, vol. 25, no. 2, pp. 319–328, 2010.

[26] L. Jian, K. Chau, W. Li and J. Li, "A novel coaxial magnetic gear using bulk HTS for industrial applications," *IEEE T-AS*, vol. 20, no. 3, pp. 981–984, 2010.

[27] X. Li, K. Chau, M. Cheng, W. Hua and Y. Du, "An improved coaxial magnetic gear using flux focusing," in *Int. Conf. on Electr. Machines & Sys. (ICEMS)*, 2011.

[28] Y.-J. Ge, C.-Y. Nie and Q. Xin, "A three dimensional analytical calculation of the air-gap magnetic field and torque of coaxial magnetic gears," *Prog. In Electromagn. Res.*, vol. 131, pp. 391–407, 2012.

[29] X. Liu, K. Chau, J. Jiang and C. Yu, "Design and analysis of interior-magnet outer-rotor concentric magnetic gears," *J. of Appl. Phys.*, vol. 105, no. 7, 2009.

[30] A. Abdel-Khalik, A. Elshebeny and S. Ahmed, "Design and evaluation of a magnetic planetary gearbox for compact harsh environments," in *Int. Symp. Power Electron. Electr. Drives Automation & Motion*, 2010, pp. 1178–1182.

[31] M. Fukuoka, K. Nakamura and O. Ichinokura, "Dynamic simulation of planetary type magnetic gear based on reluctance network analysis," in *Proc. European Power Electron. & Appl. Conf.*, 2011.

[32] ——, “A method for optimizing the design of SPM type magnetic gear based on reluctance network analysis,” in *Int. Conf. on Electrical Machines (ICEM)*, 2012, pp. 30–35.

[33] L. Bronn, R.-J. Wang and M. Kamper, “Development of a shutter type magnetic gear,” in *Proc. the 19th Southern African Universities Power Engineering Conf. (SAUPEC), Johannesburg, South Africa*, Jan 2010.

[34] N. Niguchi, K. Hirata, M. Muramatsu and Y. Hayakawa, “Transmission torque characteristics in a magnetic gear,” in *Int. Conf. on Electr. Machines (ICEM)*, 2010.

[35] N. Niguchi and K. Hirata, “Cogging torque analysis of magnetic gear,” *IEEE T-IE*, vol. 59, no. 5, pp. 2189–2197, 2012.

[36] W. J. Mabe, “Magnetic transmission,” US Patent US5 013 949, May 7, 1991.

[37] C.-C. Huang, M.-C. Tsai, D. Dorrell and B.-J. Lin, “Development of a magnetic planetary gearbox,” *IEEE Trans. Magn.*, vol. 44, no. 3, pp. 403–412, 2008.

[38] F. Kong, Y. Ge, X. Zhu, L. Qiao and L. Quan, “Optimizing design of magnetic planetary gearbox for reduction of cogging torque,” in *IEEE Vehicle Power & Prop. Conf. (VPPC)*, 2013.

[39] G. Schuesler and J. Lindner, “Eccentric drive having magnetic torque transmission,” DE Pat. 19 944 428 441, 1995.

[40] F. Jørgensen, T. Andersen and P. Rasmussen, “The cycloid permanent magnetic gear,” *IEEE Trans. Ind. Appl.*, vol. 44, no. 6, pp. 1659–1665, 2008.

[41] J. Rens, R. Clark, S. Calverley, K. Atallah and D. Howe, “Design, analysis and realization of a novel magnetic harmonic gear,” in *Int. Conf. on Electr. Machines (ICEM)*, 2008.

[42] J. Rens, K. Atallah, S. Calverley and D. Howe, “A novel magnetic harmonic gear,” *IEEE Trans. Ind. Appl.*, vol. 46, no. 1, pp. 206–212, 2010.

[43] J. Rens, K. Atallah, S. D. Calverley and D. Howe, “A novel magnetic harmonic gear,” in *IEEE Int. Electric Machines Drives Conf. (IEMDC)*, 2007, pp. 698–703.

[44] K. Uppalapati and J. Bird, “A flux focusing ferrite magnetic gear,” in *IET Int. Conf. Power Electron., Machines & Drives*, 2012.

[45] K. Uppalapati, W. Bomela, J. Bird, M. Calvin and J. Wright, “Construction of a low speed flux focusing magnetic gear,” in *IEEE Energy Conv. Congress & Expo. (ECCE)*, 2013, pp. 2178–2184.

[46] L. Shah, A. Cruden and B. Williams, “A magnetic gear box for application with a contra-rotating tidal turbine,” in *Int. Conf. on Power Electron. & Drive Sys. (PEDS)*, 2007, pp. 989–993.

[47] D. J. Evans and Z. Zhu, “Influence of design parameters on magnetic gear’s torque capability,” in *IEEE Int. Electr. Machines Drives Conf. (IEMDC)*, 2011, pp. 1403–1408.

[48] N. Frank, S. Pakdelian and H. Toliyat, “A magnetic gear with passive transient suppression capability,” in *IEEE Electr. Ship Techn. Symp.*, 2011, pp. 326–329.

[49] R. Montague, C. Bingham and K. Atallah, “Magnetic gear overload detection and remedial strategies for servo-drive systems,” in *Int. Symp. Power Electron. Electr. Drives Automation & Motion (SPEEDAM)*, 2010, pp. 523–528.

[50] ——, “Dual-observer-based position-servo control of a magnetic gear,” *IET Electric Power Appl.*, vol. 5, no. 9, pp. 708–714, 2011.

[51] ——, “Servo control of magnetic gears,” *IEEE/ASME Trans. Mech.*, vol. 17, no. 2, pp. 269–278, 2012.

[52] P. Rasmussen, T. O. Andersen, F. T. Joergensen and O. Nielsen, “Development of a high performance magnetic gear,” in *38th IEEE-IAS Annual Meeting*, vol. 3, 2003, pp. 1696–1702.

[53] K. Atallah, S. Calverley and D. Howe, “Design, analysis and realisation of a high-performance magnetic gear,” *IEE Proc. Electr. Power Appl.*, vol. 151, no. 2, pp. 135–143, 2004.

[54] S. Gerber and R.-J. Wang, “Evaluation of a prototype magnetic gear,” in *IEEE Int. Conf. on Ind. Tech. (ICIT)*, 2013, pp. 319–324.

[55] M. Fukuoka, K. Nakamura and O. Ichinokura, “Experimental tests of surface PM magnetic gear,” in *Int. Conf. Electr. Machines & Sys.*, 2012.

[56] A. Razzell and J. Cullen, “Compact electrical machine,” US Pat. 6 794 781B2, 2004.

[57] K. Chau, D. Zhang, J. Jiang, C. Liu and Y. Zhang, “Design of a magnetic-geared outer-rotor permanent-magnet brushless motor for electric vehicles,” *IEEE Trans. Magn.*, vol. 43, no. 6, pp. 2504–2506, 2007.

[58] K. Atallah, S. Calverley, R. Clark, J. Rens and D. Howe, “A new PM machine topology for low-speed, high-torque drives,” in *Int. Conf. on Electr. Machines (ICEM)*, 2008.

[59] K. Atallah, J. Rens, S. Mezani and D. Howe, “A novel "pseudo" direct-drive brushless PM machine,” *IEEE Trans. Magn.*, vol. 44, no. 11, pp. 4349–4352, 2008.

[60] L. Jian, K. Chau and J. Jiang, “An integrated magnetic-geared permanent-magnet in-wheel motor drive for electric vehicles,” in *IEEE Vehicle Power & Prop. Conf.*, 2008.

[61] ——, “A magnetic-geared outer-rotor permanent-magnet brushless machine for wind power generation,” *IEEE Trans. Ind. Appl.*, vol. 45, no. 3, pp. 954–962, 2009.

[62] P. Rasmussen, T. V. Frandsen, K. K. Jensen and K. Jessen, “Experimental evaluation of a motor integrated permanent magnet gear,” in *IEEE Energy Conv. Congress & Expo. (ECCE)*, 2011, pp. 3982–3989.

[63] R.-J. Wang, L. Bronn, S. Gerber and P. Tlali, "Design and evaluation of a disc-type magnetically geared PM wind generator," in *Int. Conf. Power Eng., Energy & Electr. Drives (POWERENG)*, 2013, pp. 1259–1264.

[64] E. Gouda, S. Mezani, L. Baghli and A. Rezzoug, "Comparative study between mechanical and magnetic planetary gears," *IEEE Trans. Magn*, vol. 47, pp. 439–450, 2011.

[65] T. Lubin, S. Mezani and A. Rezzoug, "Analytical computation of the magnetic field distribution in a magnetic gear," *IEEE Trans. Magn.*, vol. 46, no. 7, pp. 2611–2621, 2010.

[66] R. Hosoya, H. Shimada and S. Shimomura, "Design of a ferrite magnet vernier machine for an in-wheel machine," in *Energy Conversion Congress and Exposition (ECCE), 2011 IEEE*, Sept 2011, pp. 2790–2797.

[67] N. Niguchi and K. Hirata, "Cogging torque characteristics of magnetic-geared motor," *COMPEL: The Int. J. for Computation & Mathematics in Electr. & Electron. Engineering*, vol. 31, no. 5, pp. 1470–1481, 2012.

[68] ——, "Torque ripple analysis of a magnetic-geared motor," in *Int. Conf. on Electr. Machines (ICEM)*, 2012, pp. 789–794.

[69] R. Qu, D. Li and J. Wang, "Relationship between magnetic gears and vernier machines," in *Int. Conf. on Electr. Machines & Sys.*, 2011.

[70] Z. Zhu and D. Howe, "Influence of design parameters on cogging torque in permanent magnet machines," *Energy Conversion, IEEE Transactions on*, vol. 15, no. 4, pp. 407 –412, Dec 2000.

[71] G. Vanderplaats, "A robust feasible directions algorithm for design synthesis," in *24th Structures, Structural Dynamics and Materials Conference*, 1983.

[72] ——, *Multidiscipline Design Optimization*, Vanderplaats Research & Development, Inc., 126 Bonifacio Place, Suite F, Monterey, CA 93940, 2007.

[73] J. Reinert, A. Brockmeyer and R. De Doncker, "Calculation of losses in ferro- and ferrimagnetic materials based on the modified Steinmetz equation," *Industry Applications, IEEE Transactions on*, vol. 37, no. 4, pp. 1055–1061, Jul 2001.

[74] H. Polinder and M. Hoeijmakers, "Eddy-current losses in the segmented surface-mounted magnets of a PM machine," *Electric Power Applications, IEE Proceedings* -, vol. 146, no. 3, pp. 261–266, 1999.

[75] S. Ho, S. Niu and W. Fu, "Transient analysis of a magnetic gear integrated brushless permanent magnet machine using circuit-field-motion coupled time-stepping finite element method," *IEEE Trans. Magn.*, vol. 46, no. 6, pp. 2074–2077, June 2010.

[76] A. Abdel-Razek, J. Coulomb, M. Feliachi and J. Sabonnadiere, "Conception of an air-gap element for the dynamic analysis of the electromagnetic field in electric machines," *IEEE Trans. Magn.*, vol. 18, no. 2, pp. 655–659, March 1982.

[77] T. Flack and A. Volschenk, "Computational aspects of time-stepping finite element analysis using an air-gap element," in *Proc. Int. Conf. Electrical Machines*, Paris, France, 1994, pp. 158–163.

[78] A. Abdel-Razek, J. Coulomb, M. Feliachi and J. Sabonnadiere, "The calculation of electromagnetic torque in saturated electric machines within combined numerical and analytical solutions of the field equations," *IEEE Trans. Magn.*, vol. 17, no. 6, pp. 3250–3252, November 1981.

[79] Y. Li and D. Aliprantis, "Optimal design of electromechanical devices using a hybrid finite element/air-gap element method," in *IEEE Power and Energy Conference at Illinois (PECI)*, Feb 2013, pp. 106–113.

[80] B. Davat, Z. Ren and M. Lajoie-Mazenc, "The movement in field modeling," *IEEE Trans. Magn.*, vol. 21, no. 6, pp. 2296–2298, November 1985.

[81] O. Antunes, J. Bastos and N. Sadowski, "Using high-order finite elements in problems with movement," *IEEE Trans. Magn.*, vol. 40, no. 2, pp. 529–532, 2004.

[82] B. Silwal, P. Rasilo, L. Perkkio, A. Hannukainen, T. Eirola and A. Arkkio, "Evaluation and comparison of different numerical computation methods for the electromagnetic torque in electrical machines," in *Proc. Int. Conf. Electrical Machines and Systems*, Oct 2013, pp. 837–842.

[83] J. Coulomb and G. Meunier, "Finite element implementation of virtual work principle for magnetic or electric force and torque computation," *IEEE Trans. Magn.*, vol. 20, no. 5, pp. 1894–1896, 1984.

[84] O. C. Zienkiewicz, *The Finite Element Method*, 3rd ed. Maidenhead, England: McGraw-Hill, 1977.

[85] N. Gibbs, W. Poole and P. Stockmeyer, "An algorithm for reducing the bandwidth and profile of a sparse matrix," *SIAM J. Numer. Anal.*, vol. 13, no. 2, pp. 236–250, April 1976.

[86] L. Dagum and R. Menon, "Openmp: an industry standard API for shared-memory programming," *IEEE Computational Science Engineering*, vol. 5, no. 1, pp. 46–55, Jan 1998.

[87] S. Gerber and R.-J. Wang, "Design of a magnetically geared PM machine," in *Proc. 4th Int. Conf. Power Engineering, Energy and Electrical Drives*, Istanbul, Turkey, May 2013, pp. 852 – 857.

[88] ——, "Implementation of a moving band solver for finite element analysis of electrical machines," in *Southern African Universities Power Engineering Conference (SAUPEC)*, Durban, South Africa, January 2014.

[89] K. Atallah, S. Calverley and D. Howe, "Design, analysis and realisation of a high-performance magnetic gear," *Electric Power Applications, IEE Proceedings -*, vol. 151, no. 2, pp. 135–143, March 2004.

[90] P. Rasmussen, T. Andersen, F. Jorgensen and O. Nielsen, “Development of a high-performance magnetic gear,” *Industry Applications, IEEE Transactions on*, vol. 41, no. 3, pp. 764–770, May-June 2005.

[91] P. Rasmussen, T. V. Frandsen, K. K. Jensen and K. Jessen, “Experimental evaluation of a motor integrated permanent magnet gear,” in *IEEE Energy Conversion Congress and Exposition (ECCE)*, September 2011, pp. 3982–3989.

[92] N. Frank and H. Toliyat, “Analysis of the concentric planetary magnetic gear with strengthened stator and interior permanent magnet inner rotor,” *Industry Applications, IEEE Transactions on*, vol. 47, no. 4, pp. 1652–1660, July-Aug 2011.

[93] S. Gerber and R.-J. Wang, “Evaluation of a prototype magnetic gear,” in *IEEE International Conference on Industrial Technology (ICIT)*, Cape Town, South Africa, February 2013.

[94] R. Zanis, A. Borisavljevic, J. Jansen and E. Lomonova, “Modeling, design and experimental validation of a small-sized magnetic gear,” in *Electrical Machines and Systems (ICEMS), 2013 International Conference on*, Oct 2013, pp. 560–565.

[95] J. Bastos and G. Quichaud, “3D modelling of a non-linear anisotropic lamination,” *Magnetics, IEEE Transactions on*, vol. 21, no. 6, pp. 2366 – 2369, Nov 1985.

[96] D. Evans and Z. Zhu, “Influence of design parameters on magnetic gear’s torque capability,” in *IEEE International Electric Machines and Drives Conference (IEMDC)*, May 2011, pp. 1403–1408.

[97] L. Brönn, R.-J. Wang and M. J. Kamper, “Development of a shutter type magnetic gear,” in *Proceedings of the 19th Southern African Universities Power Engineering Conference*, 2010.

[98] S. E. Skaar, Ø. Krøvel and R. Nilssen, “Distribution, coil-span and winding factors for PM machines with concentrated windings,” in *Electrical Machines (ICEM), 2006 XVII International Conference on*, September 2006.

[99] N. Frank and H. Toliyat, “Gearing ratios of a magnetic gear for wind turbines,” in *IEEE International Electric Machines and Drives Conference (IEMDC)*, May 2009, pp. 1224–1230.

[100] A. J. Rix, “Design, comparison and experimental evaluation of non-overlap winding radial flux permanent magnet hub drives for electric vehicles,” Ph.D. dissertation, Stellenbosch University, 2011.

[101] N. Bianchi and S. Bolognani, “Design techniques for reducing the cogging torque in surface-mounted PM motors,” *Industry Applications, IEEE Transactions on*, vol. 38, no. 5, pp. 1259 – 1265, Sep/Oct 2002.

[102] S. Gerber and R.-J. Wang, “Evaluation of a prototype magnetic gear,” in *IEEE International Conference on Industrial Technology (ICIT)*, February 2013, pp. 319–324.

[103] P. Tlali, “Design and performance evaluation of an outer stator magnetically geared permanent magnet machine,” Master’s thesis, Stellenbosch University, 2015.

[104] P. Tlali, S. Gerber and R.-J. Wang, “Optimal design of an outer-stator magnetically geared permanent magnet machine,” *Magnets, IEEE tracsactions on*, 2015, (In press).

[105] R. Qu, D. Li and J. Wang, “Relationship between magnetic gears and vernier machines,” in *Electrical Machines and Systems (ICEMS), 2011 International Conference on*, Aug 2011, pp. 1–6.

[106] Y. Chen and P. Pillay, “An improved formula for lamination core loss calculations in machines operating with high frequency and high flux density excitation,” in *Conference Record of the 37th IAS Annual Meeting.*, vol. 2, Oct 2002, pp. 759–766.

[107] E. Dlala, “Comparison of models for estimating magnetic core losses in electrical machines using the finite-element method,” *IEEE Trans. Magn.*, vol. 45, no. 2, pp. 716–725, February 2009.

[108] R. G. Harrison, “Positive-feedback theory of hysteretic recoil loops in hard ferromagnetic materials,” *IEEE Trans. Magn.*, vol. 47, no. 1, pp. 175–191, January 2011.

[109] ——, “Modeling high-order ferromagnetic hysteretic minor loops and spirals using a generalized positive-feedback theory,” *IEEE Trans. Magn.*, vol. 48, no. 3, pp. 1115–1129, March 2012.

Appendices

Appendix A

Trigonometry

A.1 Standard integration formulae

$$\int_0^{2\pi} \cos^2(ax+b)\mathrm{d}x = \pi \tag{A.1}$$

A.2 Integration of modulated harmonics

In the derivation of the formula for torque in a magnetic gear, integrals of the following form appear

$$I = \int_0^{2\pi} \sin(ax+b)\cdot\cos(cx+d)\mathrm{d}x \tag{A.2}$$

The integrand can be expanded using the identities,

$$\sin(A \pm B) = \sin A \cos B \pm \cos A \sin B \tag{A.3}$$

$$\cos(A \pm B) = \cos A \cos B \mp \sin A \sin B \tag{A.4}$$

$$\tag{A.5}$$

giving

$$\sin(ax+b)\cos(cx+d) \tag{A.6}$$

$$= (\sin ax \cdot \cos b + \cos ax \cdot \sin b)\cdot(\cos cx \cdot \cos d - \sin cx \cdot \sin d) \tag{A.7}$$

$$\begin{aligned} &= \cos b \cdot \cos d \cdot \sin ax \cdot \cos cx - \cos b \cdot \sin d \cdot \sin ax \cdot \sin cx + \\ &\quad \sin b \cdot \cos d \cdot \cos ax \cdot \cos cx - \sin b \cdot \sin d \cdot \cos ax \cdot \sin cx \end{aligned} \tag{A.8}$$

The integral (A.2) then becomes

$$\begin{aligned} I =& \cos b \cdot \cos d \cdot \int_0^{2\pi} \sin ax \cdot \cos cx \ \mathrm{d}x - \cos b \cdot \sin d \cdot \int_0^{2\pi} \sin ax \cdot \sin cx \ \mathrm{d}x + \\ & \sin b \cdot \cos d \cdot \int_0^{2\pi} \cos ax \cdot \cos cx \ \mathrm{d}x - \sin b \cdot \sin d \cdot \int_0^{2\pi} \cos ax \cdot \sin cx \ \mathrm{d}x \end{aligned} \tag{A.9}$$

The integrals are all zero when $|a| \neq |c|$. If $a = c$ the result is

$$\begin{aligned} I &= \pi \cdot (\sin b \cdot \cos d - \cos b \cdot \sin d) \\ &= \pi \cdot \sin(b-d) \end{aligned} \tag{A.10}$$

Otherwise, if $a = -c$

$$\begin{aligned} I &= \pi \cdot (\sin b \cdot \cos d + \cos b \cdot \sin d) \\ &= \pi \cdot \sin(b + d) \end{aligned} \tag{A.11}$$

Thus, the result of the integral is

$$I = \begin{cases} 0 & \text{if } |a| \neq |c| \\ \pi \cdot \sin(b - d) & \text{if } a = c \\ \pi \cdot \sin(b + d) & \text{if } a = -c \end{cases} \tag{A.12}$$

In the derivation of the formula for the energy stored in the air-gaps of magnetic gears, integrals of the following form appear,

$$I = \int_0^{2\pi} \cos(ax + b) \cdot \cos(cx + d)\mathrm{d}x \tag{A.13}$$

The integrand can be expanded using (A.4)

$$\cos(ax + b) \cdot \cos(cx + d) \tag{A.14}$$

$$= (\cos ax \cdot \cos b - \sin ax \cdot \sin b) \cdot (\cos cx \cdot \cos d - \sin cx \cdot \sin d) \tag{A.15}$$

$$\begin{aligned} &= \cos b \cdot \cos d \cdot \cos ax \cdot \cos cx - \cos b \cdot \sin d \cdot \cos ax \cdot \sin cx - \\ &\quad \sin b \cdot \cos d \cdot \sin ax \cdot \cos cx + \sin b \cdot \sin d \cdot \sin ax \cdot \sin cx \end{aligned} \tag{A.16}$$

The integral (A.13) then becomes

$$\begin{aligned} I = {} & \cos b \cdot \cos d \cdot \int_0^{2\pi} \cos ax \cdot \cos cx \ \mathrm{d}x - \cos b \cdot \sin d \cdot \int_0^{2\pi} \cos ax \cdot \sin cx \ \mathrm{d}x - \\ & \sin b \cdot \cos d \cdot \int_0^{2\pi} \sin ax \cdot \cos cx \ \mathrm{d}x + \sin b \cdot \sin d \cdot \int_0^{2\pi} \sin ax \cdot \sin cx \ \mathrm{d}x \end{aligned} \tag{A.17}$$

The integrals are all zero when $|a| \neq |c|$. If $a = c$ the result is

$$\begin{aligned} I &= \pi \cdot (\cos b \cdot \cos d + \sin b \cdot \sin d) \\ &= \pi \cdot \cos(b - d) \quad \text{if } a = c \end{aligned} \tag{A.18}$$

Otherwise, if $a = -c$

$$\begin{aligned} I &= \pi \cdot (\cos b \cdot \cos d - \sin b \cdot \sin d) \\ &= \pi \cdot \cos(b + d) \quad \text{if } a = -c \end{aligned} \tag{A.19}$$

Thus, the result of the integral is

$$I = \begin{cases} 0 & \text{if } |a| \neq |c| \\ \pi \cdot \cos(b - d) & \text{if } a = c \\ \pi \cdot \cos(b + d) & \text{if } a = -c \end{cases} \tag{A.20}$$

Appendix B

Analytical model equations

In the case where $p_r = Q_m + p_s$, the integral (2.27) becomes

$$I_{\phi i} = \int_0^{2\pi} (\phi_s^2 + 2\phi_s\phi_{rm-} + \phi_{rmf}^2 + \phi_{rm-}^2 + \phi_{rm+}^2)\mathrm{d}\theta \tag{B.1}$$

Similarly, the integral for the outer air-gap is

$$I_{\phi o} = \int_0^{2\pi} (\phi_r^2 + 2\phi_r\phi_{hm+} + \phi_{hmf}^2 + \phi_{hm-}^2 + \phi_{hm+}^2)\mathrm{d}\theta \tag{B.2}$$

The torque on the ring gear is calculated as the change in co-energy in both air-gaps due to rotation of the ring gear:

$$T_r = \frac{\partial W_i'}{\partial \theta_r} + \frac{\partial W_o'}{\partial \theta_r} \tag{B.3}$$

$$= C_i\frac{\partial I_{\phi i}}{\partial \theta_r} + C_o\frac{\partial I_{\phi o}}{\partial \theta_r} \tag{B.4}$$

$$\frac{\partial I_{\phi i}}{\partial \theta_r} = \frac{\partial}{\partial \theta_r}\int_0^{2\pi} (\phi_s^2 + 2\phi_s\phi_{rm-} + \phi_{rmf}^2 + \phi_{rm-}^2 + \phi_{rm+}^2)\mathrm{d}\theta \tag{B.5}$$

$$\frac{\partial I_{\phi o}}{\partial \theta_r} = \frac{\partial}{\partial \theta_r}\int_0^{2\pi} (\phi_r^2 + 2\phi_r\phi_{hm+} + \phi_{hmf}^2 + \phi_{hm-}^2 + \phi_{hm+}^2)\mathrm{d}\theta \tag{B.6}$$

In the above, the integrals of the quadratic terms are all independent of θ_r, and thus they do not contribute to the torque. From these equations it can be seen that only the modulated harmonics with the same order as that of the opposite source contribute to the torque.

$$\frac{\partial I_{\phi i}}{\partial \theta_r} = \frac{\partial}{\partial \theta_r}\int_0^{2\pi} (2\phi_s\phi_{rm-})\mathrm{d}\theta \tag{B.7}$$

$$= \frac{\partial}{\partial \theta_r}\int_0^{2\pi} 2M_s\mathcal{P}_{avg}\cos(p_s\theta - p_s\theta_s)\cdot \\ \frac{M_r\mathcal{P}_{mod}}{2}\cos((p_r - Q_m)\theta - p_r\theta_r + Q_m\theta_m)\mathrm{d}\theta \tag{B.8}$$

$$\frac{\partial I_{\phi o}}{\partial \theta_r} = \frac{\partial}{\partial \theta_r}\int_0^{2\pi} (2\phi_r\phi_{hm+})\mathrm{d}\theta \tag{B.9}$$

$$= \frac{\partial}{\partial \theta_r}\int_0^{2\pi} 2M_r\mathcal{P}_{avg}\cos(p_r\theta - p_r\theta_r))\cdot \tag{B.10}$$

$$\frac{M_s\mathcal{P}_{mod}}{2}\cos((Q_m + p_s)\theta - p_s\theta_s - Q_m\theta_m)\mathrm{d}\theta \tag{B.11}$$

When $p_s = p_r - Q_m$, the integrals can be evaluated using (A.20), giving

$$\frac{\partial I_{\phi i}}{\partial \theta_r} = \frac{\partial}{\partial \theta_r}\left(M_s M_r \mathcal{P}_{avg} \mathcal{P}_{mod} \cos(-p_s\theta_s + p_r\theta_r - Q_m\theta_m)\right) \tag{B.12}$$

$$= p_r M_s M_r \mathcal{P}_{avg} \mathcal{P}_{mod} \sin(p_s\theta_s - p_r\theta_r + Q_m\theta_m) \tag{B.13}$$

$$\frac{\partial I_{\phi o}}{\partial \theta_r} = \frac{\partial}{\partial \theta_r}\left(M_s M_r \mathcal{P}_{avg} \mathcal{P}_{mod} \cos(-p_r\theta_r + p_s\theta_s + Q_m\theta_m)\right) \tag{B.14}$$

$$= p_r M_s M_r \mathcal{P}_{avg} \mathcal{P}_{mod} \sin(-p_r\theta_r + p_s\theta_s + Q_m\theta_m) \tag{B.15}$$

Note that $\frac{\partial I_{\phi i}}{\partial \theta_r} = \frac{\partial I_{\phi o}}{\partial \theta_r}$. Substituting (B.13) and (B.15) back into (B.4), the torque on the ring gear can be expressed as

$$T_r = (C_i + C_o)\, p_r M_s M_r \mathcal{P}_{avg} \mathcal{P}_{mod} \sin(p_s\theta_s - p_r\theta_r + Q_m\theta_m) \tag{B.16}$$

$$T_r = \frac{\ln \frac{r_{igo}}{r_{igi}} + \ln \frac{r_{ogo}}{r_{ogi}}}{8\mu_0\pi^2 L} p_r M_s M_r \mathcal{P}_{avg} \mathcal{P}_{mod} \sin(p_s\theta_s - p_r\theta_r + Q_m\theta_m) \tag{B.17}$$

$$T_r = \frac{p_r M_s M_r \mathcal{P}_{avg} \mathcal{P}_{mod}}{8\mu_0\pi^2 L}\left(\ln \frac{r_{igo}}{r_{igi}} + \ln \frac{r_{ogo}}{r_{ogi}}\right) \sin(p_s\theta_s - p_r\theta_r + Q_m\theta_m) \tag{B.18}$$

$$\tag{B.19}$$

Similar formulae for the torque on the sun gear and the modulator can be derived. To summarize the torque on the three components in a magnetic gear, expressed in terms of permeances per unit of stack length, are:

$$T_s = -\frac{p_s L M_s M_r \mathcal{P}^l_{avg} \mathcal{P}^l_{mod}}{8\mu_0\pi^2}\left(\ln \frac{r_{igo} r_{ogo}}{r_{igi} r_{ogi}}\right) \sin(p_s\theta_s - p_r\theta_r + Q_m\theta_m) \tag{B.20}$$

$$T_r = \frac{p_r L M_s M_r \mathcal{P}^l_{avg} \mathcal{P}^l_{mod}}{8\mu_0\pi^2}\left(\ln \frac{r_{igo} r_{ogo}}{r_{igi} r_{ogi}}\right) \sin(p_s\theta_s - p_r\theta_r + Q_m\theta_m) \tag{B.21}$$

$$T_m = -\frac{Q_m L M_s M_r \mathcal{P}^l_{avg} \mathcal{P}^l_{mod}}{8\mu_0\pi^2}\left(\ln \frac{r_{igo} r_{ogo}}{r_{igi} r_{ogi}}\right) \sin(p_s\theta_s - p_r\theta_r + Q_m\theta_m) \tag{B.22}$$

The load angle in a magnetic gear is the argument of the sine function in (B.20), (B.21) and (B.22).

$$\delta = p_s\theta_s - p_r\theta_r + Q_m\theta_m \tag{B.23}$$

Appendix C

Calculation of core loss using a dynamic hysteresis model

In the laminated cores of electrical machines, the relationship between the magnetic field strength H and the magnetic flux density B is complex. Due to the difficulty in accurately describing this relationship and the computational cost involved in doing so, common practice in finite element modeling is to assume a single-valued relationship between B and H such as shown in Fig. C.1. Although this approach is sufficiently accurate for many problems, it does have drawbacks. Using this approach, losses in laminated cores are usually calculated by post-processing the magnetic field solution. A simple way of calculating the losses is to use the Steinmetz equation [73]:

$$p_v = C_m f^{\alpha} \hat{B}^{\beta} \tag{C.1}$$

where p_v is the specific power loss, f is the excitation frequency, $\hat{B}$ is the peak flux density and C_m, α and β are model parameters. The parameters of the lamination model can be obtained by fitting the model to measured core loss data provided by manufacturers. Unfortunately, this formula is not very accurate over a wide range of frequencies and peak flux densities. Many attempts have been made to improve the accuracy of this type of approach. According to the statistical loss theory, the losses under sinusoidal excitation can be calculated using [106]

$$\begin{aligned} P_c &= P_h + P_e + P_a \\ &= k_h f B^n + k_e f^2 B^2 + k_a f^{1.5} B^{1.5} \end{aligned} \tag{C.2}$$

where k_h, n, k_e and k_a are model parameters. Two important problems with such approaches are that the losses are not accurately calculated for different excitation waveforms and that the losses are not accounted for in the solution of the magnetic field.

An alternative is to model the exact relationship between B and H over time. One method of accomplishing this is derived from the statistical loss theory. Using this approach, the magnetic field strength comprises three components [107].

$$H(t, B) = H_h(t, B) + H_{cl}(t, B) + H_{ex}(t, B) \tag{C.3}$$

In the above, H_h is obtained from a static hysteresis model, $H_{cl} = C_{cl}\frac{\mathrm{d}B}{\mathrm{d}t}$ represents the classical eddy-current field and $H_{ex} = C_{ex}\delta\sqrt{|\frac{\mathrm{d}B}{\mathrm{d}t}|}$ represents the excess field.

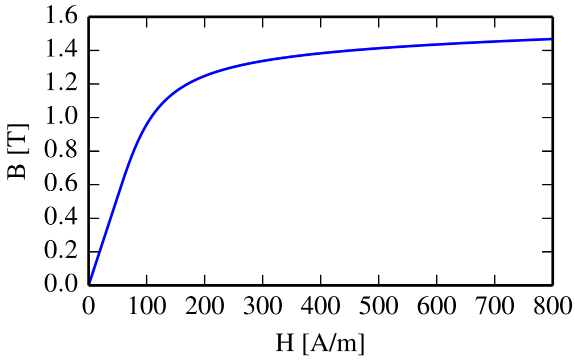

Figure C.1: A single valued BH-curve commonly used in finite element simulations.

In the work done thus far, a static hysteresis model based on the work presented in [108, 109] has been implemented. Some sample hysteresis loops produced by this model are shown in Figs. C.2 – C.4.

When the classical eddy-current and excess fields are added, the hysteresis loops change shape as the frequency is increased. This is illustrated in Fig. C.5 where hysteresis loops for sinusoidal excitation at different frequencies are compared.

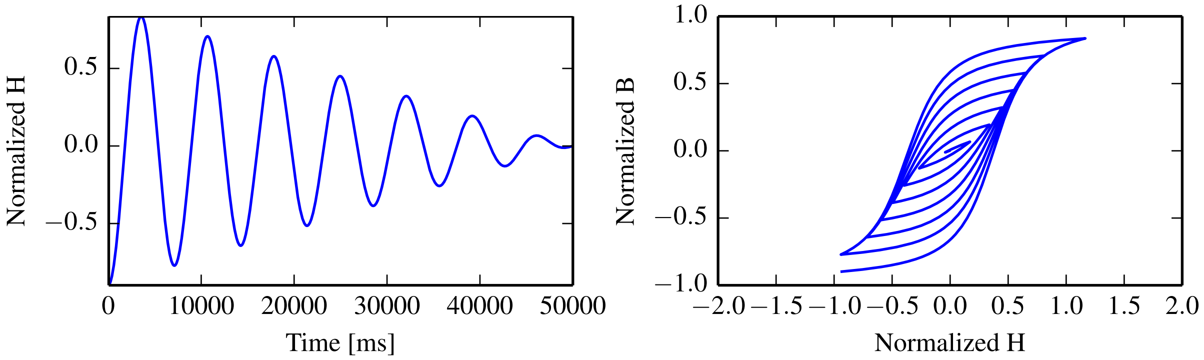

(a) Signal.

(b) Hysteresis loops.

Figure C.2: Hysteresis loops for a demagnetizing spiral.

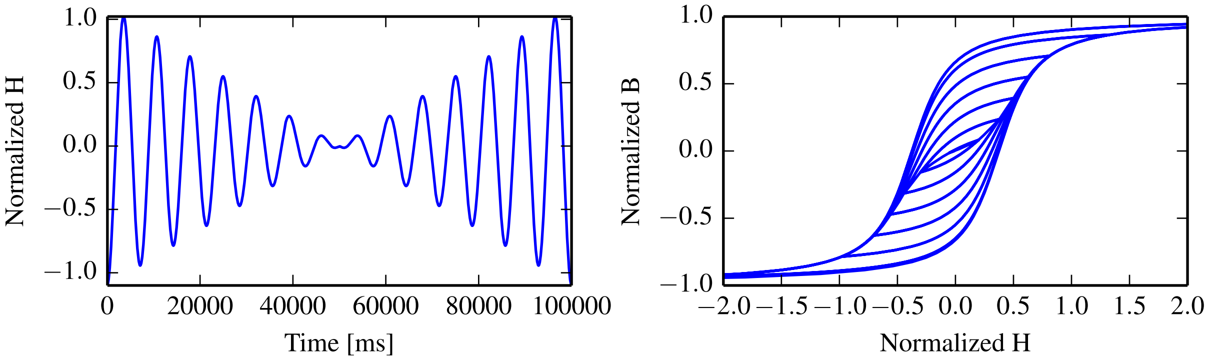

(a) Signal.

(b) Hysteresis loops.

Figure C.3: Hysteresis loops for a demagnetizing spiral followed by remagnetization with increasing amplitude.

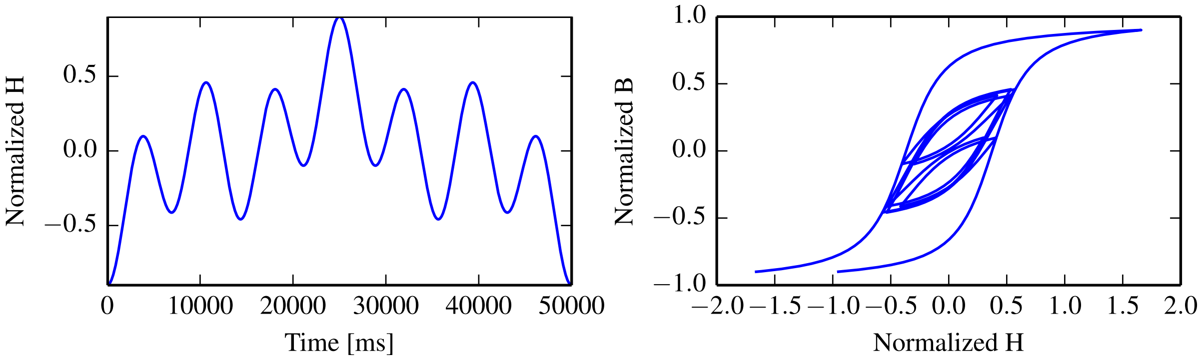

(a) Signal. (b) Hysteresis loops.

Figure C.4: Hysteresis loops for a signal consisting of three harmonics.

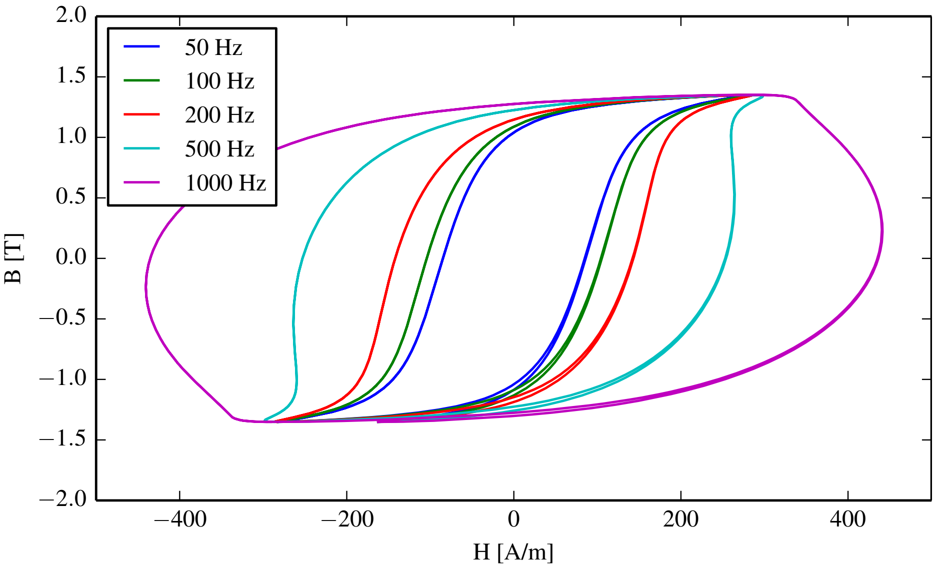

Figure C.5: Comparison of hysteresis loops for sinusoidal excitation at different frequencies.

Equation C.3 provides a dynamic hysteresis model in one dimension. In electrical machines, the magnetic field in the lamination steel usually has a two-dimensional nature. Thus, a vector hysteresis model is required. This allows “rotational loss” to be calculated. The approach followed in [107] has been adopted, whereby the magnetic field strength is calculated as the vectorial sum of several one-dimensional models given by (C.3), i.e.

$$\mathbf{H}(t,\mathbf{B}) = \frac{1}{Q(N)}\sum_{i=1}^{N}\mathbf{e}_{\varphi_i}H_{\varphi_i}(t,B_{\varphi_i}) \tag{C.4}$$

where N is the number of one-dimensional models used, Q is a parameter and $\mathbf{e}_{\varphi_i}$ is a unit vector in the direction of a one-dimensional model.

The power loss can be calculated using the Poynting vector theorem [107]

$$P = \frac{1}{T}\int_T \mathbf{H}\cdot\frac{\mathrm{d}\mathbf{B}}{\mathrm{d}t}\mathrm{d}t \tag{C.5}$$

The next step is to incorporate the dynamic vector hysteresis model given by (C.4) into a finite element simulation.